



**Type-II Superlattices for Mid and Long  
Wavelength Infrared Photodetectors  
Grown by Metal-Organic Chemical  
Vapour Deposition**

Richard James Lawson Brown

A thesis submitted as partial fulfilment for the degree  
of *Doctor of Philosophy*

School of Physics and Astronomy

**September 2024**

---

# Abstract

Infrared devices play an important role in cutting edge applications including defence and security, gas detection, biomedical sensing, thermal imaging and 3D sensing. Antimony (Sb) based type-II superlattice (T2SL) materials are a strong candidate for next generation infrared technologies and are now considered as a viable alternative to the state-of-the-art mercury cadmium telluride (MCT).

To date, molecular beam epitaxy (MBE) has been the prevailing technique for growing Sb-containing structures. However, the commercial exploitation potential using metal-organic chemical vapor deposition (MOCVD) is highly attractive if material and device performance can be improved to close the gap with MBE results. This work focuses on the two main Sb-based T2SLs, the InAs/GaSb T2SL and InAs/InAsSb T2SL. All the growth performed in this work was done via MOCVD.

The growth and fabrication of long wave infrared InAs/GaSb T2SL photodetectors were investigated. Resulting in a InAs/GaSb T2SL nBn photodetector grown on an InAs substrate with a cutoff wavelength of 13.5  $\mu\text{m}$  and a peak detectivity of  $4.43 \times 10^{10} \text{ cm Hz}^{1/2}/\text{W}$  at 77K.

The InAs/InAsSb T2SL was grown on GaSb substrates and fabricated with a cutoff wavelength of 5.5  $\mu\text{m}$  and a peak detectivity of  $1.14 \times 10^{12} \text{ cm Hz}^{1/2}/\text{W}$  at 77K.

As well as growing the InAs/InAsSb T2SL on its native GaSb substrates. The InAs/InAsSb T2SL was grown on highly mismatched GaAs and Si substrates which have large economic benefits. An InAs/InAsSb PIN photodetector with a 100% cutoff wavelength of 5.25  $\mu\text{m}$  was then successfully grown on the GaAs substrates. With a peak detectivity was  $7.44 \times 10^{10} \text{ cm Hz}^{1/2}/\text{W}$  at 77K.

The device performance in this work is competitive to current state of the art MBE results indicating that MOCVD can be considered a viable alternative to MBE for the growth of Sb based T2SL IR detectors at both mid and long Infrared wavelengths.

# Table of Contents

Abstract.....	i
Publications.....	v
List of Figures .....	vi
List of Tables .....	xii
List of Acronyms.....	xiii
Funding .....	xiv
Acknowledgements.....	xv
Chapter 1: Introduction.....	1
1.1 Infrared Detector Applications .....	1
1.2 Current Infrared Detector Technology.....	3
1.3 Thesis Overview.....	4
Chapter 2: Background.....	5
2.1 Infrared Radiation.....	5
2.2 Infrared Detectors .....	7
2.2.1 Figures of Merit.....	7
2.2.2 The PN Photodetector .....	10
2.2.3 Barrier Photodetectors.....	11
2.3 The Type-II Superlattice Detector .....	14
2.3.1 MCT and rule 07 .....	14
2.3.2 The Type-II Superlattice.....	15
2.3.3 The Ga-based InAs/GaSb T2SL.....	19
2.3.4 The Ga-free InAs/InAsSb T2SL .....	20
2.4 Review of the current state-of-the-art.....	22
2.4.1 Minority carrier lifetime .....	22
2.4.2 Dark current .....	23
2.4.3 External quantum efficiency.....	26
2.4.4 Detectivity.....	28
2.5 T2SL growth (MBE vs MOCVD).....	31
2.4.1 MOCVD Growth of InAs/GaSb .....	32
2.4.2 MOCVD Growth of InAs/InAsSb.....	33
2.4.3 Growth on non-native substrates.....	34

---

<b>Chapter 3: Research Tools</b> .....	<b>36</b>
3.1 Metal-organic chemical vapour deposition (MOCVD).....	36
3.1.1 In-situ Monitoring .....	40
3.2 Fabrication.....	41
3.3 Characterisation Techniques .....	48
3.3.1 Atomic Force Microscopy (AFM) .....	48
3.3.2 X-ray Diffraction (XRD) .....	49
3.3.3 Electron channelling contrast imaging (ECCI) .....	51
3.3.4 Transmission Electron Microscopy (TEM).....	52
3.3.5 Secondary ion mass spectrometry (SIMS).....	55
3.3.6 Photoluminescence (PL) .....	56
3.3.7 Fourier Transform Infrared Spectrometry (FTIR) .....	56
3.3.8 Electrical characterisation .....	59
<b>Chapter 4: LWIR detectors made from InAs/GaSb T2SLs</b> .....	<b>60</b>
4.1 Introduction.....	60
4.2 Growth of InAs/GaSb T2SLs .....	61
4.2.1 Growth temperature .....	62
4.2.2 GaSb V/III ratio .....	64
4.2.3 InAs V/III ratio .....	66
4.2.4 InAs/GaSb T2SLs spanning the 4-12 $\mu$ m wavelength range .....	67
4.2.5 InAs/GaSb T2SL device growth .....	72
4.3 Device Results.....	75
4.3.1 Surface Passivation.....	75
4.3.2 Wet Vs Dry etch.....	81
4.3.3 Dark current mechanisms.....	84
4.3.4 Optical device results .....	86
4.4 Summary .....	92

---

<b>Chapter 5: MWIR detectors made from InAs/InAsSb T2SLs .....</b>	<b>94</b>
5.1 Introduction.....	94
5.2 Growth of InAs/InAsSb T2SLs.....	95
5.2.1 Growth temperature .....	96
5.2.2 Growth Interruption.....	99
5.2.3 Optical Properties of the T2SL .....	101
5.2.4 InAs/InAsSb device growth.....	102
5.3 Device Results.....	104
5.3.1 Dark current .....	104
5.3.2 Optical device results .....	106
5.4 Summary .....	111
<b>Chapter 6: Growth of InAs/InAsSb T2SLs on non-native substrates.</b>	<b>112</b>
6.1 Introduction.....	112
6.2 InAs/InAsSb T2SLs Detectors on GaAs Substrates.....	113
6.2.1 Growth of GaSb on GaAs .....	115
6.2.2 MWIR InAs/InAsSb T2SL detectors on GaAs .....	119
6.3 Growth of InAs/InAsSb T2SLs on Si .....	128
6.4 Summary .....	136
<b>Chapter 7: Conclusions and Future work.....</b>	<b>137</b>
7.1. LWIR Detectors made from InAs/GaSb T2SLs .....	137
7.1.1 Conclusion.....	137
7.1.2 Future work.....	138
7.2 MWIR Detectors made from InAs/InAsSb T2SLs .....	139
7.2.1 Conclusion.....	139
7.2.2 Future work.....	140
7.3 Growth of InAs/InAsSb T2SLs on non-native Substrates .....	141
7.3.1 Conclusion.....	141
7.3.2 Future work.....	142
<b>References .....</b>	<b>143</b>

# Publications

[1] **R. Brown**, B.P. Ratiu, H. Jia, K.M. Azizur-Rahman, M. Dang, M. Tang, B. Liang, H. Liu, Q. Li, Mid-infrared InAs/InAsSb Type-II superlattices grown on silicon by MOCVD, *J. Cryst. Growth* 598 (2022).

This article is directly relevant to chapter 5 and 6 of this thesis. In this article the recipe development, growth and all data analysis was performed by me. All of the paper was written by me.

**R. Brown**, C. Liu, G. Seager, F. Alvarado, K. M. Wong, A. Craig, R. Beanland, A. Marshall, J. I. Davies, Q. Li, 13 $\mu$ m cutoff InAs/GaSb Type-II superlattice nBn detectors with high quantum efficiency grown by MOCVD. Submitted to *APL Photonics* (2024)

This article has been accepted by *APL Photonics* and is due to be published after the submission of this thesis. This article is directly relevant to chapter 4 of this thesis. In this article the recipe development, growth and all data analysis was performed by me. All of the paper was written by me.

## Papers presented in conferences:

**R. Brown**, C. Liu, G. Seager, F. Alvarado, K. M. Wong, R. Beanland, A. Marshall, J. I. Davies, Q. Li, MOVPE growth of InAs/GaSb Type-II superlattices for infrared detectors. International Conference on Metal Organic Vapor Phase Epitaxy (ICMOVPE XXI) (2024).

**R. Brown**, C. Liu, G. Seager, K. M. Wong, A. Marshall, J. I. Davies, Q. Li, MOCVD growth of InAs/GaSb Type-II superlattices for infrared detectors. *Semiconductor Integrated Optoelectronics (SIOE)* (2024).

**R. Brown**, C. Liu, G. Seager, K. M. Wong, A. Marshall, J. I. Davies, Q. Li, MOCVD growth of Sb-based Type-II superlattices from 3-10 $\mu$ m. *UK Semiconductors* (2023).

**R. Brown**, B.P. Ratiu, H. Jia, K.M. Azizur-Rahman, M. Dang, M. Tang, B. Liang, H. Liu, Q. Li, Mid-infrared InAs/InAsSb Type-II superlattices grown on Si by MOVPE. International Conference on Metal Organic Vapor Phase Epitaxy (ICMOVPE XXI) (2022).

**R. Brown**, B.P. Ratiu, H. Jia, K.M. Azizur-Rahman, M. Dang, M. Tang, B. Liang, H. Liu, Q. Li, Mid-infrared InAs/InAsSb Type-II superlattices grown on Si by MOCVD. *UK Semiconductors* (2022).

**R. Brown**, B.P. Ratiu, H. Jia, K.M. Azizur-Rahman, M. Dang, M. Tang, B. Liang, H. Liu, Q. Li, Growth of InAs/InAsSb Type-II superlattices onto Si substrates by MOCVD. *Semiconductor Integrated Optoelectronics (SIOE)* (2022).

# List of Figures

- Fig. 1.1.** Graph showing the various important gases that can be detected in the MWIR spectral region.
- Fig. 2.1.** Wien's law superimposed on blackbody radiation curves created using Plank's law.
- Fig. 2.2.** Atmospheric transmission windows from NIR to VLWIR.
- Fig. 2.3.** Schematic diagram of a PN photodetector under reverse bias.
- Fig. 2.4.** Schematic diagram of a PIN photodetector under reverse bias.
- Fig. 2.5.** Schematic diagram of a nBn photodetector under reverse bias
- Fig. 2.6.** Schematic diagram showing (a) the deep mesa etch and (b) the shallow mesa etch of an nBn photodetector.
- Fig. 2.7.** The 3 different heterostructure band alignment types.
- Fig. 2.8.** A single finite quantum well showing the first two energy levels.
- Fig. 2.9.** Two overlapping quantum wells showing the splitting of the energy levels.
- Fig. 2.10.** N quantum wells leading to the formation of minibands.
- Fig. 2.11** The formation of minibands from a type-II superlattice structure.
- Fig. 2.12.** Collected minority carrier lifetimes vs cutoff wavelength for InAs/GaSb and InAs/InAsSb type-II superlattices and MCT.
- Fig. 2.13.** Collected data of dark current density versus cutoff wavelength at 77K for Barrier-based InAs/GaSb, Non-Barrier InAs/GaSb, Barrier-Based InAs/InAsSb and Non-Barrier InAs/InAsSb detectors. To be compared with MCT detectors and the "Rule 07" line.
- Fig. 2.14.** Collected data of dark current density versus cutoff wavelength at 150K for Barrier-based InAs/GaSb, Non-Barrier InAs/GaSb, Barrier-Based InAs/InAsSb and Non-Barrier InAs/InAsSb detectors. To be compared with the "Rule 07" line.
- Fig. 2.15.** Collected data of EQE versus absorber layer thickness at 77K for (a) MWIR MCT, Barrier-based InAs/GaSb, Non-Barrier InAs/GaSb, Barrier-Based InAs/InAsSb and Non-Barrier InAs/InAsSb detectors. (b) LWIR MCT, Barrier-Based InAs/GaSb and Barrier-Based InAs/InAsSb LWIR detectors.
- Fig. 2.16.** Collected data of peak detectivity versus wavelength at (a) 77K for MCT [2,3], Barrier-based InAs/GaSb [4–19], Non-Barrier InAs/GaSb [9,12,17,20–26], Barrier-Based InAs/InAsSb [27–31] and Non-Barrier InAs/InAsSb detectors [32–37]. (b) At 150K for Barrier-based InAs/GaSb [4,7,8,38], Non-Barrier InAs/GaSb [17,20], Barrier-Based InAs/InAsSb [28–30,39–46] and Non-Barrier InAs/InAsSb detectors [33,47]. The "Rule 07" line is added for reference to (a) and is calculated from the rule 07 dark current density line at 77K with the QE of the MCT detectors assumed to be 75%.
- Fig. 2.17.** Graph showing the difference in absorption coefficients between GaSb and GaAs.

**Fig. 3.1.** Schematic diagrams of the 3 main types of MOCVD reactors: (a) horizontal reactors, (b) planetary reactors and (c) close-coupled showerhead reactors.

**Fig. 3.2.** Photographs of the Aixtron 3 x 2 inch flip top CCS reactor that was used throughout this project. (a) Shows the whole MOCVD system including the housing and glovebox. (b) Shows the CCS reactor itself which is found within the glovebox.

**Fig. 3.3.** Simplified MOCVD growth mechanism of GaSb.

**Fig. 3.4.** Schematic diagram of a typical InAs/GaSb nBn detector epitaxial stack.

**Fig. 3.5.** Schematic diagram of a typical InAs/GaSb nBn detector after; (a) SiO<sub>2</sub> hard mask deposition, (b) the deposition and development of the photoresist and (c) the plasma etching of the SiO<sub>2</sub> hard mask.

**Fig. 3.6.** (a) Schematic diagram of a typical InAs/GaSb nBn detector after the removal of the photoresist. (b) Optical microscope picture of the surface of the sample before mesa etch.

**Fig. 3.7.** (a) Schematic diagram of a typical InAs/GaSb nBn detector after the mesa etch. (b) Scanning Electron Microscope (SEM) picture of the top of an individual device after the mesa etch. (c) SEM picture of the side profile of an individual device after the mesa etch.

**Fig. 3.8.** (a) Schematic diagram of a typical InAs/GaSb nBn detector with the photoresist ready for metal deposition. (b) Optical microscope picture of the surface of the sample before metal deposition.

**Fig. 3.9.** (a) Schematic diagram of a typical InAs/GaSb nBn detector after metal deposition. (b) Optical microscope picture of the surface of the sample after metal deposition.

**Fig. 3.10.** Schematic diagram of a typical passivated InAs/GaSb nBn detector.

**Fig. 3.11.** Schematic diagram of an atomic force microscope.

**Fig. 3.12.** Schematic of XRD in a crystal lattice.

**Fig. 3.13.** Schematic diagram of an X-ray diffractometer.

**Fig. 3.14.** Schematic diagram of a typical Scanning Electron Microscope.

**Fig. 3.15.** Schematic diagram of electron channelling contrast imaging. In case A, the crystal has no defects so the probability of an electron hitting an atom is relatively low resulting in few backscattering events. In case B, the crystal has defects causing it to not be perfectly cubic, increasing the probability of an electron hitting an atom resulting in more backscattering events.

**Fig. 3.16.** Schematic diagram of a typical Transmission Electron Microscope.

**Fig. 3.17.** Schematic diagram of Secondary Ion Mass Spectrometry.

**Fig. 3.18.** Schematic diagram of the photoluminescence process.

**Fig. 3.19.** Schematic diagram of a Fourier transform infrared spectrometer.

**Fig. 3.20.** Schematic diagram of the blackbody calibration setup.

**Fig. 3.21.** Schematic diagram of the cryogenic probe station set-up.

**Fig. 3.22.** Optical microscope picture of a CTLM array from a device in this work. Probes and a device analyser have been added to help illustrate how the CTLM array is probed to find sheet and contact resistance.

**Fig. 4.1.** MOCVD growth timeline of one period of the InAs/GaSb T2SL. Shows the growth interruption interfacial sequence that creates the “GaAs-like” interfaces.

**Fig. 4.2.** AFM surface scans of 50 period 21ML/8ML InAs/GaSb T2SLs grown at three different surface temperatures.

**Fig. 4.3.** (a) Omega 2 Theta XRD scans of 50 period 21ML/8ML InAs/GaSb T2SLs grown at three different surface temperatures. (b) Plot showing how the lattice mismatch of the InAs/GaSb T2SLs changes with surface temperature.

**Fig. 4.4.** (a) Omega 2 Theta XRD scans of 50 period 21ML/8ML InAs/GaSb T2SLs grown at 3 different GaSb V/III ratios. (b) Plot showing how the lattice mismatch of the InAs/GaSb T2SLs changes with GaSb V/III ratio.

**Fig. 4.5.** Optical microscope pictures and AFM scans of 50 period 21ML/8ML InAs/GaSb T2SLs grown at 3 different GaSb V/III ratios; (a) 1.2, (b) 1.4 and (c) 1.5.

**Fig. 4.6.** (a) Omega 2 Theta XRD scans of 50 period 21ML/8ML InAs/GaSb T2SLs with different InAs V/III ratios. (b) Plot showing how the lattice mismatch of the InAs/GaSb T2SLs changes with InAs V/III ratio.

**Fig. 4.7.** AFM scans of 50 period 21ML/8ML InAs/GaSb T2SLs with different InAs V/III ratios.

**Fig. 4.8.** Plot showing how the lattice constant of different wavelength InAs/GaSb T2SLs changed with InAs V/III ratio. The closest to lattice match of each wavelength are highlighted.

**Fig. 4.9.** AFM scans of 50 period InAs/GaSb T2SLs with different cutoff wavelengths.

**Fig. 4.10.** Omega 2 Theta XRD scans of all the lattice matched InAs/GaSb T2SLs with different wavelengths. Including a dual wavelength sample with both a 4.5  $\mu\text{m}$  and 12  $\mu\text{m}$  T2SL.

**Fig. 4.11.** Normalised photoluminescence plot, taken at 77K, showing the peak wavelength of each InAs/GaSb T2SL. The scaling factors that were used to create the normalised plot are shown within the peaks. Due to the transmission windows of the optics used in the setup, the detector cutoff is at around 9  $\mu\text{m}$ .

**Fig. 4.12.** High resolution scanning transmission electron microscopy showing the “GaAs Like” interfaces within the T2SL.

**Fig. 4.13.** (a) Schematic diagram of the staircase doping calibration of Si into bulk InAs. (b) SIMS data from the doping calibration sample. The ratio of the flow of  $\text{Si}_2\text{H}_6$  to TMIIn was increased from  $5 \times 10^{-6}$  to  $5 \times 10^{-4}$  resulting in an increase of Si concentration from  $3 \times 10^{15}$  to  $6 \times 10^{16}$  Atoms /  $\text{cm}^3$ .

**Fig. 4.14.** (a) Schematic diagram of the full device epitaxial structure. (b) Transmission electron microscopy (TEM) scan of the indicated region of the device structure.

**Fig. 4.15.** Dark current density ( $J_d$ ) versus voltage for the deep, dry etched detectors, with and without surface passivation.

**Fig. 4.16.** Dark current density ( $J_d$ ) versus voltage for the deep and shallow, dry etched detectors with and without surface passivation.

**Fig. 4.17.** Dark current density ( $J_d$ ) versus the perimeter-to-area ratio for the deep and shallow, dry etched detectors with and without surface passivation. The linear fittings were obtained using equation 4.1.

**Fig. 4.18.** Schematic layout of the shallow etched pixels with different mesa etch diameters ( $D_n$ ) showing the lateral diffusion length ( $L_{Diff}$ ).

**Fig. 4.19.** Measured dark current density against mesa diameter. The fitting was obtained using equation 4.2.

**Fig. 4.20.** Dark current density ( $J_d$ ) versus voltage for the dry and wet etched detectors with and without surface passivation.

**Fig. 4.21.** Dark current density ( $J_d$ ) versus the perimeter-to-area ratio for the dry and wet deep etched detectors with and without surface passivation. The linear fittings were obtained using equation 4.1.

**Fig. 4.22.** Comparison of the dark currents in this work compared to the values in literature for Barrier-based InAs/GaSb, Non-Barrier InAs/GaSb, Barrier-Based InAs/InAsSb and Non-Barrier InAs/InAsSb detectors. As well as MCT detectors and the “Rule 07” line.

**Fig. 4.23.** Arrhenius plot of  $J_d$  against  $1000/T$  showing the activation energies ( $E_a$ ) for 400 $\mu$ m diameter devices at -0.1V. For clarity the data have been offset from each other in causing  $J_d$  to be in arbitrary units.

**Fig. 4.24.** Plot of responsivity against wavelength for the six different fabrication methods of the InAs/GaSb T2SL LWIR detector.

**Fig. 4.25.** Plot of EQE against wavelength for the six different fabrication methods of the InAs/GaSb T2SL LWIR detector.

**Fig. 4.26.** Comparison of the EQE in this work compared to the values in literature for MCT, Barrier-Based InAs/GaSb and Barrier-Based InAs/InAsSb LWIR detectors.

**Fig. 4.27.** Plot of detectivity against wavelength for the six different fabrication methods of the InAs/GaSb T2SL LWIR detector.

**Fig. 4.28.** Comparison of the detectivities in this work compared to the values in literature for MCT, Barrier-based InAs/GaSb, Non-Barrier InAs/GaSb, Barrier-Based InAs/InAsSb and Non-Barrier InAs/InAsSb detectors. The “Rule 07” line is added as a reference and is calculated from the rule 07 dark current line with the QE of the MCT detectors assumed to be 75%.

**Fig. 5.1.** MOCVD growth timeline of one period of the InAs/InAsSb T2SL with the additional growth interruption steps.

**Fig. 5.2.** AFM surface scans of 50 period 17ML/8ML InAs/InAsSb T2SLs grown at three different surface temperatures.

**Fig. 5.3.** (a) Omega 2 Theta XRD scans of 50 period 17ML/8ML InAs/InAsSb T2SLs grown at three different surface temperatures. (b) Plot showing how the lattice mismatch and the Sb incorporation of the InAs/InAsSb T2SLs changes with surface temperature.

**Fig. 5.4.** Omega 2 Theta XRD scans of 50 period 17ML/8ML InAs/InAsSb T2SLs grown at 460°C with different Sb to As gas flow ratios.

**Fig. 5.5.** MOCVD growth timeline of one period of the InAs/InAsSb T2SL with the additional growth interruption steps.

**Fig. 5.6.** Omega 2 Theta XRD scans of 50 period 17ML/8ML InAs/InAsSb T2SLs grown at 460°C with and without growth interruption.

**Fig. 5.7.** AFM surface scans of 50 period 17ML/8ML InAs/InAsSb T2SLs grown with and without growth interruptions.

**Fig. 5.8.** Photoluminescence plot of 50 period 17ML/8ML InAs/InAsSb T2SLs grown at 460°C with and without growth interruption.

**Fig. 5.9.** Schematic diagram of the InAs/InAsSb T2SL PIN detector.

**Fig. 5.10.** (a) Schematic diagram of the staircase doping calibration of Zn into bulk InAs. (b) SIMS data from the doping calibration sample. The ratio of the flow of DEZn to TMIn was increased from  $1 \times 10^{-3}$  to  $1 \times 10^{-1}$  resulting in an increase of Si concentration from  $4 \times 10^{17}$  to  $8 \times 10^{18}$  Atoms /  $\text{cm}^3$ .

**Fig. 5.11.** (a) AFM surface scans of the full device sample. (b) Omega 2 Theta XRD scans of the full device sample.

**Fig. 5.12.** Dark current density ( $J_d$ ) versus voltage for the InAs/InAsSb T2SL PIN detectors across a range of temperatures.

**Fig. 5.13.** Comparison of the dark currents from the InAs/InAsSb PIN detector in this work compared to the values found in literature for Barrier-based InAs/GaSb, Non-Barrier InAs/GaSb, Barrier-Based InAs/InAsSb and Non-Barrier InAs/InAsSb detectors. To be compared with MCT detectors and the "Rule 07" line [48]. At (a) 77K and (b) 150K.

**Fig. 5.14.** Plot of responsivity against wavelength for the InAs/InAsSb PIN detector at 77 and 150K.

**Fig. 5.15.** Plot of EQE against wavelength for the InAs/InAsSb PIN detector at 77 and 150K.

**Fig. 5.16.** Comparison of the EQE from the InAs/InAsSb PIN detector in this work compared to the values found in literature for MWIR MCT, Barrier-based InAs/GaSb, Non-Barrier InAs/GaSb, Barrier-Based InAs/InAsSb and Non-Barrier InAs/InAsSb detectors.

**Fig. 5.17.** Plot of Detectivity against wavelength for the InAs/InAsSb PIN detector at 77 and 150K.

**Fig. 5.18.** Comparison of the dark currents from the InAs/InAsSb PIN detector in this work compared to the values found in literature for MCT, Barrier-based InAs/GaSb, Non-Barrier

InAs/GaSb, Barrier-Based InAs/InAsSb and Non-Barrier InAs/InAsSb detectors. At (a) 77K and (b) 150K.

**Fig. 6.1.** Diagram showing how the two different types of misfit dislocations propagate. This figure is adapted from reference.

**Fig. 6.2.** MOCVD growth timeline of the growth of GaSb onto a GaAs substrate. Showing the growth interruption stages used to promote a 90° dislocation dominated IMF between the GaAs and GaSb.

**Fig. 6.3.** AFM scans of 500nm GaSb grown on GaAs substrates at 530°C with varying GaSb V/III ratios.

**Fig. 6.4.** AFM scan of 500nm GaSb grown on GaAs substrates at 510°C with a GaSb V/III ratio of 1.5.

**Fig. 6.5.** High resolution TEM image of the interface between the GaAs and GaSb layers showing the misfit dislocations that form the Interfacial misfit array.

**Fig. 6.6.** Burgers circuit analysis on the misfit dislocations in the high-resolution TEM image of the Interfacial misfit array.

**Fig. 6.7.** Electron channelling contrast imaging (ECCI) image of the surface of the GaSb grown on GaAs substrates.

**Fig. 6.8.** AFM scans of the InAs/InAsSb T2SL PIN detector on both (a) GaSb substrates and (b) GaAs substrates.

**Fig. 6.9.** Omega 2 Theta XRD scans of the full InAs/InAsSb T2SL PIN device sample grown on a GaAs substrate with a 500nm GaSb buffer layer.

**Fig. 6.10.** Dark current density ( $J_d$ ) versus voltage for a 300 $\mu$ m diameter InAs/InAsSb T2SL PIN detector grown on a GaAs substrate at 77K.

**Fig. 6.11.** Comparison of the dark currents for the InAs/InAsSb PIN detectors in this work grown on GaAs and GaSb substrates compared to the values in literature for: Barrier-based InAs/GaSb, Non-Barrier InAs/GaSb, Barrier-Based InAs/InAsSb and Non-Barrier InAs/InAsSb detectors. As well as MCT detectors and the "Rule 07" line.

**Fig. 6.12.** Plot of responsivity against wavelength for the InAs/InAsSb PIN detectors grown GaAs and GaSb substrates at 77K.

**Fig. 6.13.** Plot of EQE against wavelength for the InAs/InAsSb PIN detectors grown GaAs and GaSb substrates at 77K.

**Fig. 6.14.** Comparison of the EQE from the InAs/InAsSb PIN detectors in this work grown on GaAs and GaSb substrates compared to the values found in literature for MWIR MCT, Barrier-based InAs/GaSb, Non-Barrier InAs/GaSb, Barrier-Based InAs/InAsSb and Non-Barrier InAs/InAsSb detectors.

**Fig. 6.15.** Plot of Detectivity against wavelength for the InAs/InAsSb PIN detectors grown GaAs and GaSb substrates at 77K.

**Fig. 6.16.** Comparison of the detectivities from the InAs/InAsSb PIN detectors in this work grown on GaAs and GaSb substrates compared to the values in literature for MCT, Barrier-based InAs/GaSb, Non-Barrier InAs/GaSb, Barrier-Based InAs/InAsSb and Non-Barrier InAs/InAsSb detectors. The “Rule 07” line is added as a reference and is calculated from the rule 07 dark current line with the QE of the MCT detectors assumed to be 75%.

**Fig. 6.17.** Schematic diagram of the InAs/InAsSb type-II superlattice grown on Si using the GaSb/GaAs/Si buffer layer structure.

**Fig. 6.18.** AFM scans taken after the growth of (a) GaAs on Si, (b) GaSb on GaAs on Si and (c) the final InAs/InAsSb T2SL grown on the full buffer structure.

**Fig. 6.19.** Experimental and simulated XRD data of the InAs/InAsSb T2SL integrated onto a Si substrate.

**Fig. 6.20.** Cross-sectional TEM image of the whole T2SL on Si structure, showing a reduction in dislocation density from the GaAs/Si to the T2SL.

**Fig. 6.21.** Cross-sectional TEM image of the T2SL on Si buffer layer structure, showing distinct stripes indicative of high quality T2SL growth.

**Fig. 6.22.** High resolution TEM image of the interface between the GaAs and GaSb layers showing the misfit dislocations that form the Interfacial misfit array.

**Fig. 6.23.** Electron channelling contrast image of the (a) GaSb surface before T2SL growth and (b) the final T2SL surface.

**Fig. 6.24.** Temperature dependent PL data of the InAs/InAsSb T2SL on Si. The dip at 4.3  $\mu\text{m}$  is caused by CO<sub>2</sub> absorption in the FTIR.

**Fig. 6.25.** Plot showing the temperature dependent redshift of the T2SL.

**Fig. 6.26.** Arrhenius plot of the temperature dependent performance used to calculate the activation energy at different temperature ranges.

## List of Tables

**Table 2.1.** Summary of the main differences between MOCVD grown InAs/InAsSb and InAs/GaSb T2SLs.

**Table 4.1.** Surface, bulk and total dark current for the dry etched devices.

**Table 4.2.** Surface, bulk and total dark current for the wet and dry etched devices.

---

# List of Acronyms

- AFM** – atomic force microscopy
- APD** – antiphase domains
- CBIRD** – complementary barrier infrared detector
- CCS** – close-coupled showerhead
- ECCI** – electron channelling contrast imaging
- EQE** – external quantum efficiency
- FPA** – focal plane array
- FTIR** – Fourier transform infrared spectrometer
- FWHM** – full width half maximum
- HOT** – high operating temperature
- IMF** – interfacial misfit array
- IR** – infrared
- LWIR** – long-wavelength infrared radiation
- MBE** – molecular beam epitaxy
- MCT** – mercury cadmium telluride
- MOCVD** – metal-organic chemical vapor deposition
- MWIR** – mid-wavelength infrared radiation
- NIR** – near infrared
- PC** – photoconductive
- PECVD** – plasma enhanced chemical vapour deposition
- PL** – photoluminescence
- PV** – photovoltaic
- RMS** – root mean squared
- SEM** – scanning electron microscopy
- SIMS** – secondary ion mass spectrometry
- SLS** – strained layer superlattice
- SRH** – Shockley Reed Hall
- STEM** – scanning transmission electron microscopy

**SWIR** – short-wavelength infrared radiation

**T2SL** – type-II superlattice

**TAT** – trap assisted tunnelling

**TDD** – threading dislocation density

**TEM** – transmission electron microscopy

**VLWIR** – very long-wavelength infrared radiation

**XRD** - X-ray diffraction

## Funding

The author is grateful for funding from:

The Engineering and Physical Sciences Research Council (grant number EP/S024441/1)

The Future Compound Semiconductor Manufacturing Hub (grant number EP/P006973/1)

The Royal society (grant number IEC/NSFC/211054)

IQE PLC

---

# Acknowledgements

I would first like to thank my PhD supervisor Dr. Qiang Li for providing his expertise, support and the resources needed to see this project to completion. Qiang personally trained me on the majority of tools used within this project. Including most importantly the MOCVD reactor itself which is the basis of this whole project. Qiang was exceptionally generous with the amount of time he allowed me to access the busy reactor which allowed me to produce many different samples across my PhD. I would also like to thank the other members of my research group in supporting me in my work - Dr. Zhao Yan, Dr. Shangfeng Liu and Dr. Bogdan-Petrin Ratiu

The fabrication of all the samples presented in this work was performed by Ka Ming Wong in Cardiff University's Institute for compound semiconductors. I am very grateful for Ka Ming's invaluable assistance to this project.

Much of the characterisation was supported by many internal and external collaborators and they all deserve acknowledgement and thanks for their work. I would like to thank Chen Liu and the team at IQE for their support in the X-ray diffraction in the beginning of this project. I would like to thank Dr. Hui Jia from UCL for her support in the electron channelling contrast imaging in this work. I would like to thank Prof. Richard Beanland from the University of Warwick for his support in the transmission electron microscopy. I would like to thank Loughborough Surface Analysis for their support in secondary ion mass spectrometry. I would like to thank Prof. Baolai Liang and Dr. Khalifa Azizur-Rahman from UCLA for their support in photoluminescence characterisation. I would like to thank Dr. Andrew Marshall and his team at Lancaster University including George Seager and Dr. Adam Craig, for their support in the electrical and optical device characterisation.

I would also like to thank Dr. J. Iwan Davies for his invaluable support as my external supervisor and mentor. Iwan's generosity with IQE's resources, especially access to XRD early in this project was instrumental in the development of the InAs/GaSb LWIR detectors.

I would like to thank my parents for their continued support throughout my PhD. Their constant encouragement, love, and belief in me have been invaluable through this project. In particular I would like to thank my mother for her help in proofreading this thesis.

Finally, I would like to thank my wife. Thank you for being my partner, my biggest cheerleader and my best friend. Your day to day practical support has allowed me to survive the pressures of this PhD and I would not have been able to do it without you.

# Introduction

## 1.1 Infrared Detector Applications

Infrared (IR) detectors allow electromagnetic radiation that is invisible to both the naked eye and standard cameras to be observed. As a result, they have become crucial for both military and civilian uses, with the market projected to grow from USD 1.4 Billion in 2024 to USD 3.8 Billion by 2032 [49]. This work focuses on the wavelength range of around 3-12 $\mu\text{m}$  which includes both the mid-wavelength infrared radiation (MWIR) at 3-5 $\mu\text{m}$  and the long-wavelength infrared radiation (LWIR) at 8-12 $\mu\text{m}$ .

MWIR detectors have a wide range of applications including; optical gas sensors for pollution monitoring and industrial process control, medical diagnostics, as well as large defence and security applications such as night vision and missile warning systems [50]. There are many important gases, such as  $\text{CH}_4$ ,  $\text{CO}_2$  and  $\text{CO}$ , which have their fundamental absorption bands in the MWIR spectral region as shown in Fig. 1.1.

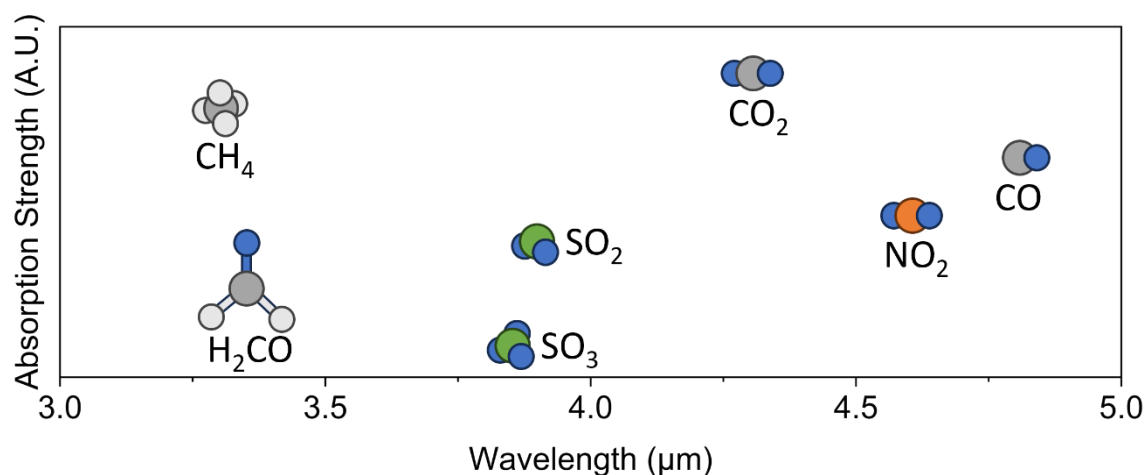


**Fig. 1.1.** Graph showing the various important gases that can be detected in the MWIR spectral region [51].

This gas imaging is constrained by the performance of the MWIR detectors, and so advancements must be made to allow for better and more accurate detection of gases for both atmospheric monitoring as well as industrial gas sensing.

Thermography is a medical technique that allows thermal imaging of the body to detect minute changes in the underlying tissues, which indicates neurological and vascular, as well as metabolic pathologies [52]. Currently thermography utilizes the MWIR spectral region but is limited by the currently available MWIR detectors which are bulky and relatively low resolution.

MWIR also has many defence applications, especially in imaging “hot” objects with their blackbody emission peaking within the MWIR range ( $\sim 500\text{-}1000\text{K}$ ). These kinds of objects include missiles, drones, fighter jets and even muzzle flashes [50].

Although the peak emission of a human is around  $9.55\mu\text{m}$ , there are still many examples of MWIR detectors being used to detect people. This is mainly due to how much easier it is to create a higher performance MWIR detector than a LWIR detector. So, even if the target peak emission is in the LWIR spectrum, the superior performance of the current MWIR detectors can allow them to produce a superior image than a LWIR detector in the right conditions. MWIR detectors are also generally preferred in high moisture conditions due to the higher water absorption of LWIR radiation reducing the amount of radiation that reaches the detector.

The main application of the LWIR spectrum is in the detection of people. The human body emits its peak blackbody radiation at  $9.55\mu\text{m}$  and so naturally a LWIR detector would be best suited to detect that radiation. Currently, due to the limitations of available LWIR detectors, there is limited medical thermography work using LWIR detectors. However, if the performance was equal between the different wavelength detectors, there would be a wide range of diagnostic capabilities that would be improved by imaging focusing on the main emitted wavelength of the subject. In terms of defence and security there are many different applications in which being able to image a person who is either obstructed or in the dark is useful. Currently, both MWIR and LWIR detectors are used in night vision and general human detection applications. Generally, MWIR is still more common due to superior detector technology. However, as the performance of LWIR detectors improves this may change as they are naturally more suited to the application.

Another important application for human detection is autonomous vehicles where currently a combination of visible light cameras and short-wave Infrared LIDAR systems are the current standard [53]. By utilizing additional detectors that work at longer wavelengths the autonomous vehicle will be able to more accurately track and avoid pedestrians especially in environments where visible light cameras struggle such as in the dark, in foggy conditions and when hit by bright headlights.

High performance, low cost, high yield, high uniformity, high operability, and high stability are essential for these applications. Moreover, the extensive use of IR detectors in space and defence applications makes it critical to reduce size, weight, and power. Size weight and power reduction can be achieved by fabricating detector elements that offer high performance without large and expensive cooling systems. Creating an IR detectors that functions at high operating temperatures ( $>77\text{K}$ ) is still incredibly challenging for MWIR detectors and is even harder for LWIR detectors. This difficulty is due to the detector itself emitting radiation in the LWIR if it is not cooled, causing large problem with signal to noise ratio as the detector struggles to distinguish the radiation from the target from itself.

## 1.2 Current Infrared Detector Technology

Mercury cadmium telluride (MCT) is currently the leading material for IR detectors, primarily because of its high external quantum efficiency (EQE), well-established fabrication technology, and overall market maturity. However, MCT faces challenges such as epitaxial difficulties, which result in poor uniformity at larger wafer sizes, leading to scalability issues and high costs. Additionally, increasingly stringent regulations regarding the use of mercury further complicate its use. These challenges drive the search for alternative material systems for IR detectors that do not contain mercury.

Antimony (Sb) based type-II superlattice (T2SL) materials are a strong candidate for next generation infrared technologies and are now considered as a viable alternative to the state of the MCT [54]. The Type-II band alignment of the T2SL gives the material system its flexible band gap engineering capability, allowing for a widely tuneable bandgap. The T2SL structure is also responsible for the suppression of band-to-band tunnelling, Auger recombination and Shockley-Read-Hall recombination which make up a large proportion of the dark current in MCT [55]. The last big advantage of the T2SL when compared to MCT is in its growth uniformity. The ability to use standard III-V growth techniques such as molecular beam epitaxy (MBE) and metal-organic chemical vapor deposition (MOCVD) to grow material with good uniformity is a big advantage for the T2SL when compared to MCT.

There are two main candidates for the Sb based T2SL, the InAs/GaSb T2SL and the InAs/InAsSb T2SL. Historically the focus has been around the InAs/GaSb T2SL due to its larger optical absorption and larger wavelength range [56]. However, more recently the Ga-free InAs/InAsSb T2SL has emerged as a promising new candidate due to its longer minority carrier lifetime [57] and higher defect tolerance [58], particularly in the mid-wave infrared region.

To date, MBE has been the prevailing technique for growing Sb-containing structures [59–61]. However, the commercial exploitation potential using MOCVD is highly attractive if material and device performance can be improved to close the gap with MBE results [47].

## 1.3 Thesis Overview

The thesis is divided into the following sections:

- 1. Introduction.** This chapter provides a short introduction to the current infrared detector technologies and their main applications.
- 2. Background.** This chapter provides an overview of the fundamental physics underlying infrared detectors. It includes an introduction to IR radiation, a description of different types of detectors, and the operation and history of T2SL. Additionally, it discusses the figures of merit for IR detectors and compares the latest advancements in the field.
- 3. Research tools.** This chapter presents the technical specifics of the methods and processes employed in this work, including growth, fabrication, and characterization.
- 4. LWIR detectors made from InAs/GaSb T2SLs.** This chapter reports on the MOCVD growth, fabrication, and characterisation of LWIR InAs/GaSb T2SL photodetectors onto InAs substrates.
- 5. MWIR detectors made from InAs/InAsSb.** This chapter reports on the MOCVD growth, fabrication, and characterisation of MWIR InAs/InAsSb T2SL photodetectors onto GaSb substrates.
- 6. Growth of InAs/InAsSb T2SLs on non-native substrates.** This chapter reports on the MOCVD growth, fabrication, and characterisation of MWIR InAs/InAsSb T2SL photodetectors onto GaAs substrates. As well as the MOCVD growth of InAs/InAsSb T2SLs onto Si substrates.
- 7. Conclusions and future work.** This chapter summarises the key conclusions of the current work and offers recommendations for future research.

# Background

This chapter introduces the fundamental principles of infrared (IR) radiation and its detection. Both the PIN and barrier-based detectors are introduced and compared. The main figures of merit for IR detectors are described to aid with the future comparisons between detector technologies. The InAs/GaSb T2SL and the InAs/InAsSb T2SL are introduced and their physical principles and relative advantages and disadvantages compared to each other and the current state-of-the-art are included.

## 2.1 Infrared Radiation

Any object with a temperature higher than absolute zero releases electromagnetic radiation, commonly referred to as blackbody radiation. A blackbody represents an object that absorbs and re-emits all energy with perfect efficiency. To characterise the blackbody radiation emanating from such an entity, three fundamental laws are employed; Planck's law, Wien's law and the Stefan-Boltzmann law [62].

Planck's law gives the probability distribution of the wavelengths of the emitted photons from the blackbody and is given by;

$$W(\lambda, T) = \frac{2\pi hc^2}{\lambda^5 e^{\frac{hc}{\lambda k_B T}} - 1} \quad (2.1)$$

where  $W$  is the spectral radiance,  $h$  is the Planck constant,  $T$  is the temperature,  $k_B$  is the Boltzmann constant,  $\lambda$  is the wavelength of the photons and  $c$  is the speed of light.

Wien's law gives the relationship between the peak wavelength,  $\lambda_{max}$ , and the temperature of the black body, which is given by;

$$\lambda_{max} = \frac{b}{T} \quad (2.2)$$

Where  $b$  is Wien's displacement constant which is equal to  $2898 \mu\text{m}\cdot\text{K}$ . Wien's law can be overlaid onto the blackbody curves created with Planck's law to be easily visualised as shown in Fig. 2.1.

The Stefan-Boltzmann law estimates the total energy radiated per unit area by a black body over a certain period. It is expressed mathematically as:

$$M = \sigma T^4 \quad (2.3)$$

where  $\sigma$  is the Stefan-Boltzmann constant.

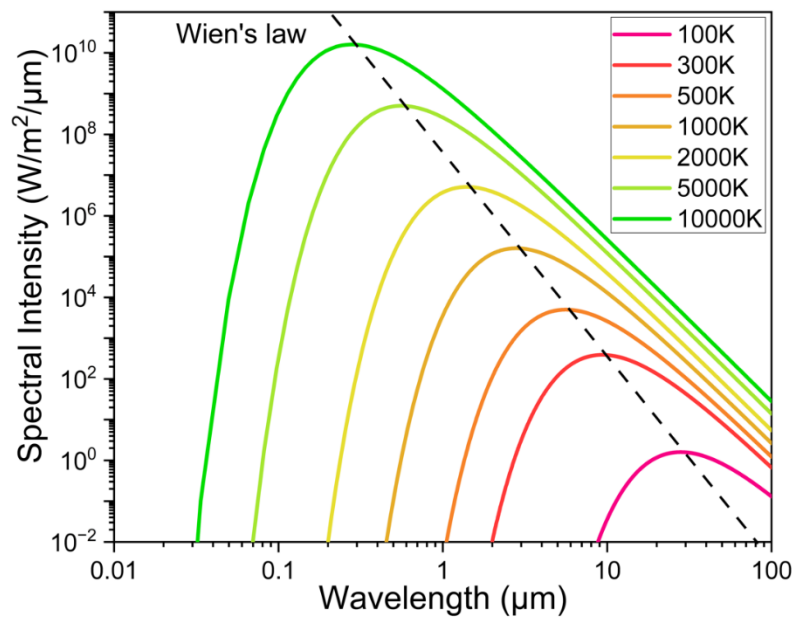


**Fig. 2.1.** Wien's law superimposed on blackbody radiation curves created using Planck's law.

Since practical applications involve detecting electromagnetic radiation through the atmosphere, it is crucial to consider the absorption effects of the atmospheric media through which this radiation travels. Fig. 2.2 The transmission of infrared (IR) radiation through the atmosphere results in various atmospheric windows of transmission. These windows include:

- **Near infrared (NIR):** 0.7 μm – 1.5 μm
- **Short-wavelength infrared (SWIR):** 1.5 μm – 2.5 μm
- **Mid-wavelength infrared (MWIR):** 3 μm – 5 μm
- **Long-wavelength infrared (LWIR):** 8 μm – 12 μm
- **Very long-wavelength infrared (VLWIR):** 12 μm – 32 μm

This work focuses on the wavelength range of around 3-12μm which includes both the MWIR at 3-5μm and the LWIR at 8-12μm.

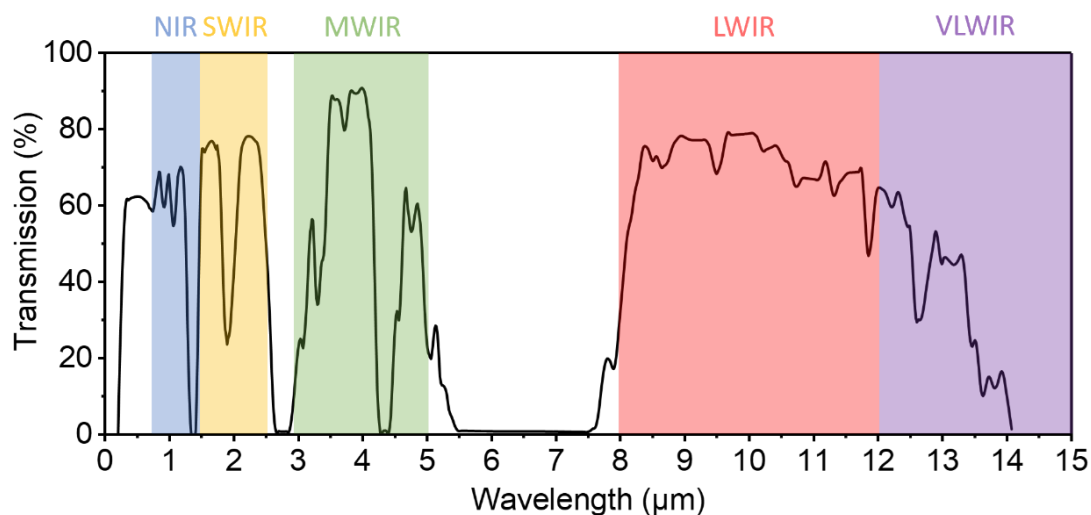


**Fig. 2.2.** Atmospheric transmission windows from NIR to VLWIR [63].

## 2.2 Infrared Detectors

An infrared detector converts energy from incident infrared radiation into another form, typically electrical. There are two main types of infrared detectors: thermal detectors and photon detectors (also known as photodetectors).

- **Thermal Detectors:** These include microbolometers and pyroelectric detectors. They work by absorbing radiation, which increases the detector's temperature. This temperature rise leads to a measurable change in the detector's physical or electrical properties, such as resistance or capacitance.
- **Photon Detectors (Photodetectors):** These operate based on the principle of photoexcitation. An incident photon with sufficient energy interacts with a bound electron, generating a free electrical carrier that can be detected using electrical circuitry. Since photodetectors do not rely on heating the detector through absorbed radiation, they are preferred for applications requiring a fast response time, such as video.

This thesis focuses on the study and application of photodetectors.

### 2.2.1 Figures of Merit

The performance of a detector can be broken down into useful figures of merit that can be used to quantify and compare different detectors.

#### 2.2.1.1 Dark Current

Dark current is the current that flows through the photodetector in the absence of light, due to the generation of non-photonically generated carriers. Minimising dark current is crucial for high sensitivity, especially at longer wavelengths like MWIR and LWIR.

This unwanted current arises from several mechanisms which are critical to understand in order to improve the performance of photodetectors. The main mechanisms contributing to dark current in a PIN photodetector are diffusion, generation-recombination (GR) tunnelling and shunt.

The diffusion current ( $J_{diff}$ ) is the most fundamental mechanism that contributes to the dark current, originating from thermally generated carriers from the Auger and radiative processes within the semiconductor [64]. In a basic PIN photodetector the diffusion current is given by [65];

$$J_{diff} = n_i^2 \sqrt{q k_B T} \left( \frac{1}{N_D} \sqrt{\frac{\mu_h}{\tau_h}} + \frac{1}{N_A} \sqrt{\frac{\mu_e}{\tau_e}} \right) \left( e^{\frac{qV}{k_B T}} - 1 \right) \quad (2.4)$$

where  $n_i$  is the intrinsic carrier concentration,  $q$  is the electron charge,  $k_B$  is the Boltzmann constant,  $T$  is the temperature,  $V$  is the device bias,  $N_A$  is the p-type doping concentration,  $N_D$  is the n-type doping concentration and  $\mu_e$ ,  $\tau_e$  and  $\mu_h$ ,  $\tau_h$  are the mobility and lifetimes of electrons and holes respectively.

There are many different types of generation-recombination current mechanisms, but the main one that is relevant in the types of photodetectors in this thesis is the Shockley Reed Hall (SRH) mechanism. SRH recombination is a fundamental process in semiconductor physics that describes how electron-hole pairs recombine through defect states within the bandgap of a semiconductor material.

In a semiconductor, defects or impurities can create energy levels within the bandgap which are referred to as trap states. These trap states can capture and hold charge carriers (electrons or holes). The energy level of a trap state is typically somewhere between the conduction band and the valence band. Once a charge carrier is captured in a trap state it can later be released via thermal generation resulting in a current produced thermally not photonically [66]. Trap states in the depletion region, due to defects or impurities, can facilitate the generation of carriers through SRH processes. This mechanism is significant in the intrinsic region of the PIN diode, where the concentration of free carriers is low, and the role of traps becomes more pronounced. The general expression for  $J_{SRH}$  is given by [67];

$$J_{SRH} = q \frac{n_i w_{dep}}{\tau_{no} + \tau_{po}} \quad (2.5)$$

where  $w_{dep}$  is the width of the depletion region and  $\tau_{no}$  and  $\tau_{po}$  are SRH specific carrier lifetimes. Since  $J_{SRH}$  is directly proportional to depletion width, minimising the size of the depletion region is necessary to minimise the dark current from SRH. The optimum depletion width size is therefore a compromise between improved quantum efficiency from a larger depletion region and reduced dark current from a smaller depletion region.

Similar to SRH, electrons can use mid gap trap states to tunnel from the valence to conduction band creating a dark current. This process is known as trap assisted tunnelling (TAT). The dark current associated with TAT,  $J_{TAT}$ , is given by [65];

$$J_{TAT} = \frac{\pi^2 q^2 m_T M^2 N_T V}{h^3 (E_g - E_T)} \exp\left(-\frac{8\pi \sqrt{2m_T (E_g - E_T)^3}}{3qhE(V)}\right) \quad (2.6)$$

where  $N_T$  is the activated trap density,  $E_T$  is the trap energy location below the effective conduction band edge and  $M^2$  is a matrix element associated with the trap potential.

In a real-world detector, there also exists an additional current component that exhibits ohmic shunt-like behaviour [65];

$$J_{shunt} = \frac{V}{R_{shunt} A} \quad (2.7)$$

where  $V$  is the applied voltage across the junction,  $R_{shunt}$  is the detector shunt resistance and  $A$  is the junction area.

The total dark current density of a photodetector ( $J_d$ ) can be expressed as a combination of its bulk ( $J_{bulk}$ ) and surface ( $J_{surf}$ ) components as [65];

$$J_d = J_{bulk} + J_{surf} \quad (2.8)$$

When a photodetector is fabricated, in order to define the photodetector area and to isolate it from the surrounding pixels, a mesa etch is generally used [68]. This is generally a deep mesa etch which exposes a large sidewall. This exposed sidewall contains many dangling bonds with a low resistivity which creates a dark current pathway on the surface of the detector.

The mesa etch also damages the sidewall creating many more defects than in the bulk material which will increase defect-based dark current mechanisms such as  $J_{SRH}$  and  $J_{TAT}$ . Surface passivation layers can be used to reduce  $J_{surf}$  by eliminating the dangling bonds and improvement of the etch process can help to reduce the number of defects caused by the mesa. However, in IR detectors due to their smaller bandgap, finding the optimal surface passivation is very difficult and still remains one of the major challenges in the field.

### 2.2.1.2 Responsivity

The responsivity of a detector relates the output signal or photocurrent with the incident power that produced that signal. The photocurrent of the detector can be calculated by illuminating the detector and then subtracting the known dark current density for the detector. Responsivity is usually given in A/W and is a function of wavelength as different detectors are more or less responsive to different wavelengths of light. Responsivity is given by;

$$R = \frac{J_{ph}}{\Phi A} \quad (2.9)$$

where  $J_{ph}$  is the photocurrent,  $\Phi$  is the photon incidence per unit area and  $A$  is the effective optical area of the detector. A detector with a higher responsivity is desired as it has a stronger photocurrent for a given input intensity.

### 2.2.1.3 Quantum Efficiency

The External Quantum Efficiency (EQE,  $\eta$ ) scales the responsivity with the energy of the individual photon's incident on the detector and it gives the percentage of incident photons that contribute to the photocurrent. The external quantum efficiency is given by;

$$\eta = Rhv \times 100 \quad (2.10)$$

where  $hv$  is the energy of incident photons and the total is multiplied by 100 to give EQE as a percentage. Similar to responsivity, a higher EQE is desired as that means that the detector is better at converting incident photons into signal.

### 2.2.1.4 Detectivity

Detectivity ( $D^*$ ) combines responsivity and dark current density and is the main figure of merit used to describe how "good" a detector is. Detectivity is given by [69];

$$D^* = R \left( 2qJ_d + \frac{4kT}{R_d A_d} \right)^{-\frac{1}{2}} \quad (2.11)$$

where  $R$  is the responsivity,  $q$  is the electronic charge,  $k$  is the Boltzmann constant,  $T$  is the device temperature and  $R_d A_d$  is the dark resistance area product. Detectivity has units of  $\text{cm Hz}^{1/2} / \text{W}$  which is often referred to as Jones (J). Detectivity is able to quantify detector performance as a function of wavelength and should be maximised in order to produce a high-performance detector.

### 2.2.2 The PN Photodetector

The most standard type of photodetector is the PN or PIN photodetector. A PN photodetector is known as a photovoltaic (PV) photodetector. The PN photodetector is formed of two regions, a p-type region where the majority carriers are holes and an n-type region where the majority carriers are electrons as shown in Fig. 2.3.

At the interface of the p-type and n-type regions, electrons from the n-type region diffuse into the p-type region and recombine with holes. This creates a depletion region that is devoid of free charge carriers and acts as an insulating layer. The depletion region creates a built-in potential barrier within the photodetector which creates the photovoltaic effect.

When the photodetector is exposed to light, photons with energy greater than the bandgap of the photodetector are absorbed generating electron-hole pairs in the photodetector. The electric field in the depletion region separates the electron-hole pairs. Electrons are pushed towards the n-type region and holes towards the p-type region.

Once the electron-hole pairs are separated by the electric field, they are collected by the respective electrodes, resulting in a flow of current. This current can then be externally measured and is used to calculate the photon flux on the photodetector. Due to the electric field and the lack of free carriers within the depletion region, any electron-hole pair generated in this region is more likely to be detected than those generated in the p-type or n-type regions. As many electron hole pairs that are generated in the p-type and n-type regions recombine with the free carriers found there. Therefore, the size of the depletion region is an important factor in the performance of the photodetector.

Generally, PN photodetectors operate in reverse bias. Applying a reverse bias across the PN junction widens the depletion region and enhances the electric field, which improves the separation of electron-hole pairs and increases the photocurrent. However, even in reverse bias, the width of the depletion region may well be below the photon absorption length so that only some fraction of the generated electron-hole pairs are generated within the depletion region, resulting in a reduced quantum efficiency.

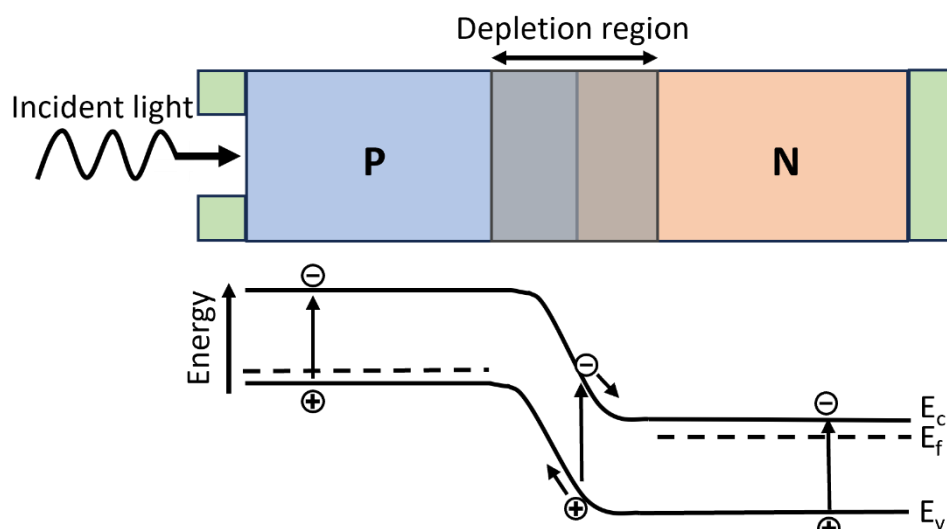


**Fig. 2.3.** Schematic diagram of a PN photodetector under reverse bias.

Another way to increase the size of the depletion region is to include an intrinsically doped (or undoped) region between the P and N regions, known as the I region. The intrinsic layer in a PIN photodetector widens the depletion region significantly compared to a PN photodetector, as shown in Fig 2.4. This larger depletion region increases the volume where electron-hole pairs can be generated by incident photons, leading to higher quantum efficiency and better light absorption. The increased depletion region allows for a greater number of electron-hole pairs to be collected, resulting in higher responsivity in photodetection applications.

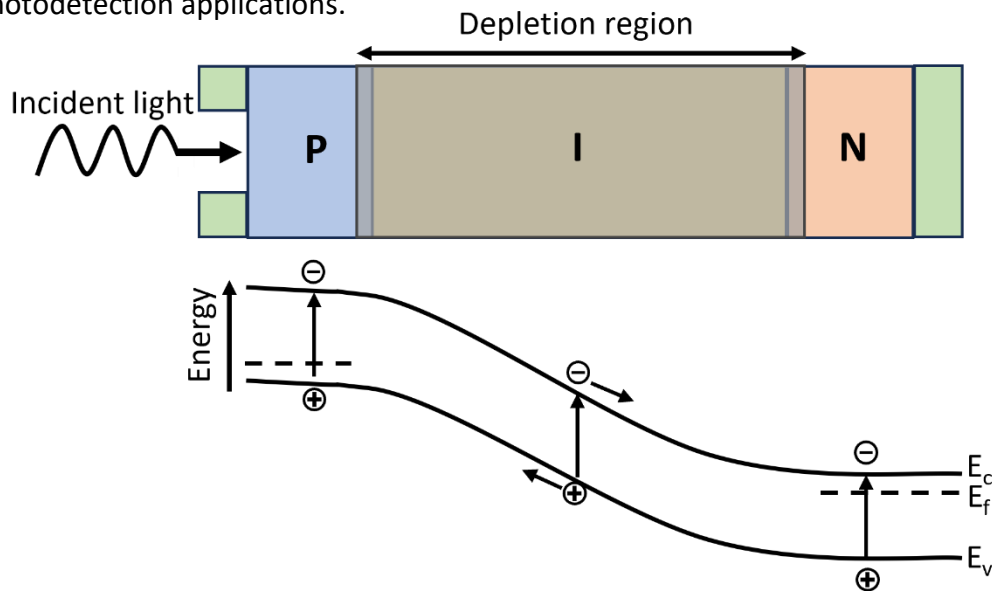


**Fig. 2.4.** Schematic diagram of a PIN photodetector under reverse bias.

### 2.2.3 Barrier Photodetectors

Reducing dark current is vital in producing high performance detectors. If a detector could be made without a depletion region then  $J_{SRH}$  would be effectively eliminated and  $J_{TAT}$  could be significantly reduced [64]. One way to do this is to replace the depletion region with a unipolar barrier layer creating a barrier photodetector.

The most common form of barrier photodetectors is the nBn [64], as shown in Fig. 2.5. The nBn can be thought of as a basic photoconductive (PC) detector with an inserted unipolar barrier. In a PC detector the conductivity of the detector is increased by the creation of extra carriers caused by incident photons. The problem with the PC detector is that it is essentially an open circuit where carriers can flow freely between the contacts. This means that the inherent dark current is very high and a large number of incident photons are required to create a measurable difference in the conductivity [70]. By inserting a barrier layer that blocks the majority carriers (electrons in the case of an nBn) the open circuit is closed and since a potential barrier is formed, the nBn can be thought of as a hybrid of the PC and PV detectors [70].

The nBn consists of an n-type top contact layer for biasing the device followed by an electron blocking barrier layer, an absorbing layer and then a second n-type contact layer to act as the ground. Finding a material suitable for an electron barrier can be challenging. An electron barrier must have a large enough offset in the conduction band to prevent electrons from “jumping” over the barrier due to thermal excitation and as close to 0 offset as possible in the valence band so as not to impede the flow of holes.

The most common materials used for electron barriers in IR detectors are AlSb based ternaries and quaternaries such as AlGaSb [71] and AlGaAsSb [42].

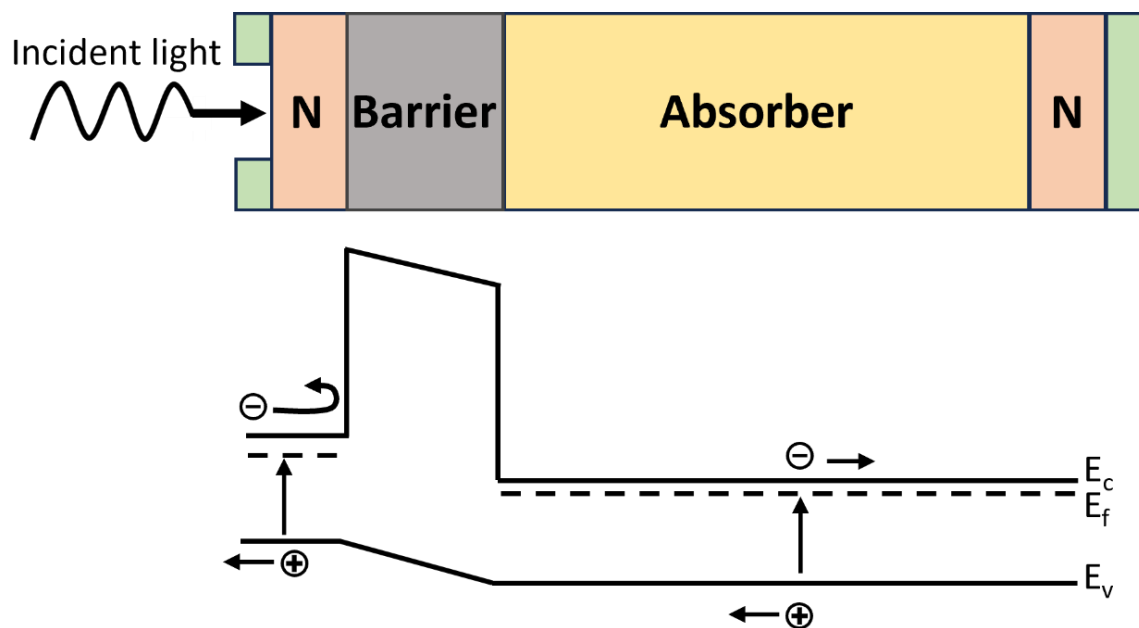


**Fig. 2.5.** Schematic diagram of a nBn photodetector under reverse bias

The barrier serves three important purposes when it comes to dark current compared to PN photodetectors; to remove the need for a depletion region, to block majority carriers which reduces  $J_{diff}$  from the top contact layer and to allow for a shallow etch which reduces the size of the exposed sidewall, reducing  $J_{surf}$ .

As mentioned previously, pixel isolation is required to create an array of detectors. For a PN photodetector, the depletion region of each pixel needs to be electrically isolated from each other to prevent crosstalk. This means that the mesa etch must extend past the depletion region and therefore is required to be deep and expose a large amount of sidewall. In the case of the nBn, pixel isolation can be achieved by only etching through the top contact layer as shown in Fig. 2.6. In the case of the shallow etch, the size of the pixel is defined by the diameter of the etch plus the lateral diffusion length of the minority carriers [72].

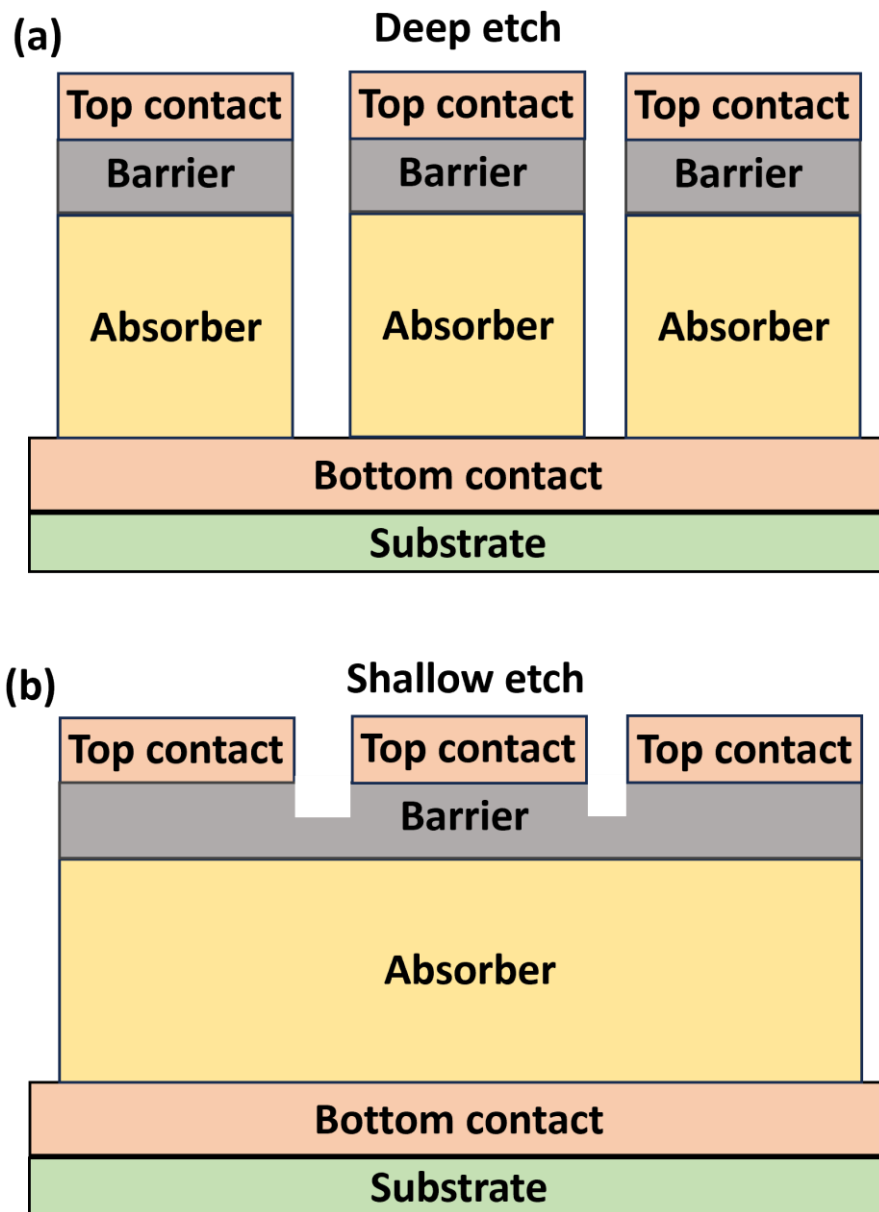


**Fig. 2.6.** Schematic diagram showing (a) the deep mesa etch and (b) the shallow mesa etch of an nBn photodetector.

The nBn is the simplest form of barrier detector, but there are more complex structures such as the complementary barrier infrared detector (CBIRD) [73]. The CBIRD uses both a hole and an electron unipolar barrier to further increase the performance from the nBn at the cost of added device complexity and growth difficulty.

In general, for LWIR detectors where dark current reduction is at its most paramount, barrier-based detectors such as the nBn are most common [74]. For MWIR detectors PN based devices are still the most common commercially due to their simplicity and ease of growth. However, as the MWIR detector industry pushes towards higher operating temperatures, the move towards barrier detectors is inevitable [45].

## 2.3 The Type-II Superlattice Detector

### 2.3.1 MCT and rule 07

For many years, MCT has been the preferred material for MWIR and LWIR photodetection. Its well-established technology, high performance, and tuneable wavelength response make it an ideal choice for these applications. Rule 07 [48] is a simple empirical relationship which is commonly used term to describe the state of the art dark current performance for MCT photodetectors. Rule 07 was developed by analysing the dark current density data of state of the art MCT detectors in 2007 [48] and is still often used as a benchmark to determine how “good” an MCT detector is. Rule 07 is given by [75];

$$J_{07} = J_0 \exp\left(\frac{1.239C}{k \lambda_{cutoff} T}\right) \quad (2.12)$$

where  $k$  is the Boltzmann constant in eV/K,  $T$  is the operating temperature,  $\lambda_{cutoff}$  is the cutoff wavelength of the detector and  $J_0$  and  $C$  are fitting parameters corresponding to MCT and are equal to  $8367 \text{ cm}^{-2}$  and  $-1.1624$  respectively.

Generally, the dark current density of current state of the art MCT detectors fall along the rule 07 line [75]. With current targets to produce detectors which perform better than rule 07, especially at higher operating temperatures or LWIR applications. Detectors that perform at rule 07 levels are generally considered good enough in low temperature MWIR detection as rule 07 is very low at around  $10^{-12} \text{ A cm}^{-2}$  at 77K for a detector with a  $6 \mu\text{m}$  cutoff.

However, if higher operating temperatures are required, rule 07 quickly increases to around  $10^{-5} \text{ A cm}^{-2}$  at 150K and  $10^{-1} \text{ A cm}^{-2}$  at 300K which essentially prevents room temperature operation of MCT in the MWIR. In LWIR even low temperature detection is difficult, for an MCT detector with a cutoff wavelength of  $12 \mu\text{m}$  rule 07 is of the order of  $10^{-4} \text{ A cm}^{-2}$  quickly increasing to  $10^{-1} \text{ A cm}^{-2}$  and  $10^3 \text{ A cm}^{-2}$  at 150K and 300K respectively.

As well as the dark current problems, MCT also suffers from poor scalability due to uniformity problems at larger wafer sizes. These uniformity problems mean that growth of MCT is generally limited to 2 in wafers which keeps cost high.

The regulatory challenges MCT faces are also a major disadvantage of the technology. The use of mercury is becoming increasingly scrutinised and regulated and so the IR detector market is in need of a material system that can compete or improve on MCT's performance without the use of mercury.

### 2.3.2 The Type-II Superlattice

The type-II superlattice was first proposed in 1977 by Sai-Halasz and Esaki [76] and has emerged as a highly promising alternative to MCT. A superlattice is a periodic structure consisting of alternating layers of different materials [77]. The type-II superlattice (T2SL) is a particular kind of superlattice with a type-II band alignment between the two materials.

There are three main types of band alignment in a semiconductor heterojunction [78]. Type-I refers to a junction where the conduction band minimum of the first semiconductor is above the conduction band minimum of the second and the valence band maximum of the first is below the valence band maximum of the second.

Type-II band alignment occurs when both the conduction band minimum and valence band maximum of the second material are below their respective conduction band minimum and valence band maximum.

The type-II band alignment can take on two forms; type-II staggered gap, where the conduction band minimum of the second material is above the valence band maximum of the first and type-II broken gap (also known as type-III) where the conduction band minimum of the second material is below the valence band maximum of the first material. The band alignments are shown in Fig. 2.7.

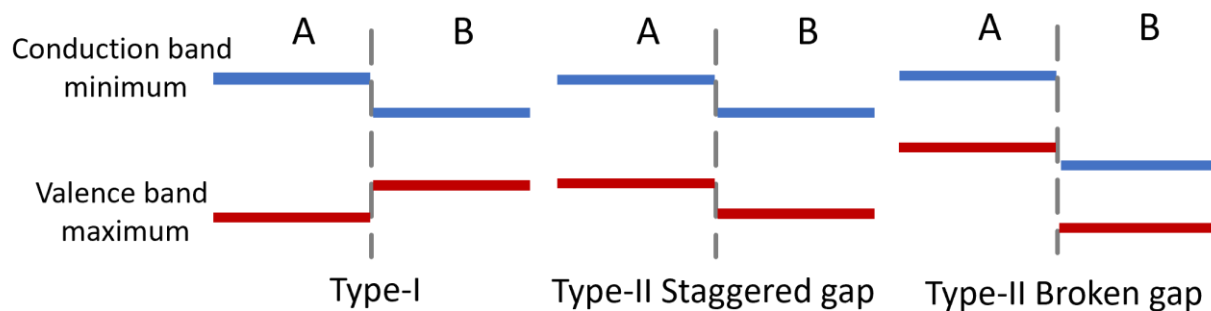


**Fig. 2.7.** The 3 different heterostructure band alignment types.

The type-II band alignment leads to spatial separation of charge carriers within the superlattice, with the electrons confined in quantum wells of one of the materials of the superlattice and the holes confined to the other. If the layers of the superlattice are correctly designed, the interactions between adjacent quantum wells form a periodic potential resulting in the formation of electron and hole minibands analogous to the band structure of a bulk semiconductor [54]. The band gap of the T2SL is given by the distance between these minibands. The distance between the minibands is determined by the width of the quantum wells and the strength of the wave function overlap between the wells.

Therefore, by controlling the layer thickness and composition, the bandgap of the superlattice can be tuned. Importantly, the bandgap of the T2SL can be made smaller than the band gap of the individual semiconductor material making up the individual layers [79] allowing for longer wavelength applications ranging from 4 to 15  $\mu\text{m}$  [80].

The formation of minibands within the superlattice can be explained by first considering a single finite quantum well, as shown in Fig. 2.8.

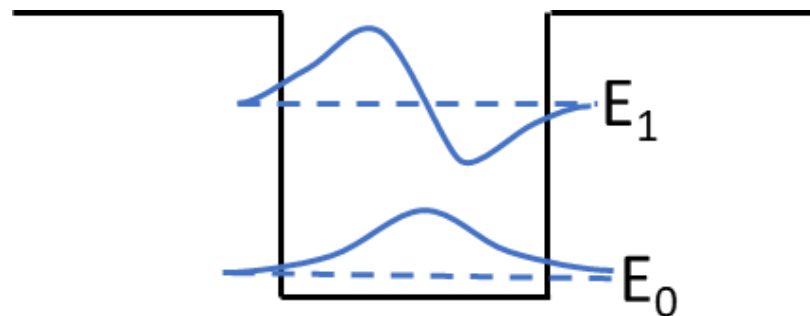


**Fig. 2.8.** A single finite quantum well showing the first two energy levels.

A single finite quantum well consists of wavefunctions at discrete energy levels. When a second identical quantum well is brought close enough to the first, the wavefunctions overlap and couple as shown in Fig. 2.9.

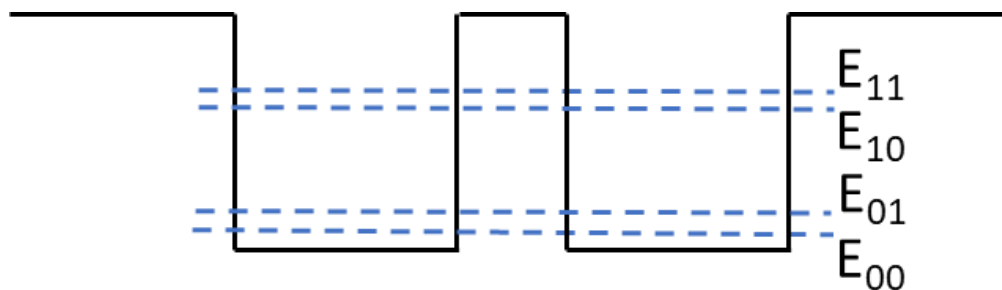


**Fig. 2.9.** Two overlapping quantum wells showing the splitting of the energy levels.

Since it is forbidden by the Pauli exclusion principle for the coupled wavefunctions to exist at the same energy level, a splitting of the energy levels occurs. Creating two new energy levels corresponding to each initial energy level. For example, this is shown as  $E_0$  splitting and forming  $E_{00}$  and  $E_{01}$  in Fig. 2.9.

When  $N$  quantum wells are brought together,  $N$  energy levels are formed. For large  $N$  this will result in a semi-continuous band known as a miniband as shown in Fig. 2.10. The magnitude of the splitting and therefore the width of the miniband depends on the magnitude of the overlap, with quantum wells that are closer together resulting in a wider miniband.



**Fig. 2.10.**  $N$  quantum wells leading to the formation of minibands.

Since the T2SL can be thought of as a large periodic structure of overlapping quantum wells for both electrons and holes it forms both electron and hole minibands as shown in Fig. 2.11.

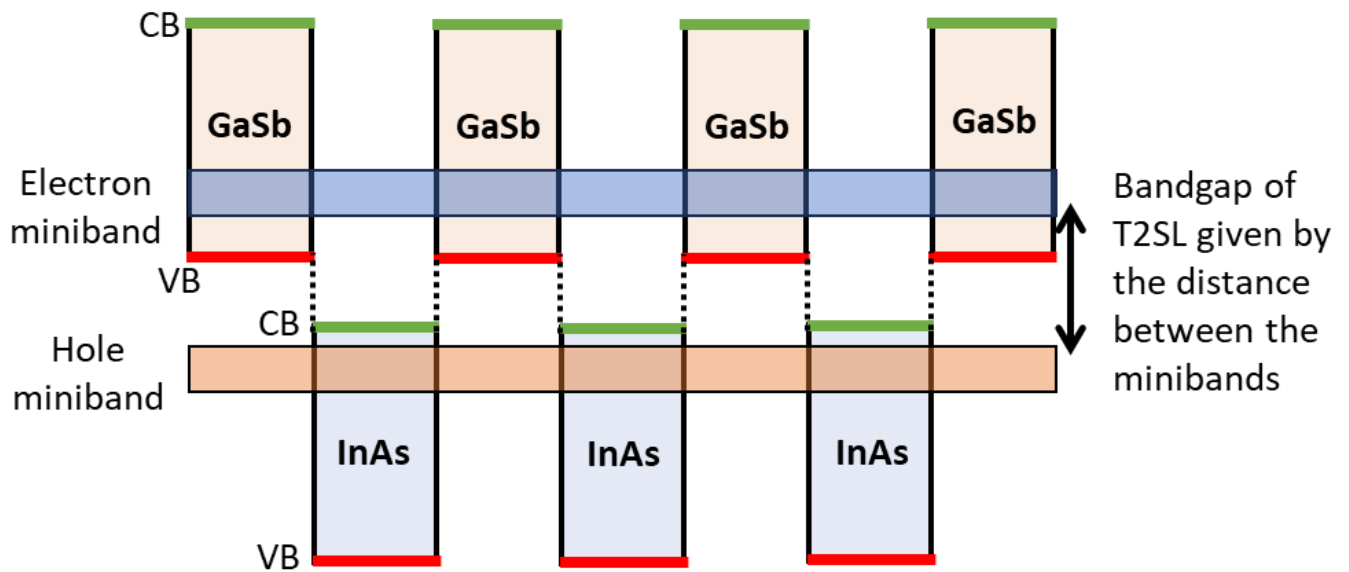


**Fig. 2.11** The formation of minibands from a type-II superlattice structure.

In 1987 Smith and Mailhot proposed that these properties could be leveraged to manufacture T2SLs for IR detector applications [81]. Additionally, due to the minimal lattice mismatch among the materials of the 6.1 Å family (III-V materials with lattice constants close to 6.1 Å), the T2SL structure offers the necessary flexibility to combine different material systems. This flexibility enables the development of devices with high performance in optoelectronic applications. Consequently, any combination of InAs, GaSb, and AlSb binaries and their alloys from the 6.1 Å family can be used for superlattice applications.

The unique properties of T2SLs lead to several theoretical advancements over the current state-of-the-art MCT LWIR detectors. A large proportion of the dark current in MCT is caused by band-to-band tunnelling and Auger recombination. These recombination processes can be reduced by using a T2SL allowing T2SLs to have lower dark currents than bulk materials such as MCT which leads to higher performance. Band-to-band tunnelling which depends on the gap between the conduction band and the light hole band [80,82] is less likely in T2SL due to the splitting of the highest heavy hole miniband and the highest light hole minibands [83].

The splitting of the heavy hole and light hole bands also results in the suppression of Auger recombination [84]. Auger recombination occurs when an electron hole pair recombines in a band-to-band transition similar to a standard radiative recombination. However, the resulting energy given off by an Auger recombination is given off to another electron or hole instead of as a photon, which reduces the photo-efficiency of a device. Specifically in a T2SL the Auger recombination that is suppressed is Auger-7 [85] in which the energy given off from the recombination excites a hole [86].

Due to the splitting of the heavy and light hole bands, the separation of the hole bands is actually larger than the separation of the conduction band and the heavy hole band. This separation suppresses the Auger recombination as it becomes more energy efficient and therefore more likely for the transition to occur between the conduction and heavy hole band, instead of between the hole bands resulting in photon emission [87]. The flexibility of the 6.1 Å family has also been utilized in designing and growing innovative barrier photodetector architectures that can mitigate SRH current.

In the growth of bulk semiconductor layers, it is crucial to match the lattice constant of the grown layer with the substrate to minimise strain caused by the mismatch. As the layer thickens, the strain accumulates and eventually relaxes by forming dislocations within the crystal, which can negatively impact device performance.

In the field of T2SLs it is equally common to talk about “lattice matching” the T2SL to its substrate. However, a T2SL does not have a single lattice constant; it consists of individual layers, each with its own lattice constant. Typically, one layer is strained in compression and the other in tension, creating a balance between these strains. For example, increasing the thickness of the compressively strained layers results in a more compressively strained T2SL structure. Ideally, the layers of the T2SL are designed to balance these strains, ensuring that adding more layers does not change the net strain within the T2SL. T2SL-based devices often require T2SLs with hundreds of periods, so maintaining this balance is essential to prevent dislocations similar to those in bulk layers.

Additionally, there is strain induced by the lattice constant mismatch between the substrate and the T2SL layers. Since the substrate is much thicker than the T2SL, it is assumed that all the strain is absorbed by the T2SL. A T2SL structure can be designed to account for this substrate-induced strain by balancing it with the relative thicknesses of the T2SL layers, creating a fully balanced system. In this case, the net strain on the T2SL remains unchanged as more periods are added. This process is referred to as lattice matching the T2SL to the substrate, similar to the bulk case.

Lattice matching is commonly measured using X-ray diffraction (XRD) by comparing the distance between the 0<sup>th</sup> order T2SL and substrate XRD peaks. A T2SL and substrate are considered lattice matched when the 0<sup>th</sup> order T2SL peak overlaps with the substrate peak.

### 2.3.3 The Ga-based InAs/GaSb T2SL

Interest in developing T2SLs was sparked by impressive theoretical results from studies conducted in the late 1970s. In 1978, research by Sai-Halasz et al. [88] revealed that InAs/GaSb superlattices could exhibit semiconducting characteristics. Concurrently, Nucho and Madhukar [89] showed that enhancing the discontinuity between superlattice layers could alter the bandgap from a direct to an indirect type. However, despite these promising theoretical proposals, due to the precise layer thickness and interfacial control needed, it was not possible to produce high-quality T2SL detectors until significant advancements in molecular beam epitaxy (MBE) technology occurred.

The first experimental demonstration of an InAs/GaInSb T2SL detector was performed by Johnson et al. in 1996 [90], achieving a photo response up to 10.6  $\mu\text{m}$ . The next year, Mohseni et al. [91] demonstrated the MBE growth and characterization of InAs/GaSb T2SLs for LWIR detectors. In the same year, Fuchs et al. [92] demonstrated LWIR photodetection using an InAs/GaInSb T2SL, significantly suppressing band-to-band tunnelling currents and improving material quality. A significant milestone was reached in 2004 [93] with the development of the first high-performance T2SL focal plane array (FPA), confirming the suitability of the T2SL material system for IR photodetection.

More recently the most common form of T2SL is the InAs/GaSb T2SL, especially for LWIR detectors. InAs/GaSb T2SLs are conventionally grown via MBE on GaSb substrates. In order to lattice match the InAs/GaSb to the GaSb substrates, a thin InSb interfacial layer is grown between the layers of InAs and GaSb to act as a strain balancing layer. The wavelength of the InAs/GaSb can be adjusted by changing the relative layer thicknesses of the InAs and GaSb, with thicker InAs causing the band gap to get smaller. Changing the layer thickness of GaSb has a much smaller effect on the band gap than InAs but it can still be used to engineer the bandgap, with a thicker GaSb layer increasing the bandgap.

Generally, the GaSb layer thickness is kept relatively constant, usually in the range of 4-10 ML. The InAs layer thickness is then adjusted to tune the wavelength, usually in the range of 8-25ML. For example, in the case of an InAs/GaSb T2SL with a GaSb layer thickness of 8ML, an InAs layer thickness of 8 ML will create a bandgap of around 0.3eV (4.5 $\mu\text{m}$ ) and an InAs layer thickness of 21 ML will create a bandgap of around 0.1eV (12  $\mu\text{m}$ ). This large change of bandgap and therefore detection wavelength with only a relatively small change in layer thickness is what makes the InAs/GaSb T2SL such an exciting material system for IR detection.

There are two main limitations on the wavelength range of the InAs/GaSb T2SL. The lower limit is caused by the physical ability to grow thin repeatable layers, which causes the shortest wavelength InAs/GaSb T2SLs to cut off at around 3  $\mu\text{m}$ . The upper limit is not due to the epitaxy but due to how the T2SL functions. In order to form minibands, there must be sufficient wavefunction overlap between the layers of the T2SL. The thicker the layers the weaker the overlap which in turn reduces the quantum efficiency of the detector. This reduction in quantum efficiency causes the upper limit of the InAs/GaSb T2SL wavelength range to be around 15  $\mu\text{m}$ . The wavelength range of the InAs/GaSb bandgap is therefore between 3 and 15  $\mu\text{m}$  which is perfect for detectors in the MWIR and LWIR.

InAs/GaSb T2SLs however, suffer from a short minority carrier lifetime, in the region of 10s of nanoseconds [94]. Minority carrier lifetime is critical in photodetector performance as it relates directly to the signal to noise ratio due to the increase in dark current [95]. The cause of this short minority carrier lifetime appears to be GaSb related as the lifetime has been shown to correlate with the GaSb volume in the InAs/GaSb T2SL [96].

Bulk GaSb has a number of intrinsic point defects, but the most relevant one is the Ga anti-site where a Ga atom takes the place of an Sb atom, causing bulk GaSb to be intrinsically p-doped [97]. These Ga anti-sites do not have a detrimental effect on the minority carrier lifetime of bulk GaSb as the energy level of the anti-site is not in the bandgap. In the case of the InAs/GaSb T2SL however, the Ga anti-site energy level is within the bandgap creating a non-radiative SRH pathway. Whilst it may be possible to engineer the bandgap of the InAs/GaSb T2SL so that the defect is not in the band gap, it is difficult and provides a major design constraint [96].

#### 2.3.4 The Ga-free InAs/InAsSb T2SL

The other way to reduce the effect of the Ga anti-sites on the minority carrier lifetime is to remove the Ga from the superlattice entirely. In recent decades Ga-free T2SL detectors, typically made from InAs/InAsSb, have been developed as potential alternatives to the more established Ga-containing variants.

The Ga-free T2SL was first proposed by Osbourn in 1984 [98] as an  $\text{InAs}_{0.4}\text{Sb}_{0.6} / \text{InAs}_{1-x}\text{Sb}_x$  strained-layer superlattice. Osbourn used the strain and type-II band alignment of the InAsSb/InAsSb material system to achieve a bandgap reduction beyond what was possible with bulk semiconductors at the time.

Throughout the 1990s, Ga-free T2SL growth and fabrication witnessed significant advancements. However, interest in LWIR Ga-free T2SLs waned until around 2011, when it was reported that InAs/InAsSb T2SLs exhibit significantly longer minority carrier lifetimes compared to their Ga-based counterparts [57]. The InAs/InAsSb T2SL has been shown to have a 10x longer minority carrier lifetime than InAs/GaSb, of the order of 100s of nanoseconds.

In addition to its longer minority carrier lifetimes, a notable advantage of the InAs/InAsSb T2SL is its tolerance to defects. This defect tolerance comes from the defect states existing above the conduction miniband within the InAs/InAsSb T2SL instead of within the band gap [58]. This defect tolerance makes the InAs/InAsSb T2SL a promising candidate for growth on highly mismatched substrates such as Ge, GaAs [99] or Si [1] where threading defect densities are high.

The last main advantage of the InAs/InAsSb T2SL over the InAs/GaSb is in its relative ease of growth. The InAs/InAsSb T2SL can be grown lattice matched to GaSb substrates without the need of interfacial strain balancing layers like the InAs/GaSb T2SL. The growth sequence for InAs/InAsSb is therefore relatively simple; all that is needed it to switch on and off the Sb flow to change between the InAs and InAsSb layers.

There are two main ways to change the wavelength of the InAs/InAsSb T2SL, either increase the thickness of the InAsSb layer or increase the Sb percentage within the InAsSb. Due to the volatility and ease of segregation of the Sb, it is very difficult to increase the Sb % much past 35% [99] without the Sb diffusing out from the InAsSb layer into the InAs layer. So generally, the only way to produce an InAs/InAsSb T2SL at longer wavelengths is to increase the InAsSb layer thickness.

Unfortunately, unlike InAs/GaSb, a much larger increase to layer thickness is needed to change the cutoff wavelength. This requirement for thicker layers leads to a much lower upper wavelength limit as the thicker layers quickly reduce the wavefunction overlap and therefore the quantum efficiency of the detector. This reduction in quantum efficiency causes the practical upper wavelength limit of the InAs/InAsSb T2SL to be around 10  $\mu\text{m}$ . This may be increased by finding solutions to the Sb diffusion problems such as growth interruptions and lower growth temperatures and much work is currently being done in this field to create LWIR InAs/InAsSb detectors. Unfortunately, as of the time of writing, no major practical breakthroughs have been published.

The lower limit is very similar to the InAs/GaSb T2SL, it is caused by the physical ability to grow thin repeatable layers. The lower wavelength limit of the InAs/InAsSb T2SL is around 3  $\mu\text{m}$ . So, the total wavelength range of the InAs/InAsSb T2SL is between 3 and 10  $\mu\text{m}$ . Therefore, at the moment the InAs/InAsSb T2SL is confined to MWIR detector applications.

Also, whilst both the InAs/GaSb and InAs/InAsSb T2SLs have similar electron masses, the hole effective mass of the InAs/InAsSb T2SL is considerably larger, resulting in unfavourable hole transport properties [83]. This issue also worsens at longer wavelengths further reinforcing that the InAs/InAsSb T2SL is confined to the MWIR.

In the MWIR however, due to the advantages of the longer minority carrier lifetimes the InAs/InAsSb exhibits superior performance and so the choice of InAs/GaSb or InAs/InAsSb mainly comes down to application, with InAs/GaSb being preferred for LWIR applications and InAs/InAsSb being preferred for MWIR applications.

Both types of T2SL are being researched to minimise their downsides, such as longer wavelength InAs/InAsSb [99] and InAs/GaSb with improved minority carrier lifetime [100]. So, it is highly possible that which T2SL is appropriate for which application may change in time as more discoveries are made.

## 2.4 Review of the current state-of-the-art

### 2.4.1 Minority carrier lifetime

The lifetime of minority carriers is a crucial factor influencing both the dark current and the quantum efficiency of photodetectors. The minority carrier lifetime is therefore an important metric to help understand the performance differences between the T2SLs and MCT. The minority carrier lifetime,  $\tau$ , is given by;

$$\tau = \frac{L}{\sqrt{\frac{k_b T}{q} \mu}} \quad (2.1)$$

where  $L$  is the minority carrier diffusion length,  $k_b$  is the Boltzmann constant,  $T$  is temperature,  $q$  is the electron charge and  $\mu$  is the carrier mobility.

The minority carrier lifetime is linked to the dark current of a detector via both the diffusion and G-R/SRH pathways as shown in equations 2.4 and 2.5, where a higher carrier lifetime results in a lower dark current which is preferred.

Additionally, the minority carrier lifetime affects the quantum efficiency of a photodetector via the minority carrier diffusion length. The diffusion length defines the maximum thickness of the absorber region; if the absorber region is larger than the diffusion length, some carriers will recombine within the absorber region and not contribute to the photocurrent.

To achieve high quantum efficiencies, it is generally understood that the active region thickness of a detector should be equal to, if not greater than, the target cutoff wavelength. Therefore, a diffusion length equal or greater than the target cutoff wavelength is desired. Fig. 2.12 shows the minority carrier lifetimes for InAs/GaSb and InAs/InAsSb T2SLs, as well as MCT.

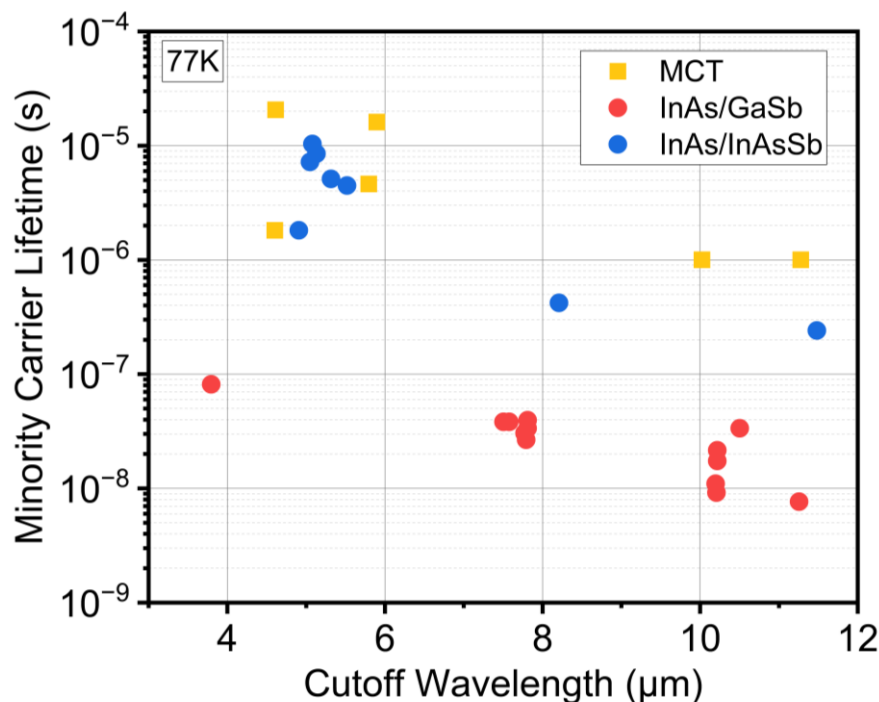


**Fig. 2.12.** Collected minority carrier lifetimes vs cutoff wavelength for InAs/GaSb [101–106] and InAs/InAsSb [31,57,101,107–110] type-II superlattices and MCT [103,111,112].

Fig. 2.12 shows a near-linear decrease in carrier lifetime with increasing wavelength for both InAs/GaSb and InAs/InAsSb T2SLs. This trend underscores the challenge of LWIR detection due to minority carrier lifetime. However, InAs/InAsSb T2SLs exhibit lifetimes comparable to MCT in the MWIR range, and their LWIR lifetimes are within an order of magnitude of those of MCT.

Since the lifetime directly influences the diffusion current in T2SL devices, following the relationship  $J_{diff} \sim \tau^{-1}$ , the performance of diffusion-limited InAs/InAsSb T2SL devices is expected to significantly surpass that of InAs/GaSb detectors. This trend is beginning to manifest in the MWIR range. However, for LWIR detectors, the challenges of incorporating high Sb percentages, as described in section 2.3.4, are still preventing InAs/InAsSb from outperforming InAs/GaSb.

#### 2.4.2 Dark current

As shown by the “rule 07” line in Fig. 2.10, the dark current of a detector is highly sensitive to its wavelength. Longer wavelength detectors have smaller bandgaps, making them more susceptible to thermally excited carriers, which increases dark currents. Consequently, most LWIR detectors operate at 77K to minimize thermal noise. In contrast, high operating temperature devices in the MWIR range are becoming more common, with operating temperatures around 150K.

In the LWIR range, dark current performance at 77K is comparable to current state-of-the-art MCT detectors, as shown in Fig. 2.13. However, the anticipated superior performance of T2SL detectors due to the suppression of Auger recombination compared to MCT has yet to be realised. This performance limitation may be due to the shorter minority carrier lifetimes of T2SLs compared to MCT at longer wavelengths, or the less mature T2SL technology.

When comparing T2SLs in the LWIR range, there are significantly more examples of InAs/GaSb detectors than InAs/InAsSb detectors. This is primarily due to the challenges in realising LWIR InAs/InAsSb T2SLs, as discussed in section 2.3.4. Interestingly, the few examples of LWIR InAs/InAsSb T2SLs perform similarly to InAs/GaSb detectors, suggesting that the longer minority lifetime may not be sufficient to further reduce dark current. Alternatively, the benefits of the longer minority lifetime may not be fully realised due to growth difficulties. Improvements in the growth of InAs/InAsSb, allowing for higher Sb incorporation and better crystal quality, may be necessary to translate the superior minority lifetime into better dark current performance.

It is also important to note that all LWIR T2SL detectors in Fig. 2.13 are barrier-based, as barriers are required to address the more challenging dark current issues at longer wavelengths.

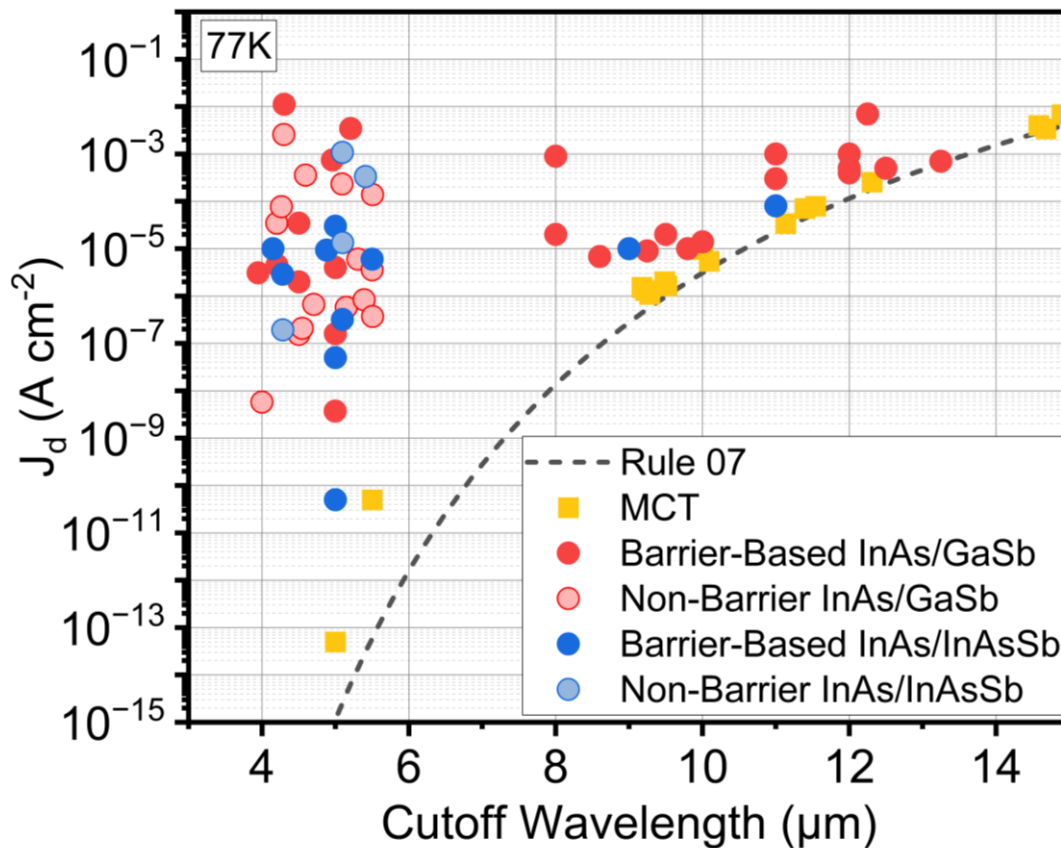


**Fig. 2.13.** Collected data of dark current density versus cutoff wavelength at 77K for Barrier-based InAs/GaSb [4–7,113,114,71,115,116,8,117–119,9,10,120,11–14,121,15,122,16,123], Non-Barrier InAs/GaSb [124,20,125–127,21,128,17,22,23,129–135], Barrier-Based InAs/InAsSb [136,27–29,40,42,137–139,30,140,141] and Non-Barrier InAs/InAsSb detectors [32,47,33–35,142,36]. To be compared with MCT detectors [143,144] and the “Rule 07” line [48].

In the MWIR detector region, the theoretical advantages of T2SL detectors over MCT have yet to be experimentally demonstrated in terms of superior dark current density performance at 77K. It is important to note that experimental readings of  $J_d$  less than  $10^{-8}$   $\text{A cm}^{-2}$  are very rare due to the limitations of standard experimental setups. Therefore, high-performance MWIR detectors are typically compared to MCT at higher temperatures, such as 150K, as shown in Fig. 2.14.

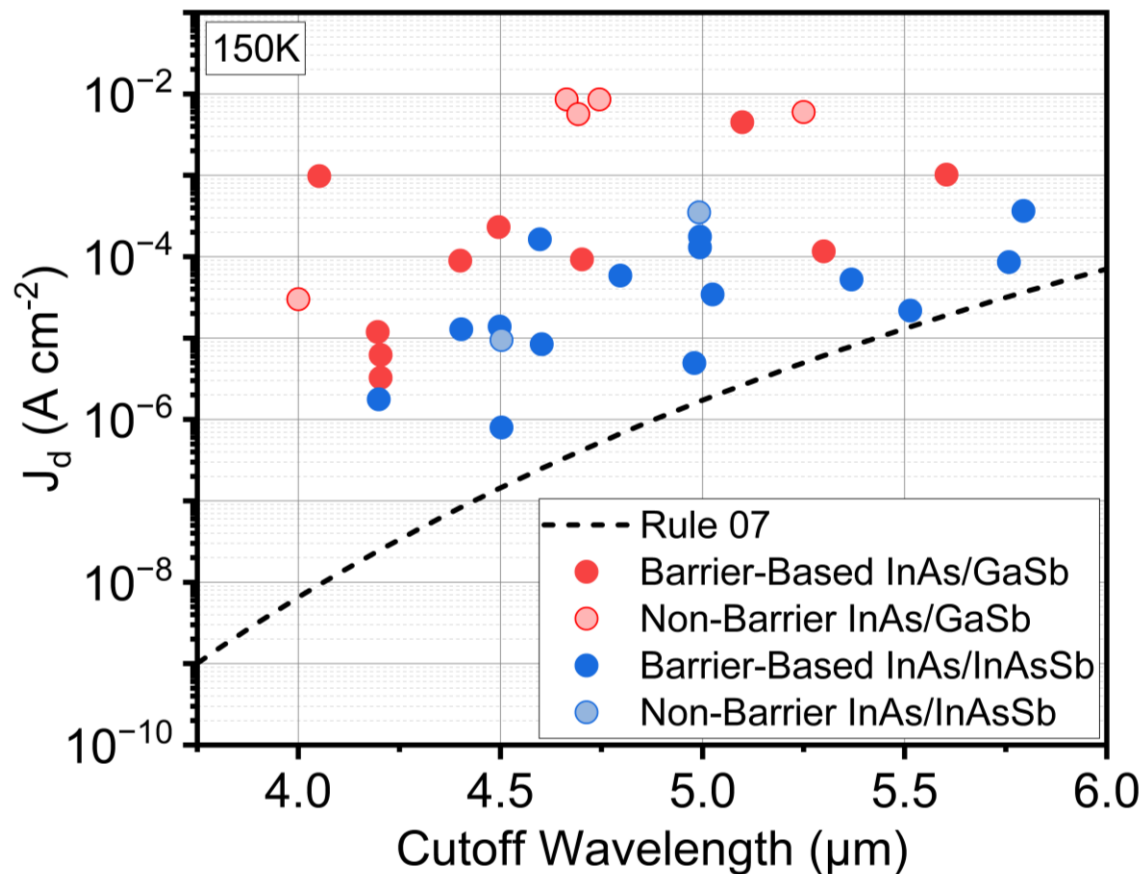


**Fig. 2.14.** Collected data of dark current density versus cutoff wavelength at 150K for Barrier-based InAs/GaSb [4–8,38,71,113,115–119], Non-Barrier InAs/GaSb [17,21,22,124,128,145], Barrier-Based InAs/InAsSb [27,28,39–43,137–140,146] and Non-Barrier InAs/InAsSb detectors [33,47]. To be compared with the “Rule 07” line [48].

At higher temperatures, the benefits of the longer minority carrier lifetime of InAs/InAsSb detectors compared to InAs/GaSb detectors become evident. Fig. 2.14 illustrates a general trend of InAs/InAsSb detectors outperforming InAs/GaSb detectors. It also shows that the dark current density values of InAs/InAsSb detectors are very comparable to the “rule 07” line, which indicates that they are approaching the theoretical maximum performance of MCT detectors.

Additionally, at higher temperatures, barrier-based detectors outperform non-barrier detectors. This provides strong experimental evidence supporting the theoretical advantages of barrier-based detectors discussed in section 2.2.3.

### 2.4.3 External quantum efficiency

EQE is where the most significant discrepancy between T2SL and MCT detectors is observed. As mentioned in section 2.4.1, the thickness of the absorber region greatly impacts the EQE of the detector. If the absorber thickness is less than the detection wavelength, only a fraction of the incident light will be absorbed, reducing the EQE. Therefore, EQE depends on both the cutoff wavelength and absorber layer thickness, necessitating separate comparison figures for MWIR and LWIR.

As shown in Figs. 2.15 a and b, the EQE of MCT detectors is significantly higher than that of T2SL detectors in both MWIR and LWIR. The primary reason is that the MCT absorber layer is much thicker than those of InAs/GaSb and InAs/InAsSb T2SLs. The longer minority carrier lifetime and diffusion length in MCT, as illustrated in Fig. 2.12, allow for thicker absorber regions. This difference in minority carrier lifetime is more pronounced when comparing MCT with InAs/GaSb T2SLs, explaining the EQE discrepancy. However, the minority carrier lifetime difference between InAs/InAsSb and MCT is smaller, requiring a different explanation for the EQE discrepancy.

Another limiting factor in absorber layer thickness is the difficulty of growing thick, high-quality T2SL sections. The inherent strain in a T2SL structure, combined with the volatility issues of Sb growth, makes growing thick T2SL sections challenging. Minor discrepancies in strain balancing may not significantly affect a few superlattice periods, but as the periods increase, the problems compound, resulting in low quality, highly defective crystals.

Even with constant absorber layer thickness, differences in EQE persist, largely due to crystal quality in both the layers and interfaces. Epitaxial developments are crucial for producing high quality T2SLs with higher EQEs. Additionally, device design plays a role; designing a device structure often involves compromising between dark current and EQE. Generally, devices with larger depletion regions have higher EQEs and higher dark currents. Most barrier-based designs aim to eliminate the depletion region to reduce dark currents, but clever doping can induce small depletion regions between the barriers and absorber to enhance EQE with minimal impact on dark current [122,123].

To increase T2SL EQE to levels comparable with MCT, higher quality, better strain-balanced and ultimately T2SLs with a higher number of periods need to be developed, along with novel device designs.

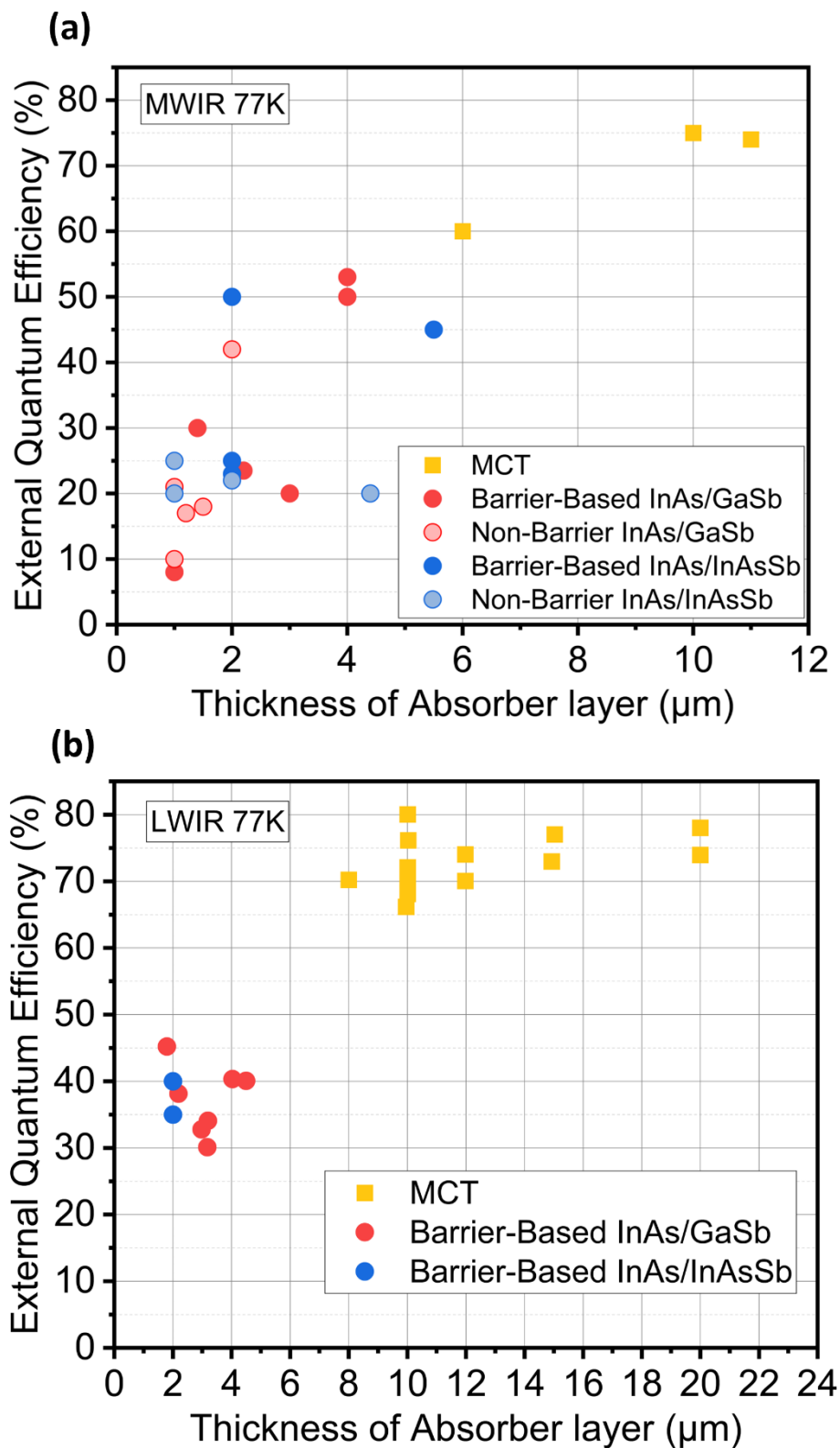


**Fig. 2.15.** Collected data of external quantum efficiency versus absorber layer thickness at 77K for (a) MWIR MCT [143,147,148], Barrier-based InAs/GaSb [6,7,71,113–115], Non-Barrier InAs/GaSb [20,124–126,149], Barrier-Based InAs/InAsSb [30,140,141] and Non-Barrier InAs/InAsSb detectors [33–35,142]. (b) LWIR MCT [2,3,150,151], Barrier-Based InAs/GaSb [9–12,120,152] and Barrier-Based InAs/InAsSb LWIR detectors [141,153].

#### 2.4.4 Detectivity

Detectivity, which combines dark current density and quantum efficiency as shown in Eq. 2.11, is the standard figure of merit for evaluating detector performance. A “rule 07” line has been added to Fig. 2.13a for illustrative purposes. This line was derived from the “rule 07” dark current density line at 77K, assuming an average EQE of 75% for an MCT detector. 75% was taken as an estimate of the current MCT EQE performance based on the MCT EQE data in Fig. 2.13. While this assumption may not hold true across all wavelengths, it provides a convenient comparison for detectivity, particularly in the LWIR region.

Since detectivity is wavelength-dependent, peak detectivities were chosen for comparison. Generally, the peak detectivity for an MWIR detector is close to the cutoff wavelength, as responsivity is relatively flat across the wavelength range. For LWIR detectors, peak detectivity is usually around 2  $\mu\text{m}$  less than the cutoff wavelength. For instance, a detector designed for 10  $\mu\text{m}$  detection would typically have a cutoff wavelength of around 12  $\mu\text{m}$ .

In the LWIR, the combination of superior dark current and especially EQE cause the MCT detectors to perform better than the T2SL detectors. Although comparison between wavelengths is difficult, it does appear clear that at the longer wavelengths MCT is still superior to T2SLs. There is a clear difference between InAs/GaSb and InAs/InAsSb however, InAs/GaSb detectors consistently outperform InAs/InAsSb detectors in the LWIR. Even with InAs/InAsSb's inherent advantages from its longer minority carrier lifetime, superior detector performance has yet to be realised. The reason for this comes back to the difficulty of creating high quality LWIR InAs/InAsSb. Once again, barrier-based detectors seem to have consistently superior performance in LWIR applications, and it seems clear as to why much of the research to date focuses on LWIR detectors with a barrier-based design.

In the MWIR there is little difference between InAs/GaSb and InAs/InAsSb detectors at 77K. However, at 150K, InAs/InAsSb detectors outperform InAs/GaSb detectors, particularly in the 4.25 to 5.5  $\mu\text{m}$  range, as illustrated in Fig. 2.16b. The barrier-based detectors consistently show the best performance at each wavelength, with superior dark current performance being crucial at higher operating temperatures.

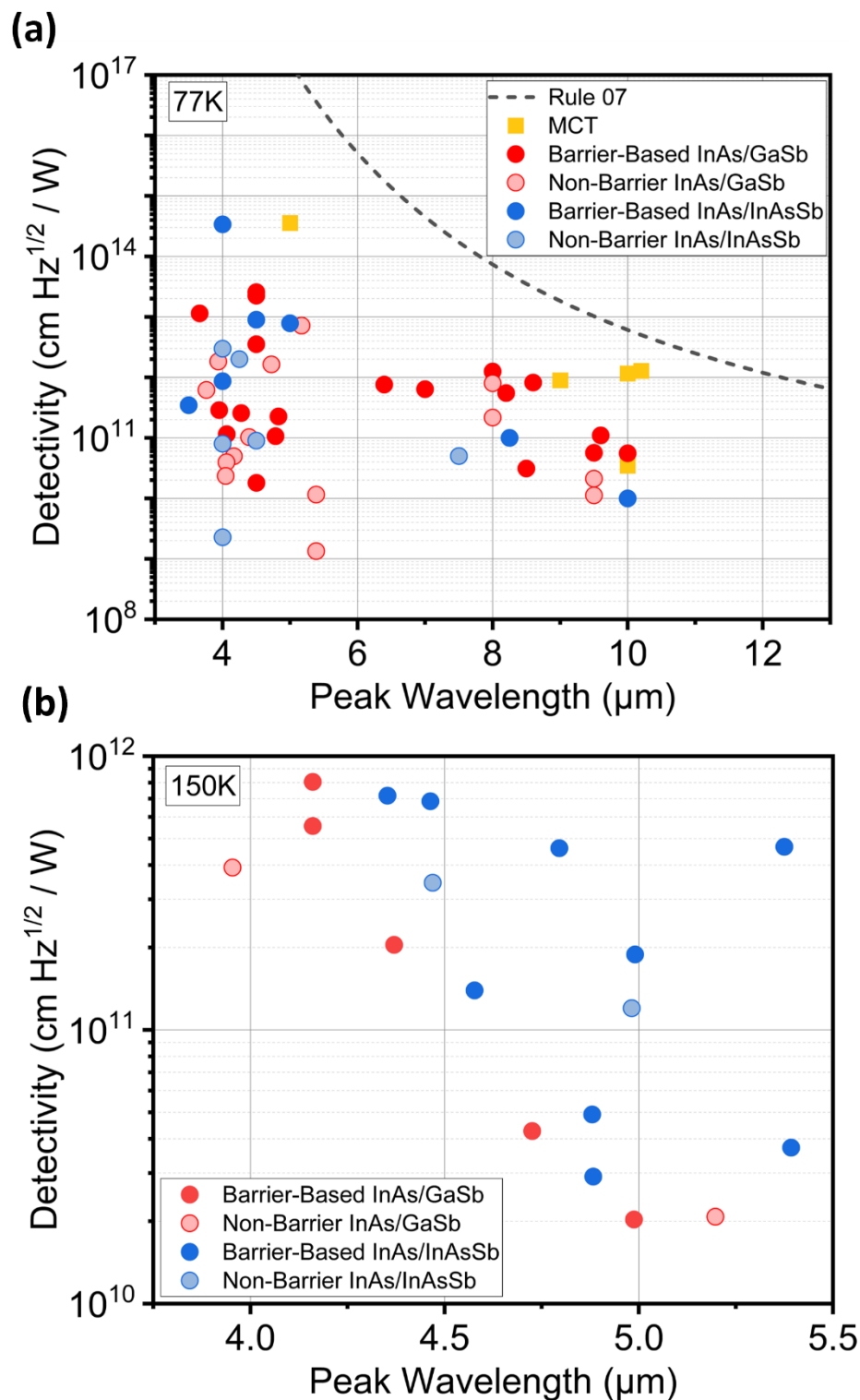


**Fig. 2.16.** Collected data of peak detectivity versus wavelength at (a) 77K for MCT [2,3], Barrier-based InAs/GaSb [4–19], Non-Barrier InAs/GaSb [9,12,17,20–26], Barrier-Based InAs/InAsSb [27–31] and Non-Barrier InAs/InAsSb detectors [32–37]. (b) At 150K for Barrier-based InAs/GaSb [4,7,8,38], Non-Barrier InAs/GaSb [17,20], Barrier-Based InAs/InAsSb [28–30,39–46] and Non-Barrier InAs/InAsSb detectors [33,47]. The “Rule 07” line is added for reference to (a) and is calculated from the rule 07 dark current density line at 77K with the QE of the MCT detectors assumed to be 75%.

In conclusion, barrier-based device structures consistently outperform non-barrier devices and should be used whenever possible. For LWIR applications, InAs/GaSb is superior to InAs/InAsSb due to the challenges of growing InAs/InAsSb with high Sb composition. This may change as InAs/InAsSb growth technology advances and the benefits of its longer minority carrier lifetime are realised.

It is important to note that high Sb incorporation is more difficult in MOCVD than in MBE due to the higher growth temperatures. Therefore, achieving high-performance LWIR InAs/InAsSb through MOCVD may require significant innovation. Even if MOCVD-grown LWIR InAs/InAsSb T2SL becomes feasible, finding Al-free barriers remains a challenge, meaning initial LWIR InAs/InAsSb detectors grown by MOCVD will likely be non-barrier based. Thus, for MOCVD growth of LWIR detectors, InAs/GaSb barrier-based detectors are the superior choice. These barriers can be achieved by adjusting the period thicknesses of the T2SL, which are reasonable for LWIR InAs/GaSb.

For MWIR applications grown by MOCVD, InAs/GaSb barriers are not feasible, so the choice is between non-barrier InAs/GaSb or InAs/InAsSb detectors. In MWIR, InAs/InAsSb consistently outperforms InAs/GaSb in both dark current and detectivity, especially at higher operating temperatures. Therefore, for MOCVD-grown detectors, barrier-based InAs/GaSb should be used for LWIR, and non-barrier InAs/InAsSb should be used for MWIR.

## 2.5 T2SL growth (MBE vs MOCVD)

Conventionally, both T2SLs are grown via MBE onto lattice matched GaSb substrates. In general, MBE provides very precise source switching allowing for tight layer thickness, composition and interfacial control [154]. Specifically for the growth of antimonides such as the T2SLs, the most significant advantage of MBE is the low growth temperatures. Low growth temperatures are advantageous because of the low equilibrium vapour pressure of antimony, meaning that at higher temperatures, surface desorption of the antimony begins to dominate preventing high antimony incorporation. Furthermore, some antimonides such as InSb and GaSb have relatively low melting points (527 °C and 712 °C respectively) meaning that it is not possible to grow them above those temperatures [155].

The main disadvantage of MBE is related to commercialisation as MBE growth rates are notoriously slow at around 1 Å/s resulting in relatively low throughput [156]. The primary reason for the slow growth rates in Molecular Beam Epitaxy (MBE) is the achievable atomic flux at the surface. In MBE, the atomic flux generated by the effusion cells is controlled by their temperature. Increasing the temperature of the effusion cells produces more flux, leading to a higher growth rate. However, there are practical limitations to how hot the effusion cells can be heated. At higher temperatures, a phenomenon known as MBE spitting occurs, where the atomic source starts producing larger particles instead of singular atoms [157]. These particles, such as clusters of source atoms or molecules formed due to reactions between the molten source and residual gases in the chamber, cause defects in the epitaxy. This creates a practical limitation on the effusion cell temperature and, consequently, the growth rate.

On the other hand, Metal-Organic Chemical Vapour Deposition (MOCVD) can increase its atomic flux at the surface by increasing the flow rate of the precursor gases used. Although there is a limit to the number of atoms that can react in a given time, this limit is much higher than in the MBE case. Growth rates of around 10 Å/s are common for commercial MOCVD. These higher growth rates make MOCVD generally preferred for large-scale commercial fabrication [158].

However, MOCVD growth temperatures are much higher than MBE due to the temperature requirement to crack the precursor gases used. The higher temperatures have been a fundamental issue in the growth of antimonides, as antimony's high volatility and low vapour pressure require low growth temperatures to prevent large surface desorption [159]. The antimonides are also far more sensitive to growth parameters such as III/V ratio and temperature than more standard materials such as arsenides and phosphides. This sensitivity makes the development of growth recipes more challenging as there is very little room for flexibility within the recipe as each parameter has a very narrow window that allows for high quality growth. However, with the development of higher quality precursors that crack at lower temperatures such as tertiarybutylarsine (TBAs) and triethylantimony (TESb) these challenges are starting to be overcome [160].

#### 2.4.1 MOCVD Growth of InAs/GaSb

As well as the general challenges of growing antimonides by MOCVD, there are two main challenges when converting the growth of InAs/GaSb from MBE. Firstly, InAs/GaSb is not naturally lattice matched to any standard commercially available substrate. Due to it being a combination of InAs and GaSb the lattice constant of the InAs/GaSb T2SL will always be somewhere between InAs and GaSb. In MBE, this challenge is overcome by the use of thin InSb interfacial layers which allow the InAs/GaSb T2SL to be lattice matched to GaSb substrates. Unfortunately, due to its low melting point, growth of InSb via MOCVD is very difficult. A solution to this problem is to instead use GaAs interfacial layers to lattice match the T2SL to InAs substrates.

The other challenge is to find an effective electron barrier to be able to create the superior barrier-based detectors needed to reduce dark current density for LWIR applications. The standard AlSb based ternaries and quaternaries used in MBE suffer from very high unintentional p-type carbon doping ( $\sim 10^{18} \text{ cm}^{-3}$ ) when grown by MOCVD [161] which can be detrimental to their optical properties and limits their use due to them being very hard to dope n-type. This carbon incorporation can be reduced by growing at higher temperatures which more fully crack the precursor gases used, however this higher temperature is detrimental to the material quality.

A proposed solution is to use more novel precursors such as TTBAI or DMEAI which crack at lower temperatures to the standard TMAI [161]. However, due to the novelty of TTBAI and DMEAI, they suffer from a lower purity than TMAI which in turn causes more unintended doping problems. AlSb based ternaries and quaternaries also suffer from segregation problems where clusters of binary AlSb, GaSb or AlAs form instead of remaining in their combined ternary or quaternary form. This segregation changes the electrical and optical properties of the layer and makes designing the layer very difficult. These challenges mean that generally the growth of AlSb is avoided in MOCVD.

Due to the Type-II broken gap band alignment of the InAs/GaSb T2SL, it is possible to create electron barriers using the T2SL itself, removing the need for AlSb entirely. In an InAs/GaSb T2SL, if the GaSb layer thickness is kept constant but the InAs layer thickness is decreased, the conduction band moves upwards and the valence band does not change. Therefore, InAs/GaSb T2SLs with the same GaSb thickness but different InAs thickness will create an electron barrier. However, the height of the electron barrier that can be made is limited by the contrast between the band gaps of the two T2SLs. This height limitation means that a T2SL barrier is only really usable in LWIR detectors where the absorber layer is made from a T2SL with a band gap of around 0.1eV and the barrier layer is made from a MWIR T2SL with a band gap of around 0.3eV. This produces an electron barrier height of 0.2eV which is still much smaller than what could be achieved using AlSb but is large enough to still function as an effective barrier, especially in low temperature conditions.

#### 2.4.2 MOCVD Growth of InAs/InAsSb

In contrast to InAs/GaSb, the conversion from the growth of InAs/InAsSb from MBE to MOCVD is relatively simple. InAs/InAsSb can be lattice matched to GaSb substrates without the use of strain balancing layers so no major modifications to the growth sequence are required.

The big challenge for the MOCVD growth of InAs/InAsSb T2SL is the lack of an easy non-AlSb based electron barrier layer. Unfortunately, the same technique used for InAs/GaSb cannot be used in InAs/InAsSb as the layer thickness required to provide a big enough barrier would greatly reduce the wavefunction overlap. For this reason, MOCVD grown InAs/InAsSb T2SL detectors are confined to non-barrier-based architectures such as the PIN detector. This lack of barrier restricts the wavelength range that a MOCVD grown InAs/InAsSb detector can work at to around 3-5  $\mu\text{m}$  instead of the 3-10  $\mu\text{m}$  that can be achieved using barrier-based detectors grown by MBE. As although it is possible to grow InAs/InAsSb T2SLs at wavelengths up to 10  $\mu\text{m}$  via MOCVD, the large dark currents caused by the lack of barrier become a practical device limitation at these wavelengths.

**Table 2.1.** Summary of the main differences between MOCVD grown InAs/InAsSb and InAs/GaSb T2SLs.

Wavelength range	T2SL	Substrate	Pros	Cons
3-5 $\mu\text{m}$	InAs/ InAsSb	GaSb	<ul style="list-style-type: none"> <li>• Does not require additional interfacial layers for strain balancing</li> <li>• Growth sequence relatively simple</li> <li>• Long minority carrier lifetime means high theoretical QE</li> <li>• Evidence of defect tolerance makes it a good candidate for growth on non-native substrates</li> </ul>	<ul style="list-style-type: none"> <li>• Confined to non-barrier-based devices which have higher dark current</li> <li>• Difficult to increase Sb composition past 35% confining the InAs/InAsSb to MWIR applications</li> </ul>
3-15 $\mu\text{m}$	InAs/ GaSb	InAs	<ul style="list-style-type: none"> <li>• Large wavelength range allowing for LWIR applications</li> <li>• Barrier-based device structures possible</li> </ul>	<ul style="list-style-type: none"> <li>• Interfacial strain balancing layers are required, making growth sequence complex</li> <li>• No evidence of defect tolerance may prevent the use of non-native substrates</li> </ul>

### 2.4.3 Growth on non-native substrates

Both InAs and GaSb substrates are small, expensive and brittle and so finding alternatives that are more commercially desirable is important. Also, the absorption coefficient for both InAs and GaSb is high in the MWIR and especially in the LWIR [162,163]. This high absorption coefficient is a problem for the conventional backside illuminated devices as it caused the majority of the incident light to be absorbed before reaching the detector. This absorption can be minimised by the use of mechanical backside thinning processes, but this adds an extra step and therefore extra cost into the manufacturing process.

There are three main substrate alternatives proposed for the T2SLs: GaAs, Si and Ge. Unfortunately, the integration of InAs to any of these substrates has proved to be very challenging. The integration of an InAs/GaSb T2SL that is lattice matched to InAs to any of these substrates has yet to be achieved.

Integration of GaSb onto non-native substrates has been far more fruitful however. The integration of GaSb onto GaAs is the most reported due to the fact that there exists an interfacial strain balancing technique known as the interfacial misfit array (IMF) between the interface of GaAs and GaSb. The IMF helps to overcome the 7.8% lattice mismatch between the two layers and helps reduce the threading dislocations caused by the mismatch. The threading dislocation density is still much higher than if the device was grown on native substrates and so more progress needs to be made before GaAs substrates can fully replace GaSb.

GaAs substrates are much cheaper than GaSb substrates and are commercially available at much larger sizes making them a very promising alternative economically. The absorption coefficient of GaAs is also around 100x lower than GaSb as shown in Fig. 2.17 [163] making it a very promising replacement for backside illuminated devices as it would remove the need of a substrate thinning step. This higher absorption coefficient of GaSb is caused by the higher defect densities of commercially available GaSb substrates when compared to GaAs. Due to this higher defect density, GaSb has much higher levels of free carrier and defect related absorption than GaAs causing it to have a much higher absorption coefficient at longer wavelengths [163].

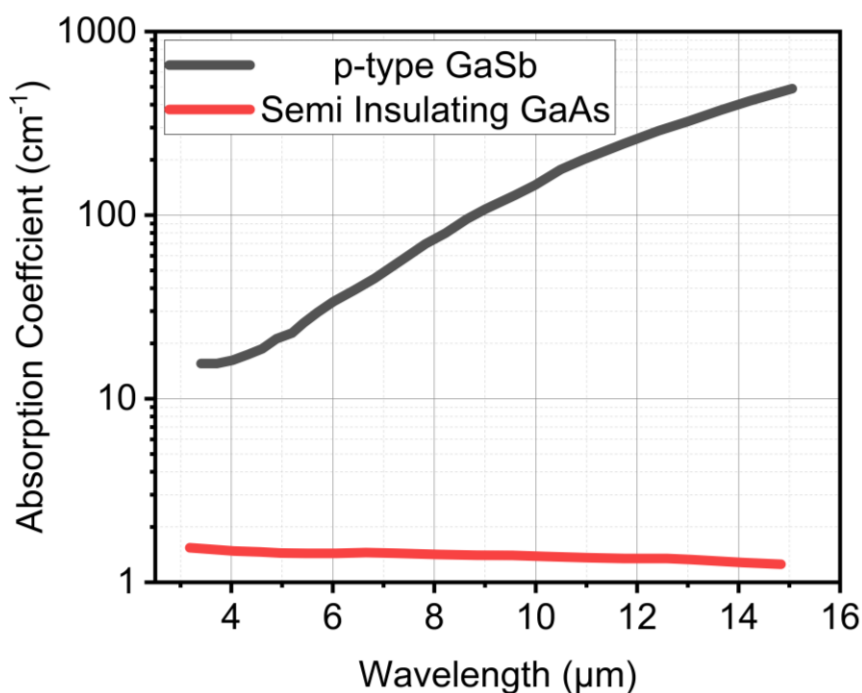


**Fig. 2.17.** Graph showing the difference in absorption coefficients between GaSb and GaAs [163].

The integration of III-Vs onto Si substrates has long been the holy grail of compound semiconductors. To be able to combine the optical advantages of III-V with the commercial advantages of Si would be a massive achievement and is highly sought after. The integration of GaSb onto Si is no different.

There are three main difficulties in integrating GaSb with Si; the large 12% lattice mismatch, the polar / non-polar interfaces and cracks caused by the thermal mismatch. Thermal cracking can be eliminated by making sure that the layer thicknesses are not too large so that the built-up strain from the thermal mismatch is not too large. The polar / non-polar interface is a problem as it causes the formation of antiphase domains (APDs) which act as non-radiative recombination centres. The problem of APDs can be removed by using off-cut Si substrates or by the use of in situ plasma etching [164]. The large lattice mismatch is still a problem, but buffer schemes utilising defect filtering layers are being employed to reduce the threading dislocation density caused by the mismatch [42].

Si substrates are even bigger and cheaper than GaAs substrates and so the economic advantages are even more relevant for Si than GaAs. The absorption coefficient of Si is also much lower than GaSb in the IR making it a superior substrate for backside illumination.

The use of Ge substrates for GaSb integration is far less mature than GaAs and Si. The cost of a Ge substrate is similar to a GaAs and since Ge is a group IV material it has the same issues with APDs caused by polar / non-polar interfaces. The interesting advantage of Ge however, is that it can be used as the basis of MWIR photonic circuits [165]. As the Ge based MWIR passive device technology matures there will be a need for active components such as lasers and detectors that can be easily integrated with the Ge platform. The InAs/InAsSb would be an obvious choice for such circuits and so the integration of it onto Ge unlocks many new applications that use MWIR photonic circuitry.

# Research Tools

All the samples in this thesis are grown using Metal-Organic Chemical Vapour Deposition (MOCVD) which is described in section 3.1. After growth some of the samples are then used to fabricate devices, following the processes and techniques specified in Section 3.2. Finally, both fabricated and unfabricated samples undergo characterisation using the methods outlined in Section 3.3.

## 3.1 Metal-organic chemical vapour deposition (MOCVD)

Due to its high growth rates, MOCVD has become the leading technique for the commercial production of III-V compound semiconductor optoelectronic and electronic devices. Currently, there are three main types of MOCVD reactor geometries available in the market: horizontal reactors, planetary reactors, and close-coupled showerhead (CCS) reactors [166].

Horizontal reactors, such as the aix200, are generally considered outdated technology and are typically used for lower-budget applications. In a horizontal reactor, the gas flows horizontally over the substrate inside of a quartz tube, as shown in Fig. 3.1a. Because the gas flow is horizontal across the substrates, these reactors suffer from growth uniformity problems as deposition rates differ from the side where the gas is injected and where it is removed [167].

Planetary reactors, like the Aixtron G5, represent the current state-of-the-art technology for commercial applications. In a planetary reactor, the gas still flows horizontally across the substrate. However, the key difference between a planetary reactor and a basic horizontal reactor is that the planetary reactor rotates, as shown in Fig. 3.1b. This rotation allows for much higher growth uniformities even on larger substrates. This capability to grow on very large wafers with high uniformity makes the planetary reactors ideal for high-volume production applications.

CCS reactors, such as the Aixtron CCS, are generally used for applications requiring smaller wafers, such as academic research. CCS reactors inject their gases vertically across the entire susceptor as show in Fig 3.1c. This vertical injection further increases uniformity, but is a lot more complex than the radial gas distribution of a planetary reactor, which is what generally limits the maximum size of the CCS reactor. The reactor used throughout this thesis is an Aixtron 3 x 2 inch flip top CCS reactor, as shown in Fig. 3.2. All samples were grown on either full or partial 2-inch wafers.

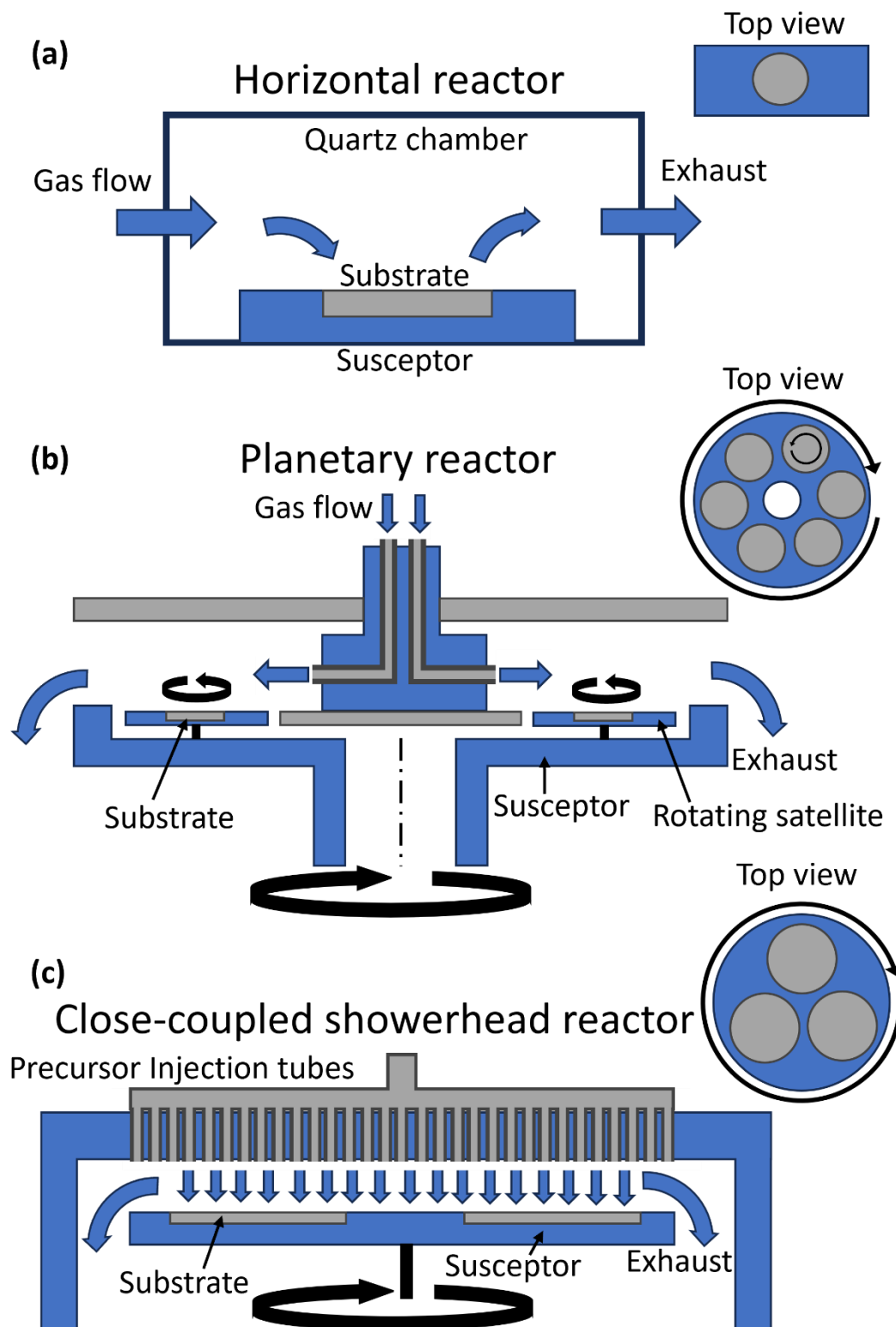


**Fig. 3.1.** Schematic diagrams of the 3 main types of MOCVD reactors: (a) horizontal reactors, (b) planetary reactors and (c) close-coupled showerhead reactors.

(a)



(b)

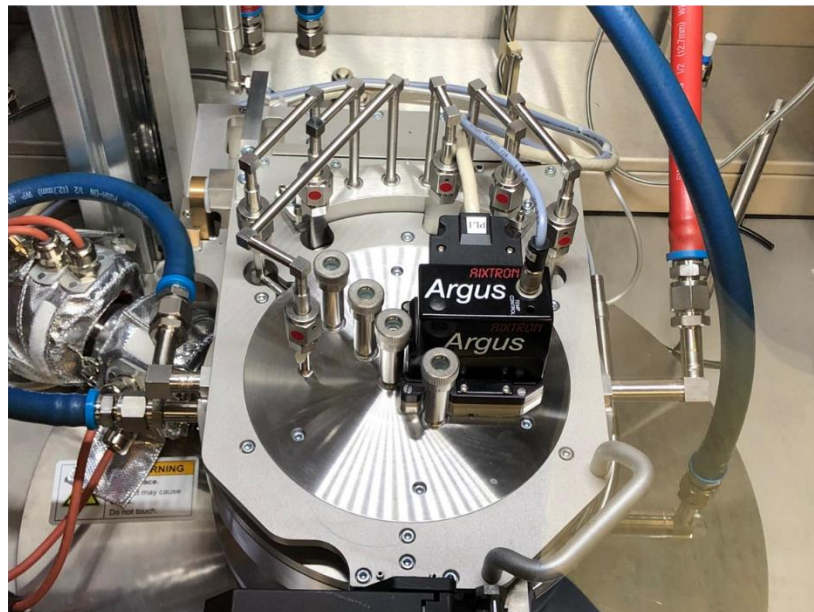


**Fig. 3.2.** Photographs of the Aixtron 3 x 2 inch flip top CCS reactor that was used throughout this project. (a) Shows the whole MOCVD system including the housing and glovebox. (b) Shows the CCS reactor itself which is found within the glovebox.

In an MOCVD system, all sources are vaporised and transported into the reactor using a carrier gas. These injected gases are ultra-pure and can be finely controlled. Fig. 4.3 illustrates the simplified growth mechanism of GaSb using MOCVD. The initial precursor gases, TEGa and TESb, are transported into the reactor using H<sub>2</sub> as a carrier gas. These precursor gases contain the desired atoms, surrounded by hydrocarbon chains. The bonds between the central atom and the hydrocarbons are very weak so as the precursor gases diffuse towards the heated substrate, they begin to decompose or “crack” in an area known as the boundary layer. This decomposition process is chemically complex, involving multiple stages and by-products. Essentially, the precursor gases shed their hydrocarbons, leaving only the deposited atoms (Ga or Sb).

After reaching the surface, the Ga and Sb atoms diffuse laterally along the surface until they reach a suitable crystal site where they become incorporated. The decomposed hydrocarbon groups are then exhausted as waste products from the reaction. Typically, the Group V precursor is supplied in excess and the growth rate is controlled by the Group III flow. The temperature of the substrate as well as the flow rates of the precursors are all carefully controlled to ensure high crystal quality. Different III-V materials have different optimum temperatures and precursor flow ratios which often differ on a reactor-to-reactor basis. So, the optimal growth parameters are normally found experimentally with growth calibrations.

At low growth temperatures the growth rate is limited by the surface reaction rate, known as the kinetically limited regime. As the growth temperature increases, the growth rate of the nucleation layer rises significantly for the same amount of precursor flow rate. When the growth temperature is further elevated, the surface reaction rate becomes sufficiently high that the growth rate is then limited by the diffusion rate of the reactant species onto the wafer surface. This is known as the mass-transport-limited regime.

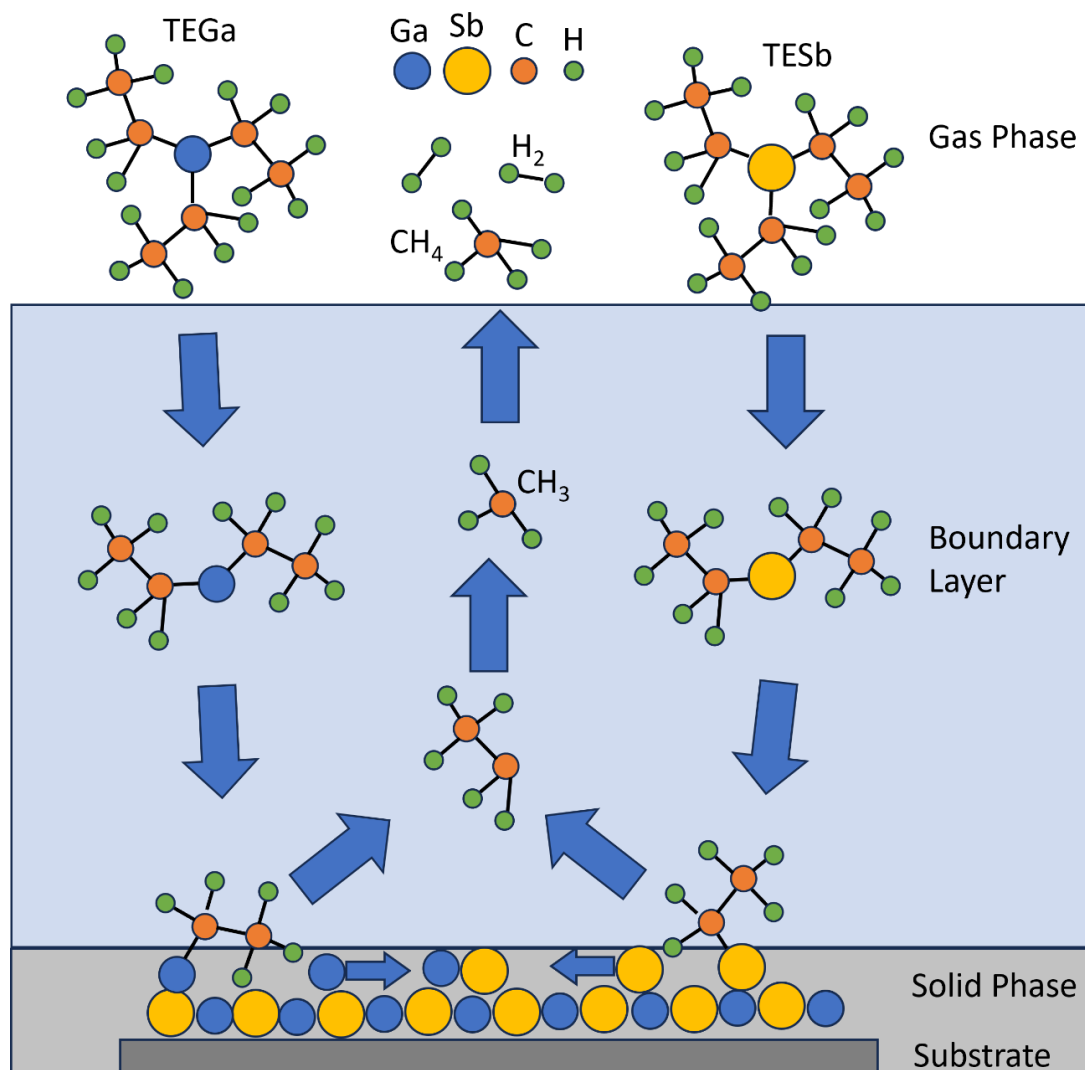


**Fig. 3.3.** Simplified MOCVD growth mechanism of GaSb.

### 3.1.1.1 In-situ Monitoring

The CCS reactor used was equipped with two different in-situ monitors, and ARGUS pyrometric profiling system to monitor surface temperature and an LAYTEC EpiTT reflectometry measurement system to monitor surface reflectivity and growth rates.

ARGUS is an emissivity detector that operates based on Planck's Law, which describes the distribution of radiative energy in relation to black body temperature. A small amount of radiation passes through holes in the showerhead and is collected by photodetectors within ARGUS. As the susceptor rotates it is fully scanned, allowing the system software to display a temperature map. Calibration of ARGUS is achieved by placing it over a black body calibrator, which is scanned across all detectors.

EpiTT is a reflectometry measurement which involves shining light at specific wavelengths onto the substrate and monitoring its reflection. Higher quality crystal growth typically exhibits greater reflection. This reflection data can be used to qualitatively monitor the crystal growth process and identify the stages at which issues may occur. If well calibrated and the growth material is well known, the oscillations in the reflection data can also be used to calculate the growth rate of the layer.

## 3.2 Fabrication

This section outlines the standard fabrication process for a photodetector which was developed for this project and is the basis of all the fabrication within this thesis. The fabrication steps were developed by myself and Ka Ming Wong and the fabrication was performed by Ka Ming Wong at Cardiff University's Institute for compound semiconductors. This fabrication process flow will be discussed and developed in the experimental chapters of this thesis. The fabrication process can be sub divided into nine steps.

### Step 1 – Starting Epitaxial Stack

Fig. 3.4 shows a typical InAs/GaSb nBn detector that will be the starting point of the fabrication.

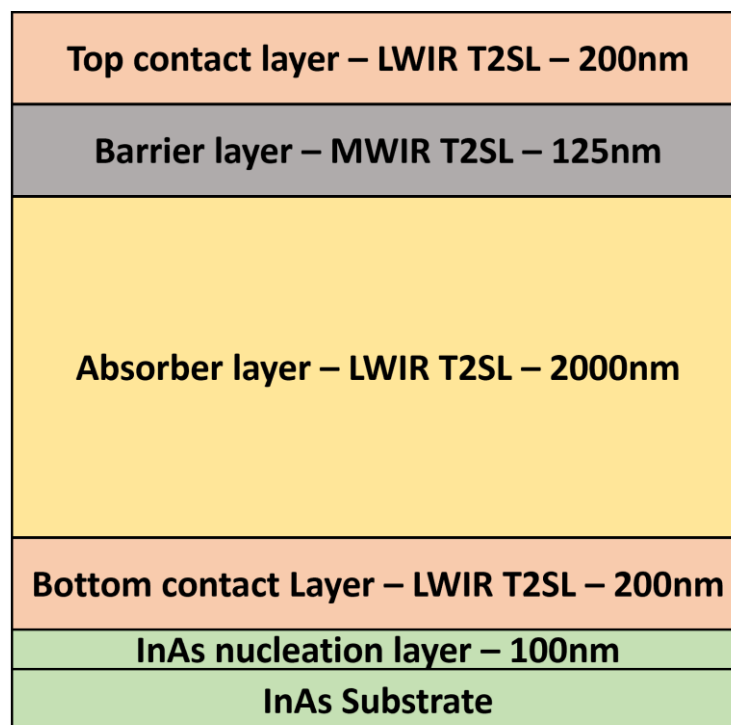


**Fig. 3.4.** Schematic diagram of a typical InAs/GaSb nBn detector epitaxial stack.

### Step 2 – SiO<sub>2</sub> Hard Mask

First a SiO<sub>2</sub> hard mask is deposited onto the top of the wafer as shown in Fig. 3.5a. The SiO<sub>2</sub> is deposited via plasma enhanced chemical vapour deposition. The hard mask layer thickness is dictated by the etching selectivity between the mask and the T2SL and in this case was set to 1000nm.

### Step 3 – Photolithography

The photoresist S1813 is then spun at 4000 rpm to achieve a thickness of 1300nm and baked at 115°C for 60 seconds onto the SiO<sub>2</sub> hard mask. It is then exposed using a Durham Magneto Optics ML3, a maskless, direct-write photolithography machine. The ML3 is set to a resolution of 1µm and has a dose of 120mJ/cm<sup>2</sup>. AZ726 is then used as a developer for the photo resist. Finally, O<sub>2</sub> plasma is used to clean the surface.

### Step 4 – SiO<sub>2</sub> Plasma Etch

After the photoresist has developed, a Plasma Etch Inc. PE-100 Plasma Asher is used to etch away the exposed SiO<sub>2</sub>. The PE-100 uses inductively coupled plasma to etch away the exposed SiO<sub>2</sub>. The plasma used to etch the SiO<sub>2</sub> is C<sub>4</sub>F<sub>8</sub>.

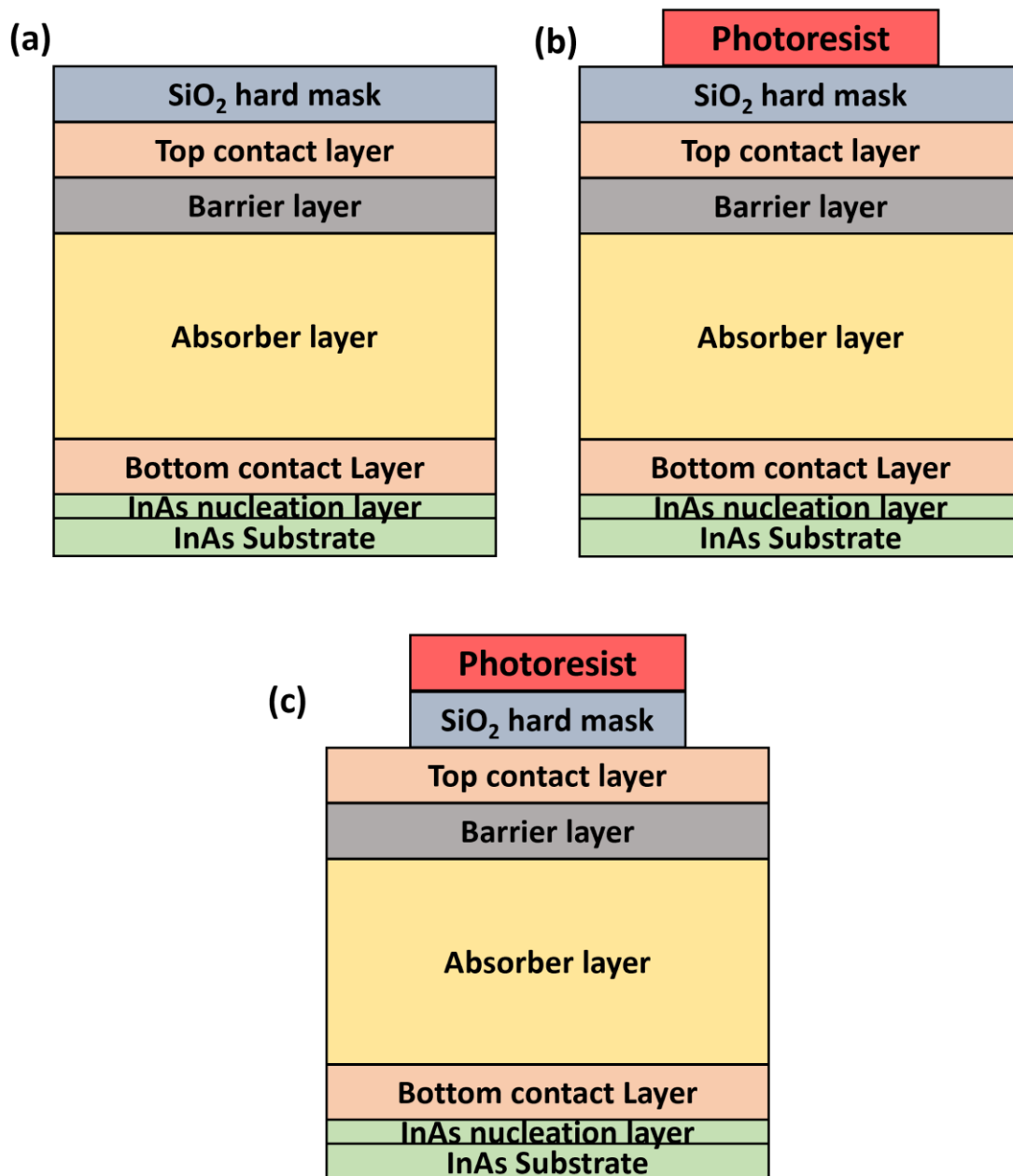


**Fig. 3.5.** Schematic diagram of a typical InAs/GaSb nBn detector after; (a) SiO<sub>2</sub> hard mask deposition, (b) the deposition and development of the photoresist and (c) the plasma etching of the SiO<sub>2</sub> hard mask.

**Step 5 – Photoresist removal**

The photoresist is then removed using NMP leaving only the  $\text{SiO}_2$  hard mask and the exposed T2SL which will be etched as shown in Fig. 3.6.

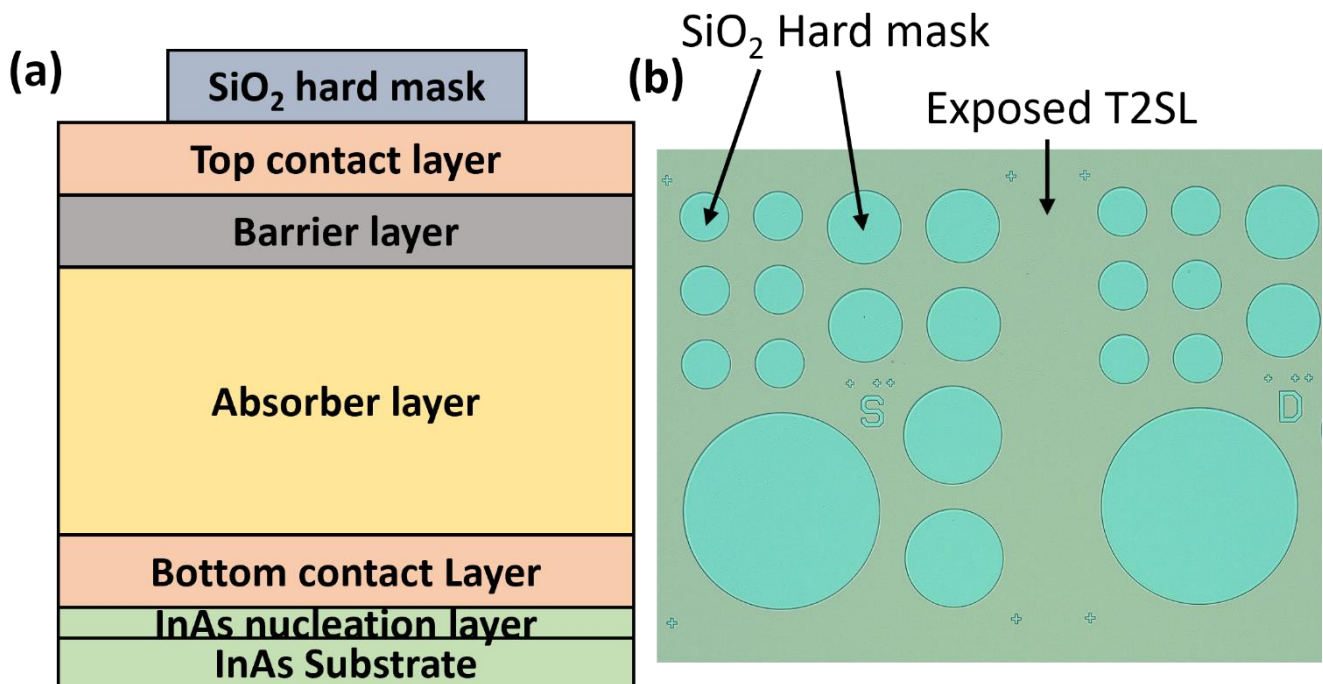


**Fig. 3.6.** (a) Schematic diagram of a typical InAs/GaSb nBn detector after the removal of the photoresist. (b) Optical microscope picture of the surface of the sample before mesa etch.

### Step 6 – Mesa Etch

The PE-100 then uses  $\text{BCl}_3$  to perform the mesa etch which isolates the individual devices from each other by etching away the material between the detectors which is exposed in Fig. 3.6b. As shown in Fig. 3.7, the mesa etch stops within the bottom contact layer. This means that all the devices have an electrically common bottom contact, but the top contacts are physically isolated from each other.

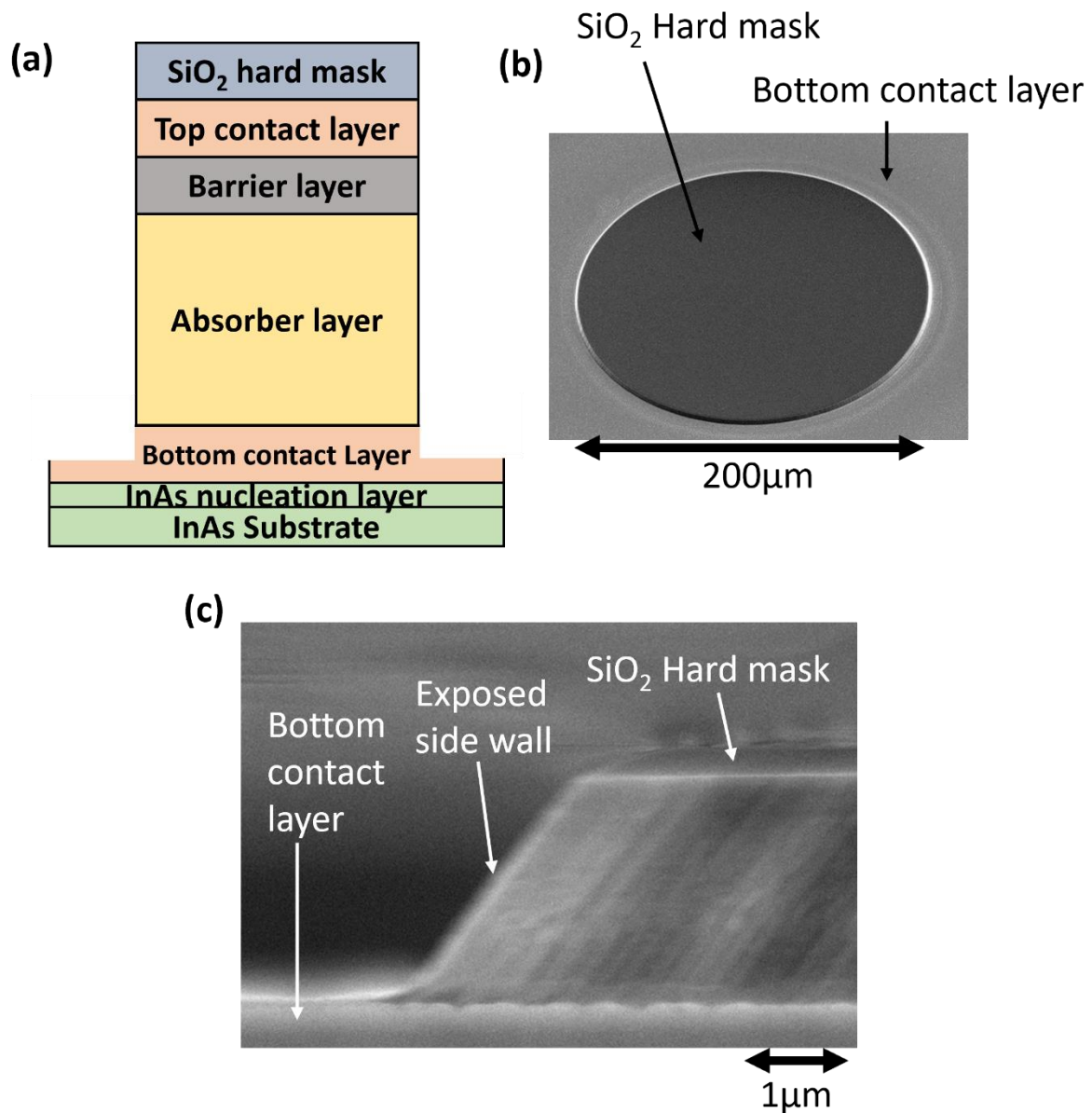


**Fig. 3.7.** (a) Schematic diagram of a typical InAs/GaSb nBn detector after the mesa etch. (b) Scanning Electron Microscope (SEM) picture of the top of an individual device after the mesa etch. (c) SEM picture of the side profile of an individual device after the mesa etch.

**Step 7 – Metal Contact Photolithography**

The SiO<sub>2</sub> hard mask is then removed with hydrogen fluoride (HF) and a new photoresist mask is applied. The photoresist used in this step is AZ2070 but it is applied and exposed in the same way as in step 3, albeit with a different mask design for the direct writer, as shown in Fig. 3.8b.

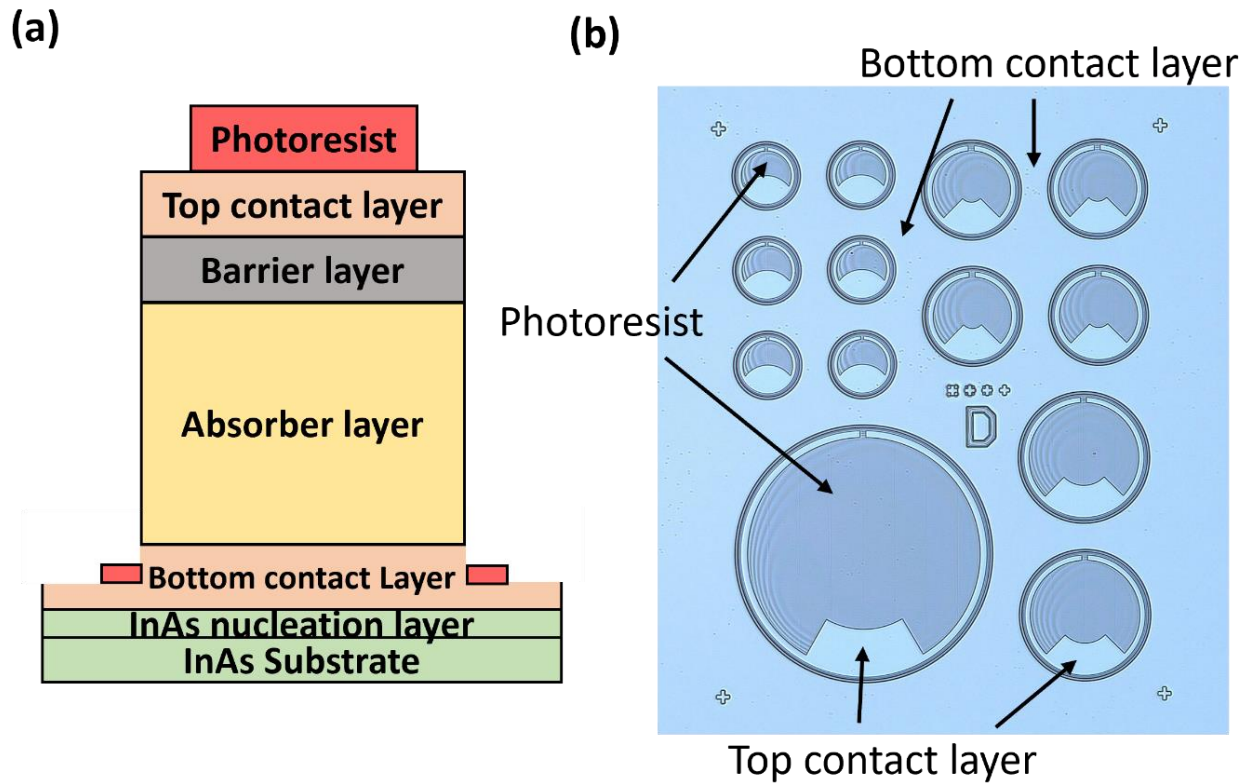


**Fig. 3.8.** (a) Schematic diagram of a typical InAs/GaSb nBn detector with the photoresist ready for metal deposition. (b) Optical microscope picture of the surface of the sample before metal deposition.

**Step 8 – Metal Deposition**

A 40nm layer of Ti followed by a 150nm layer of Au is then deposited using a Buhler Boxer Dielectric Thermal Evaporator. Metal lift off is then performed by removing the remaining photoresist with NMP which also removes any metal that is deposited on the photoresist. This leaves only the metal that was deposited directly on the top and bottom contact layers as shown in Fig. 3.9.

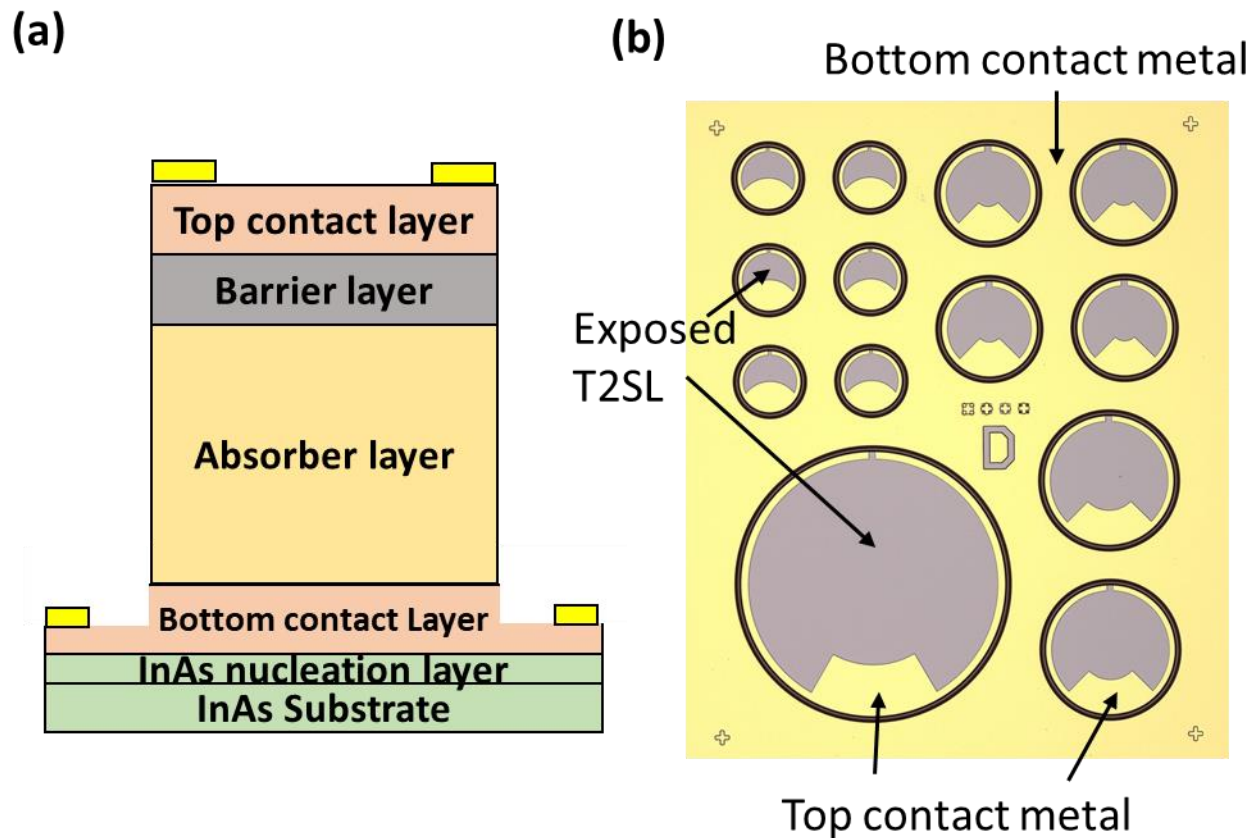


**Fig. 3.9.** (a) Schematic diagram of a typical InAs/GaSb nBn detector after metal deposition. (b) Optical microscope picture of the surface of the sample after metal deposition.

**Step 9 – Passivation**

After the metal deposition the sample was cleaned using O<sub>2</sub> plasma and AZ3027 photoresist was spun onto the sample. The AZ3027 was then exposed using the ML3 direct writer using a mask which prevented exposure to the photoresist on the sides of the device. The AZ3027 was then hard baked and was developed using AZ726. AZ3027 is a positive photoresist so after it is developed only the photoresist on the sidewalls remain, as shown in Fig. 3.10.

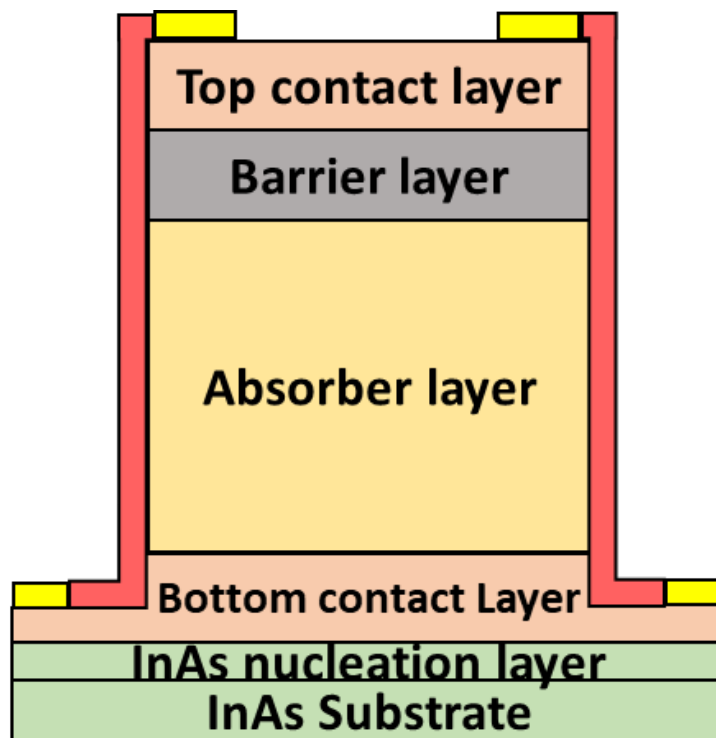


**Fig. 3.10.** Schematic diagram of a typical passivated InAs/GaSb nBn detector.

## 3.3 Characterisation Techniques

### 3.3.1 Atomic Force Microscopy (AFM)

Atomic force microscopy (AFM) is a versatile imaging technique that allows the visualisation of surfaces at the nanoscale. At the heart of AFM lies a tiny sharp tip attached to a cantilever. The cantilever acts as a mechanical spring with a defined spring constant, and it deflects when interacting with the surface of the sample. As the tip approaches the surface, attractive and repulsive forces between the atoms/molecules of the tip and sample lead to cantilever deflection. This deflection changes the amount of laser light reflected onto the photodiode. The height of the cantilever is then adjusted to restore the response signal, resulting in the measured cantilever height tracing the surface.

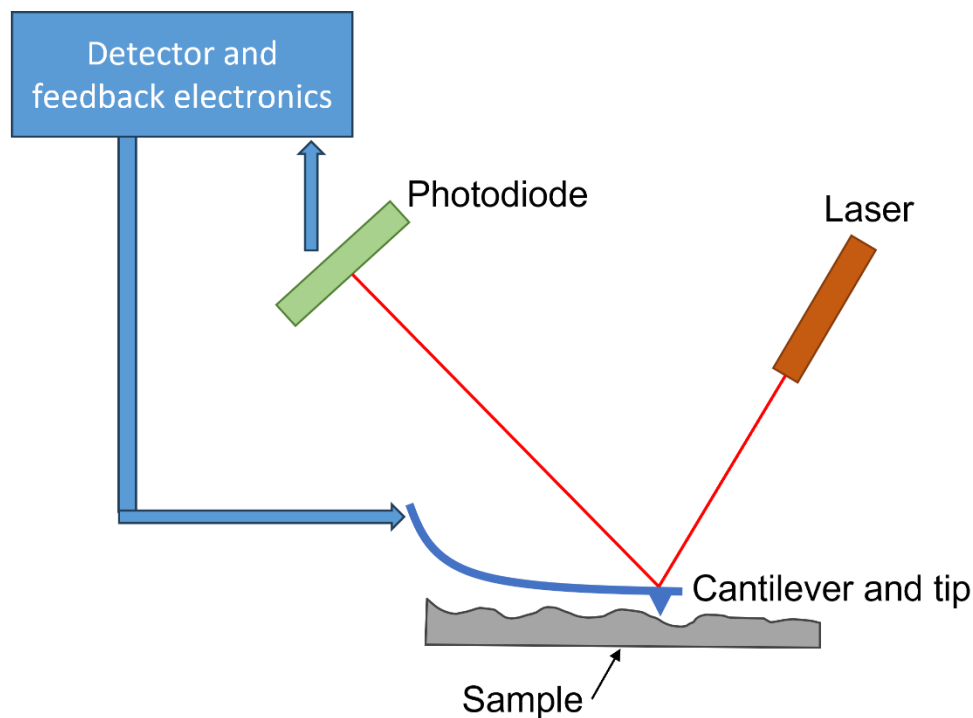


**Fig. 3.11.** Schematic diagram of an atomic force microscope.

AFM is relatively fast and cheap when compared to other characterisation methods and so it is often the first method used to determine how “good” a sample is. AFM is able to provide a 3D map of the surface which can be used to view the surface morphology and calculate the surface roughness.

In epitaxial thin film growth, the surface roughness is normally a very good indicator of the growth quality. If a sample is correctly lattice matched and grown under the correct conditions, one would expect a low surface roughness. AFM roughness is often given in terms of the root mean square (RMS) roughness. RMS roughness is calculated by taking the square root of the average of the squared deviations of the surface's height values from the mean. RMS roughness is generally the preferred way of presenting a surface roughness as it is able to describe the average roughness for a given area whilst being sensitive to large peaks and valleys [168].

The AFM is able to provide quick feedback of the growth to help indicate how the growth parameters should be adjusted for the next runs. Although the surface quality provides a good indication as to the quality of the whole sample, it is not perfect and so other techniques must be used in order to investigate the sample below the surface, such as transmission electron microscopy and X-ray diffraction.

### 3.3.2 X-ray Diffraction (XRD)

X-ray diffraction (XRD) is a powerful technique used to study the crystal structure of materials. It is based on the principle that X-rays, when incident on a crystal lattice, will be scattered by the atoms within the lattice, resulting in constructive interference at specific angles. This phenomenon, known as Bragg diffraction, provides valuable information about the crystallographic properties of materials, including lattice parameters, crystal symmetry, and crystal defects. The wavelength of the X-rays is usually set to 1.54nm as this is comparable to the distances between atoms in the lattice, ensuring interferences occur between the scattered X-rays.

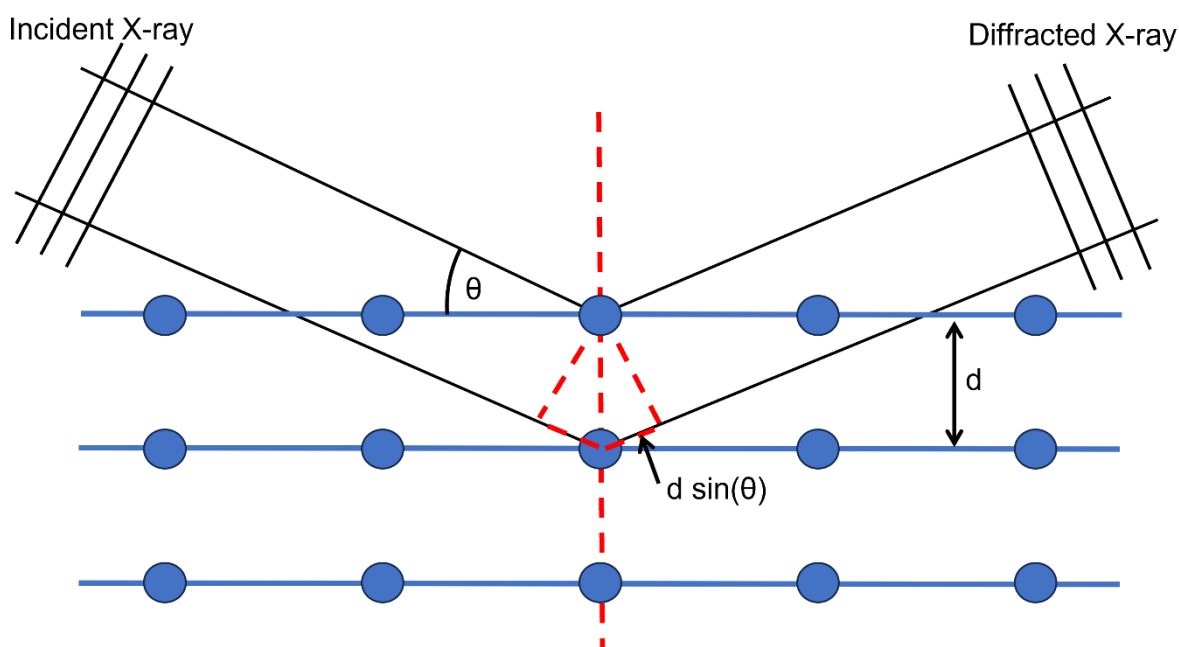


**Fig. 3.12.** Schematic of XRD in a crystal lattice.

Bragg's law is the foundation of X-ray diffraction analysis. It describes the relationship between the X-ray wavelength ( $\lambda$ ), the scattering angle ( $\theta$ ), and the lattice spacing ( $d$ ) of a crystal. Mathematically, Bragg's law is expressed as:

$$n\lambda = d \sin(\theta) \quad (3.1)$$

where,  $n$  is the order of diffraction (an integer),  $\lambda$  is the X-ray wavelength,  $d$  is the lattice spacing between planes of atoms, and  $\theta$  is the angle of incidence of the X-ray beam with respect to the crystal lattice planes. Bragg's law allows us to determine the interplanar spacing ( $d$ ) of the crystal lattice based on the measured diffraction angle ( $\theta$ ) and X-ray wavelength ( $\lambda$ ). From the interplanar spacing it is possible to calculate the lattice constant of the crystal. From the lattice constant, the specific material including its ternary composition can be obtained.

Within this work only the 004 reflection was used to characterise the samples using XRD. The 004 reflection is only able to directly measure the vertical component of the lattice constant, shown as  $d$  in Fig 3.12. The horizontal component of was not directly measured and was calculated by approximating the relaxation based on the critical thicknesses of the layers.

An X-ray source and detector are mounted on a goniometer which allows the source and detector to rotate around the sample, as shown in Fig. 3.13. This is known as an  $\omega/2\theta$  scan.

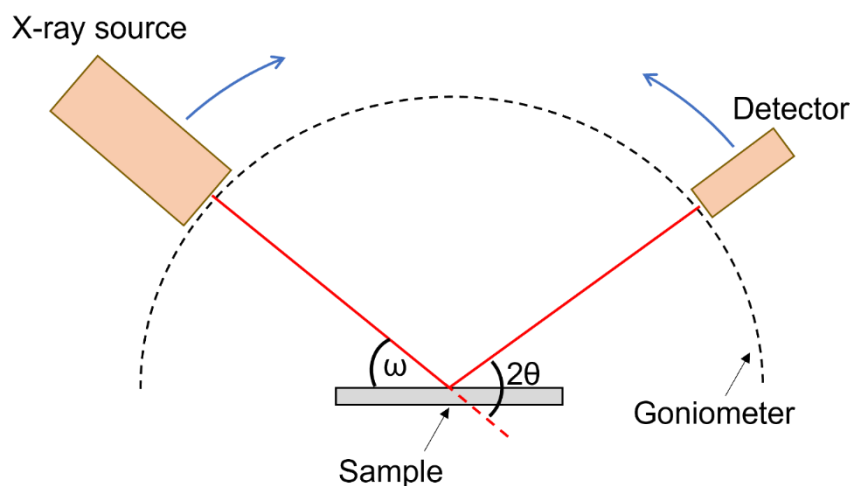


**Fig. 3.13.** Schematic diagram of an X-ray diffractometer.

X-ray diffraction is a very powerful tool as it allows for non-destructive characterisation of the whole sample, not just the surface. This means that a sample with multiple layers of different materials can be fully characterised.

The full width half maximum (FWHM) of a peak in XRD can be used to give an indication of the defect density of a sample. In an ideal, uniform crystal with an ideal XRD setup, it follows from Eq. 3.1 that the result of an XRD scan would be a single delta function with a FWHM of 0 as there is no variation in interplanar spacing,  $d$ . Defects, however, disrupt the regular atomic spacing and create slight variations in  $d$  throughout the crystal which causes the XRD peak to broaden. A higher number of defects will cause greater variations in  $d$  resulting in a larger FWHM. The FWHM is therefore correlated to the defect density and can be used as a rough guide to indirectly measure the defect density. The Ayers model [169] can be used to estimate an upper limit of the dislocation density from the FWHM, as shown in equation 4.2:

$$D = \frac{\beta}{4.36b^2} \quad (3.2)$$

where  $D$  is the upper limit of the defect density in  $\text{cm}^{-2}$ ,  $\beta$  is the FWHM in arcseconds, the 4.36 was derived experimentally by J.E. Ayers [169] and is in arcseconds and  $b$  is the length of the Burgers vector of dislocation. Since XRD looks at the whole sample, the defect density calculated is an average across the whole layer [170]. For device performance, the more important metric is the defect density at the surface. In order to more comprehensively investigate the sample's surface defect density, a technique that directly measures the surface defect density such as electron channelling contrast imaging (ECCI) must be used

### 3.3.3 Electron channelling contrast imaging (ECCI)

ECCI is an imaging technique in scanning electron microscopy (SEM) that uses the channelling effect of electrons with respect to crystallographic lattice planes. ECCI is particularly useful for characterising and quantifying the distribution and density of threading dislocations in semiconductor materials.

The SEM operates by firing a beam of electrons from an electron source towards the surface of a sample, as shown in Fig. 3.14.

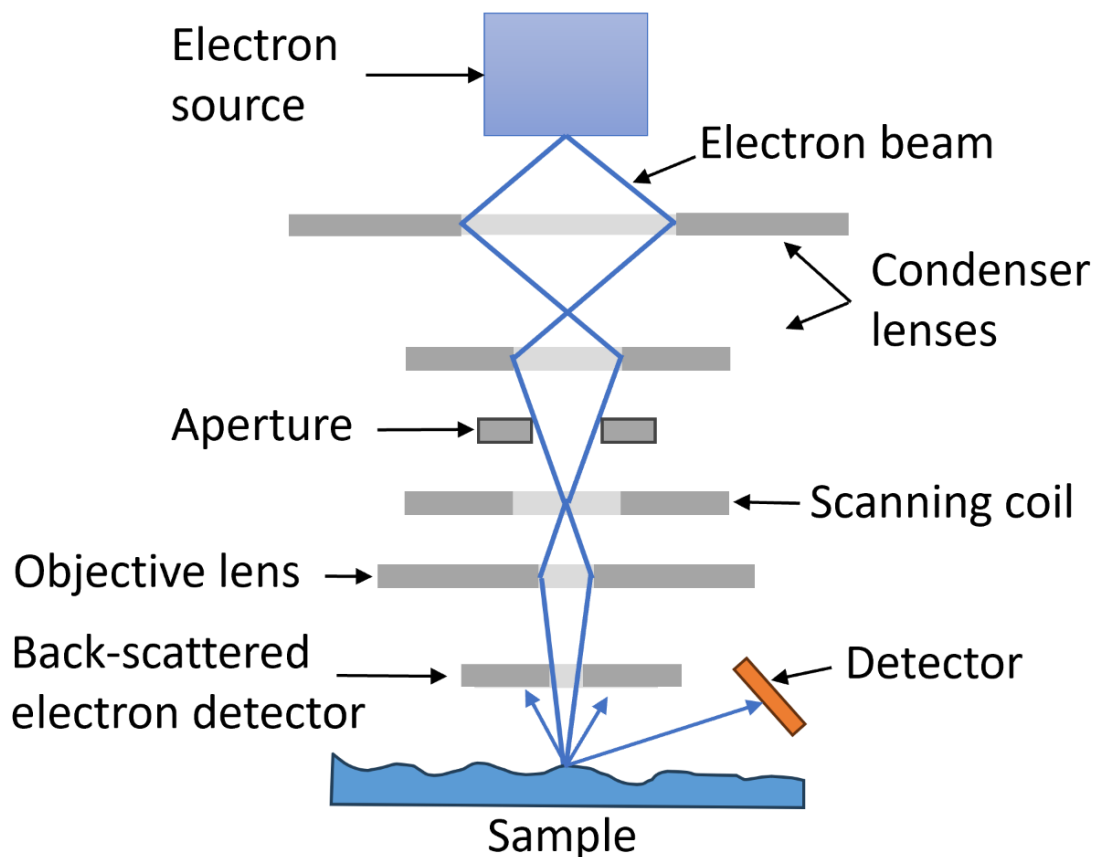


**Fig. 3.14.** Schematic diagram of a typical Scanning Electron Microscope.

When high-energy primary beam electrons from an SEM interact with a crystalline sample, they generate a standing electron-density wave within the crystal lattice that is coherent with it. The distribution of electron density maxima in this wave depends on the orientation of the primary electron beam relative to the lattice. If the beam is aligned such that the maxima are at the atomic nuclei, strong backscattering of electrons occurs. However, if the maxima lie between the nuclei, fewer electrons are backscattered. As a result, the backscatter signal provides insight into the crystal lattice structure and its orientation in relation to the primary beam. The minimum backscattering occurs when the primary beam is nearly aligned with the Bragg angle of a lattice plane, causing the electrons to travel deeper into the crystal with minimal interaction. This phenomenon is known as electron channelling.

When a defect, such as a dislocation or stacking fault, is present in the crystal, it disrupts the coherency of the channelling primary electron wave field with the lattice. This disturbance causes strong backscattering at the location of the defect. Consequently, the defect appears as a bright feature against a dark background when observed with a backscatter electron detector.

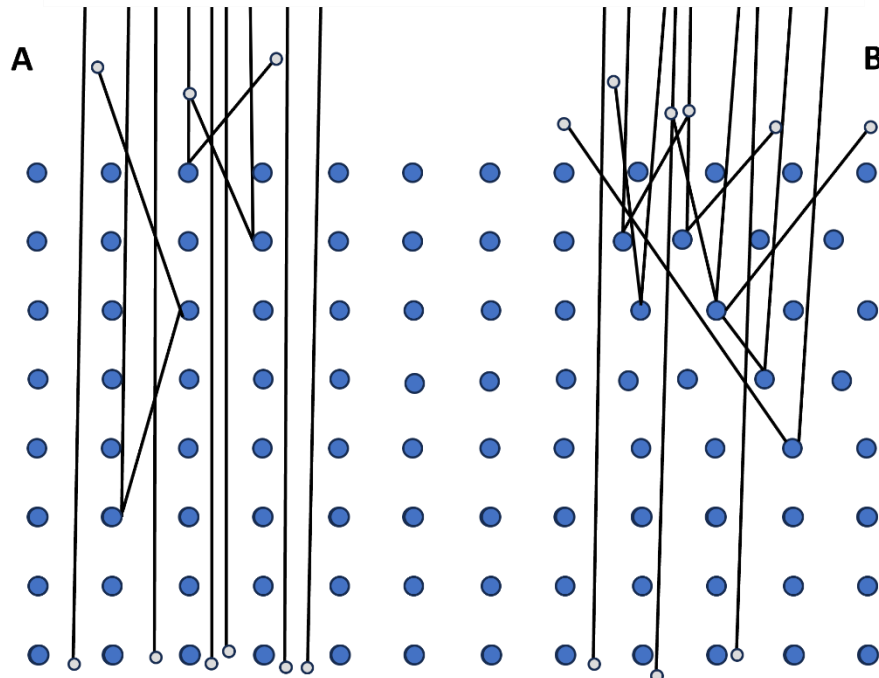


**Fig. 3.15.** Schematic diagram of electron channelling contrast imaging. In case A, the crystal has no defects so the probability of an electron hitting an atom is relatively low resulting in few backscattering events. In case B, the crystal has defects causing it to not be perfectly cubic, increasing the probability of an electron hitting an atom resulting in more backscattering events.

#### 3.3.4 Transmission Electron Microscopy (TEM)

Transmission electron microscopy (TEM) is similar to SEM as it also fires a beam of electrons at a sample and analyses how they interact. The main difference between the two is that TEM relies on detecting electrons transmitted through a thin sample, rather than detecting the electrons that are scattered from a sample as in SEM. The general thickness of a sample in TEM is around 100-200nm.

In TEM a focused electron beam is directed onto the thin sample. As the electrons pass through the sample, they interact with the atoms and crystal lattice of the material. These interactions can include elastic scattering, inelastic scattering, diffraction and absorption. Some electrons are transmitted through the sample with minimal interaction. Others are scattered, and these scattered electrons carry information about the sample's internal structure, defects, and composition.

The scattering of electrons also leads to the formation of an electron diffraction pattern, providing insights into the crystallography of the material. The transmitted and scattered electrons are then collected by a phosphor viewing screen which is able to convert an electron image into a visible form. High resolution cameras are then used to take this image and digitally record it.

By manipulating the electron beam with lenses and apertures, TEM can create images showing various contrasts, such as bright-field and dark-field images, which highlight different features of the material. A bright-field TEM is the most common type of TEM image. In bright field TEM, the areas of the sample that transmit electrons appear brighter and the areas of the sample that scatter or absorb the electrons appear darker. The main advantage of bright-field TEM is the better contrast it provides, making it the more widely used technique. However, this technique can also suffer when measuring very small features. As a result, dark-field TEM is often preferred for observing features like crystal defects and dislocations. In dark-field TEM, the primary, unscattered electron beam is blocked from the collected image using an aperture. This ensures that the image is composed solely of scattered electrons. Areas with no scattering appear black, while the brightness of the brighter regions is determined by the number of scattered electrons in those areas.

Since TEM is able to measure a cross section of a sample at very high resolution, it is one of the few ways to directly measure and determine the true structure of a crystal lattice. The other big advantage of the TEM is that since it is looking at a cross section of a sample, it can be used to analyse defect propagation throughout the sample. Where XRD can only estimate a defect density average through a whole layer and ECCI can only directly measure the surface defect density, TEM is able to directly image defects as they propagate. This is very useful as it can show how each heterointerface contributes to the overall defect density and show how the defect density changes throughout each layer. This can also be used to directly measure the effectiveness of any defect filtering mechanisms that are used. Unfortunately, TEM is both destructive and expensive.

Since the technique requires a thin cross section of the sample, the sample must be cleaved and thinned which is a time-consuming process. In general, the other quicker and cheaper characterisation techniques are used first to get a general idea of the quality of a sample. However, when direct measurement of the cross section of a sample at high resolution is required, TEM is the best option.

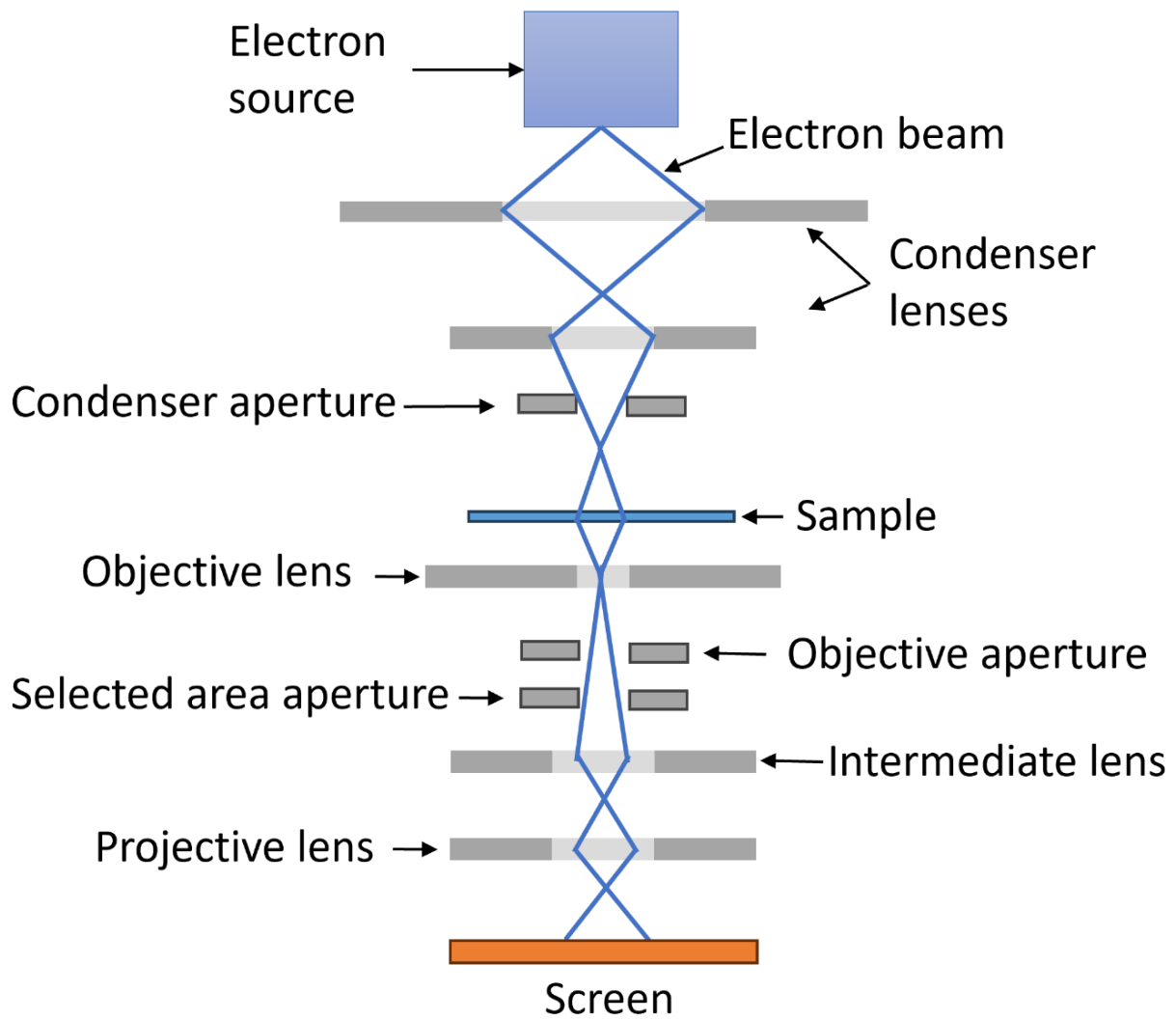


**Fig. 3.16.** Schematic diagram of a typical Transmission Electron Microscope.

### 3.3.5 Secondary ion mass spectrometry (SIMS)

Whilst high resolution TEM can be used to directly image the crystal lattice, it is unable to determine which atoms make up the crystal. In order to directly measure the atomic composition of a sample, secondary ion mass spectrometry (SIMS) is used. SIMS is a destructive technique that works by firing an ion beam at the sample which ionises the sample and causes atoms to splutter off the sample. These spluttered atoms or “secondary ions” are then fed through an electromagnetic field which separates the ions according to their mass-to-charge ratio. Once separated the ions enter the detector and can be identified.

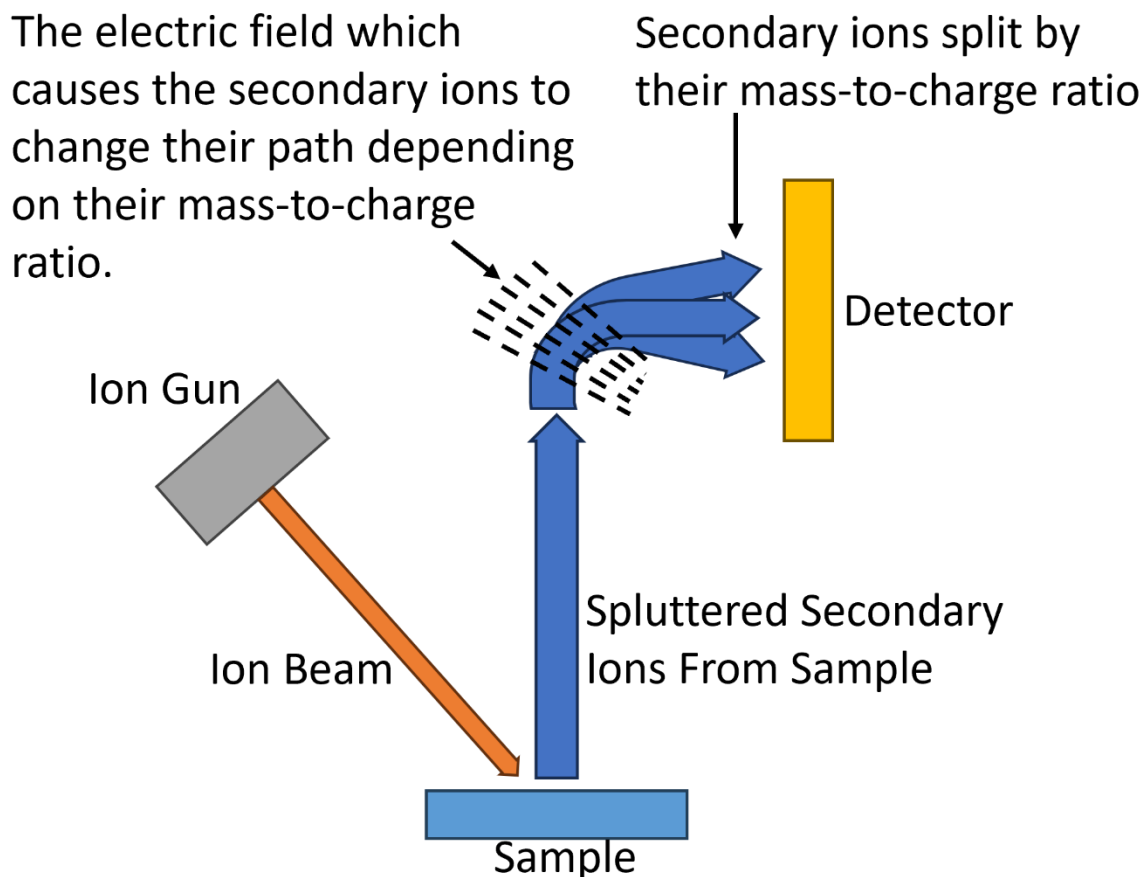


**Fig. 3.17.** Schematic diagram of secondary ion mass spectrometry.

SIMS is especially useful as it is the main way to determine dopant concentrations which is something that needs to be accurately controlled in semiconductor device design. SIMS is also able to determine ternary and quaternary compositions much more precisely than XRD and so would generally be used as a benchmark to calibrate XRD results. Like TEM, SIMS is destructive and expensive and so would generally be used either as an initial calibration of growth rates and atomic incorporation or, if specific information about atomic concentrations is needed that the other quicker and cheaper techniques cannot provide.

The SIMS measurements within this work were performed by Loughborough surface analysis.

### 3.3.6 Photoluminescence (PL)

Photoluminescence (PL) is a characterisation technique which can be used to study the band structure of semiconductors. In PL, an incident photon with higher energy than the band gap is used to excite an electron from the valence band to the conduction band. This electron then recombines with the emission of a photon. The photons that are emitted can then be detected creating a PL spectrum. The PL intensity, peak position and FWHM can then be used to investigate the material composition and quality.

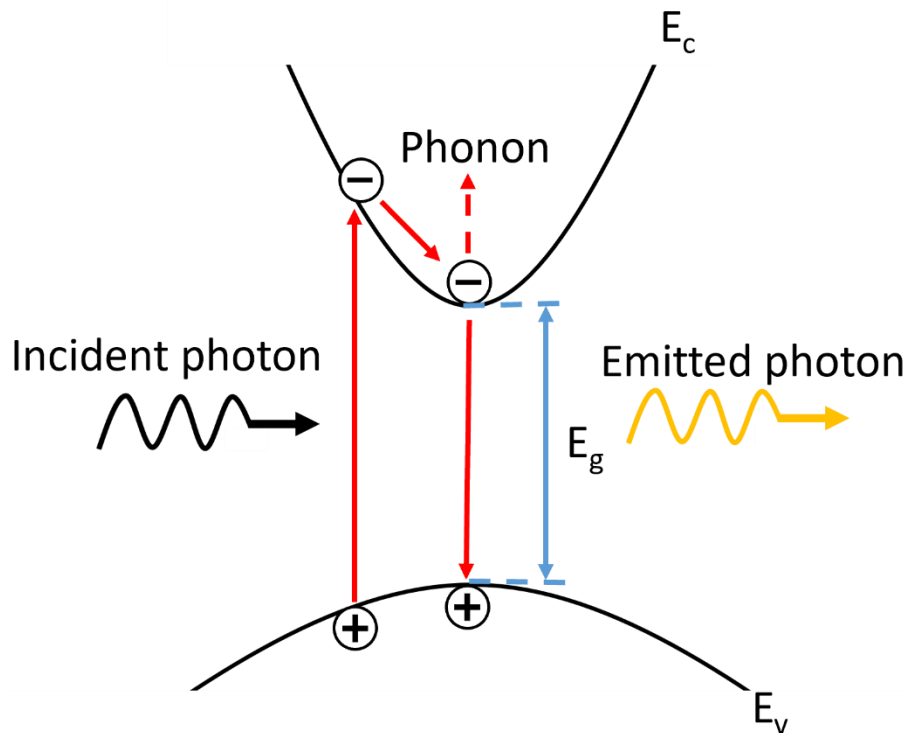


**Fig. 3.18.** Schematic diagram of the photoluminescence process.

Due to the atmospheric absorption problems and general difficulty of MWIR and LWIR PL it is common to use a Fourier transform infrared spectrometer (FTIR) as the source of the incident radiation and detector for the emitted radiation from the sample.

The PL characterisation in the work was performed by Prof. Baolai Liang and Dr. Khalifa Azizur-Rahman at the University of California, Los Angeles.

### 3.3.7 Fourier Transform Infrared Spectrometry (FTIR)

FTIR is a powerful characterisation tool for infrared materials. In this project, the FTIR served two primary functions: it acted as both a source and detector for infrared photoluminescence, typically used for unfabricated T2SL samples to investigate their bandgap, and it was also employed to characterise the spectral response of the fabricated detectors. The FTIR works similarly to a Mach-Zehnder interferometer [171] with a moving mirror. As shown in Fig. 3.22, a broadband IR light source, such as a tungsten glow bar, emits light that is split by a 50/50 beam splitter. One path of this light hits a fixed mirror and is reflected back to the beam splitter. The other path hits a mirror moving at a known velocity and is also reflected back to the beam splitter, where the two beams recombine. Due to the different optical path lengths, the beams have a phase difference, creating an interference pattern.

Since the position and velocity of the moving mirror are known, the interference pattern changes over time as the optical path difference varies. This pattern can be plotted as a time-domain interferogram, which is then transformed into an FTIR spectrum via a Fourier transform. The recombined optical signal can be directed to an external detector sample for characterisation. By using a known reference detector, the spectral intensity sent to the detector sample can be calculated. If the incident spectral intensity is known, the responsivity of the detector sample can be determined from the difference between the incident light and the detector's spectral response.

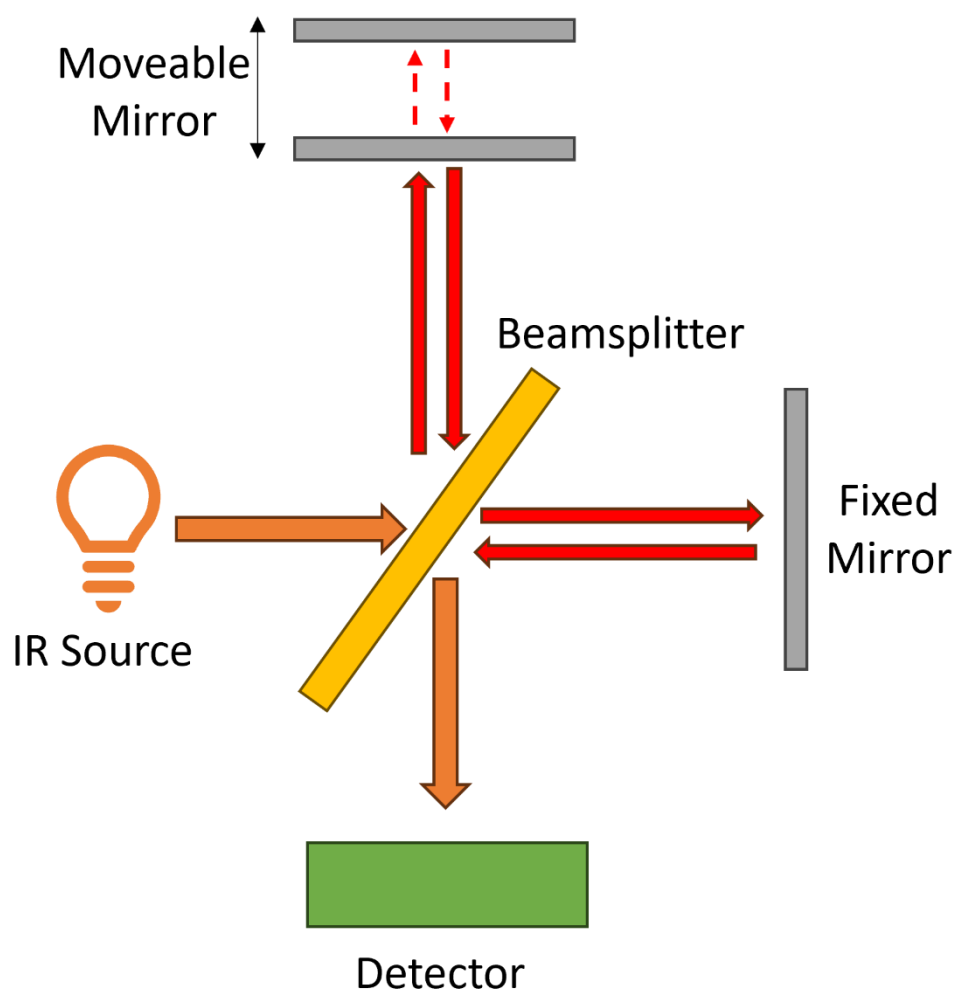


**Fig. 3.19.** Schematic diagram of a Fourier transform infrared spectrometer.

However, this method makes it challenging to align the sample detector exactly as the reference detector. Any misalignment will result in a difference in the absolute spectral intensity, meaning this method alone can only provide the shape of the sample detector's spectral response, not its absolute spectral responsivity.

To determine the absolute spectral responsivity of the sample detector, a blackbody responsivity calibration is necessary, as shown in Fig. 3.20. This calibration involves shining a known calibrated blackbody source through an aperture, a 50/50 chopper connected to a lock-in amplifier, and a band-pass filter onto the sample, then measuring the photocurrent. By using a calibrated blackbody source and an aperture, the incident intensity on the sample can be accurately known. The 50/50 chopper only allowed light to be incident onto the sample 50% of the time and a lock-in amplifier was synchronised to the chopper. The chopper allows the separation of the photocurrent from the dark current, while the band-pass filter ensures only a specific wavelength range reaches the detector.

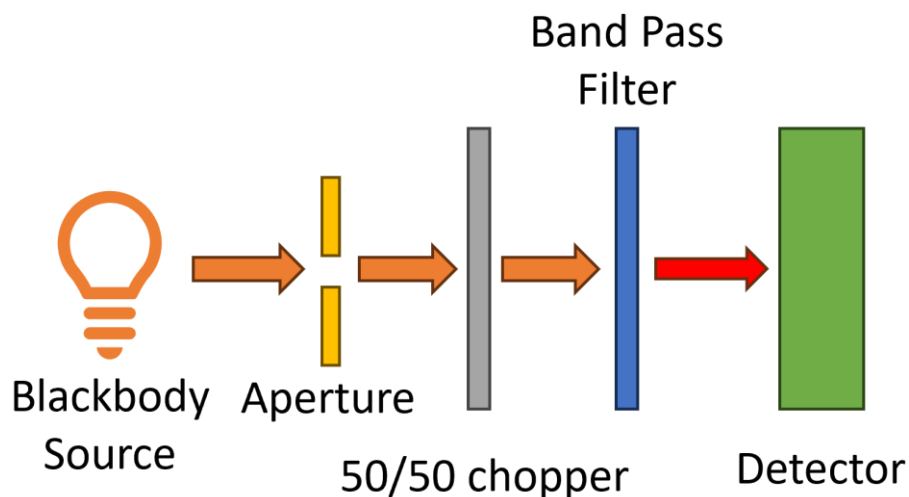


**Fig. 3.20.** Schematic diagram of the blackbody calibration setup.

From the blackbody calibration, the average responsivity of the detector across a specific wavelength range can be determined. This responsivity value can then be used to scale the full wavelength spectral response obtained from the FTIR.

The optical device characterisation was performed by myself at Lancaster university with the assistance of Dr. Andrew Marshall, George Seager and Dr. Adam Craig. The optical device characterisation was performed using a Bruker Vertex 70 FTIR calibrated using a combination of both Vigo PVMI-2TE MCT and Bruker DLTGS reference detectors. A 550K blackbody source synced to a chopper and a lock-in amplifier was then used to calibrate the absolute responsivity values.

### 3.3.8 Electrical characterisation

In addition to photonic characterisation, it is essential to quantify the electrical properties of infrared detectors, such as dark current density. This electronic characterisation is conducted in a cryogenic probe station, as illustrated in Fig. 3.21. The sample is mounted on a sample holder and cooled to the desired temperature using liquid nitrogen. Probes are then connected to the top and bottom contacts. A voltage is applied between the probes, and the device analyser measures the resulting current. A temperature controller is used to adjust the temperature from 77 K to room temperature.

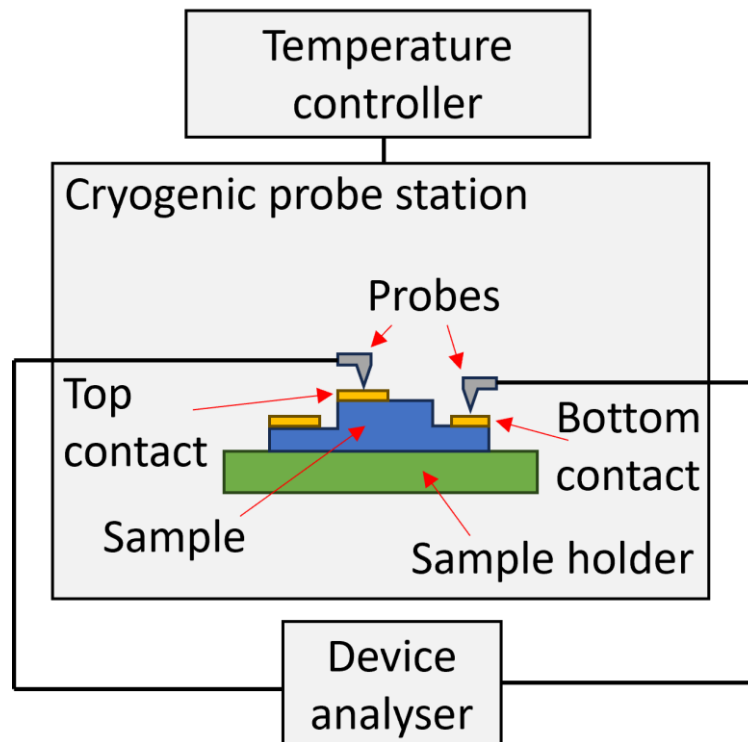


**Fig. 3.21.** Schematic diagram of the cryogenic probe station set-up.

The electrical device characterisation was performed by myself at Lancaster university with the assistance of Dr. Andrew Marshall, George Seager and Dr. Adam Craig. The cryogenic probe station that was used was the Lakeshore Cryotronics TTPX and the device analyser was a Keithley 2401 source meter.

# LWIR detectors made from InAs/GaSb T2SLs

## 4.1 Introduction

Long wavelength infrared (LWIR) photodetectors have a wide range of applications including biomedical sensing [172], thermal imaging, 3D sensing [173] and many different defence applications [174].

Human blackbody emission peaks at  $9.55\ \mu\text{m}$  [175] and so detectors that peak in the range of  $9\text{-}10\ \mu\text{m}$  are very desirable for all applications that involve detecting people. The InAs/GaSb Type-II superlattice (T2SL) [81] is a strong candidate for LWIR detectors due to its flexible bandgap engineering [176,177], high material uniformity [178] and low Auger recombination rates [179] when compared to the current state of the art mercury cadmium telluride (MCT) technology [180].

To date, molecular beam epitaxy (MBE) has been the prevailing technique for growing InAs/GaSb T2SLs [54]. However, the commercial exploitation potential using metal-organic chemical vapour deposition (MOCVD) is highly attractive if material and device performance can be improved to close the gap with MBE results.

There are two main material challenges in transferring the current MBE growth to MOCVD, a suitable interfacial layer needed to strain balance the T2SLs [181] and the AlSb-based ternaries and quaternaries that are used as barriers within the device structures [31,182]. Conventionally, MBE grown InAs/GaSb T2SLs are grown lattice matched to GaSb substrates via the use of InSb interfacial layers for strain balancing. InSb is very difficult to grow via MOCVD due to its low melting point ( $527^\circ\text{C}$ ) [183] being very close to conventional MOCVD growth temperatures. Instead of using InSb to lattice match to GaSb substrates, it is possible to use GaAs as an interfacial layer and lattice match the T2SL to InAs substrates.

The second material challenge is the AlSb-based barriers which are required to suppress the generation-recombination dark current present in more basic PN and PIN detector structures, which is crucial at longer wavelengths [71]. There are significant carbon and oxygen contamination problems with growing AlSb-containing alloys due to the reactivity of Al [184] along with material segregation problems within the ternaries and quaternaries [185]. However, it is possible to create electron barriers from wider band gap InAs/GaSb T2SLs, as long as the GaSb layer thickness is kept constant between the barrier and absorber T2SL meaning the valence band offset is near  $0\ \text{eV}$  [186].

InAs/GaSb T2SLs are known to be prone to surface related dark currents, especially at longer wavelengths [187] and surface passivation still remains an important challenge in this field. A good way to resolve this surface problem is to employ a shallow etched mesa design where each pixel is defined by the lateral carrier diffusion length, not a deep mesa etch. Unfortunately in InAs/GaSb T2SLs with GaAs like interfaces, this lateral diffusion length can be very large, up to  $251\ \mu\text{m}$  [72].

The high lateral diffusion length leads to problems when creating high pixel density focal plane arrays (FPA) as the minimum distance between pixels must be twice the lateral diffusion length to prevent crosstalk [188]. Therefore, for a LWIR InAs/GaSb T2SL FPA grown via MOCVD, there exists a trade-off between lower dark currents and higher pixel density via shallow or deep mesa etched devices.

This chapter describes the growth, fabrication and characterisation of MOCVD grown InAs/GaSb T2SL LWIR detectors.

## 4.2 Growth of InAs/GaSb T2SLs

The first step in developing InAs/GaSb T2SL detectors is the investigation of the growth parameters. The goal of the investigation is to grow a T2SL which is lattice matched to an InAs substrate, and which has an average root mean square (RMS) surface roughness of between 0.1 and 0.2nm with no visible surface defects with an optical microscope.

If a T2SL is not lattice matched to its substrate, the resulting strain will cause dislocations which act as non-radiative recombination centres to form reducing the optical performance of the T2SL. This strain worsens with T2SLs with a higher number of periods which are needed for device structures and so lattice matching between the T2SL and the substrate is vital for devices. The lattice mismatch was investigated using an omega 2 theta XRD scan. The lattice mismatch was defined as the distance in arcseconds between the substrate peak and the central T2SL peak in the omega 2 theta scan. In the omega-2 theta scan, a positive lattice mismatch was defined as when the T2SL peak appears to the right of the InAs peak (indicating a smaller lattice constant), while a negative lattice mismatch was defined as when the T2SL peak appears to the left of the InAs peak (indicating a larger lattice constant). When the T2SL and InAs peaks overlap and the lattice mismatch is zero, the T2SL can then be said to be lattice matched to the substrate. AFM was used to quantify the surface roughness as well as investigate the surface morphology.

The MOCVD growth was performed in an Aixtron Close Coupled Showerhead reactor. The precursors used were trimethylindium (TMIn), tertiarybutylarsine (TBAs), triethylgallium (TEGa), triethylantimony (TESb) and disilane ( $\text{Si}_2\text{H}_6$ ), with hydrogen used as the carrier gas. The device structure was grown on a 2 inch unintentionally doped (u.i.d) InAs (001) substrate, with the reactor pressure kept at 100 mbar. The main growth parameters investigated in this work were the growth temperature and the ratio of the group V and group III precursor gases used to grow the InAs and the GaSb known as the V/III ratio. The standard test structure used to investigate the growth parameters was a 50-period InAs/GaSb T2SL. The growth timeline for the InAs/GaSb T2SL can be found in Fig. 4.1.

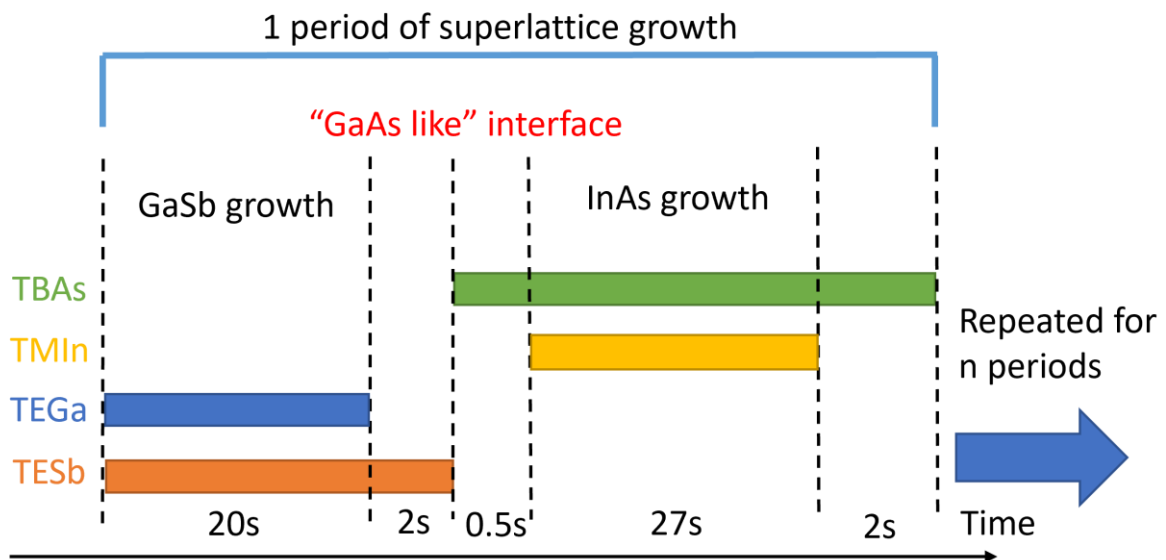


**Fig. 4.1.** MOCVD growth timeline of one period of the InAs/GaSb T2SL. Shows the growth interruption interfacial sequence that creates the “GaAs-like” interfaces.

The InAs layer thickness was 21 ML, and the GaSb layer thickness was 8 ML, resulting in a bandgap of approximately 0.1 eV, which corresponds to a wavelength of 12  $\mu\text{m}$ . This structure was chosen because it has a cutoff wavelength of around 12  $\mu\text{m}$  when used as an absorbing layer in a device. A device with a cutoff wavelength at 12  $\mu\text{m}$  will have a peak detectivity at around 10  $\mu\text{m}$ , making it ideal for many LWIR detector applications, such as imaging humans.

Conventionally, T2SL layer thicknesses are given in monolayers (MLs) which can be conveniently measured using RHEED in MBE. Due to the lack of vacuum, MOCVD does not have RHEED and so it is difficult to directly measure the number of monolayers grown. In this work, layer thicknesses were measured in nm using TEM and were converted to ML by utilising the relation that 1 ML is equal to half of a lattice constant in a zinc blende crystal.

#### 4.2.1 Growth temperature

As with all antimonide growth, the InAs/GaSb T2SL is very sensitive to growth temperature. When the T2SL was grown with a surface temperature of 510°C, the surface exhibited a step flow morphology and had an RMS of 0.14nm, as shown in Fig. 4.2b. When the surface temperature was decreased to 500°C, the majority of the surface remained similar with an RMS of 0.14nm. However, at this lower temperature, large surface stripe defects can be observed in the optical microscope, as shown in Fig. 4.2c. These surface stripe defects are likely caused by indium segregation due to the lower surface mobility at the lower temperatures [189]. Indium segregation causing surface striping is commonly observed in highly strained Indium containing low temperature growth and provides a lower limit to the growth temperature of the T2SL [190]. When the temperature was increase to 530°C the surface roughness greatly increased, and the morphology changed, as shown in Fig. 4.2a.

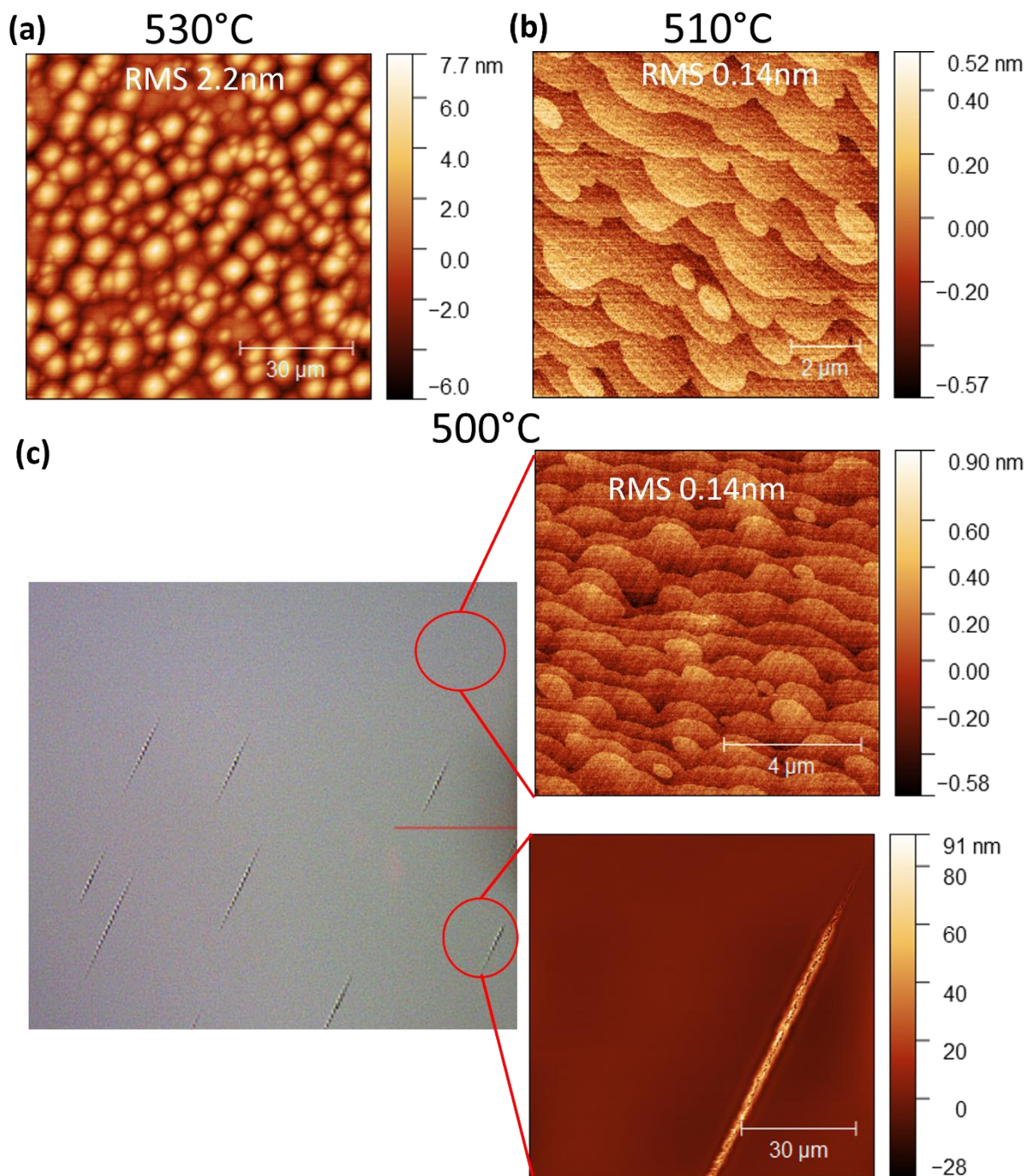


**Fig. 4.2.** AFM surface scans of 50 period 21ML/8ML InAs/GaSb T2SLs grown at three different surface temperatures.

The surface temperature also affected the lattice constant of the T2SL. This can be explained by the temperature dependence of the As for Sb exchange that takes place during the growth interruptions to form the GaAs like interfaces. At higher temperatures, the Sb is more volatile and is more likely to leave the surface to be replaced by an As atom. This was shown experimentally in Fig. 4.3, where the T2SLs grown at higher temperatures have lattice constants closer to GaAs. Consequently, this results in higher lattice mismatches to the InAs substrate.

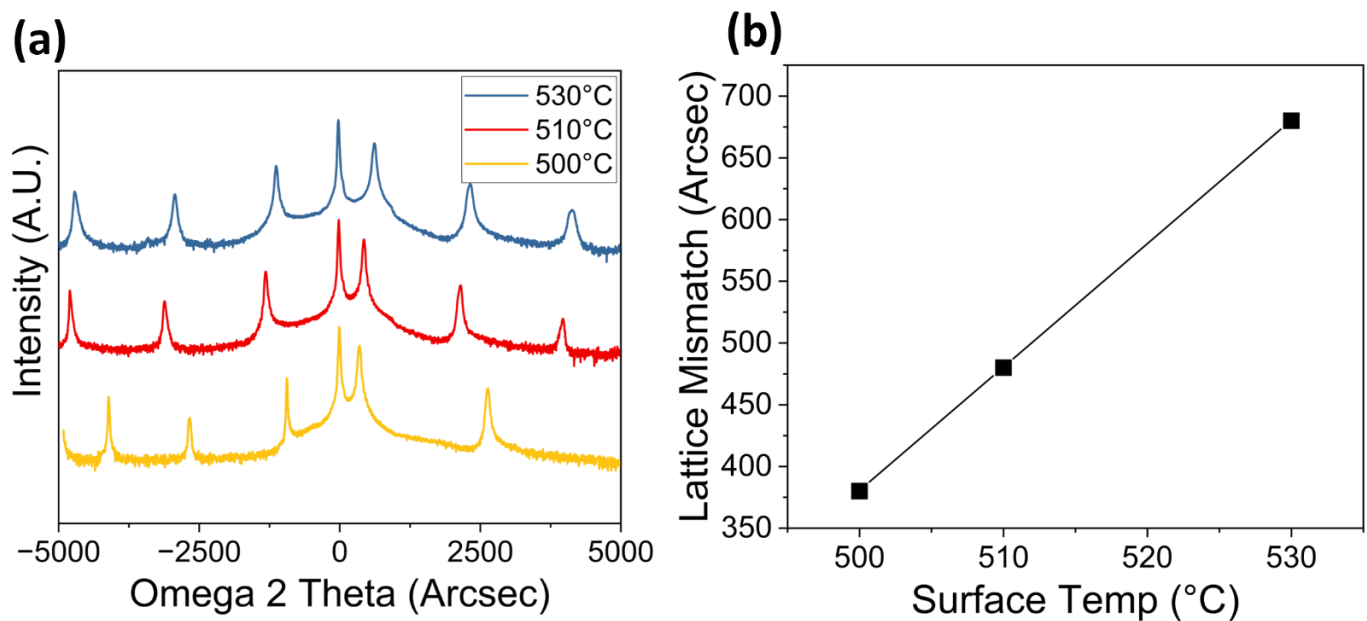


**Fig. 4.3.** (a) Omega 2 Theta XRD scans of 50 period 21ML/8ML InAs/GaSb T2SLs grown at three different surface temperatures. (b) Plot showing how the lattice mismatch of the InAs/GaSb T2SLs changes with surface temperature.

#### 4.2.2 GaSb V/III ratio

After setting the growth temperature to 510°C, the next parameter that was investigated was the GaSb V/III ratio. Three samples were grown with different TESb flows resulting in GaSb V/III ratios of 1.2, 1.4 and 1.5. As shown in Fig. 4.4, a higher TESb flow and therefore higher GaSb V/III ratio results in a smaller lattice mismatch. This can be explained by the higher Sb flow resulting in more TESb in the chamber during the growth interruption, resulting in less net Sb for As exchange and therefore a thinner GaAs like interface.

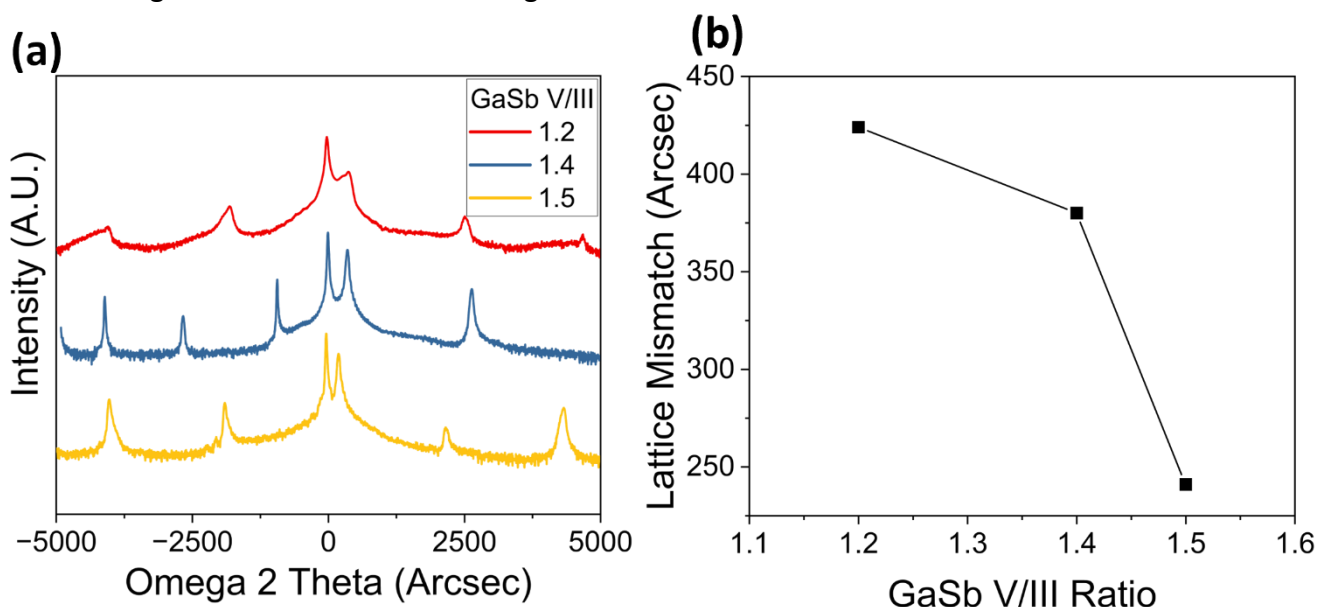


**Fig. 4.4.** (a) Omega 2 Theta XRD scans of 50 period 21ML/8ML InAs/GaSb T2SLs grown at 3 different GaSb V/III ratios. (b) Plot showing how the lattice mismatch of the InAs/GaSb T2SLs changes with GaSb V/III ratio.

As well as the change in lattice constant, the GaSb V/III ratio also had a large effect on the surface morphology, as shown in Fig. 4.5. At lower GaSb V/III ratios, the same stripe defects became visible. The density of these defects drastically increased as the GaSb V/III ratio decreased. At a growth temperature of 510°C, a GaSb V/III ratio of 1.5 was found to be sufficient to remove all stripe defects and gave a good surface roughness of 0.15nm.

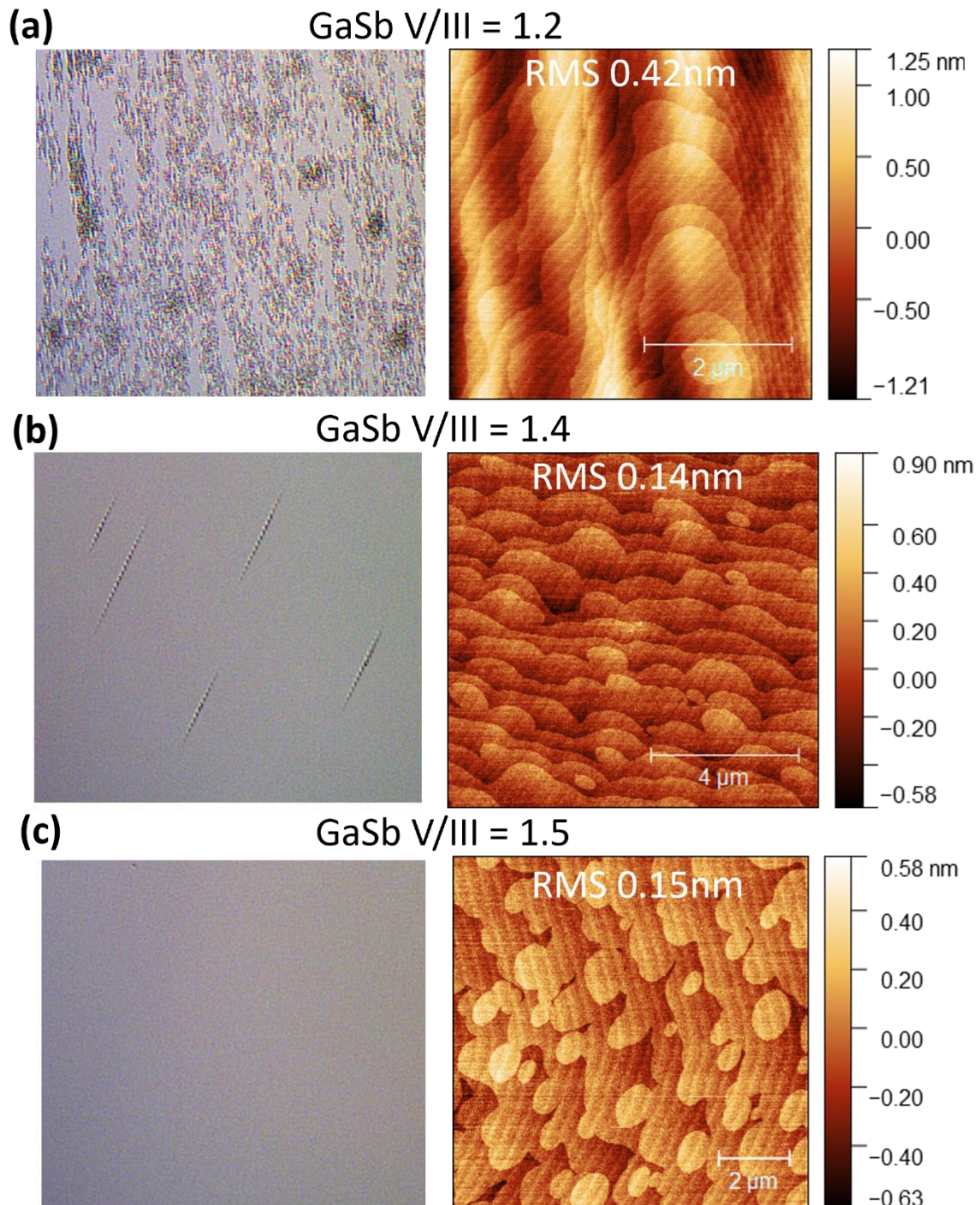


**Fig. 4.5.** Optical microscope pictures and AFM scans of 50 period 21ML/8ML InAs/GaSb T2SLs grown at 3 different GaSb V/III ratios; (a) 1.2, (b) 1.4 and (c) 1.5.

### 4.2.3 InAs V/III ratio

After identifying a growth temperature and GaSb V/III ratio that produced a smooth, stripe-defect-free surface, the next parameter to investigate was the InAs V/III ratio. In the calibrations of temperature and GaSb V/III ratio, the InAs V/III ratio was kept at 10. For the previous growth calibrations, the lattice mismatch was always positive. This means that the “GaAs like” interfaces were too effective at moving the T2SL lattice constant toward GaAs. Reducing the effect or strength of the “GaAs like” interfaces can be thought of as either reducing the thickness of the interface itself or by reducing how GaAs like the interface is by reducing the As composition of the interface.

As shown with the temperature and GaSb V/III results, the strength of the “GaAs like” interfaces can be controlled with temperature and GaSb V/III. However, their effect on the lattice match is relatively small and changing temperature and GaSb V/III ratio also has a large effect on the surface of the T2SL. The formation of the ‘GaAs-like’ interface is influenced by the growth interruption time and the amount of As atoms that can exchange with Sb. Naturally, a shorter growth interruption results in a thinner ‘GaAs-like’ interface due to the reduced formation time. However, the physical limitations of the mass flow controller within the MOCVD reactor prevent further reduction of the growth interruption time.

Instead of shortening the As for Sb exchange time, it is possible to reduce the amount of As flowing into the chamber, thereby decreasing the rate at which the ‘GaAs-like’ interface forms. Since the TMIn flow rate was kept constant to maintain the InAs growth rate, changes in the TBAs flow rate can be considered as changes in the InAs V/III ratio. The InAs V/III ratio was therefore reduced from 10 in order to achieve lattice match, as shown in Fig 4.6. The InAs V/III ratio that was able to lattice match the 21ML/8ML InAs/GaSb T2SLs onto the InAs substrate was 6.4.

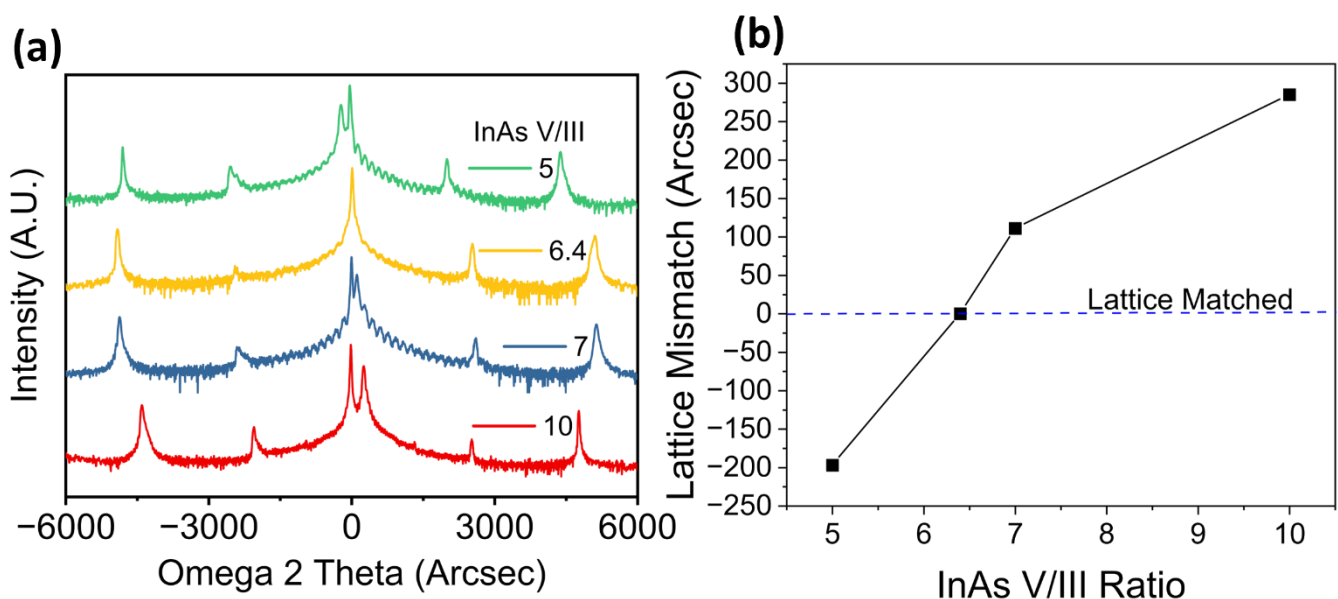


**Fig. 4.6.** (a) Omega 2 Theta XRD scans of 50 period 21ML/8ML InAs/GaSb T2SLs with different InAs V/III ratios. (b) Plot showing how the lattice mismatch of the InAs/GaSb T2SLs changes with InAs V/III ratio.

The InAs V/III ratio is a very useful growth parameter as it has a large effect on the lattice constant, whilst having a minimal effect on the surface roughness, as shown in Fig 4.7.

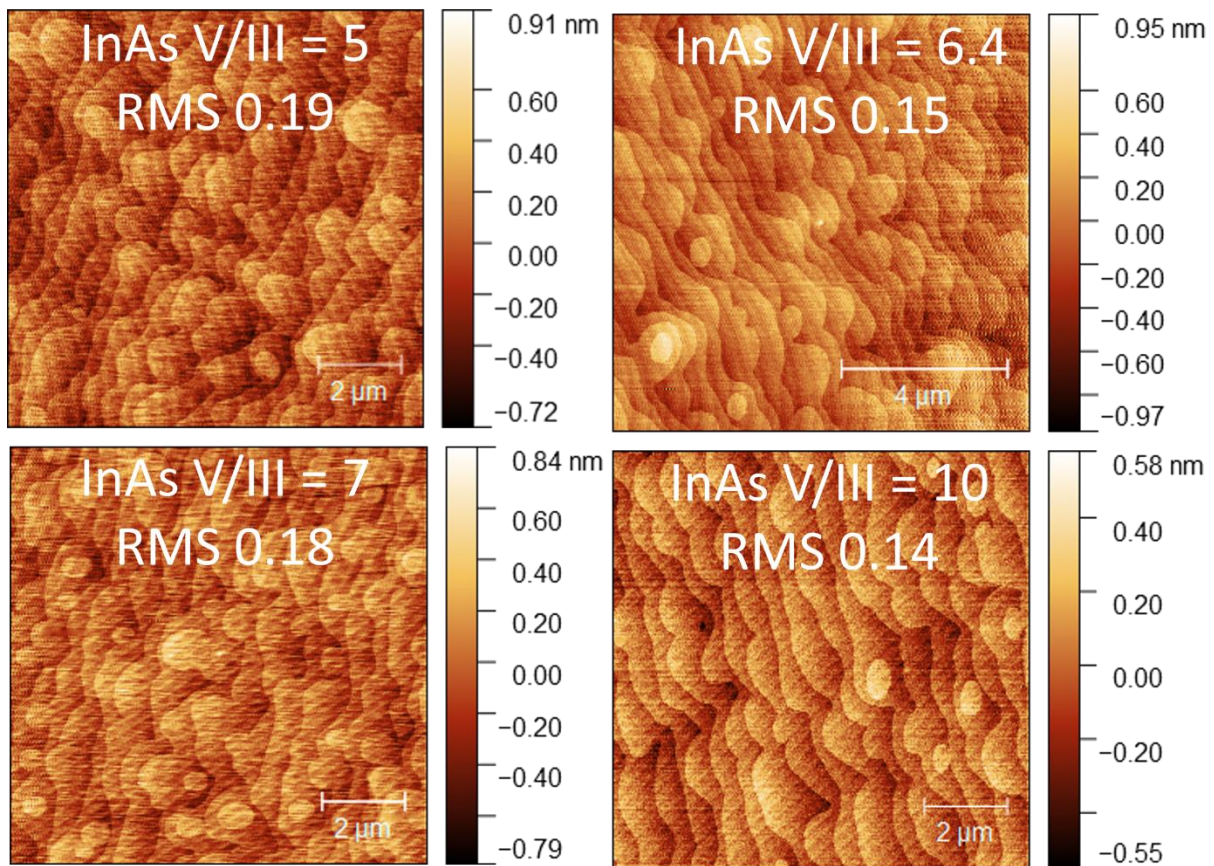


**Fig. 4.7.** AFM scans of 50 period 21ML/8ML InAs/GaSb T2SLs with different InAs V/III ratios.

#### 4.2.4 InAs/GaSb T2SLs spanning the 4-12 $\mu$ m wavelength range

Now that the 21ML/8ML InAs/GaSb T2SL has been grown. The next step is to grow InAs/GaSb T2SLs with different bandgaps to span the full MWIR and LWIR wavelength range. As explained in section 2.3.3, the bandgap of the InAs/GaSb T2SL can be changed by changing the InAs layer thickness. Five different InAs thicknesses were investigated: 21 ML, 16 ML, 11 ML, 8 ML and 6 ML, which correspond to approximate cutoff wavelengths of 12  $\mu$ m, 10  $\mu$ m, 6  $\mu$ m, 4.5  $\mu$ m and 4  $\mu$ m, respectively. The GaSb layer thickness was kept constant at 8 ML.

In theory, since the GaSb layer thickness is kept constant, changing the InAs layer thickness should not affect the lattice match onto InAs substrates. However, it was found experimentally that there was a small difference in lattice match between the different wavelength T2SLs which could be adjusted for by changing the InAs V/III ratio, as shown in Fig. 4.8. All wavelengths were found to be lattice matched with InAs V/III ratios between 6.4 and 6.7.

It is worth noting that a change in the InAs ratio by 0.1 corresponds to the smallest possible flow change on the TBAs mass flow controller. When operating the mass flow controller at its limits, the reliability and repeatability of the results can be questioned. Therefore, it is appropriate to claim these V/III ratios with an error margin of  $\pm 0.1$ .

This means that, in reality, the theory that the lattice match should not change with InAs layer thickness is largely supported by the experimental data, and any deviation is likely due to experimental error.

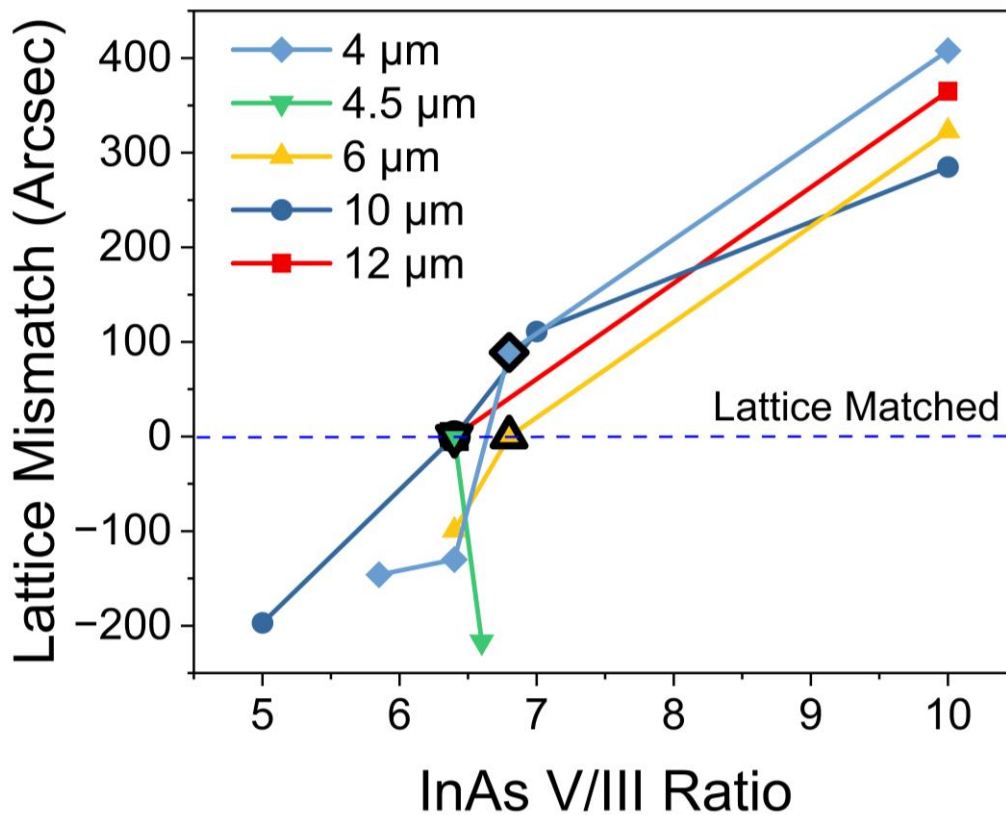


**Fig. 4.8.** Plot showing how the lattice constant of different wavelength InAs/GaSb T2SLs changed with InAs V/III ratio. The closest to lattice match of each wavelength are highlighted.

AFM was used to investigate if the change in InAs layer thickness had any effect on the surface morphology and roughness. For every T2SL where InAs thickness was greater than GaSb thickness there was no real difference in surface morphology or roughness. For the 6ML/8ML sample with a wavelength target of 4 μm however, there was a change in morphology and a surface roughening that can be seen in Fig 4.9.

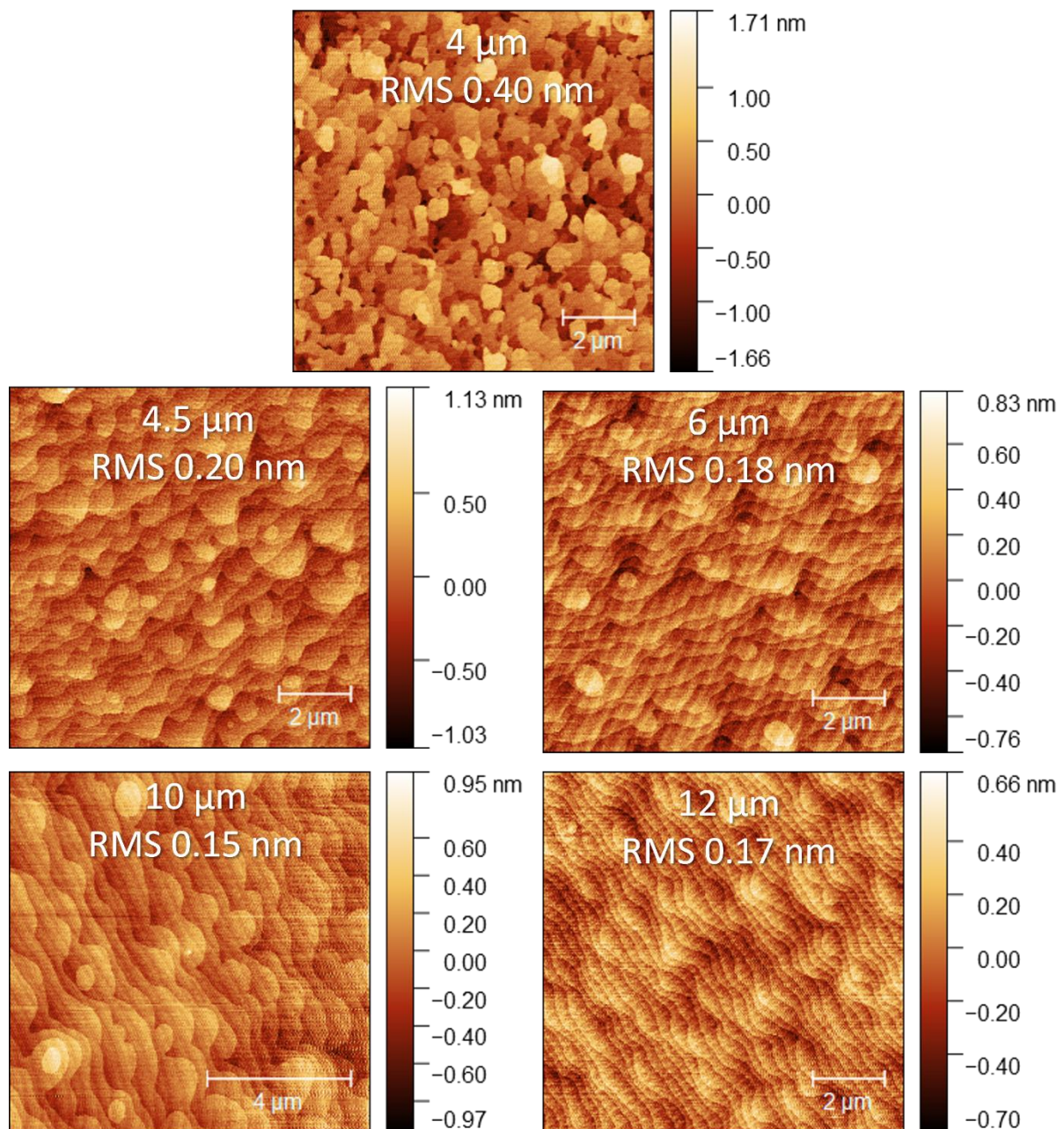


**Fig. 4.9.** AFM scans of 50 period InAs/GaSb T2SLs with different cutoff wavelengths.

It seems that there are challenges in growing InAs/GaSb T2SLs when the InAs layer is thinner than the GaSb layer. While achieving T2SLs with wavelengths shorter than 4 μm would be ideal, time constraints prevented a thorough investigation. Consequently, the 4.5 μm wavelength, 8ML/8ML T2SL was used as the shortest wavelength T2SL available for designing device structures.

To create an nBn detector, both short and long wavelength T2SLs need to be integrated within the same structure. With the T2SLs now sharing the same lattice constant, it is possible to grow multiple T2SLs of varying wavelengths on top of each other, as illustrated in the dual wavelength sample in Fig. 4.10.

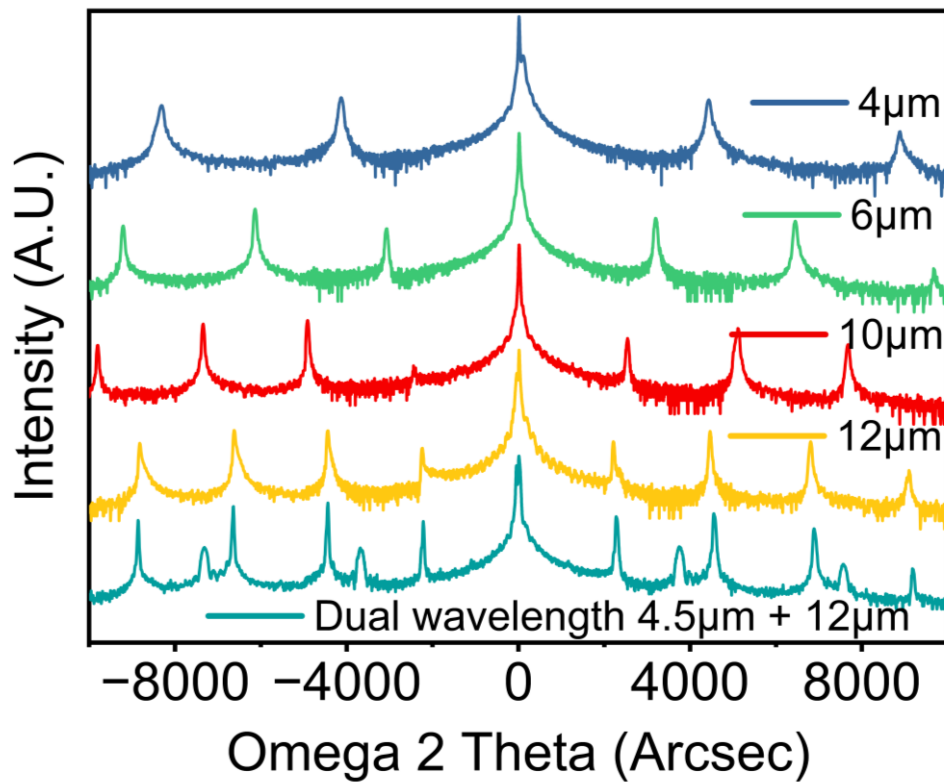


**Fig. 4.10.** Omega 2 Theta XRD scans of all the lattice matched InAs/GaSb T2SLs with different wavelengths. Including a dual wavelength sample with both a 4.5  $\mu\text{m}$  and 12  $\mu\text{m}$  T2SL.

To verify the wavelengths of the T2SLs, FTIR PL was employed, as depicted in Fig. 4.11. However, due to the transmission windows of the optics used in the setup, the detector cutoff occurred at around 9  $\mu\text{m}$ . This means there is no data for the 21ML/8ML sample, which has a target wavelength of 12  $\mu\text{m}$ . Fig. 4.11 demonstrates that the target wavelengths are close to the measured values in the PL setup, confirming that the band gaps of the grown T2SLs were as expected.

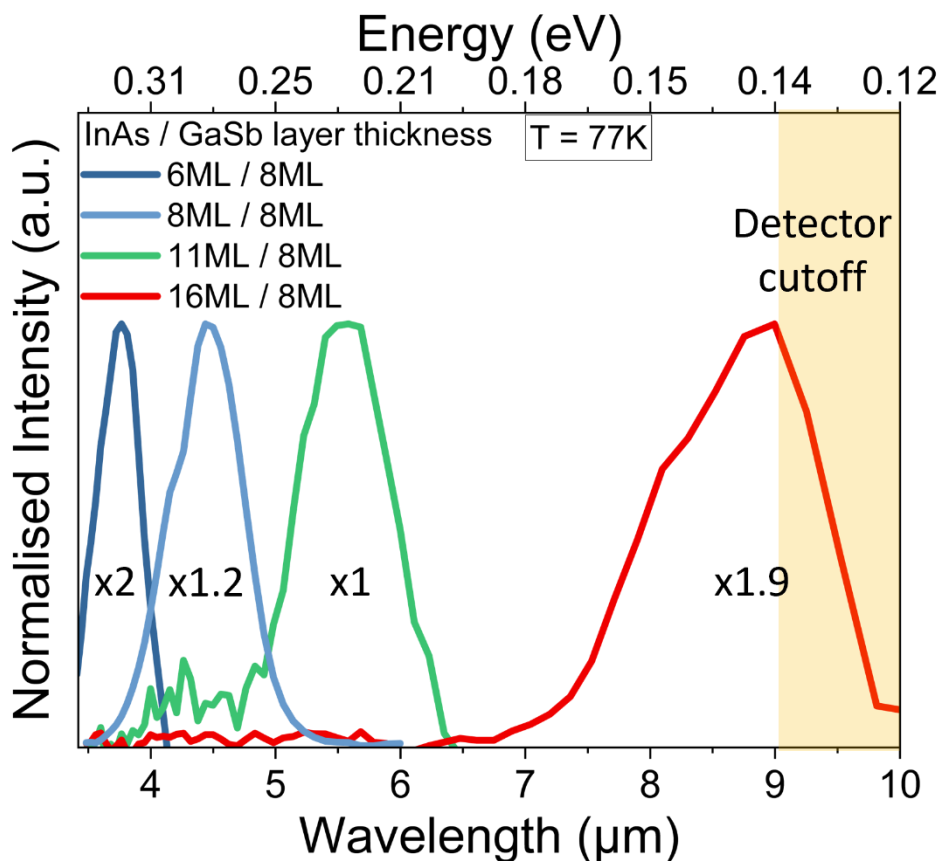


**Fig. 4.11.** Normalised photoluminescence plot, taken at 77K, showing the peak wavelength of each InAs/GaSb T2SL. The scaling factors that were used to create the normalised plot are shown within the peaks. Due to the transmission windows of the optics used in the setup, the detector cutoff is at around 9  $\mu\text{m}$ .

Once the wavelengths were verified, the “GaAs like” interfaces were investigated. The full width half maximum (FWHM) of the first order satellite peak in an omega 2 theta XRD scan is a good indication of superlattice interface sharpness [191]. The FWHM of the first order satellite peaks was found to range from 50-100 arcsec, with no clear trend relating to InAs layer thickness. This value is slightly higher than the best value that has been previously reported and so scanning transmission electron microscopy was used to further investigate the interface.

From the scanning transmission electron microscopy in Fig. 4.12 it is clear that whilst the interface may be considered “GaAs like” as is the convention, it is clearly quite far from a pure binary GaAs interface. The interface can be more accurately described as a graded InGaAsSb interface or a “mixed interface” [192]. The interface width is defined as the distance between 10% and 90% cation/anion intensity ratio [193]. The GaSb on InAs interface is  $6 \pm 1$  ML thick and the InAs on GaSb interface is around  $5 \pm 1$  ML thick. These interfaces are generally thicker than what has been previously reported [194] which could be due to their mixed nature as opposed to a pure GaAs interface which would require less thickness for the same strain balance.

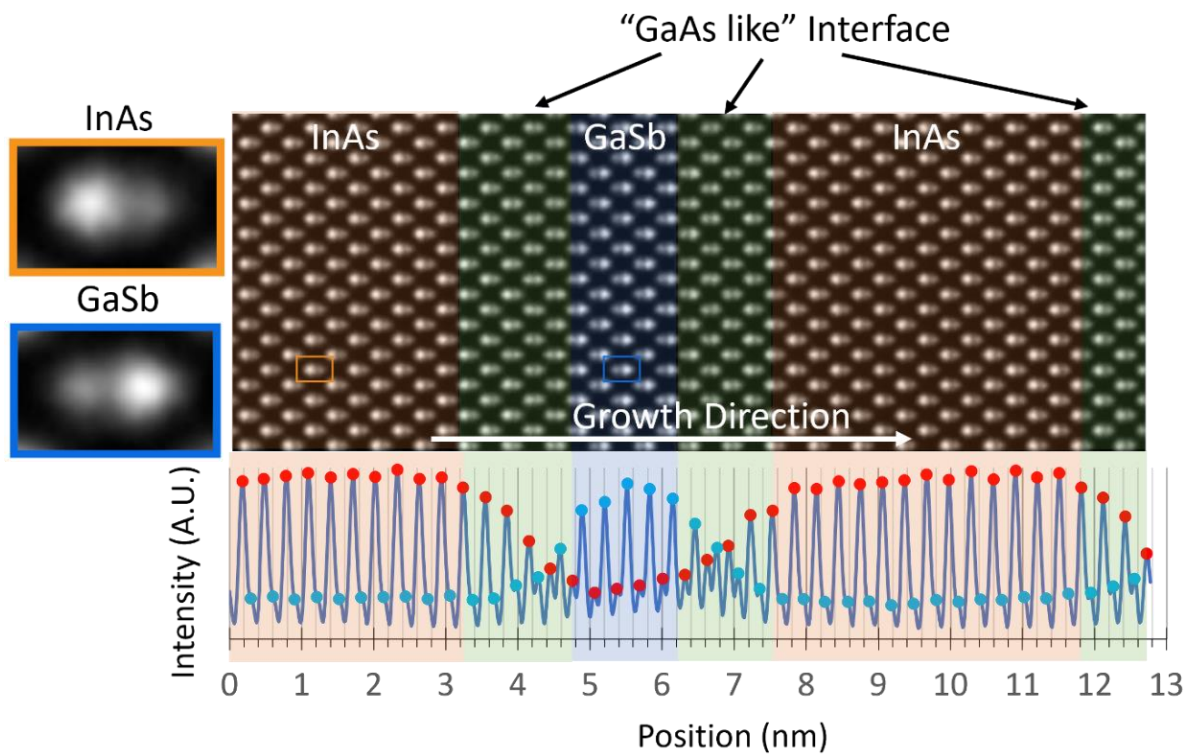


**Fig. 4.12.** High resolution scanning transmission electron microscopy showing the “GaAs Like” interfaces within the T2SL.

#### 4.2.5 InAs/GaSb T2SL device growth

Now that InAs/GaSb T2SLs can be grown lattice matched to InAs substrates with low surface roughness, the next step is to design and grow a InAs/GaSb T2SL device structure. As discussed in section 2.2, barrier-based photodetectors offer superior dark current performance which is essential for LWIR detectors. The nBn structure was selected due to its relative simplicity as it can be formed from only InAs/GaSb T2SLs and only requires n-doping.

The nBn device contains two different InAs/GaSb T2SLs with different InAs thicknesses. The LWIR T2SL consists of 21 monolayers of InAs and 8 monolayers of GaSb (21 ML/8 ML) and has a band gap of  $\sim 0.1$  eV ( $\lambda \approx 12\mu\text{m}$ ). The MWIR T2SL consists of 8 monolayers of InAs and 8 monolayers of GaSb (8 ML/8 ML) and has a band gap of  $\sim 0.28$  eV ( $\lambda \approx 4.5\mu\text{m}$ ). Since the GaSb thickness is the same in both of the T2SLs, their valence band offset is near 0 eV [195]. This 0 eV valence band offset means that the difference in bandgap is entirely within the conduction band which creates an electron barrier of 0.18 eV.

This barrier height is notably lower than those reported in comparable Al-containing nBn structures [196]. However, it should still be large enough to suppress thermionic emission since at 77 K,  $3kT$  is only 0.02 eV. The finalised device structure consists of a 205 nm n-type ( $n \approx 10^{18} \text{ cm}^{-3}$ ) 21 ML/8 ML T2SL bottom contact, a 2050 nm u.i.d 21 ML/8 ML T2SL absorber layer, a 125nm u.i.d 8 ML/8 ML T2SL barrier layer and a 205 nm n-type ( $n \approx 10^{18} \text{ cm}^{-3}$ ) 21 ML/8 ML T2SL top contact.

To grow the device structure, doping calibration is required. Silicon (Si), provided by the precursor disilane, was used as the N-dopant. Being a group IV element, Si can act as either an N-type or P-type dopant depending on the material. Specifically, Si serves as an N-dopant for InAs but acts as a P-dopant for GaSb. Therefore, to N-dope an InAs/GaSb T2SL with Si, the Si flow is only activated during the InAs growth phase, while the GaSb remains undoped. This separation of the dopant makes accurate doping calibration very challenging as the resolution of SIMS is not high enough to resolve individual layers of a T2SL. Therefore, doping calibration was performed on thicker bulk InAs samples, and these results were used to estimate the doping concentration for the T2SL.

The absolute values for doping presented in this work may not be fully accurate as the calibration standards were calibrated from InGaAs samples instead of InAs, due to the difficulty of obtaining InAs calibration samples. While this method may not fully optimise the doping, a rough estimate should be sufficient to produce functional devices, as only the contact layers in the nBn structure are actively doped.

A structure consisting of three InAs layers each with a different ratio of  $\text{Si}_2\text{H}_6$  to TMIIn was grown and SIMS was used to calibrate the Si incorporation, as shown in Fig. 4.13.

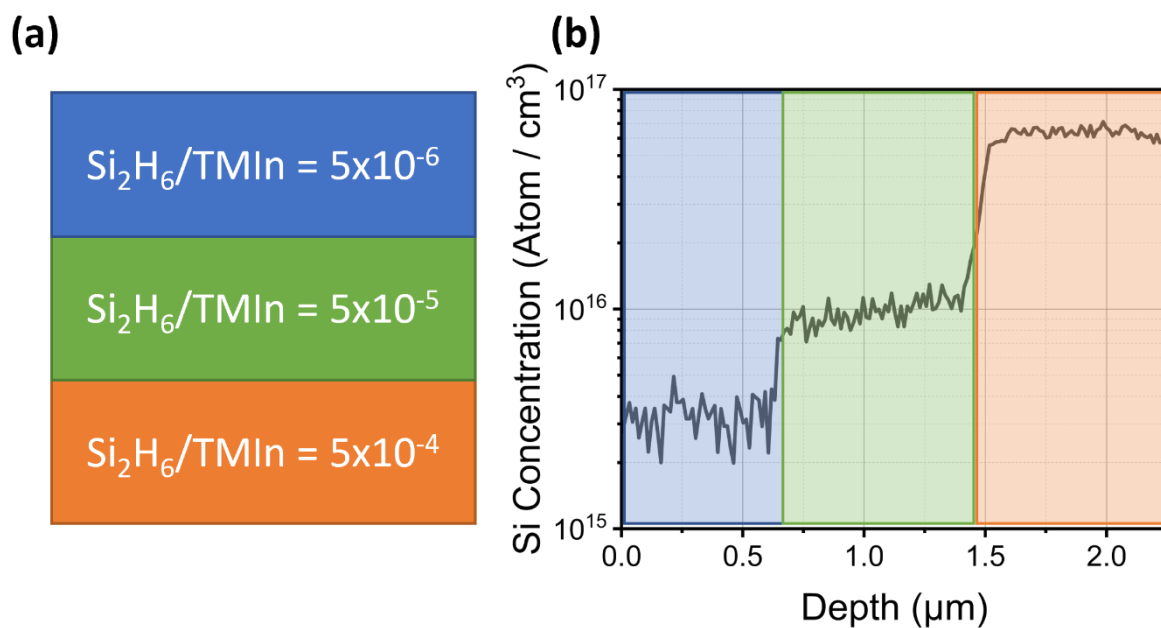


**Fig. 4.13.** (a) Schematic diagram of the staircase doping calibration of Si into bulk InAs. (b) SIMS data from the doping calibration sample. The ratio of the flow of  $\text{Si}_2\text{H}_6$  to TMIIn was increased from  $5 \times 10^{-6}$  to  $5 \times 10^{-4}$  resulting in an increase of Si concentration from  $3 \times 10^{15}$  to  $6 \times 10^{16}$  Atoms / cm<sup>3</sup>.

The highest Si concentration from the doping calibration was  $6 \times 10^{16}$  Atoms / cm<sup>3</sup> which occurred when the  $\text{Si}_2\text{H}_6$  to TMIIn ratio was  $5 \times 10^{-4}$ . The desired Si concentration of the n-contact layers in the device structure was around  $10^{18}$  Atoms / cm<sup>3</sup>. Therefore, the flow of  $\text{Si}_2\text{H}_6$  to TMIIn used in the device contact layers was set to  $5 \times 10^{-3}$ .

Once the doping was calibrated, the full device structure was then grown from a combination of 21 ML/8 ML and 8 ML/8 ML T2SLs, as shown in Fig. 4.14. The layer thicknesses were confirmed using TEM.

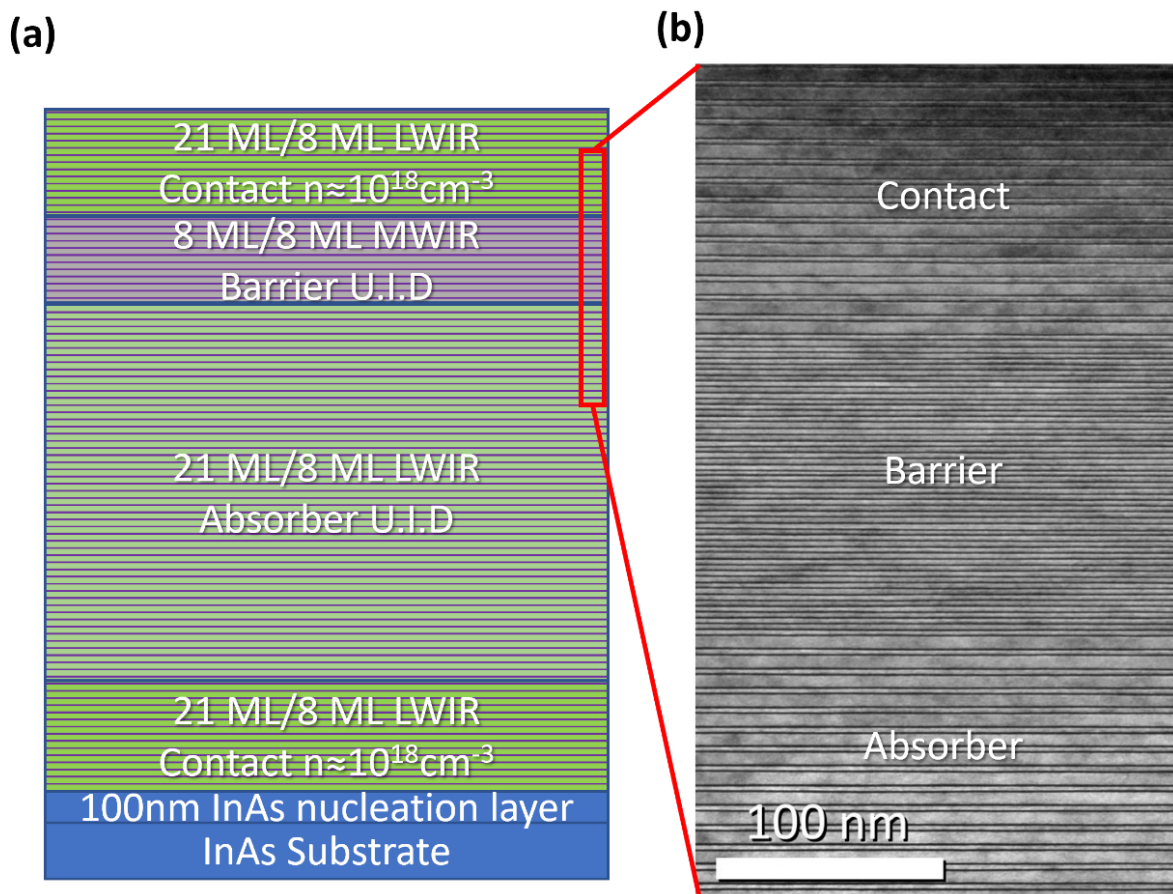


**Fig. 4.14.** (a) Schematic diagram of the full device epitaxial structure. (b) Transmission electron microscopy (TEM) scan of the indicated region of the device structure.

## 4.3 Device Results

### 4.3.1 Surface Passivation

The grown device structure was divided into multiple pieces and different fabrication methodologies were investigated. Dark current remains the main challenge in the field of LWIR detectors, especially dark current related to exposed sidewalls. Finding an acceptable surface passivation technique is therefore important in developing LWIR detectors.

The exposed detector sidewalls contain dangling bonds which form surface states that act as mid bandgap trap states. These trap states create a carrier recombination pathway which increases dark current. In order to reduce this dark current the dangling bonds must be capped with a material that can change the surface states to no longer exist within the bandgap. Due to the nature of the T2SL containing multiple materials as well as its narrow bandgap making recombination easier, an optimal surface passivation technique has yet to be found. Surface passivation for the T2SL remains a large challenge for the commercialisation of T2SL detectors and is an actively researched field.

Common passivation techniques for T2SL-based IR detectors include the use of  $\text{Si}_x\text{N}_y$ ,  $\text{SiO}_2$ , polyimide, and ammonium sulfide. The effectiveness of these techniques varies based on treatment conditions. Ammonium sulfide passivation is known for its lack of reproducibility and long-term stability.  $\text{Si}_x\text{N}_y$  and  $\text{SiO}_2$  deposited at the standard temperature of  $300^\circ\text{C}$  result in very high surface leakage currents on InAs and GaSb p-i-n diodes. Therefore, lower temperature deposition of  $\text{Si}_x\text{N}_y$  or  $\text{SiO}_2$  is necessary, although this slows the process and can degrade the electrical characteristics of T2SL photodiodes. Photoresists such as BCB and SU-8 have been shown to be simple and effective alternatives to these other passivation techniques [197]. However, since they are photoresists, they are not as durable as the other techniques and so may not be as applicable in commercial settings. In this work, the photoresist AZ3027 was used for surface passivation, as shown in section 3.2. AZ3027 was chosen as it is easy to apply and has not yet been as deeply investigated as the other more common photoresists.

The first set of devices fabricated follow the fabrication steps laid out in section 4.2. These devices were deep etched, as shown in Fig. 2.7. The deep etch was performed using a PE-100 plasma etching machine. These devices are therefore known as deep, dry etched devices. The fabrication process was split into two with half the devices receiving the AZ3027 surface passivation and half remaining unpassivated for comparison.

The dark current density of 5 of the passivated and unpassivated samples was then taken and the lowest of each was plotted, in Fig. 4.15.

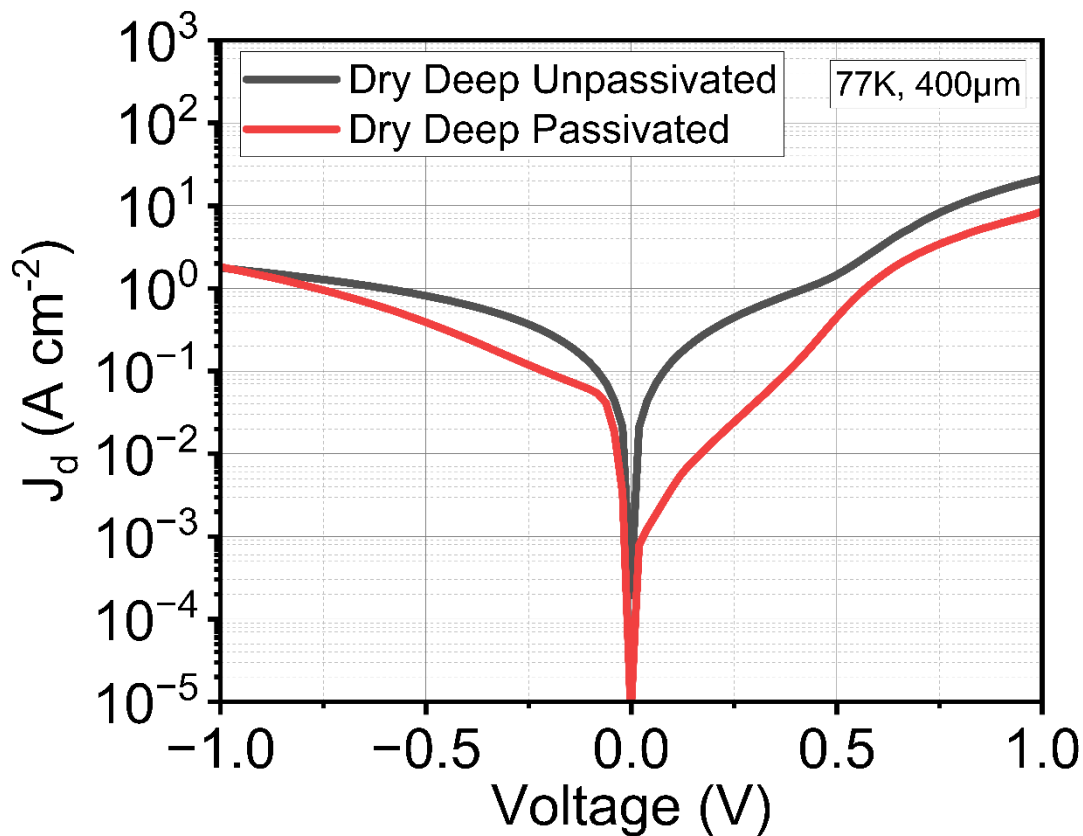


**Fig. 4.15.** Dark current density ( $J_d$ ) versus voltage for the deep, dry etched detectors, with and without surface passivation.

The operating voltage for these devices is  $-0.1\text{V}$ , so any reduction in dark current density at this voltage will enhance detector performance. The reduction in dark current density in the forward bias was not investigated as these devices do not function in the forward bias. As shown in Fig. 5.14, the AZ3027 reduced the dark current density of the deep, dry etched device from  $0.12$  to  $0.06\text{ A/cm}^2$  at  $-0.1\text{V}$ , achieving a 50% reduction.

Another method to reduce surface-related dark currents is to fabricate shallow etched devices with significantly smaller exposed sidewalls. The same fabrication procedure was used, differing only in the depth of the dry mesa etch. As illustrated in Fig. 2.7, a deep mesa etch extends to the bottom contact, whereas a shallow mesa etch stops at the barrier layer. These shallow etched devices were then split into two groups: one half was passivated, and the other half was left unpassivated to determine if passivation remains effective for shallow devices.

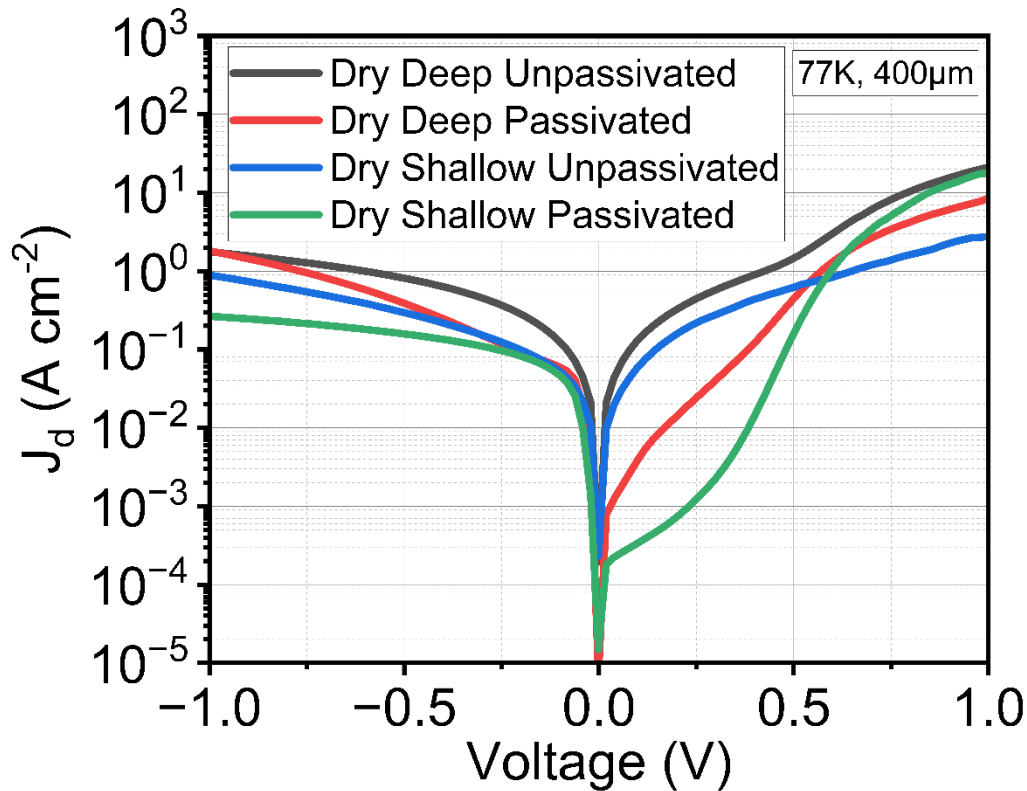


**Fig. 4.16.** Dark current density ( $J_d$ ) versus voltage for the deep and shallow, dry etched detectors with and without surface passivation.

As shown in Fig. 4.16, the shallow etched devices exhibited lower dark current densities at -0.1V. The passivated shallow etched device had a dark current density of 0.05 A/cm<sup>2</sup>, while the unpassivated shallow etched device had a dark current density of 0.04 A/cm<sup>2</sup>. This indicates that the reduced exposed sidewall in shallow etched devices diminishes the impact of sidewall passivation, compared to the significant decrease observed in deeply etched devices.

In order to further investigate the surface dark currents, devices of multiple different diameters were fabricated and compared. The total dark current density ( $J_d$ ) can be expressed as:

$$J_d = \varphi \times \frac{P}{A} + J_{bulk} \quad (4.1)$$

where  $\varphi$  is the sidewall current per unit length,  $\frac{P}{A}$  is the perimeter-to-area ratio of the detector and  $J_{bulk}$  is the bulk component of the dark current density. Fig. 5.17 shows a plot of  $J_d$  against the device perimeter-to-area ratio,  $\frac{P}{A}$ .

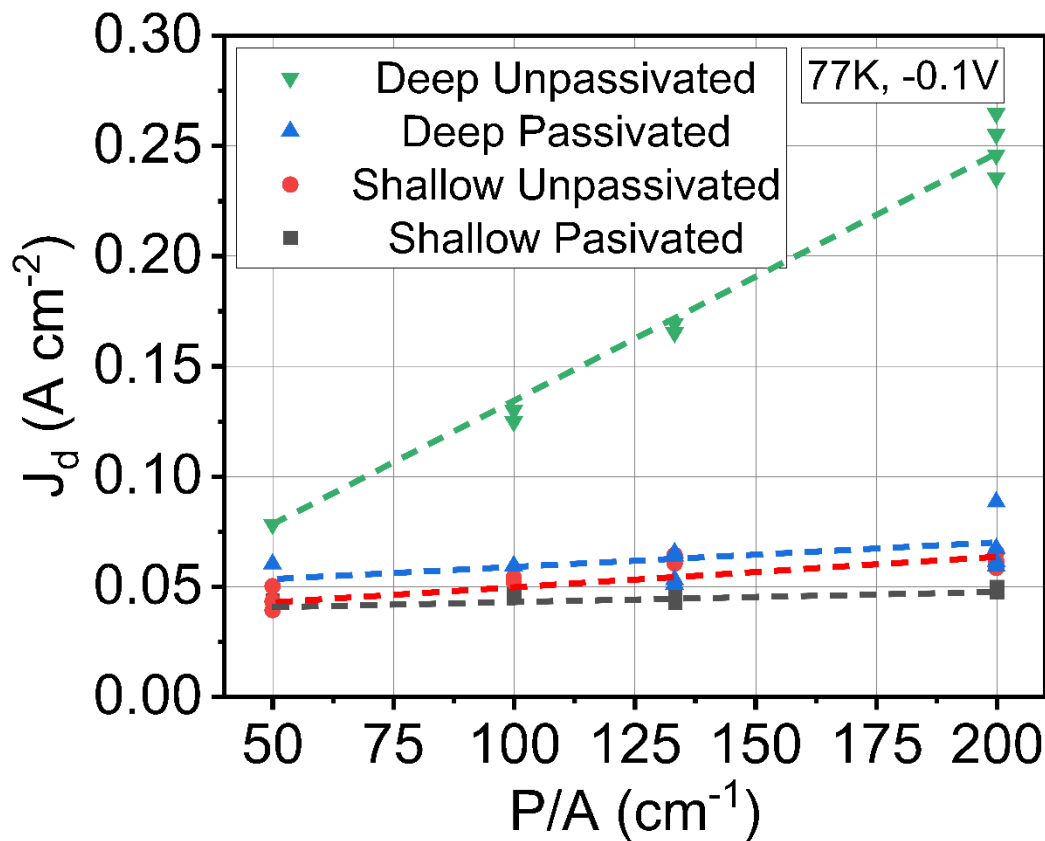


**Fig. 4.17.** Dark current density ( $J_d$ ) versus the perimeter-to-area ratio for the deep and shallow, dry etched detectors with and without surface passivation. The linear fittings were obtained using equation 4.1.

From Fig. 4.17, the bulk and surface components of the dark current densities for each detector can be calculated. The bulk and surface components of the dark current densities are shown in Table 4.1 along with the total dark current density from Fig. 4.15.

**Table 4.1.** Surface, bulk and total dark current for the dry etched devices.

Device	Surface Dark current (A/cm)	Bulk Dark current density (A/cm <sup>2</sup> )	Total dark current density (A/cm <sup>2</sup> )
Deep Unpassivated	$1.1 \times 10^{-1}$	$3.5 \times 10^{-2}$	$1.2 \times 10^{-1}$
Deep Passivated	$8.3 \times 10^{-3}$	$5.0 \times 10^{-2}$	$5.9 \times 10^{-2}$
Shallow Unpassivated	$1.2 \times 10^{-2}$	$4.2 \times 10^{-2}$	$5.1 \times 10^{-2}$
Shallow Passivated	$2.7 \times 10^{-3}$	$4.2 \times 10^{-2}$	$4.3 \times 10^{-2}$

For all devices the sum of surface and bulk dark currents is very close to the total measured dark current density which gives confidence to the linear fitting in Fig. 4.16. When the surface and bulk dark currents are separated, the effect of the passivation becomes clear. The total dark current density of the deep unpassivated sample is completely dominated with surface dark currents. When passivated, the surface dark currents reduce by 92%. However, the bulk dark current densities are all still around  $10^{-2}$  which is around 100x higher than the “rule 07” value at this wavelength. This indicates that there is still further optimisation needed before these detectors can directly compete with the state-of-the-art

MCT. Whilst the shallow detectors did perform better than the deep detectors, the trade-off still exists between dark current reduction and detector density within a focal plane array. The shallow detectors need to be kept two lateral diffusion lengths apart from each other to prevent crosstalk, as shown in Fig. 4.18.

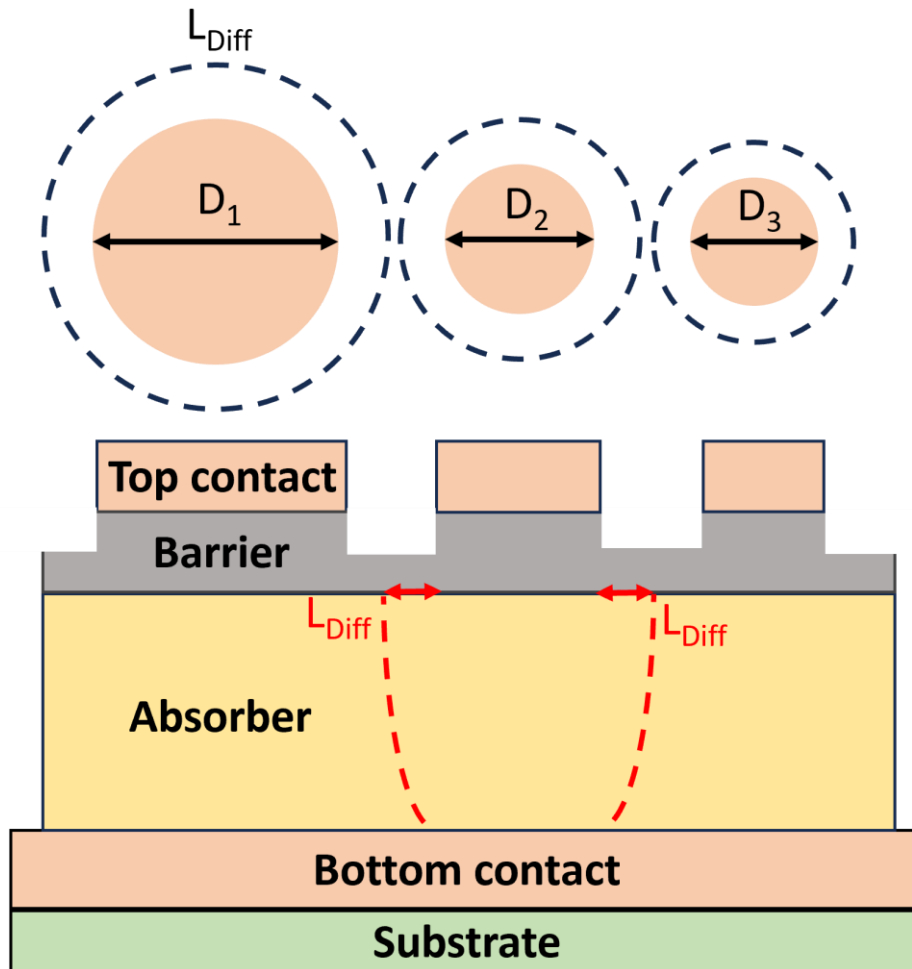


**Fig. 4.18.** Schematic layout of the shallow etched pixels with different mesa etch diameters ( $D_n$ ) showing the lateral diffusion length ( $L_{Diff}$ ).

By varying the mesa sizes of the shallow etched devices, the lateral diffusion length ( $L_{Diff}$ ) can be calculated via:

$$J(D) = \frac{J_{bulk} (D + 2L_{Diff})^2}{D^2} \quad (4.2) [72]$$

where  $J(D)$  is the total dark current density at a given mesa diameter,  $J_{bulk}$  is the bulk dark current density,  $D$  is the mesa diameter and  $L_{Diff}$  is the lateral diffusion length. Fig. 4.19 shows a plot of  $J_d$  against mesa diameter which is used to calculate  $L_{Diff}$ .

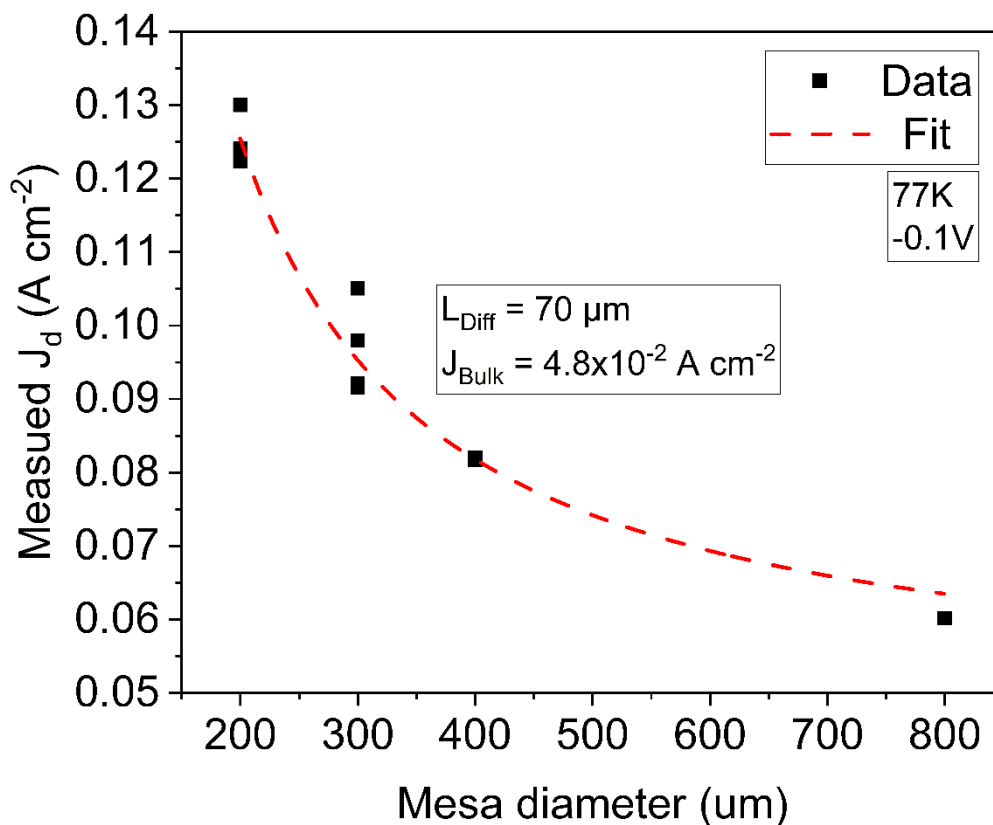


**Fig. 4.19.** Measured dark current density against mesa diameter. The fitting was obtained using equation 4.2.

From Fig. 4.19, the lateral diffusion length was determined to be  $70\ \mu\text{m}$ . Consequently, the “true” shallow device diameter was calculated as the mesa diameter plus  $140\ \mu\text{m}$ . This “true” shallow device diameter was used for all other shallow device data calculations, such as those in Fig. 4.15 and 4.16. This lateral diffusion length is notably shorter than the  $200\text{--}250\ \mu\text{m}$  reported in previous literature [72]. The reduction in diffusion length is likely due to the mixed “GaAs-like” interfaces. In cases with longer diffusion lengths, a more “GaAs-like” and less mixed interface was used. A large bandgap “GaAs-like” interface may promote lateral carrier movement, as it hinders vertical movement through the interface, thereby increasing the lateral diffusion length.

Despite the reduction, a lateral diffusion length of  $70\ \mu\text{m}$  is still substantial and significantly limits potential pixel density. Typically, the spacing between pixels in an FPA is less than  $10\ \mu\text{m}$ . A lateral diffusion length of  $70\ \mu\text{m}$  implies a minimum spacing of  $140\ \mu\text{m}$  between these shallow pixels, which is much higher than current FPAs. Due to this pixel spacing issue and the effectiveness of the surface passivation layer in reducing the sidewall dark current of deep pixels, the deep etched pixels in this work were considered superior to the shallow etched pixels.

### 4.3.2 Wet Vs Dry etch

The final fabrication parameter investigated was the mechanism of the mesa etch. Previously all samples used a  $\text{BCl}_3$  based dry etch to perform the mesa etch, as shown in section 3.2. Dry etching works by physically bombarding the sample with plasma which can cause a lot of surface damage to the sample. This surface damage results in a large number of dangling bonds and defects which act as pathways to increase surface related dark currents. A wet etch works by chemically removing the desired material within a solution which causes far less surface damage than dry etching. In theory the wet etch should result in lower dark current densities than dry etched samples. The fabrication of the wet etched samples was exactly the same as set out in 3.2, except the mesa etch was performed using a citric acid based wet etch consisting of  $\text{C}_6\text{H}_8\text{O}_7$ ,  $\text{H}_3\text{PO}_4$ ,  $\text{H}_2\text{O}_2$  and  $\text{H}_2\text{O}$  in the ratio; 15 g : 20 ml : 12 ml : 40 ml.

The dark current density of these deep wet etched devices was then plotted and compared to the previous deep dry etched devices, as shown in Fig. 4.20.

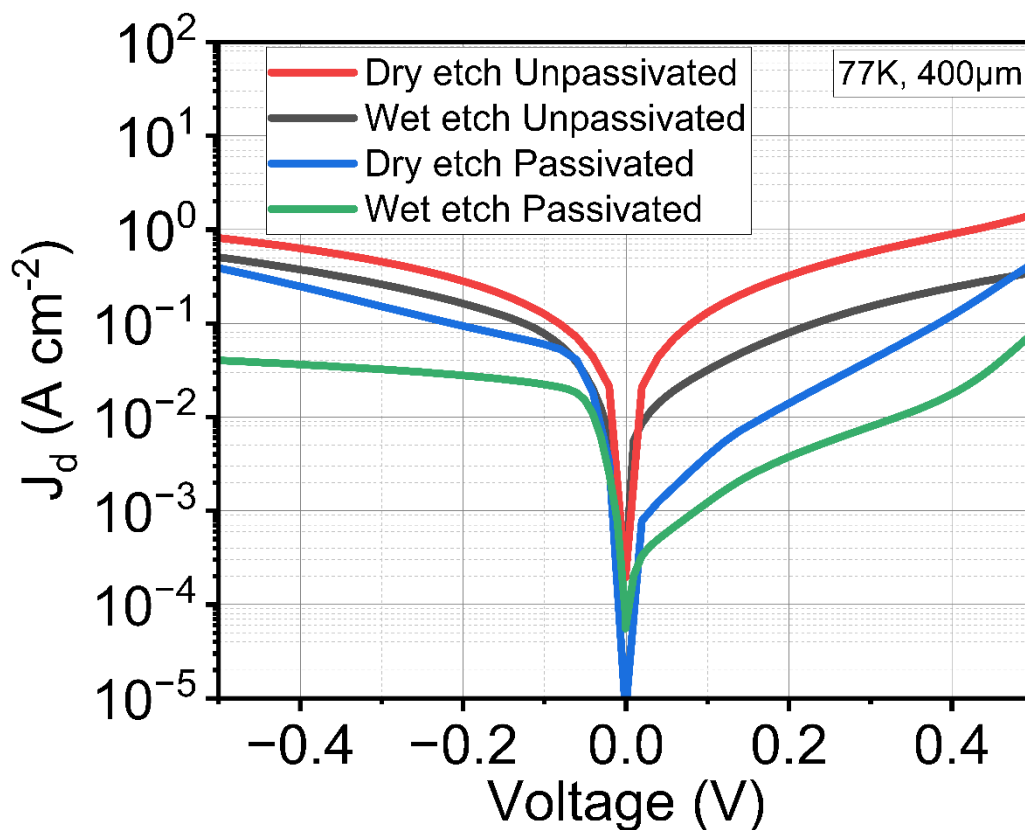


**Fig. 4.20.** Dark current density ( $J_d$ ) versus voltage for the dry and wet etched detectors with and without surface passivation.

As shown in Fig. 2.20, for the device diameter of  $400\mu\text{m}$ , the wet etched devices exhibited lower dark current densities than the dry etched devices. The dark current density at  $-0.1\text{V}$  for the wet etched unpassivated device was  $7.7 \times 10^{-2} \text{ A/cm}^2$ , and the dark current density at  $-0.1\text{V}$  for the wet etched passivated device was  $2.2 \times 10^{-2} \text{ A/cm}^2$ . The same  $J_d$  against device perimeter-to-area ratio,  $\frac{P}{A}$  analysis was performed as in Fig. 5.16, and is plotted in Fig. 4.21.

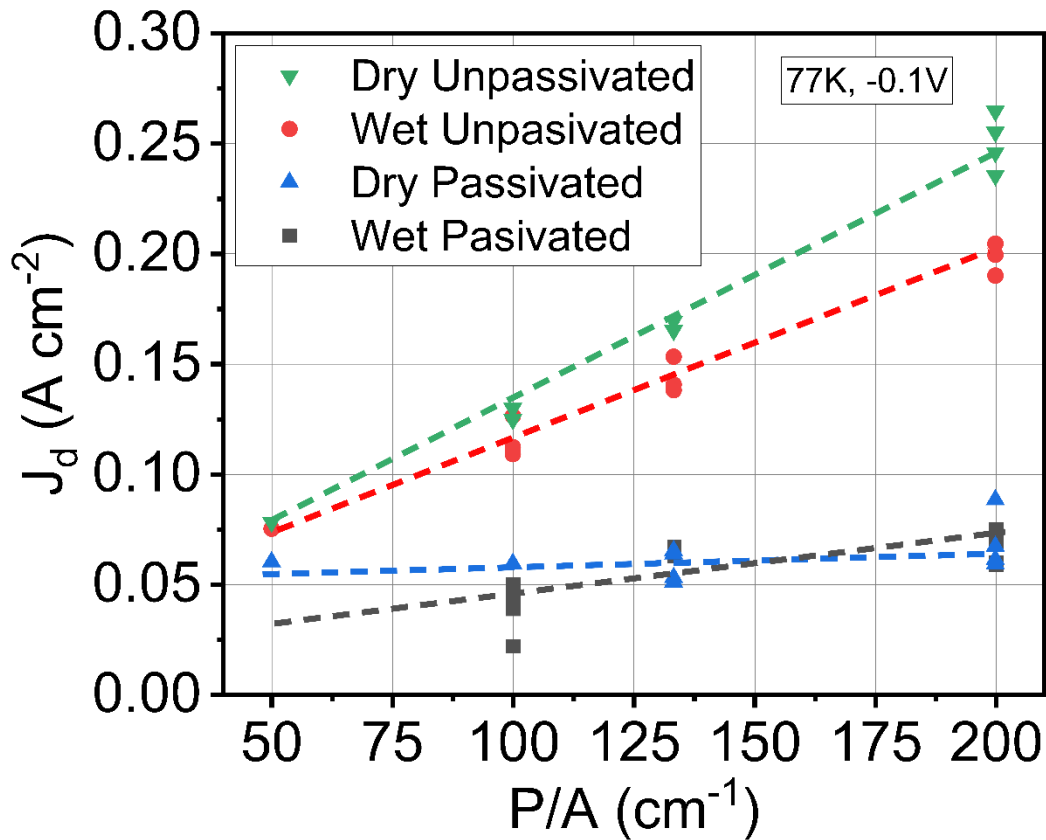


**Fig. 4.21.** Dark current density ( $J_d$ ) versus the perimeter-to-area ratio for the dry and wet deep etched detectors with and without surface passivation. The linear fittings were obtained using equation 4.1.

From Fig. 4.21, the bulk and surface components of the dark currents for each detector were calculated. The bulk and surface components of the dark currents are shown in table 4.2 along with the lowest total dark current density for a 400  $\mu\text{m}$  device from Fig. 4.20.

**Table 4.2.** Surface, bulk and total dark current for the wet and dry etched devices.

Device	Surface Dark current (A/cm)	Bulk Dark current density (A/cm <sup>2</sup> )	Total dark current density (A/cm <sup>2</sup> )
Dry Unpassivated	$1.1 \times 10^{-1}$	$3.5 \times 10^{-2}$	$1.2 \times 10^{-1}$
Dry Passivated	$8.3 \times 10^{-3}$	$5.0 \times 10^{-2}$	$5.9 \times 10^{-2}$
Wet Unpassivated	$8.2 \times 10^{-2}$	$3.3 \times 10^{-2}$	$7.7 \times 10^{-2}$
Wet Passivated	$2.5 \times 10^{-2}$	$1.9 \times 10^{-2}$	$2.2 \times 10^{-2}$

By analysing the wet and dry unpassivated surface dark currents, it is evident that the dry etching process generates more surface currents than the wet etching process. Specifically, the wet etched surface dark currents were 1.3 times lower than those of the dry etched samples. Similar to the dry etched samples, surface passivation effectively reduced the surface dark currents of the wet passivated devices, achieving a 70% reduction.

However, when comparing the passivated dry and wet etched samples, the differences are less pronounced. While the fittings of the wet etched samples somewhat align with their total dark current densities, there appears to be some discrepancy due to variations between devices of the same type. Therefore, it is challenging to definitively determine which fabrication method is superior between passivated dry and wet etched samples. Nonetheless, AZ3027 has proven to be an effective surface passivation technique for both wet and dry etched InAs/GaSb T2SLs. Despite significant improvements from surface passivation, the bulk dark current densities remain relatively high compared to current state-of-the-art devices, as illustrated in Fig. 4.22.

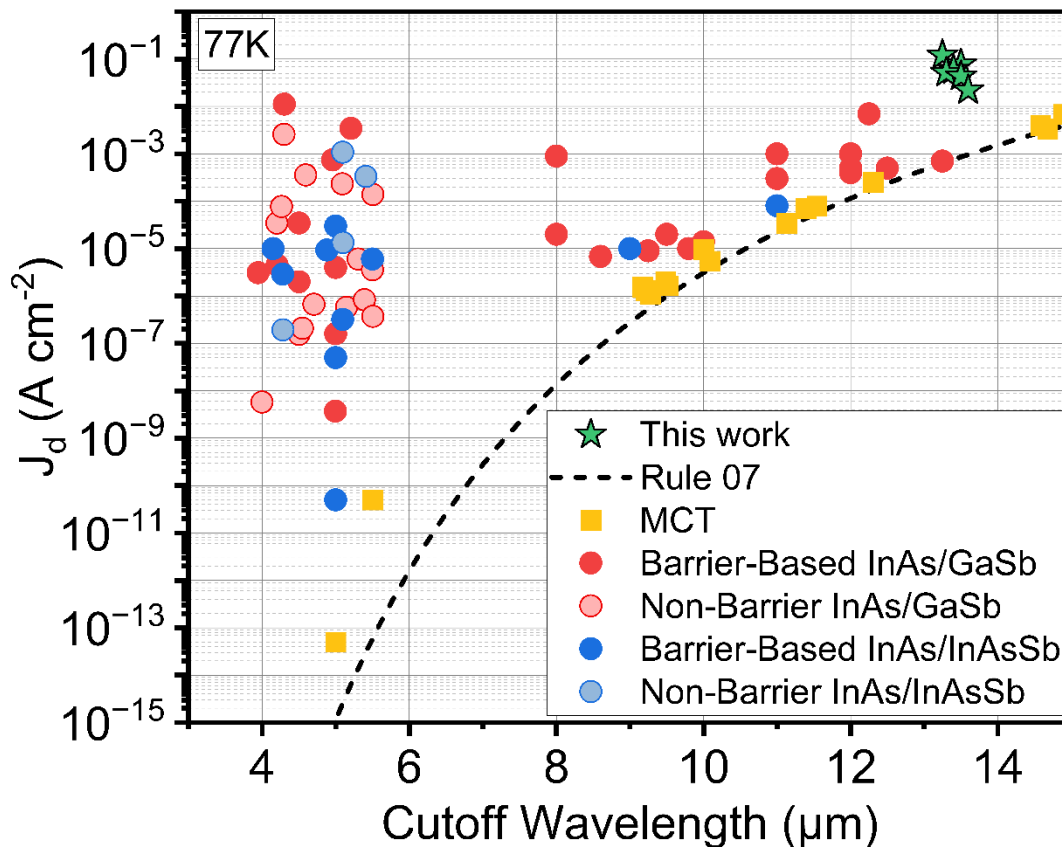


**Fig. 4.22.** Comparison of the dark current densities in this work compared to the values in literature for Barrier-based InAs/GaSb [4–7,113,114,71,115,116,8,117–119,9,10,120,11–14,121,15,122,16,123], Non-Barrier InAs/GaSb [124,20,125–127,21,128,17,22,23,129–135], Barrier-Based InAs/InAsSb [136,27–29,40,42,137–139,30,140,141] and Non-Barrier InAs/InAsSb detectors [32,47,33–35,142,36]. As well as MCT detectors [143,144] and the “Rule 07” line [48].

One possible explanation for this elevated  $J_{\text{bulk}}$  is the formation of a depletion region between the barrier and absorber regions due to inadequate doping control. Both regions were left unintentionally doped, with the assumption that their doping levels would be similar. However, this assumption may be flawed because the InAs layer thickness varies significantly between the two regions. InAs typically dopes n-type unintentionally, while GaSb dopes p-type. Consequently, the absorber region is likely to be more n-doped than the barrier region, potentially leading to the formation of a depletion region.

If a depletion region forms between the barrier and absorber, it could create an area for Shockley-Reed-Hall (SRH) based generation-recombination (GR) current, which is usually suppressed in an nBn device. A depletion region is formed due to the diffusion of majority carriers, leaving behind fixed ionised impurities. These ionised impurities act as trap sites within the band gap which act as intermediary states for carrier to recombine through via SRH recombination. This SRH recombination creates a pathway for current to flow even when the device is not illuminated, hence it increases the dark current of the device.

A doping difference of one order of magnitude between the barrier and absorber regions has been shown to increase dark current density by two orders of magnitude [123]. Additionally, this doping difference can increase the external quantum efficiency (EQE) by five times [123]. These effects can be attributed to the introduction of a depletion region, as both SRH generation-recombination currents and EQE increase with the size of the depletion region, as shown in equation 2.5 and section 2.2.

To confirm if the formation of a depletion region is occurring in these devices, the dominant dark current mechanism needs to be identified. If GR-related dark current dominates, it is highly likely that the high dark current density is due to insufficient doping control in the barrier and absorber regions.

#### 4.3.3 Dark current mechanisms

In order to investigate the dominant dark current mechanism within the devices, temperature dependant dark current density measurements were taken. How the dark current density changes with temperature can be used to calculate the activation energy ( $E_a$ ) of the detector, which in turn can be used to estimate the dominant dark current mechanism [198]. An  $E_a$  of around the size of the band gap of the detector indicates that the detector is limited by diffusion currents. If the  $E_a$  is equal to around 50% of the detectors band gap, then the detector is said to be limited by generation-recombination dark current mechanisms. If the  $E_a$  is close to 0 then the detector is dominated by temperature insensitive tunnelling currents. The activation energy can be calculated from the expression:

$$J_d = \exp\left(\frac{-E_a}{K_B T}\right) \quad (4.3)[198]$$

where  $J_d$  is the total dark current density,  $E_a$  is the activation energy,  $K_B$  is the Boltzmann constant and  $T$  is temperature. Arrhenius plots of  $J_d$  against  $1000/T$  were then created for each device, as shown in Fig. 4.23 and values for  $E_a$  were calculated.

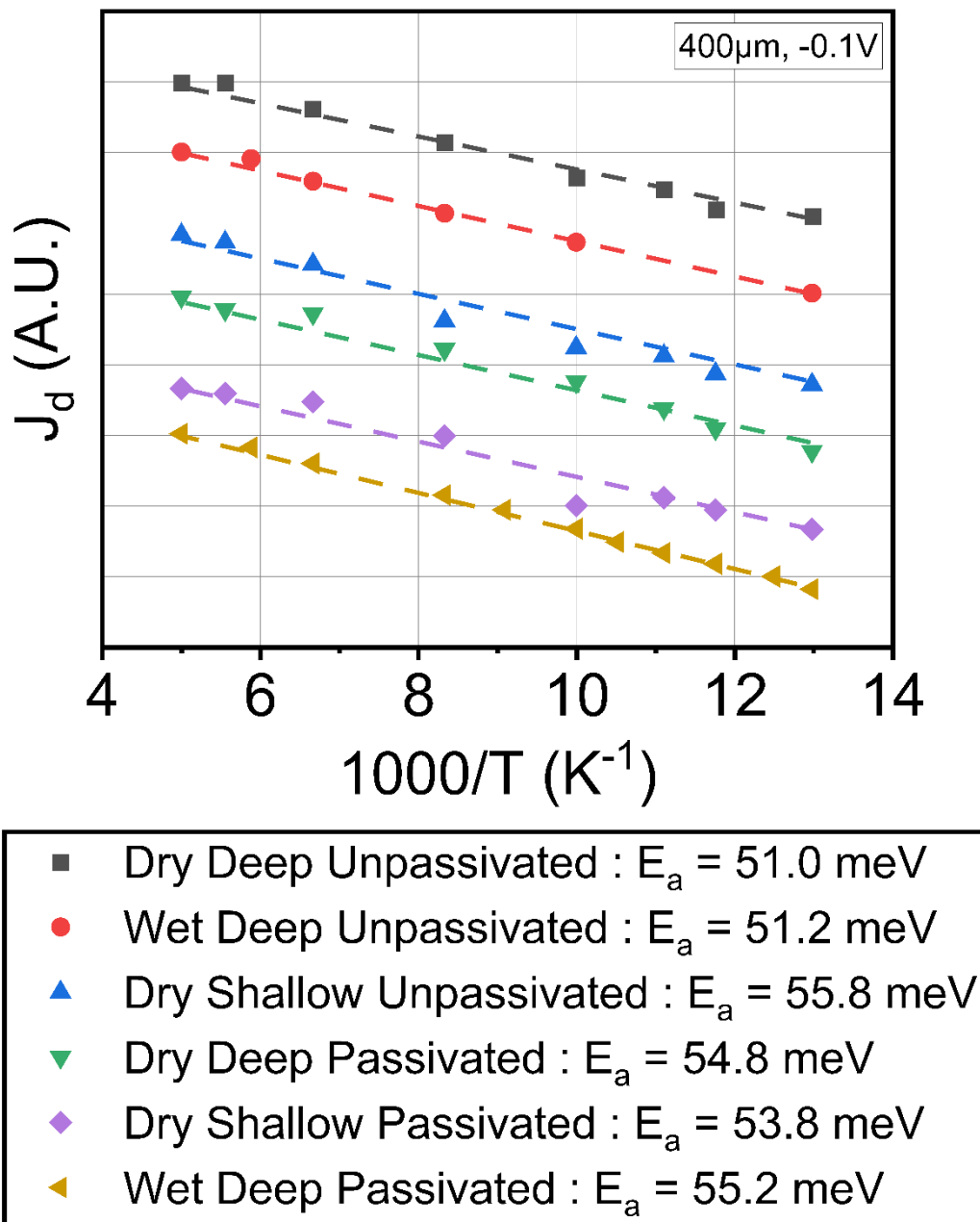


**Fig. 4.23.** Arrhenius plot of  $J_d$  against  $1000/T$  showing the activation energies ( $E_a$ ) for  $400\mu\text{m}$  diameter devices at  $-0.1\text{V}$ . For clarity the data have been offset from each other in causing  $J_d$  to be in arbitrary units.

The absorber layer of the detectors has a band gap of approximately  $100$  meV. The activation energies of all the detectors measured in Fig. 4.23 are around 50% of this band gap, indicating that the detectors are dominated by generation-recombination (GR) based dark current mechanisms. This supports the theory that the high dark current is due to an unintentional depletion region caused by a lack of doping control.

#### 4.3.4 Optical device results

Once the devices have been electrically characterised, the next step is to characterise their optical properties in order to achieve a final detectivity value for each detector. The spectral response curve of the detectors was measured using a Bruker Vertex 70 FTIR calibrated using a combination of both Vigo PVMI-2TE MCT and Bruker DLTGS reference detectors. A 550K blackbody source synced to a chopper and a lock-in amplifier was then used to calibrate the absolute responsivity values, as shown in Fig. 4.24.

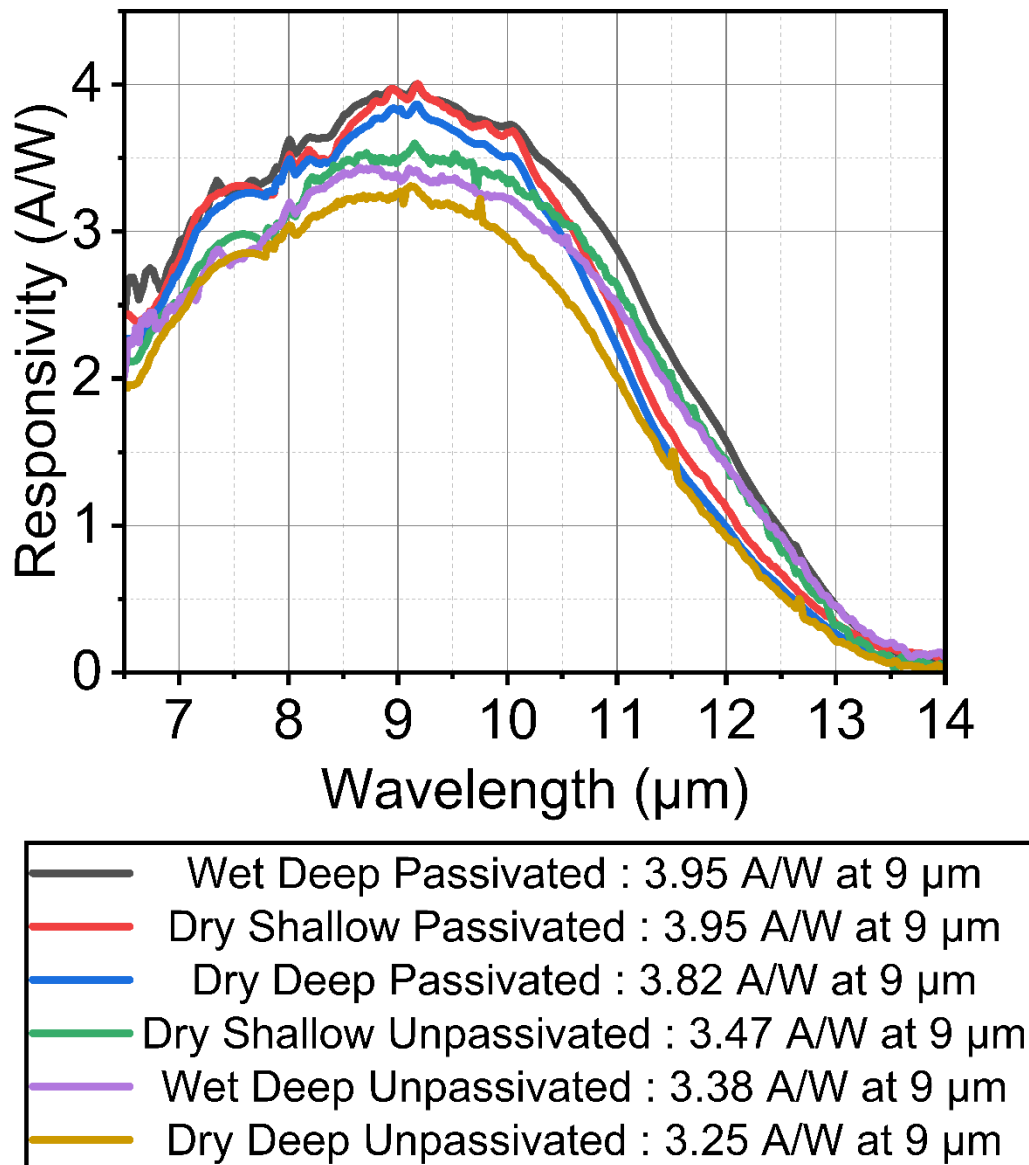


**Fig. 4.24.** Plot of responsivity against wavelength for the six different fabrication methods of the InAs/GaSb T2SL LWIR detector.

The 100% cutoff wavelength of these detectors is defined as the wavelength where responsivity reaches zero, which occurs at approximately 13.5 μm for all detectors. There is a noticeable difference in the rate at which responsivity drops between the 10 and 13 μm wavelengths, leading to a variation in the 50% cutoff wavelength, which ranges from 11 to 11.5 μm. However, it is challenging to identify any consistent pattern in this variation.

Generally, the 50% cutoff wavelength is lower for the dry deep devices, but without additional data, this observation is difficult to confirm and may be attributed to device-to-device variation.

From the responsivity, the EQE was calculated using equation 2.10, as shown in Fig. 4.25.

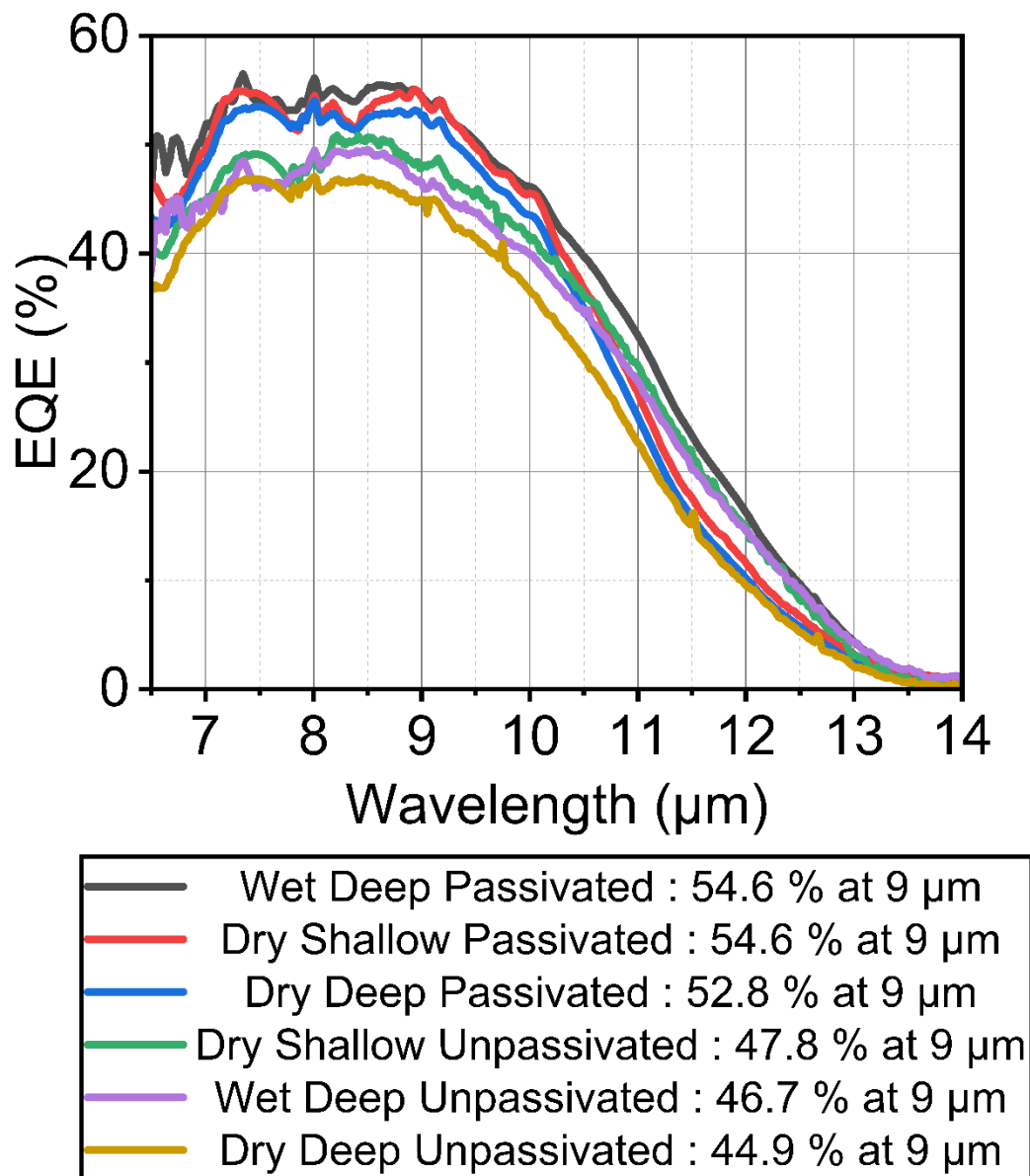


**Fig. 4.25.** Plot of EQE against wavelength for the six different fabrication methods of the InAs/GaSb T2SL LWIR detector.

The EQE for these detectors is above the current state of the art for LWIR T2SLs detectors, as shown in Fig. 4.26.

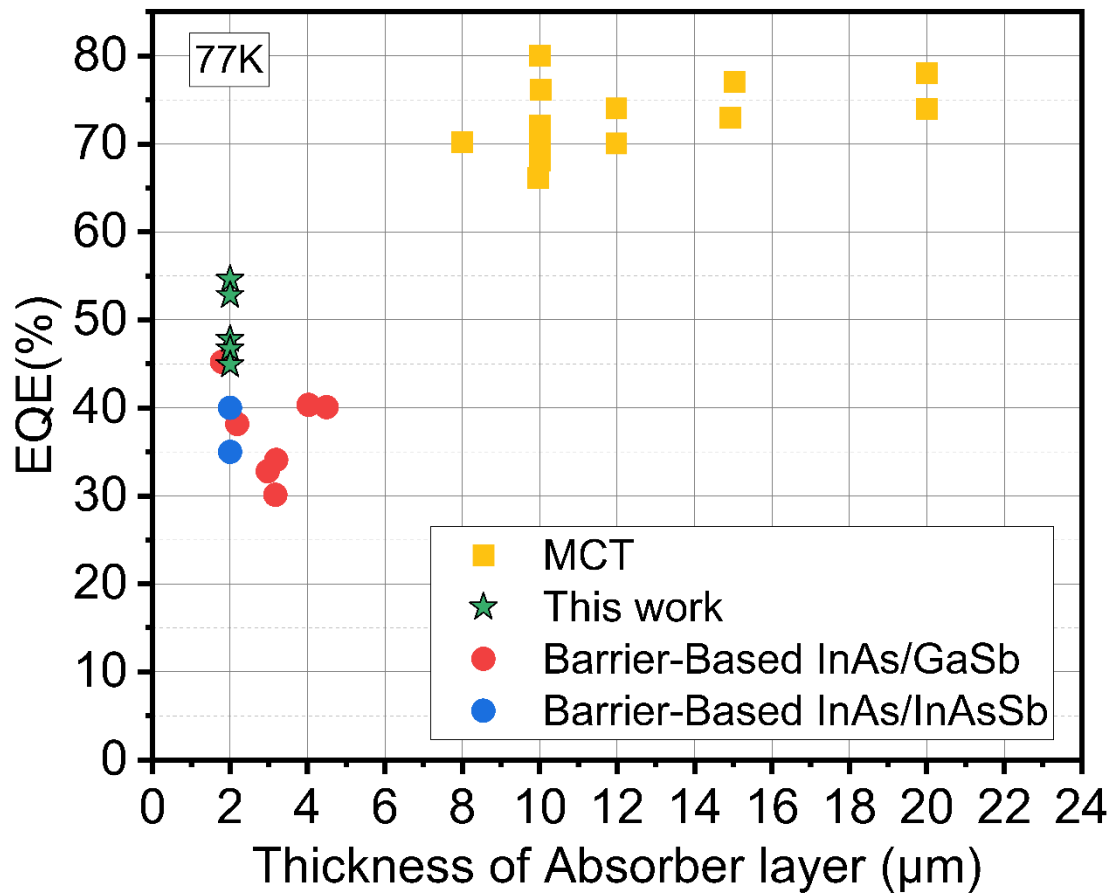


**Fig. 4.26.** Comparison of the EQE in this work compared to the values in literature for MCT [2,3,150,151], Barrier-Based InAs/GaSb [9–12,120,152] and Barrier-Based InAs/InAsSb LWIR detectors [141,153].

The high EQE observed in this work supports the theory that a depletion region has formed within the nBn structure, resulting in increased dark current density and EQE. To determine if the increase in EQE justifies the higher dark current, the detectivity of the detectors must be calculated. The detectivity will help quantify the overall performance of the detectors.

The detectivity of each detector was then calculated using the responsivity, dark current density and resistance area product using equation 2.11, and is shown in Fig. 4.27.

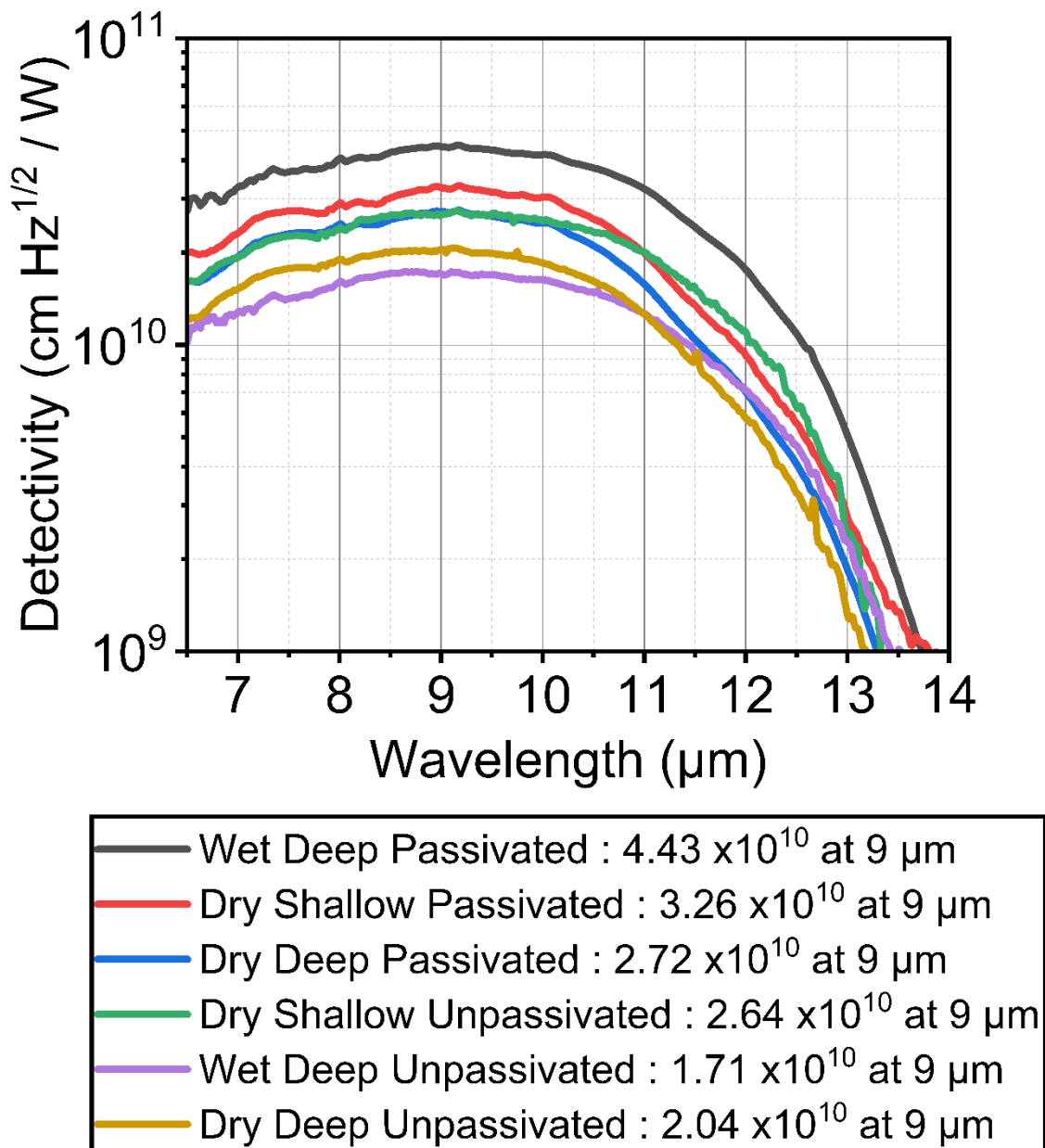


**Fig. 4.27.** Plot of detectivity against wavelength for the six different fabrication methods of the InAs/GaSb T2SL LWIR detector.

The detectivity of these detectors was then compared to the current state of the art, as shown in Fig. 4.28.

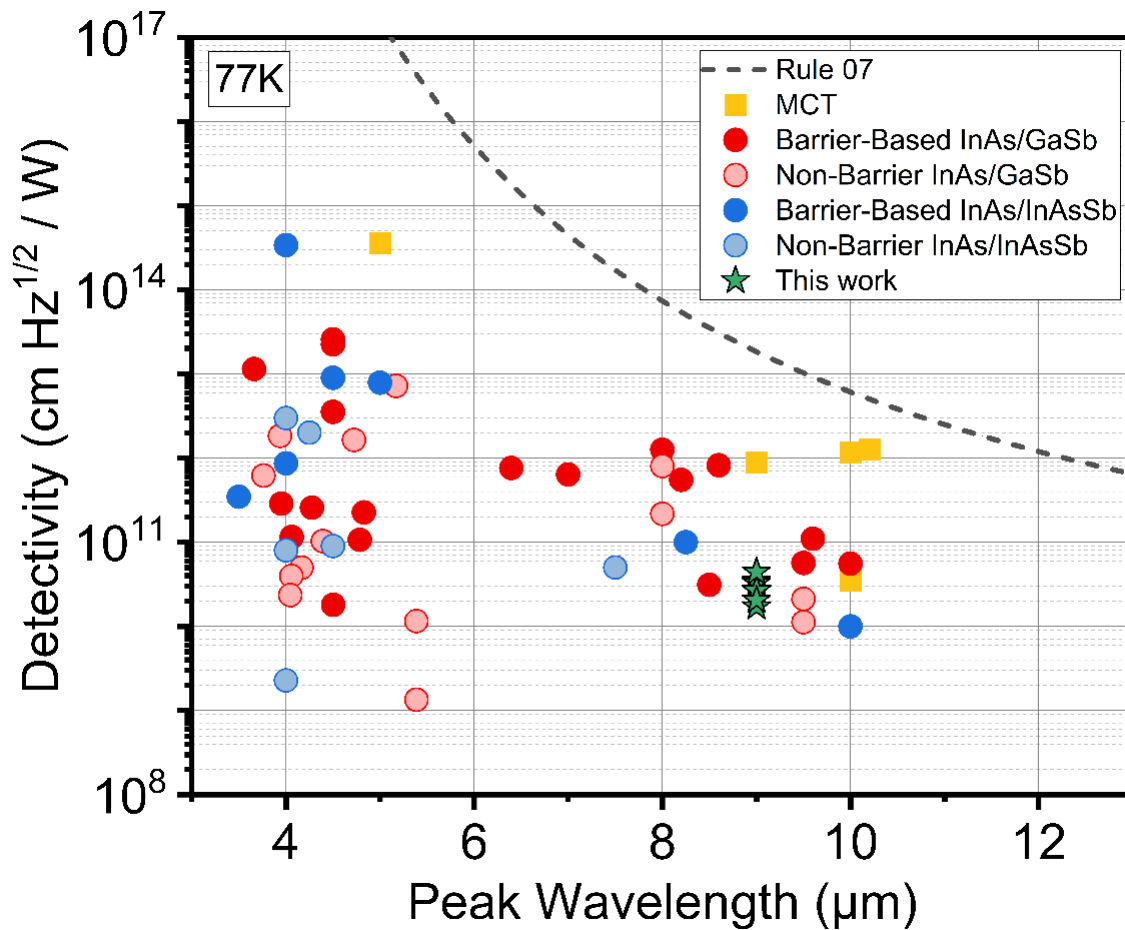


**Fig. 4.28.** Comparison of the detectivities in this work compared to the values in literature for MCT [2,3], Barrier-based InAs/GaSb [4–19], Non-Barrier InAs/GaSb [9,12,17,20–26], Barrier-Based InAs/InAsSb [27–31] and Non-Barrier InAs/InAsSb detectors [32–37]. The “Rule 07” line is added as a reference and is calculated from the rule 07 dark current density line with the QE of the MCT detectors assumed to be 75%.

The detectivities of the devices in this work are approximately one order of magnitude lower than the current state-of-the-art shallow etched T2SL single pixel performance [15]. However, if the aim is to create a FPA with a high pixel density via MOCVD, the isolation of shallow etch is not currently sufficient [72] and so deep etching is required. The peak detectivity of  $4.43 \times 10^{10}$  cm Hz<sup>1/2</sup>/W at 9 μm is very comparable to deep etched detectors grown by MBE at similar cutoff wavelengths [19,26]. This detectivity shows that this MOCVD technique can be used as a reasonable alternative to the currently more established MBE growth of InAs/GaSb T2SLs for LWIR FPA detectors.

The relatively low detectivity is attributed to the high dark current densities shown in Fig. 4.22. The lack of control over the doping of the barrier and absorber layers appears to be responsible for the high dark current density and, consequently, the lower detectivity. Adjusting the doping to align the concentrations could significantly reduce the dark current density. Previous studies have shown that reducing a doping mismatch by one order of magnitude to a matched absorber and barrier can decrease dark current density by two orders of magnitude [123]. If the dark current density could be improved by just one order of magnitude through better alignment of the doping levels, even if the EQE were halved, the detectivity of these detectors would be comparable to the current state-of-the-art, around  $2 \times 10^{11}$  cm Hz<sup>1/2</sup> / W. The simplest way to achieve this alignment is by adding light n-doping to the barrier layer.

Since the InAs layer thickness is greater in the absorber than in the barrier, the absorber should naturally be more n-type. By slightly n-doping the barrier, the doping concentrations between the barrier and the absorber should be more closely aligned. This growth was performed with comparable quality to the device samples discussed in this chapter. Unfortunately, due to time constraints this intentionally doped device structure could not be fabricated or tested as a device.

## 4.4 Summary

The growth temperature, GaSb V/III ratio, and InAs V/III ratio were all investigated to enable the growth of InAs/GaSb T2SLs with surface roughness less than 0.2 nm RMS, all lattice-matched to InAs substrates. Surface roughness and morphology were found to be highly sensitive to changes in both growth temperature and GaSb V/III ratio. In this work the temperature and GaSb V/III ratio which gave the best InAs/GaSb T2SLs were 510°C and 1.5.

Growth temperature also influenced the lattice match, as the formation of “GaAs-like” interfaces was temperature-dependent, with higher temperatures creating more “GaAs-like” interfaces. The GaSb V/III ratio had a minor effect on the lattice match, with higher ratios correlating with less “GaAs-like” interfaces. The InAs V/III ratio did not affect surface morphology but significantly impacted the lattice match, with higher As flow resulting in more “GaAs-like” interfaces.

By controlling the As flow, it was possible to grow InAs/GaSb T2SLs lattice-matched to InAs substrates using “GaAs-like” interfacial layers via MOCVD. The wavelength of the InAs/GaSb T2SL can be tuned by adjusting the InAs layer thickness. This technique demonstrated that it is possible to grow InAs/GaSb T2SLs with wavelengths ranging from 4.5 to 12  $\mu\text{m}$  under the same interface growth conditions. This eliminates the need for interfacial recalibration when changing wavelengths, simplifying the growth design workflow compared to MBE.

The T2SLs were fabricated into nBn detectors with a 100% cutoff at 13.5  $\mu\text{m}$ . Six different devices were created using varied fabrication steps, investigating three parameters: passivated vs. unpassivated, deep vs. shallow etching, and wet vs. dry etching. AZ3027 was used as the surface passivation layer, successfully reducing surface-related dark currents by up to 92% for the deep dry etched detector.

After demonstrating the effectiveness of surface passivation, shallow etched devices were fabricated to compare their performance with deep etched devices. The shallow etched devices exhibited lower dark current densities than the deep etched devices, and surface passivation remained beneficial for these shallow devices. Although the shallow detectors outperformed the deep detectors, a trade-off exists between dark current reduction and detector density within a FPA.

Shallow detectors need to be spaced two lateral diffusion lengths apart to prevent crosstalk. The lateral diffusion length for the shallow etched devices was found to be 70  $\mu\text{m}$ , which significantly limits potential pixel density. Typically, the spacing between pixels in an FPA is less than 10  $\mu\text{m}$ . A lateral diffusion length of 70  $\mu\text{m}$  implies a minimum spacing of 140  $\mu\text{m}$  between these shallow pixels, which is much higher than current FPAs. Due to this pixel spacing issue and the effectiveness of the surface passivation layer in reducing the sidewall dark current of deep pixels, the deep etched pixels in this work were considered superior to the shallow etched pixels for FPA applications.

The final fabrication parameter investigated was the etching mechanism, comparing dry vs. wet etching. The wet etched devices exhibited lower dark current densities than the dry etched devices. The passivated wet etched device had a dark current density of  $2.2 \times 10^{-2} \text{ A cm}^{-2}$ , the lowest among all the devices in this study. However, this dark current density is still relatively high compared to current state-of-the-art detectors. The high dark current density appears to be caused by the formation of a depletion region within the nBn structure due to the lack of doping control in the barrier and absorber regions.

The devices were then characterised optically. The peak EQE of the detectors ranged from 54.4 to 44.9% which is exceptionally high for this wavelength when compared to similar devices. This high EQE correlates with the depletion region formation theory that caused the high dark current density.

The best performance was observed in the wet deep passivated detector with a peak detectivity of  $4.43 \times 10^{10} \text{ cm Hz}^{1/2}/\text{W}$  at  $9 \mu\text{m}$ . This detectivity is very comparable to deep etched detectors grown by MBE at similar cutoff wavelengths. This demonstrates that the MOCVD technique can serve as a viable alternative to the more established MBE growth method for InAs/GaSb T2SLs in LWIR FPA detectors.

# MWIR detectors made from InAs/InAsSb T2SLs

## 5.1 Introduction

Mid-Wavelength Infrared (MWIR) detectors are used in a variety of fields, including optical gas sensors for pollution monitoring and industrial process control, medical diagnostics, and significant defence and security applications such as night vision and missile warning systems [50].

Antimony (Sb) based type-II superlattice (T2SL) materials are a strong candidate for next generation infrared technologies and are now becoming a viable alternative to the state of the art mercury cadmium telluride (MCT) [54]. The Type-II band alignment of the T2SL gives the material system its flexible band gap engineering capability, allowing for a widely tuneable bandgap. The T2SL structure is also responsible for the suppression of band-to-band tunnelling, Auger recombination and Shockley-Read-Hall recombination which make up a large proportion of the dark current in MCT [55]. The other major advantage of the T2SL when compared to MCT is in its growth uniformity. The ability to use standard III-V growth techniques such as molecular beam epitaxy (MBE) and metal-organic chemical vapour deposition (MOCVD) to grow material with good uniformity is a significant advantage for the T2SL when compared to MCT.

There are two main candidates for the Sb based T2SL; the InAs/GaSb T2SL and the InAs/InAsSb T2SL. Historically the focus has been on the InAs/GaSb T2SL due to its larger optical absorption and larger wavelength range [56]. However, more recently the Ga-free InAs/InAsSb T2SL has emerged as a promising new candidate for MWIR detectors due to its longer minority carrier lifetime [57] and higher defect tolerance [58].

Historically, MBE has been the dominant method for growing Sb-containing structures [59–61]. However, MOCVD presents a highly attractive commercial potential, provided that material and device performance can match MBE results [47].

As shown in chapter 4, standard MOCVD growth of InAs/GaSb T2SLs is largely hindered by the volatility of InSb used for strain balancing to GaSb substrates [199]. This challenge is conveniently circumvented in Ga-free structures as they do not require extra interfacial strain balancing layers in order to lattice match to their native GaSb substrates.

The big challenge for the MOCVD growth of InAs/InAsSb T2SL is the lack of an easy non-AlSb based electron barrier layer. Unfortunately, the same technique used for InAs/GaSb cannot be used in InAs/InAsSb as the layer thickness required to provide a big enough barrier would greatly reduce the wavefunction overlap. For this reason, MOCVD grown InAs/InAsSb T2SL detectors are confined to non-barrier-based architectures such as the PIN detector. This lack of a barrier does restrict potential dark current performance of MOCVD grown InAs/InAsSb T2SL detectors, but for MWIR detectors this is less of an issue than in the LWIR where dark current is naturally high.

Many of the same growth challenges exist for the InAs/InAsSb T2SL as the InAs/GaSb T2SL. The InAs/InAsSb T2SL is very sensitive to growth parameters such as temperature and InAs V/III ratio making recipe development difficult. The main challenge specific to the MOCVD growth of the InAs/InAsSb T2SL is the volatility of the Sb within the InAsSb. Extremely low growth temperatures for MOCVD are therefore required to maintain a high enough Sb incorporation. The Sb volatility can also cause the Sb to segregate throughout the T2SL instead of staying within the desired InAsSb layers. This segregation can weaken the quantum confinement of the T2SL and reduce the quantum efficiency of the detector. Therefore, sharp interfaces between the InAs and InAsSb are required to produce high performance detectors.

This chapter describes the growth, fabrication and characterisation of MOCVD grown InAs/InAsSb T2SL LWIR detectors.

## 5.2 Growth of InAs/InAsSb T2SLs

The first step in developing InAs/InAsSb T2SL detectors is the investigation of the growth parameters. The goal of this investigation is to grow a T2SL which is lattice matched to a GaSb substrate, and which has an average root mean square (RMS) surface roughness of less than 0.3 nm with no visible surface defects with an optical microscope.

The lattice mismatch was examined using an omega-2 theta XRD scan. This mismatch is defined as the distance in arcseconds between the substrate peak and the central T2SL peak in the omega-2 theta scan. In this scan, a positive lattice mismatch occurs when the T2SL peak appears to the right of the GaSb peak, indicating a smaller lattice constant. Conversely, a negative lattice mismatch is when the T2SL peak appears to the left of the GaSb peak, indicating a larger lattice constant. If the T2SL and GaSb peaks overlap, resulting in zero lattice mismatch, the T2SL is considered lattice-matched to the substrate. The full width at half maximum (FWHM) of the first satellite peak in an XRD omega 2 theta scan was used as a measure of interface quality. The aim was to have a FWHM value of less than 40 arcsecs which would be comparable with MBE results. AFM was employed to quantify surface roughness and investigate surface morphology.

The MOCVD growth was performed in an Aixtron Close Coupled Showerhead reactor. The precursors used were trimethylindium (TMIn), tertiarybutylarsine (TBAs), triethylgallium (TEGa), triethylantimony (TESb), disilane ( $\text{Si}_2\text{H}_6$ ) and diethylzinc (DEZn), with hydrogen used as the carrier gas. The device structure was grown on a 2-inch n-doped GaSb (001) substrate, with the reactor pressure kept at 100 mbar. The main growth parameters investigated in this work were the growth temperature, InAs V/III ratio, As to Sb ratio in the InAsSb and growth interruptions. The standard test structure used to investigate the growth parameters was a 50-period InAs/InAs<sub>72</sub>Sb<sub>28</sub> T2SL.

The InAs layer thickness was 17 ML and the InAsSb layer thickness was 8 ML resulting in a band gap of around 0.28eV corresponding to a wavelength of 4.5 $\mu\text{m}$ . An example growth timeline of the InAs/InAsSb T2SL is shown in, Fig. 5.1.

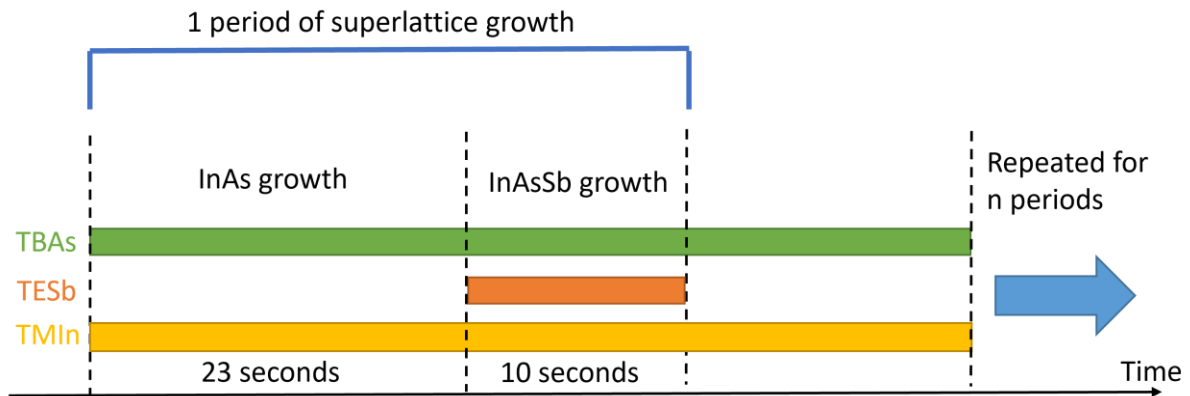


**Fig. 5.1.** MOCVD growth timeline of one period of the InAs/InAsSb T2SL with the additional growth interruption steps.

### 5.2.1 Growth temperature

The InAs/InAsSb T2SL is very sensitive to growth temperature due to the volatility of the Sb within the InAsSb. This volatility requires growth at very low temperatures for MOCVD to ensure a high enough Sb incorporation within the InAsSb. The Sb incorporation is important to both lattice match the T2SL to its substrate and to ensure the T2SL bandgap is as intended. As shown in Fig. 5.2, the surface roughness and morphology of the InAs/InAsSb T2SL is very sensitive to the surface temperature during growth. Increasing the growth temperature beyond 460°C led to an increase in surface roughness and a move from a more step flow like morphology to a more amorphous and hillock like surface morphology. Growth temperatures this low are non-standard for industrial MOCVD processes and so could face some pushback from some parts of the industry as they are not used to working with temperatures this low. Unfortunately, the temperature requirements appear to be unavoidable, and this work shows that the growth is completely possible using an industrially relevant reactor. It is not yet clear if these low temperatures will cause problems scaling the growth to larger planetary reactors and that is something that will need to be investigated separately.

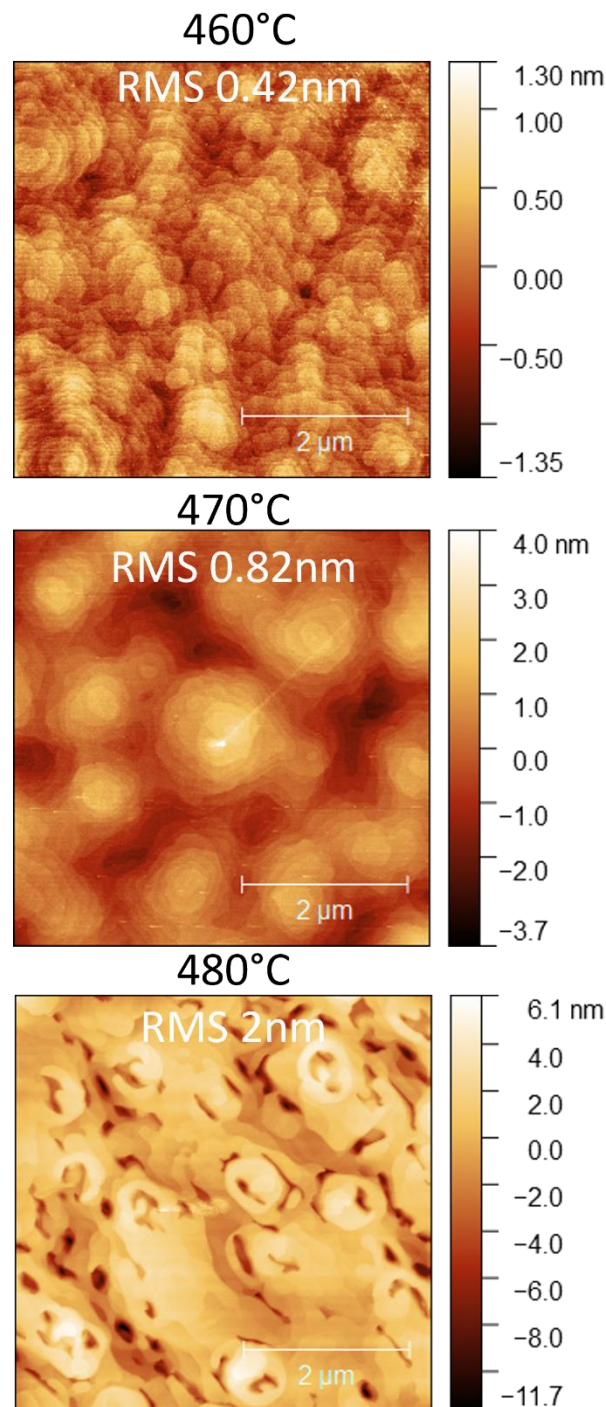


**Fig. 5.2.** AFM surface scans of 50 period 17ML/8ML InAs/InAsSb T2SLs grown at three different surface temperatures.

The surface temperature also affected the lattice constant of the T2SL. This can be explained by the temperature dependence of the Sb incorporation within the InAsSb layers. XRD simulation was used to calculate the InAs and InAsSb layer thicknesses as well as the InAsSb composition from the peak positions in the Omega 2 Theta XRD scans. The InAs and InAsSb layer thicknesses were 17ML/8ML as intended. As shown in Fig. 5.3, as the surface temperature increases, the percentage of Sb compared to As within the InAsSb layers decreased.

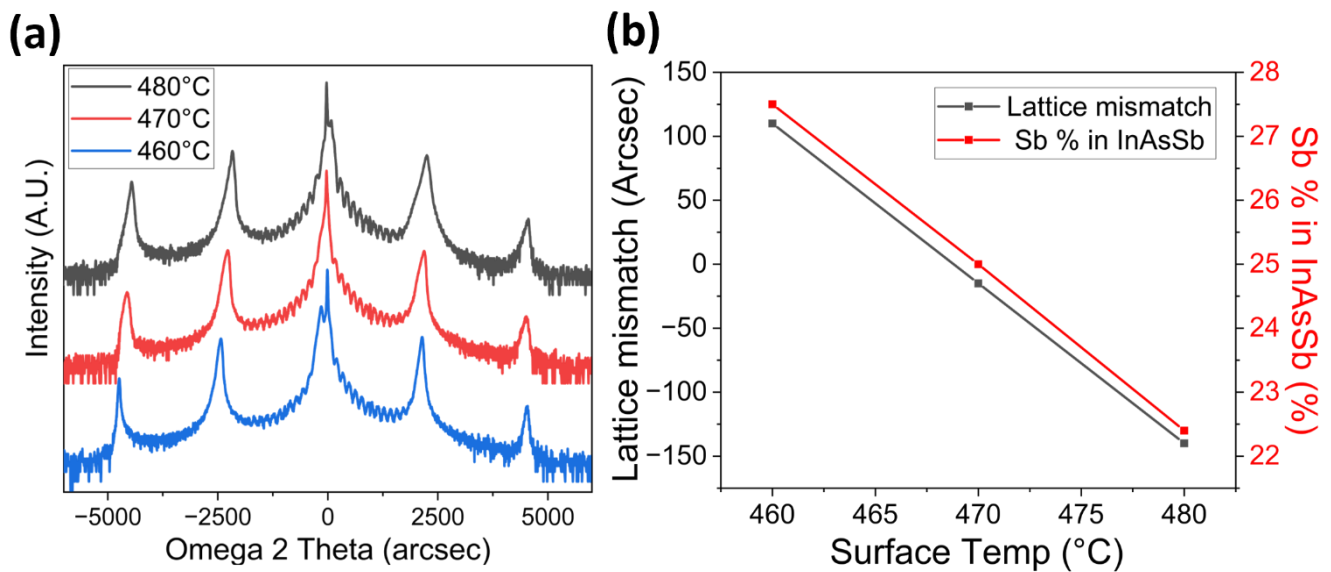


**Fig. 5.3.** (a) Omega 2 Theta XRD scans of 50 period 17ML/8ML InAs/InAsSb T2SLs grown at three different surface temperatures. (b) Plot showing how the lattice mismatch and the Sb incorporation of the InAs/InAsSb T2SLs changes with surface temperature.

In order to keep the improved surface from the reduced temperature, whilst maintaining lattice match and 28% Sb, the Sb flow must be adjusted. For the samples in Fig. 5.2, the Sb to As gas flow ratio was 30%. This ratio was decreased to 28% resulting in an incorporation of 28% at 460°C, as shown in Fig. 5.4.

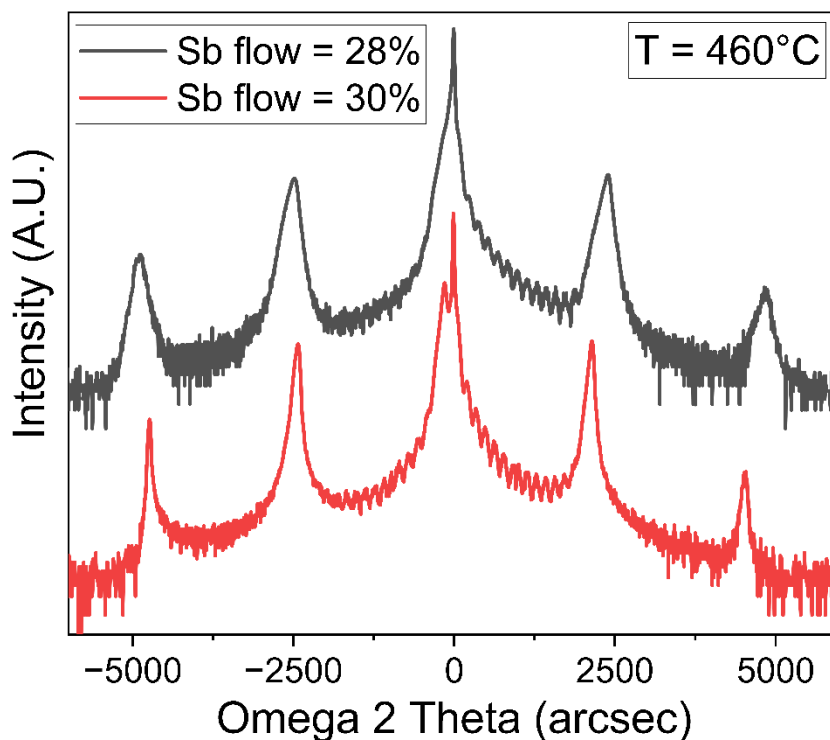


**Fig. 5.4.** Omega 2 Theta XRD scans of 50 period 17ML/8ML InAs/InAsSb T2SLs grown at 460°C with different Sb to As gas flow ratios.

### 5.2.2 Growth Interruption

Now that InAs/InAsSb T2SL could be grown lattice matched to the GaSb substrate with the correct InAsSb composition, the next step is to improve the surface roughness and interface quality. The first satellite peaks FWHM of the omega 2 theta scans shown in Figs. 5.3 and 5.4 are all greater than 100 arcsec implying that interfaces within the T2SL are not very sharp. It is likely that the surface roughness is caused by these rough interfaces and so improving the sharpness of the interfaces within the T2SL should also reduce the surface roughness. To improve interfacial quality, a growth interruption step was introduced between the T2SL layers, as shown in Fig. 5.5.

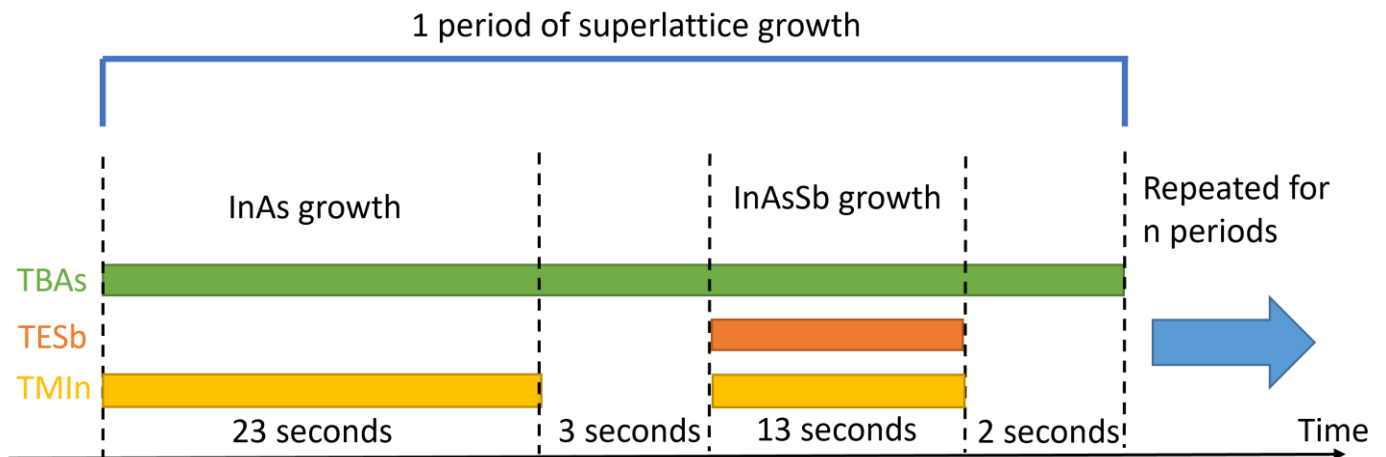


**Fig. 5.5.** MOCVD growth timeline of one period of the InAs/InAsSb T2SL with the additional growth interruption steps.

The growth interruption was successfully implemented and was able to drastically reduce the FWHM of the first satellite peak from 134 to 38 arcsecs, as shown in Fig. 5.6. This new lower FWHM is very comparable with MBE grown InAs/InAsSb T2SL showing that MOCVD is able to achieve similar interface quality as MBE.

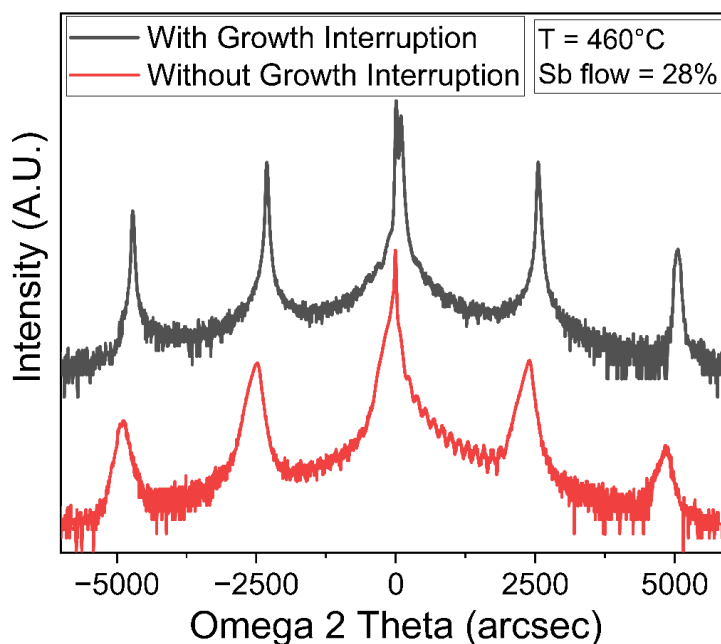


**Fig. 5.6.** Omega 2 Theta XRD scans of 50 period 17ML/8ML InAs/InAsSb T2SLs grown at 460°C with and without growth interruption.

Interestingly, the growth interruption step slightly decreased Sb incorporation within the InAsSb layer. This decrease appears to be due to the volatility of Sb in the InAsSb layer. During the growth interruption following InAsSb growth, only As is supplied, suggesting an As-for-Sb exchange that reduces Sb composition. To compensate, the Sb flow was slightly increased during InAsSb growth for the device samples.

As well as improving the FWHM of the first satellite peak, the growth interruption was able to reduce the surface RMS roughness from 0.42 to 0.25 nm, as shown in Fig. 5.7.

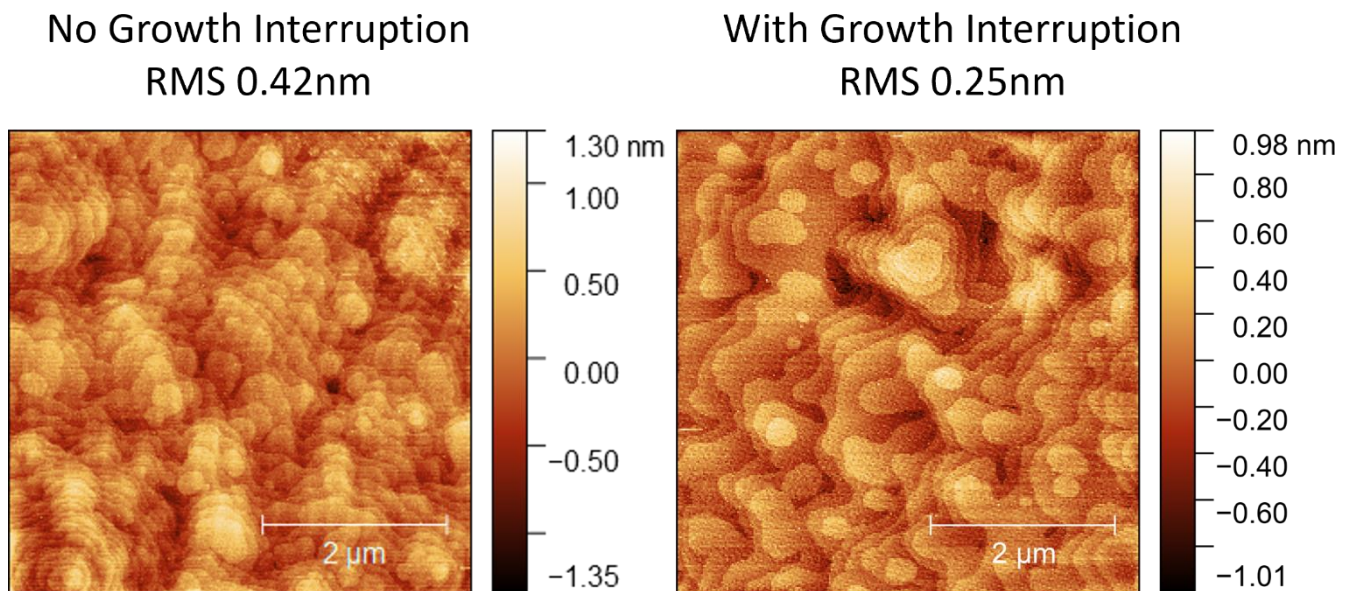


**Fig. 5.7.** AFM surface scans of 50 period 17ML/8ML InAs/InAsSb T2SLs grown with and without growth interruptions.

By combining low growth temperature with growth interruption steps, InAs/InAsSb T2SLs were successfully grown lattice-matched to GaSb, exhibiting low surface roughness and sharp interfaces. This further supports the viability of MOCVD as an alternative to MBE for producing high-quality InAs/InAsSb T2SLs.

### 5.2.3 Optical Properties of the T2SL

Once the physical properties of the InAs/InAsSb T2SLs were investigated, the optical properties were investigated. Both the samples with and without the growth interruption were investigated using FTIR PL, as shown in Fig. 5.8.

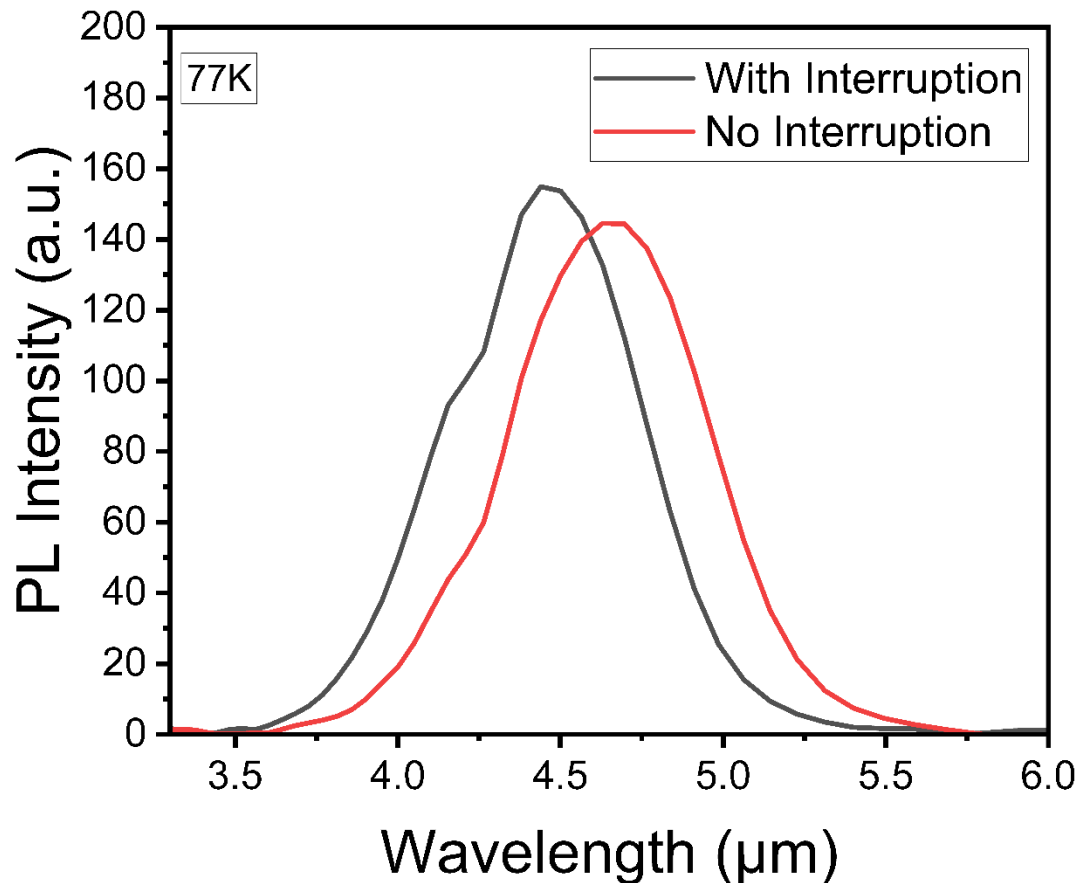
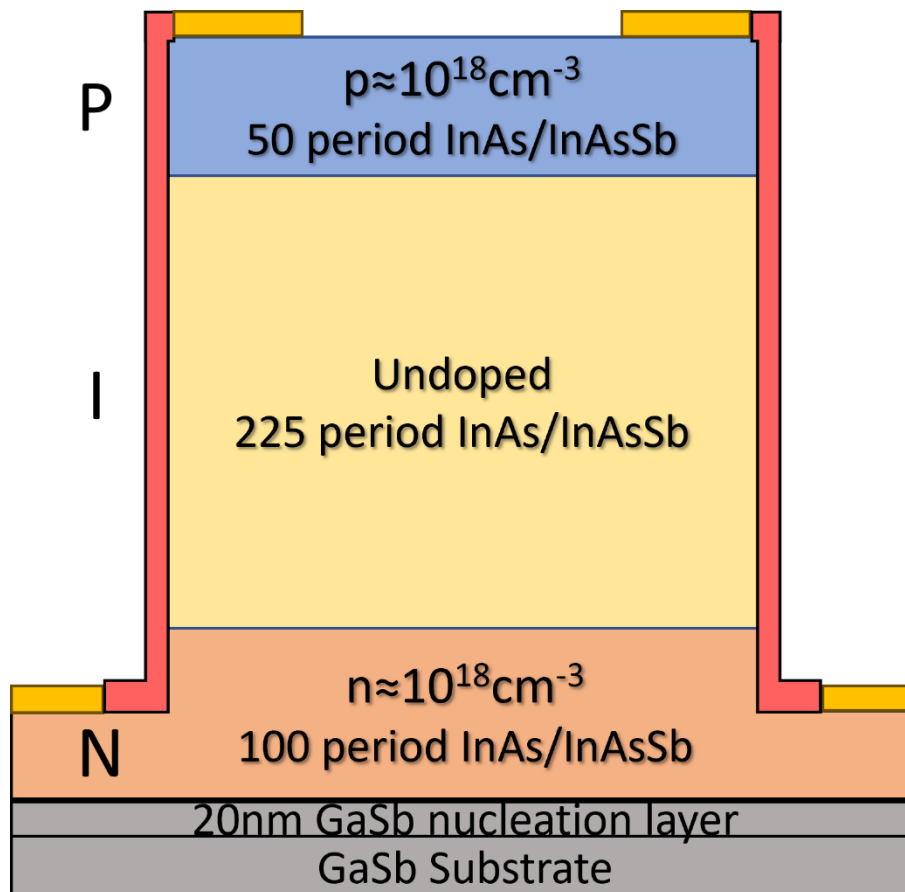


**Fig. 5.8.** Photoluminescence plot of 50 period 17ML/8ML InAs/InAsSb T2SLs grown at 460°C with and without growth interruption.

The sample with growth interruptions exhibits a slight blue shift compared to the sample without growth interruptions. Specifically, the peak wavelength of the sample with growth interruptions is 4.4 μm, while the peak wavelength of the sample without growth interruptions is 4.6 μm. This wavelength shift can be attributed to the previously discussed changes in Sb incorporation. Additionally, the sample with growth interruptions shows a slight increase in PL intensity and a decrease in FWHM from 38 meV to 34 meV, indicating higher interface quality.

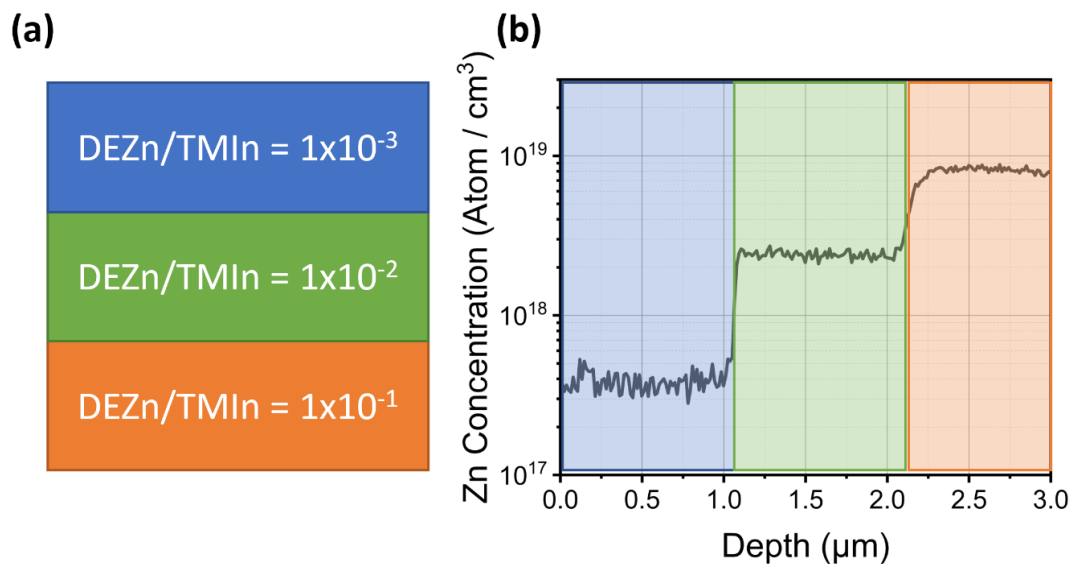
### 5.2.4 InAs/InAsSb device growth

Now that InAs/InAsSb T2SLs can be grown lattice-matched to GaSb substrates with low surface roughness and high interface quality, the next step is to design and grow an InAs/InAsSb T2SL device structure. Due to the previously mentioned restrictions regarding the MOCVD growth of AlSb, the designed structure was a PIN diode. The PIN structure consisted of a 100 period, 660 nm n-type ( $n \approx 10^{18} \text{ cm}^{-3}$ ) bottom contact layer followed by a 225 period, 1500 nm un-doped I region, topped with a 50 period, 330 nm p-type ( $p \approx 10^{18} \text{ cm}^{-3}$ ) top contact layer as shown in Fig. 5.9.



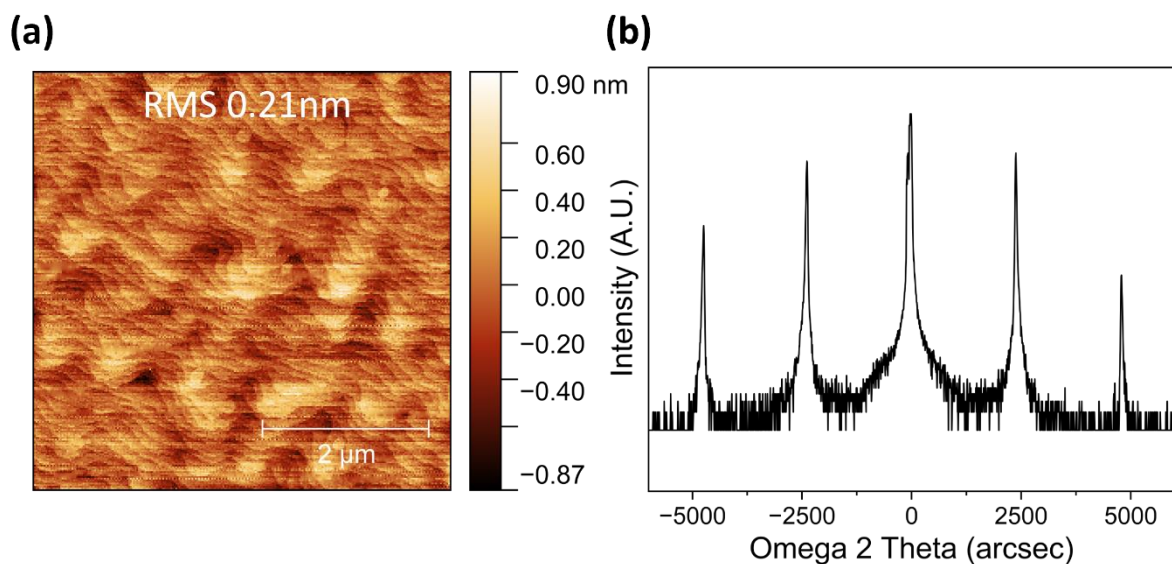
**Fig. 5.9.** Schematic diagram of the InAs/InAsSb T2SL PIN detector.

In order to grow this PIN structure, doping calibrations were needed. To simplify the doping in the T2SL, only the InAs layers were doped. Since Fig. 4.13 was able to calibrate  $\text{Si}_2\text{H}_6$  n-doping of InAs, only the p-type doping calibration of DEZn into InAs was needed to grow the whole structure. Another structure consisting of three InAs layers each with a different ratio of DEZn to TMIIn was grown and secondary ion mass spectrometry (SIMS) was used to calibrate the Si incorporation, as shown in Fig. 5.10. It is worth noting that SIMS gives the total dopant concentration, not the amount of electrically active dopant. In order to quantify the electrically active doping concentrations in the PIN devices a capacitance voltage measurement needs to be taken. Unfortunately, due to time constraints, it was not possible to take this capacitance voltage measurement and so the actual electrically active dopant levels are unknown in these devices.



**Fig. 5.10.** (a) Schematic diagram of the staircase doping calibration of Zn into bulk InAs. (b) SIMS data from the doping calibration sample. The ratio of the flow of DEZn to TMIn was increased from  $1 \times 10^{-3}$  to  $1 \times 10^{-1}$  resulting in an increase of Si concentration from  $4 \times 10^{17}$  to  $8 \times 10^{18}$  Atoms / cm<sup>3</sup>.

Fig. 5.10 shows that in order to achieve a Zn concentration of  $10^{18}$  Atoms / cm<sup>3</sup>, the DEZn to TMIn ratio needs to be around  $1 \times 10^{-2}$ . Once the doping was calibrated, the device structure was grown and fabricated. AFM and XRD were then used to characterise the full device sample as shown in Fig. 5.11.



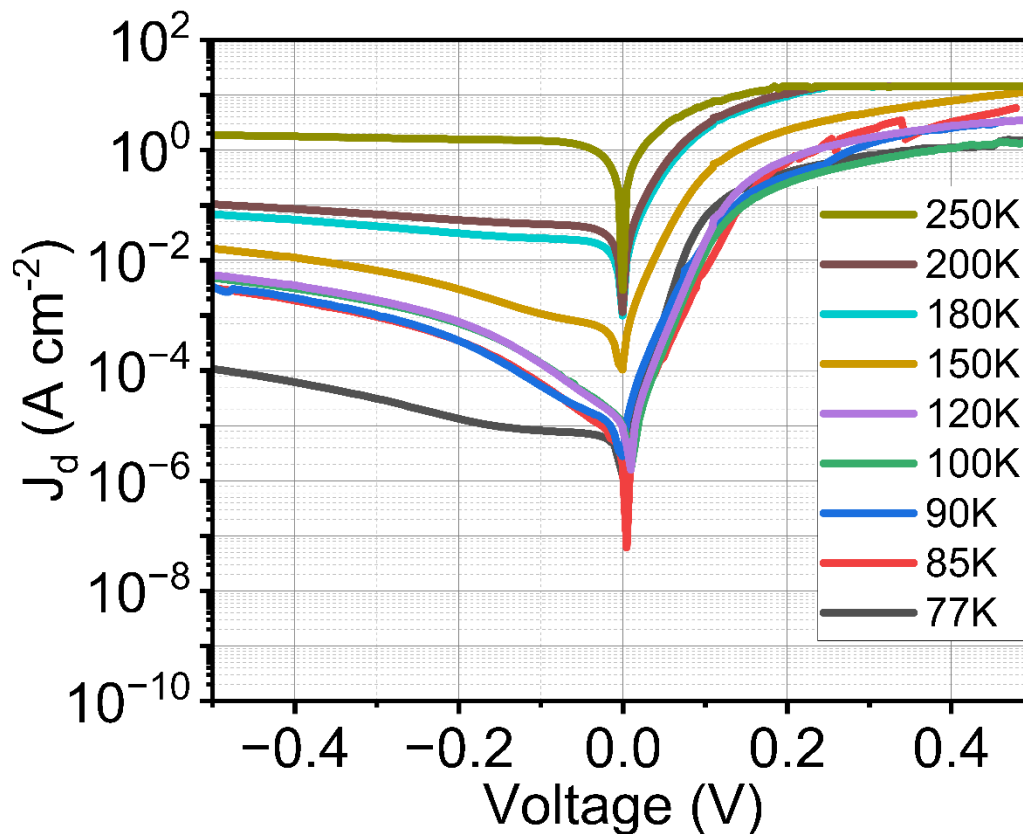
**Fig. 5.11.** (a) AFM surface scans of the full device sample. (b) Omega 2 Theta XRD scans of the full device sample.

Fig. 5.11 shows that the device sample was able to be successfully grown lattice matched to the GaSb substrate with a low surface RMS roughness of 0.21nm. The FWHM of the first satellite peak in Fig. 5.11b, is 22 arcsec showing that the interface quality remains high even when the sample thickness increases.

## 5.3 Device Results

### 5.3.1 Dark current

The fabrication of the PIN device followed the same fabrication process as the deep, wet etched and passivated InAs/GaSb nBn device in section 4.3.2. Once the PIN devices were fabricated, their dark current densities were taken, as shown in Fig. 5.12.



**Fig. 5.12.** Dark current density ( $J_d$ ) versus voltage for the InAs/InAsSb T2SL PIN detectors across a range of temperatures.

The operating voltage for these devices is -0.1V, so dark current density values were taken at -0.1V. The two main temperatures of interest for this device are at 77K and 150K which are generally regarded as the standard low operating temperature and the high operating temperature for devices of this type. At 77K the InAs/InAsSb PIN diode had a dark current density of  $7.9 \times 10^{-6} \text{ A/cm}^2$ . At 150K the InAs/InAsSb PIN diode had a dark current density of  $1.1 \times 10^{-3} \text{ A/cm}^2$ . Current state of the art dark current densities for MOCVD grown InAs/InAsSb non barrier detectors at this wavelength and bias are around  $5 \times 10^{-6} \text{ A/cm}^2$  at 77K [33] and  $1.5 \times 10^{-3} \text{ A/cm}^2$  at 150K [47]. The results in Fig. 5.12 are therefore very competitive with the comparable state of the art results. These results were also compared to all the different detector types available in literature, as seen in Fig. 5.13.

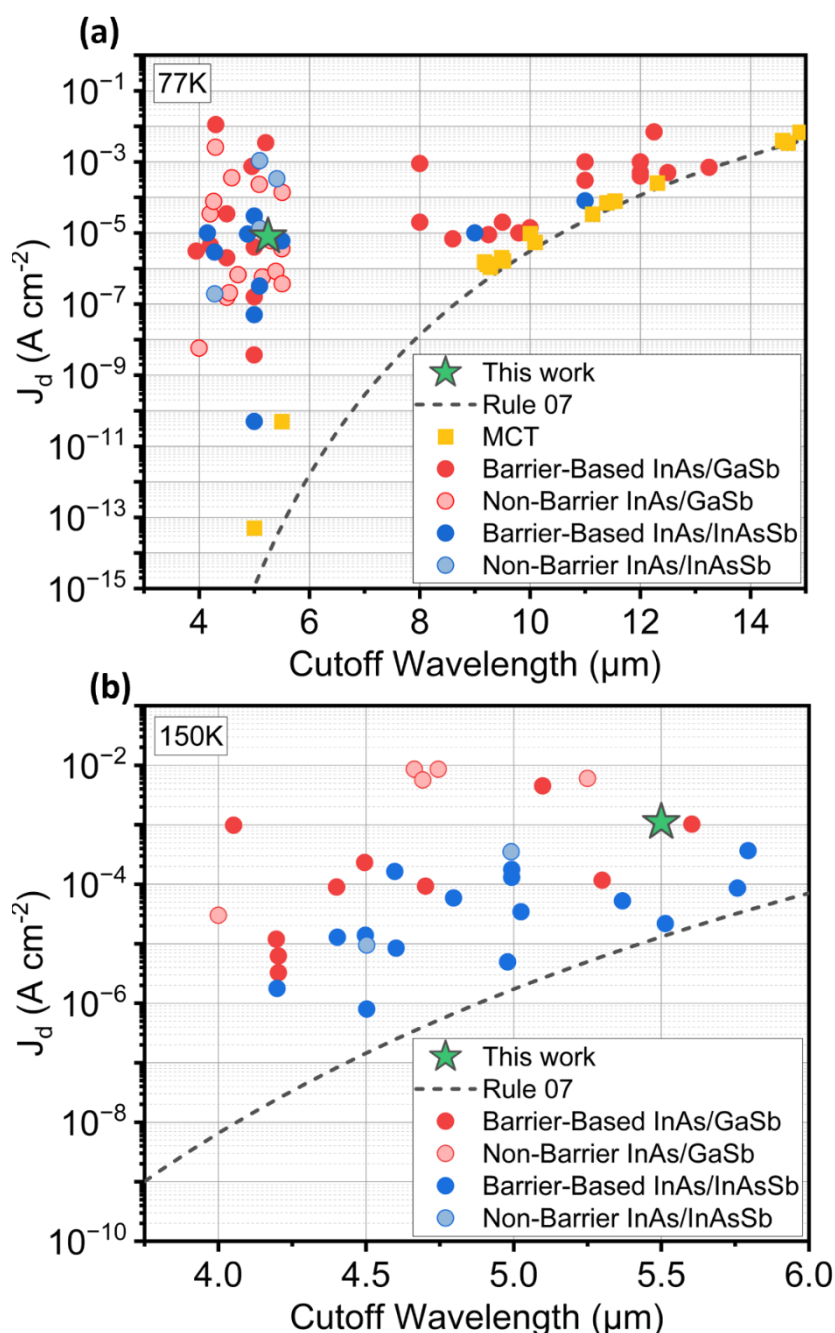


**Fig. 5.13.** Comparison of the dark current densities from the InAs/InAsSb PIN detector in this work compared to the values found in literature for Barrier-based InAs/GaSb [4–7,113,114,71,115,116,8,117–119,9,10,120,11–14,121,15,122,16,123,38], Non-Barrier InAs/GaSb [124,20,125–127,21,128,17,22,23,129–135,145], Barrier-Based InAs/InAsSb [136,27–29,40,42,137–139,30,140,141,146,39,41,43] and Non-Barrier InAs/InAsSb detectors [47,33,32,34,35,142,36]. To be compared with MCT detectors [143,144] and the “Rule 07” line [48]. At (a) 77K and (b) 150K.

The InAs/InAsSb PIN detectors in this work have very comparable dark current densities to current MWIR detectors at both 77 and 150K. This provides further evidence that MOCVD is a viable alternative to MBE when it comes to the growth of InAs/InAsSb T2SLs for MWIR detectors.

### 5.3.2 Optical device results

Once the devices were electrically characterised, the next step was to characterise their optical properties in order to achieve a final detectivity value for each detector. The spectral response curve of the detectors was measured in the same way as the InAs/GaSb detectors in section 4.3. The responsivity of the MWIR InAs/InAsSb PIN detectors at both 77K and 150K is shown in Fig. 5.14.

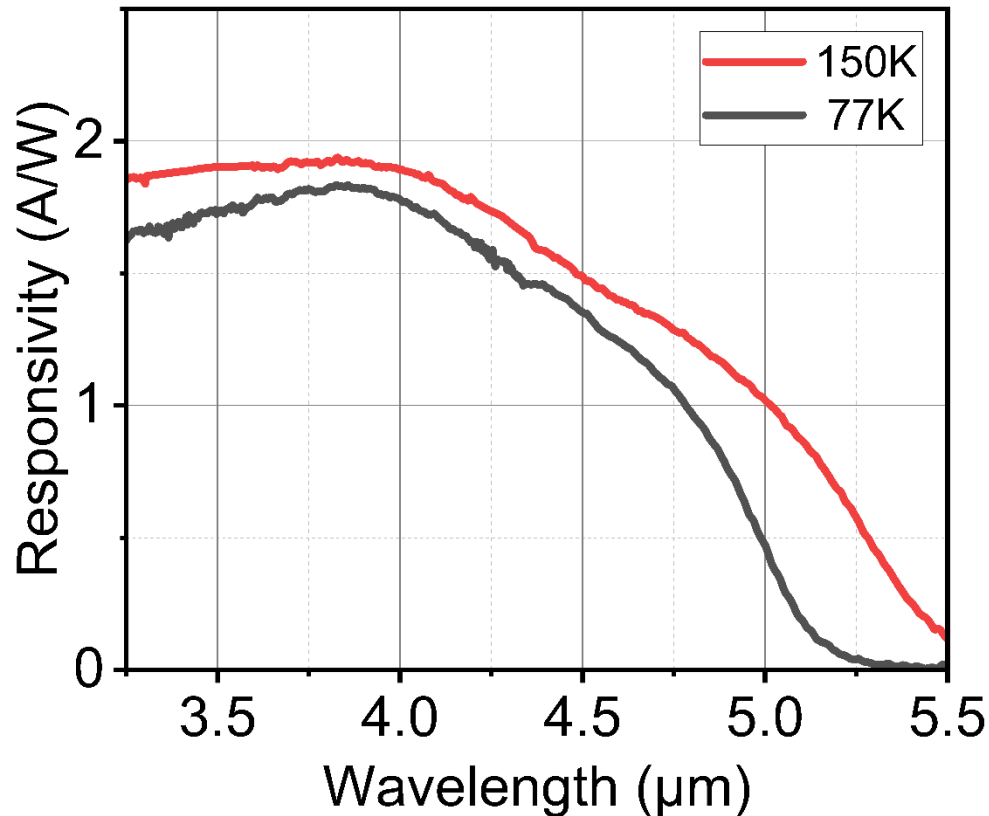


**Fig. 5.14.** Plot of responsivity against wavelength for the InAs/InAsSb PIN detector at 77 and 150K.

The peak responsivity for at both 77 and 150K occurred at 3.8 μm. The peak responsivity was 1.83 A/W at 77K and 1.94 A/W at 150K. This slight increase of responsivity with temperature has been observed previously on similar structures [33] and appears to be caused by the band gap narrowing at higher temperatures meaning that more of the incident photons from the broadband source are able to produce a photocurrent [200]. This bandgap narrowing also explains the increase in the 100% cutoff wavelength from 5.25 to 5.5 μm.

From the responsivity, the external quantum efficiency (EQE) was calculated using equation 2.10, as shown in Fig. 5.15.

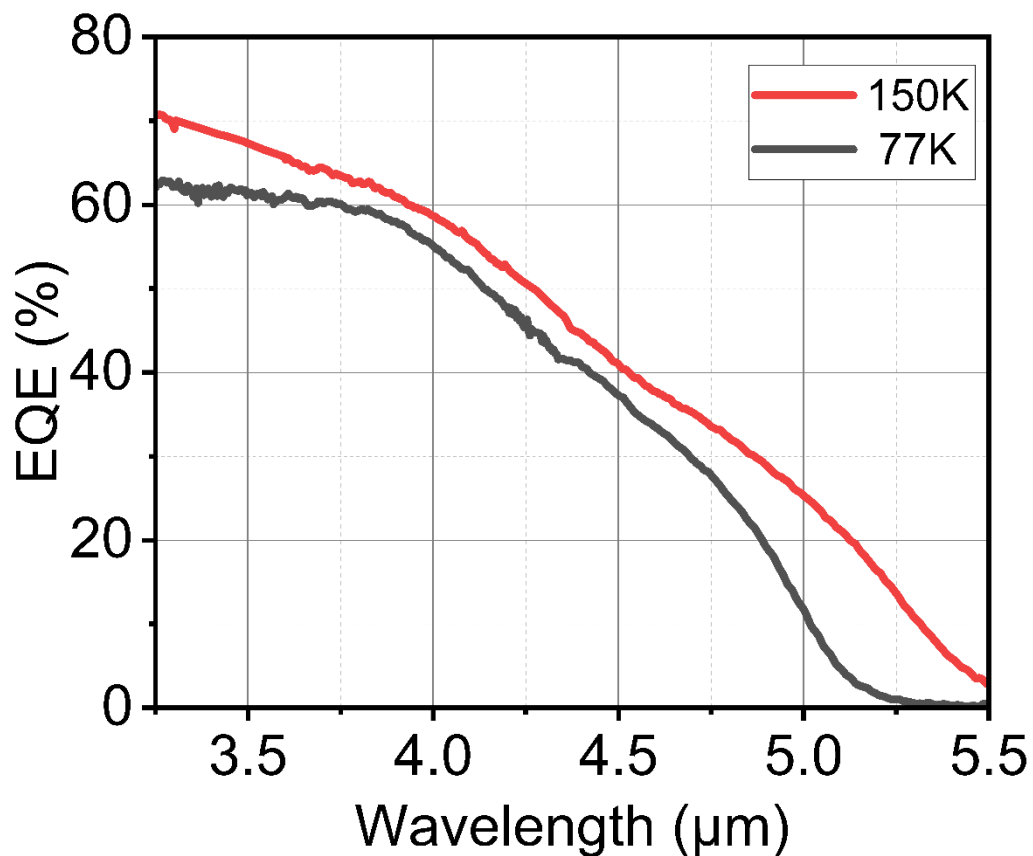


**Fig. 5.15.** Plot of EQE against wavelength for the InAs/InAsSb PIN detector at 77 and 150K.

The EQE at 3.8 μm was 59.3% at 77K and 62.5% at 150K. The EQE for these detectors is above the current state of the art for both MOCVD and MBE grown MWIR T2SLs detectors, as shown in Fig. 5.16.

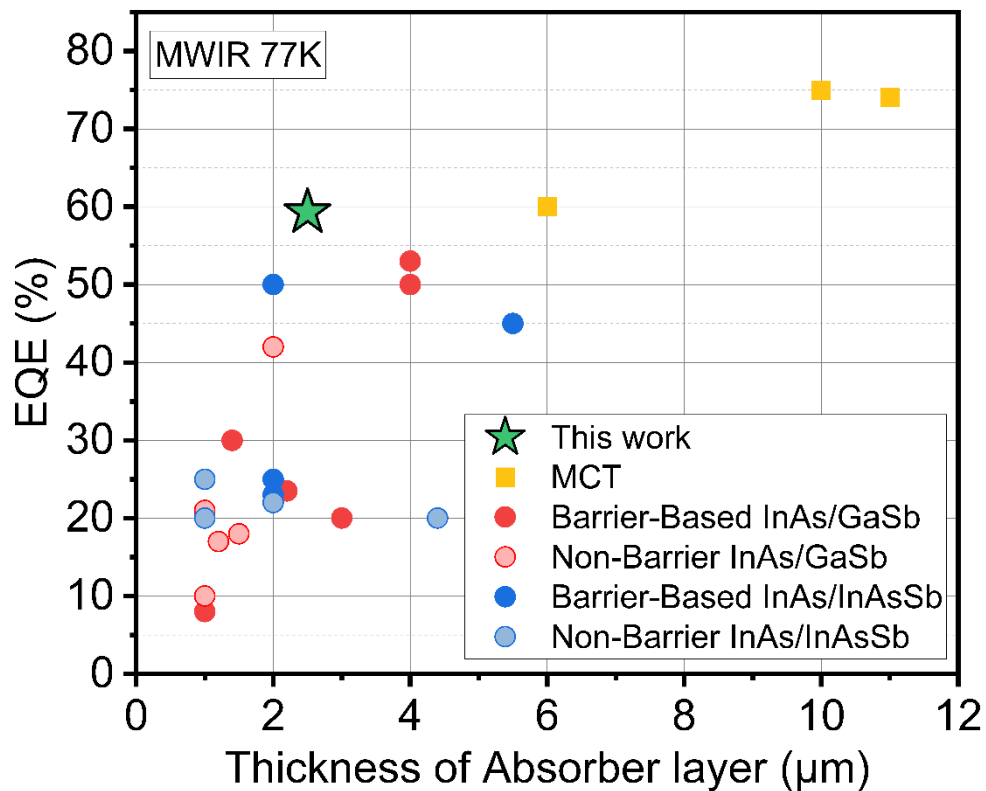


**Fig. 5.16.** Comparison of the EQE from the InAs/InAsSb PIN detector in this work compared to the values found in literature for MWIR MCT [143,147,148], Barrier-based InAs/GaSb [6,7,71,113–115], Non-Barrier InAs/GaSb [20,124–126,149], Barrier-Based InAs/InAsSb [30,140,141] and Non-Barrier InAs/InAsSb detectors [33–35,142].

The high EQE shown in Fig. 5.16, is further evidence of the high-quality interfaces produced via the growth interruption technique discussed in section 5.2.2.

The detectivity of each detector was then calculated using the responsivity, dark current density and resistance area product using equation 2.11, and is shown in Fig. 5.17.

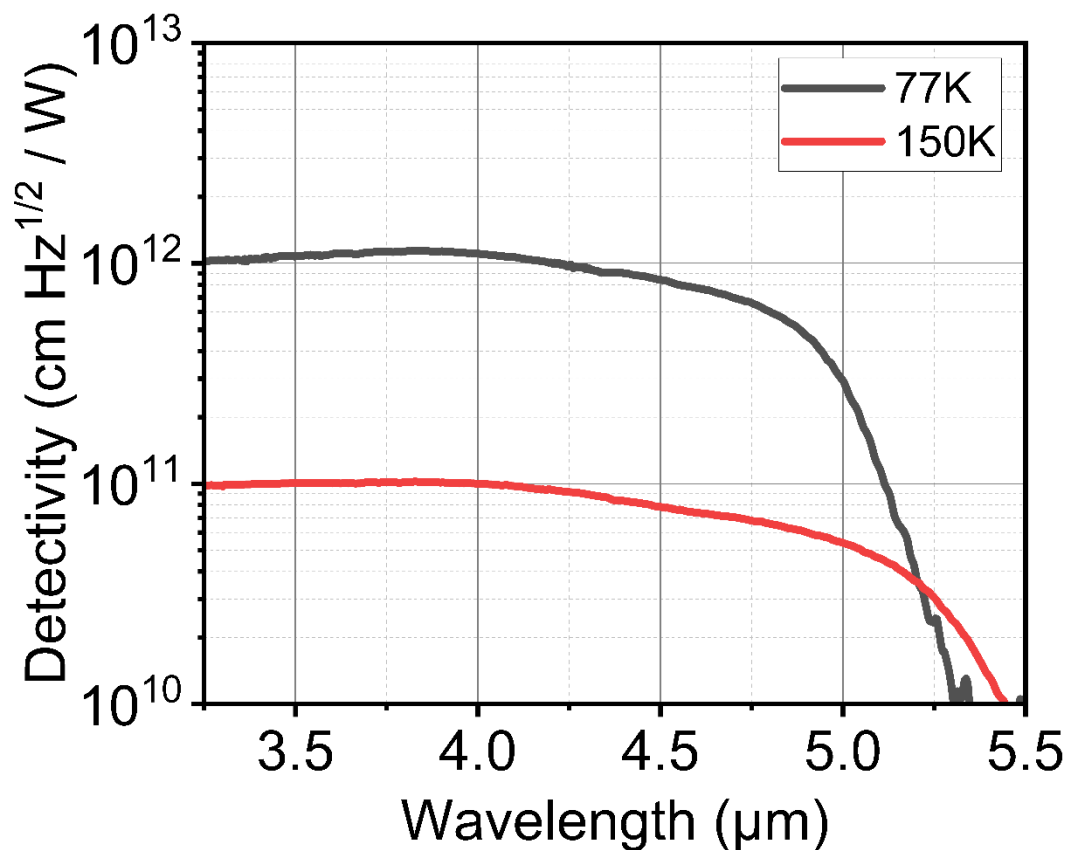


**Fig. 5.17.** Plot of Detectivity against wavelength for the InAs/InAsSb PIN detector at 77 and 150K.

The detectivity at 3.8 μm was  $1.14 \times 10^{12}$  cm Hz<sup>1/2</sup>/W at 77K and  $1.00 \times 10^{11}$  cm Hz<sup>1/2</sup>/W at 150K. Current state of the art detectivity for MOCVD grown InAs/InAsSb non barrier detectors at this wavelength are around  $3 \times 10^{12}$  cm Hz<sup>1/2</sup>/W at 77K [33] and  $1.2 \times 10^{11}$  cm Hz<sup>1/2</sup>/W at 150K [47]. The results in Fig. 5.16 are therefore very competitive with the comparable MOCVD grown state of the art results. The detectivity values for this work are also very comparable to the current literature at both 77K and 150K, as shown in Fig. 5.18. This detectivity provides good evidence that MOCVD grown InAs/InAsSb T2SLs are a viable technology for MWIR photodetectors even if they are currently restricted to non-barrier-based architecture which restricts dark current performance. Although the development of viable MOCVD-based barrier solutions might hinder the InAs/InAsSb PIN from achieving state-of-the-art performance, the significant economic advantages of MOCVD over MBE, along with the scalability benefits of T2SLs compared to MCT, could be considered more beneficial overall, even with the performance limitations.

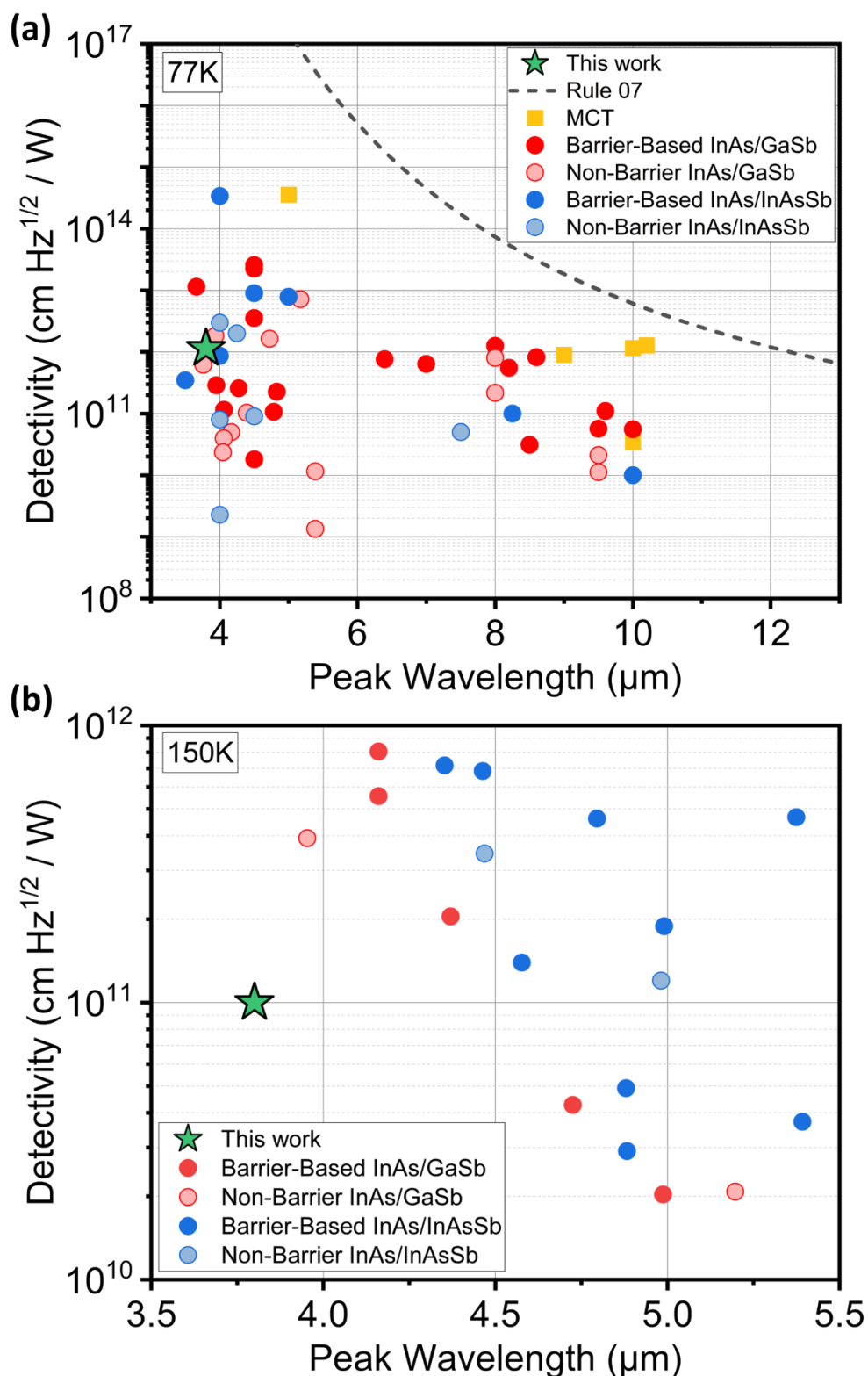


**Fig. 5.18.** Comparison of the dark current densities from the InAs/InAsSb PIN detector in this work compared to the values found in literature for MCT [2,3], Barrier-based InAs/GaSb [4–19,38], Non-Barrier InAs/GaSb[9,12,17,20–26], Barrier-Based InAs/InAsSb [27–31,39–46] and Non-Barrier InAs/InAsSb detectors [32–37,47]. At (a) 77K and (b) 150K.

## 5.4 Summary

An InAs/InAsSb T2SL MWIR detector was grown and fabricated with a cutoff wavelength of  $5.5\mu\text{m}$  and a peak detectivity of  $1.14 \times 10^{12} \text{ cm Hz}^{1/2}/\text{W}$  at 77K.

The InAs/InAsSb T2SL was found to be very sensitive to growth temperature. Increasing the growth temperature beyond  $460^\circ\text{C}$  led to an increase in surface roughness, so  $460^\circ\text{C}$  was deemed to be the highest growth temperature for the InAs/InAsSb T2SL. To improve surface roughness and quantum efficiency of the detector, a growth interruption step was introduced after each InAs and InAsSb layer. This growth interruption was very successful at improving interface quality, indicated by a reduction in the first satellite peak FWHM from 134 to 38 arcsecs, which is very comparable to state-of-the-art MBE results. The growth interruption also nearly halved the surface roughness of the T2SL from 0.42 to 0.25 nm.

A 2500 nm thick PIN device was then grown using these growth parameters and fabricated. The fabrication consisted of a deep wet etch and surface passivation from AZ3027, as used in the InAs/GaSb device fabrication. The detectors were found to have very comparable dark current densities to both the current MOCVD-grown MWIR detectors and the other MBE-grown MWIR detectors at both 77K and 150K. At 77K, the InAs/InAsSb PIN diode had a dark current density of  $7.9 \times 10^{-6} \text{ A/cm}^2$ . At 150K the InAs/InAsSb PIN diode had a dark current density of  $1.1 \times 10^{-3} \text{ A/cm}^2$ . Current state-of-the-art dark current densities for MOCVD-grown InAs/InAsSb non-barrier detectors at this wavelength and bias are around  $5 \times 10^{-6} \text{ A/cm}^2$  at 77K [33] and  $1.5 \times 10^{-3} \text{ A/cm}^2$  at 150K [47]. However, the lack of a barrier seems to prevent these MOCVD-grown PINs from reaching the true state-of-the-art dark current performance achieved by MBE-grown devices, especially at 150K.

The peak EQE of the detector was 59.3% at 77K and 62.5% at 150K, and the cutoff wavelength was between 5.25 and  $5.5 \mu\text{m}$ . The EQE for these detectors is above the current state-of-the-art for both MOCVD and MBE-grown MWIR T2SL detectors. This high EQE provides further evidence of the high-quality interfaces produced via the growth interruption technique.

The detectivity at  $3.8 \mu\text{m}$  was  $1.14 \times 10^{12} \text{ cm Hz}^{1/2}/\text{W}$  at 77K and  $1.00 \times 10^{11} \text{ cm Hz}^{1/2}/\text{W}$  at 150K. Current state of the art detectivity for MOCVD grown InAs/InAsSb non barrier detectors at this wavelength are around  $3 \times 10^{12} \text{ cm Hz}^{1/2}/\text{W}$  at 77K [33] and  $1.2 \times 10^{11} \text{ cm Hz}^{1/2}/\text{W}$  at 150K [47]. These detectivity values are also somewhat competitive with the current MBE results. The main discrepancy is caused by the higher dark current due to the lack of barrier. This provides good evidence that MOCVD grown InAs/InAsSb T2SLs are a viable technology for MWIR photodetectors even if they are currently restricted to non-barrier-based architecture. Although the development of viable MOCVD-based barrier solutions might hinder the InAs/InAsSb PIN from achieving state-of-the-art performance, the significant economic advantages of MOCVD over MBE, along with the scalability benefits of T2SLs compared to MCT, could be considered more beneficial overall, even with the performance limitations.

# Growth of InAs/InAsSb T2SLs on non-native substrates

## 6.1 Introduction

GaSb substrates are limited by their small size, high cost and brittleness, necessitating the exploration of more commercially favourable alternatives. Furthermore, GaSb's high absorption coefficient in the MWIR range is problematic for conventional backside illuminated devices, as it leads to significant absorption of incident light before it reaches the detector. While mechanical backside thinning can reduce this absorption, it adds extra steps and costs to the manufacturing process.

The InAs/InAsSb type-II superlattice (T2SL) stands out as an excellent candidate for integration on non-native substrates, thanks to its defect tolerance. This tolerance arises because the defect states are located above the conduction miniband within the InAs/InAsSb T2SL, rather than within the band gap [58]. Consequently, the InAs/InAsSb T2SL shows great promise for growth on substrates with significant lattice mismatches. Whilst this defect tolerance has been demonstrated experimentally for the T2SL itself, how it translates into device performance is less clear.

This chapter focuses on the growth of InAs/InAsSb T2SLs on the two main GaSb substrate alternatives, GaAs and Si.

GaAs substrates are a promising alternative to GaSb due to their lower cost, larger wafer size and transparency to MWIR radiation, as long as the 7.8% lattice mismatch can be overcome. Si substrates provide even stronger economic arguments than GaAs, but this comes at the cost of an even higher 12% lattice mismatch, as well as the challenge of controlling antiphase domains (APDs) from growing polar V/III materials on non-polar Si.

## 6.2 InAs/InAsSb T2SLs Detectors on GaAs Substrates

Since the InAs/InAsSb T2SLs are lattice matched to GaSb, the first step in integrating the InAs/InAsSb T2SLs detector with the GaAs substrate is to grow fully relaxed GaSb on GaAs substrates. The lattice mismatch between GaSb and GaAs is very large at 7.8% and therefore requires strain relaxation in order to reduce the dislocations associated with such a large mismatch [201]. In the case of the GaSb/GaAs interface there exists a strain relaxation mechanism known as the interfacial misfit array (IMF) [202], in which, a 2d array of regularly spaced misfit dislocations are able to confine the strain relaxation to the material interface. The IMF can significantly reduce the number of threading dislocations that reach the surface of the GaSb.

Misfit dislocations occur in the interface between two materials with different lattice constants. Due to the difference in lattice constant some bonds are left “free” or “dangling”. These free bonds are known as misfit dislocations. As shown in Fig. 6.1, there are two main types of misfit dislocations:  $60^\circ$  and  $90^\circ$  [202]. The angle of the dislocation is calculated between the Burgers vector and the dislocation vector.

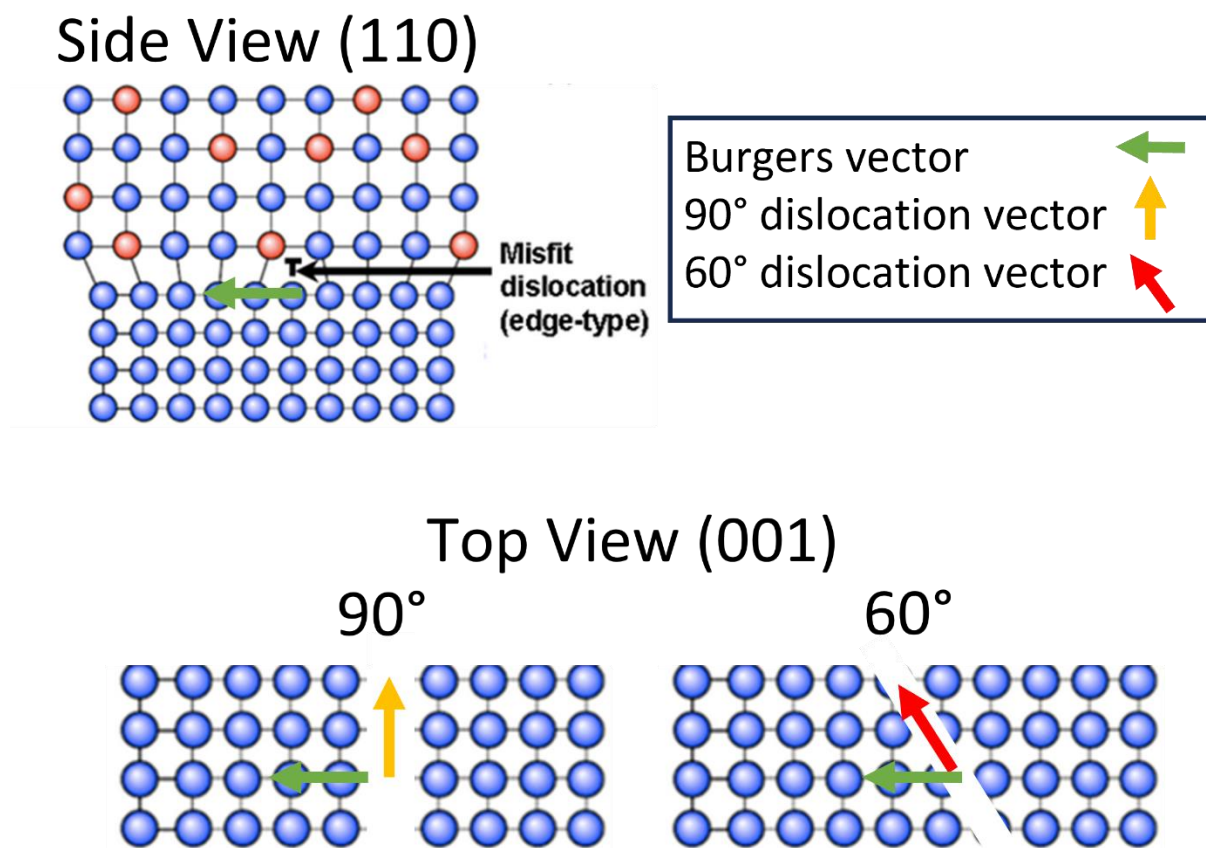


**Fig. 6.1.** Diagram showing how the two different types of misfit dislocations propagate. This figure is adapted from reference [203].

The difference between 60° and 90° misfit dislocations is the plane in which the dislocation propagates. The 60° misfit dislocation propagates along the (111) and (1-11) planes and the 90° misfit dislocation propagates along the (110) and (1-10) planes. Unfortunately, the (111) plane is a slip plane. A slip plane is the plane with the greatest atomic density which makes it energetically favourable for the dislocations to travel up it as the nearest neighbour interactions are more shared meaning the atoms are less strongly bound [204]. Therefore, if a misfit dislocation propagates along a slip plane, it is likely for it to travel up the slip plane turning into a threading dislocation. Since these threading dislocations travel vertically up the structure, they can reach the device and impact its performance.

90° misfit dislocations are far more desirable due to them not propagating along slip planes. Not propagating along slip planes mean that they do not turn into threading dislocations and remain confined to the interfacial layer and therefore do not impact device performance [205]. Therefore, maximising the formation of 90° dislocations and minimising the formation of 60° dislocations is required to grow GaSb on GaAs with a minimal threading dislocation density.

It has been shown previously that a variety of factors contribute to which type of misfit dislocation is formed with the main factor being the coalescence of GaSb islands [206]. During growth, these GaSb islands have been shown to have near 100% 90° dislocations [205]. However, as the growth continues and these islands coalesce, many of these 90° dislocations turn into 60° dislocations. In order to minimise this effect, island growth and coalescence must be minimised and larger area, layer growth must be encouraged. There are a few factors which determine how “island like” the growth will be. A large factor is the surface roughness of the GaAs layer before GaSb growth. A substrate with high surface roughness contains many nucleation points for island growth and will therefore create an IMF dominated by 60° dislocations. Therefore, achieving a GaAs surface with as low a roughness as possible is fundamental in minimising 60° dislocations formation.

As well as the roughness of the surface, it is important to control which atom is on the surface. Generally, in the growth of GaAs, As overpressure is used which creates an As rich surface. In order to create a growth as close to a single monoatomic layer as possible, a Ga-rich surface is desirable. If a surface is perfectly smooth and Ga-rich, a flux of the correct amount of Sb atoms would theoretically form a single monolayer of GaSb resulting in an IMF consisting of majority 90° dislocations akin to the individual islands. Therefore, growth conditions that get as close to this idealised monolayer growth are desired. Once the GaSb is grown, the InAs/InAsSb T2SL can be grown and fabricated in the same way as in chapter 6.

The MOCVD growth was performed in an Aixtron Close Coupled Showerhead reactor. The precursors used were trimethylindium (TMIn), tertiarybutylarsine (TBAs), triethylgallium (TEGa), triethylantimony (TESb), disilane ( $\text{Si}_2\text{H}_6$ ) and diethylzinc (DEZn), with hydrogen used as the carrier gas. The device structure was grown on a 2-inch undoped GaAs (001) substrate, with the reactor pressure kept at 100 mbar.

### 6.2.1 Growth of GaSb on GaAs

In order to create growth conditions that maximise the number of 90° dislocations, a growth switching sequence was developed in order to create a Ga-rich GaAs surface and as close to monolayer growth of GaSb as possible, as shown in Fig. 7.2.

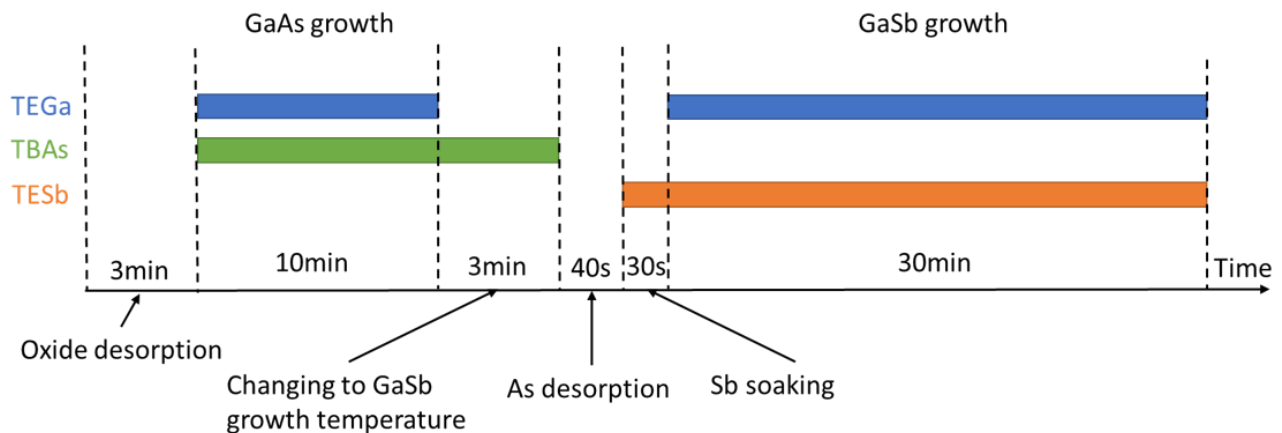


**Fig. 6.2.** MOCVD growth timeline of the growth of GaSb onto a GaAs substrate. Showing the growth interruption stages used to promote a 90° dislocation dominated IMF between the GaAs and GaSb.

As shown in Fig. 6.2, the growth starts with a thin 100nm layer of GaAs in order to try and smooth the surface ready for the IMF formation. The GaAs was grown at 645°C with a V/III ratio of 21. After the GaAs growth, a 40 second As desorption step was used to create a Ga-rich GaAs surface. After the Ga-rich surface was formed, a 30 second Sb soaking step was used to try to create the first layer of GaSb as monolayer like as possible. Once the switch from GaAs growth to GaSb growth was complete, a 500nm GaSb layer was grown.

The first parameter that was investigated was the GaSb V/III ratio. Four samples were grown at a surface temperature of 530°C with V/III ratios ranging from 2 to 1.3. The AFM scans of these samples are shown in Fig. 6.3.

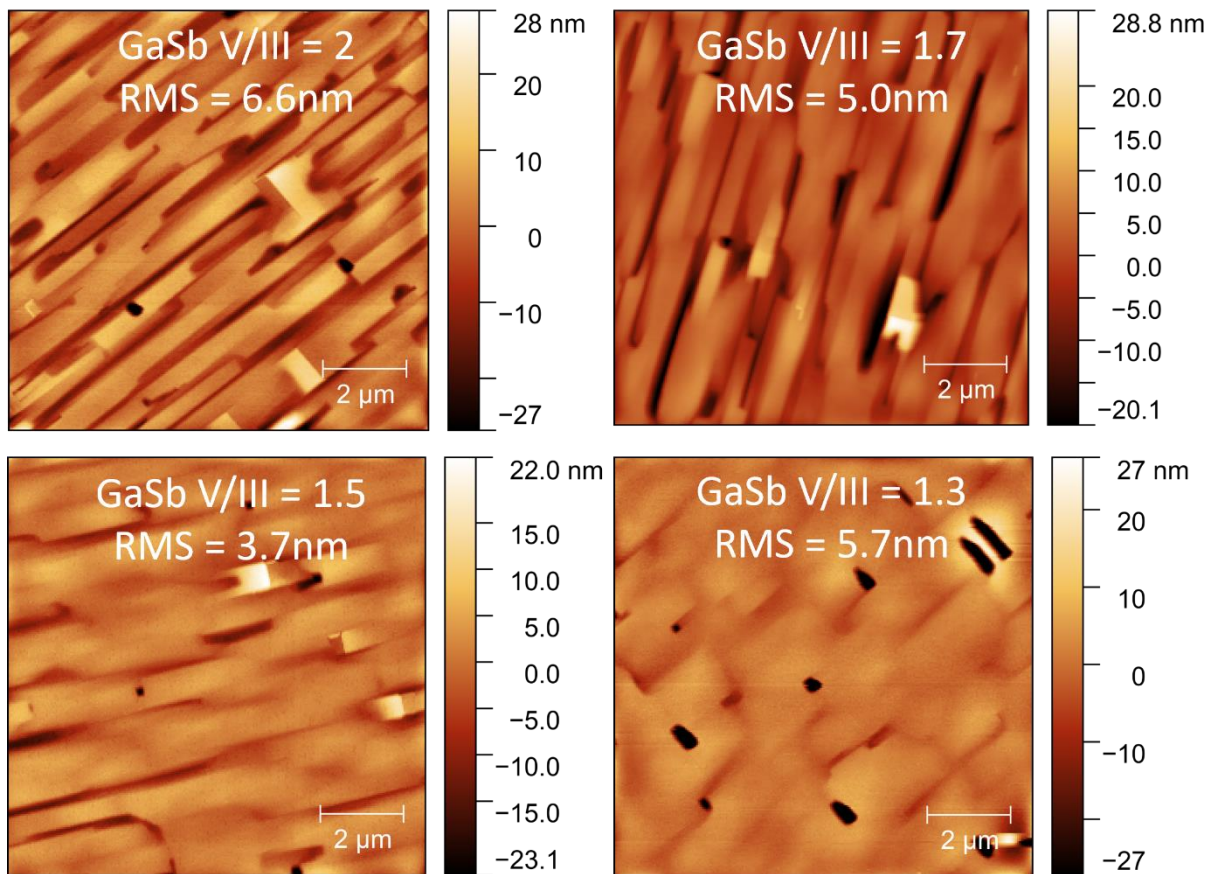


**Fig. 6.3.** AFM scans of 500nm GaSb grown on GaAs substrates at 530°C with varying GaSb V/III ratios.

As shown in Fig. 6.3, higher GaSb V/III ratios seem to cause this surface striping along the [1-10] plane which increases surface roughness. This striping is reduced when the GaSb V/III is reduced to 1.3. However, when the GaSb V/III is reduced to 1.3, the striping is replaced by 20nm deep surface pits which increase the surface roughness once again. The GaSb V/III ratio with the lowest surface roughness was 1.5. In order to further improve the surface, the growth temperature was reduced to 510°C, as shown in Fig. 6.4.

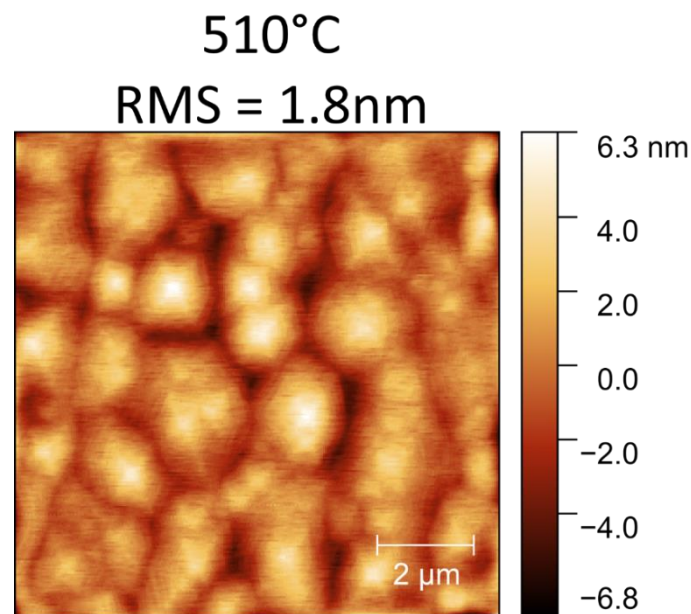


**Fig. 6.4.** AFM scan of 500nm GaSb grown on GaAs substrates at 510°C with a GaSb V/III ratio of 1.5.

When the growth temperature was reduced to 510°C from 530°C the surface roughness was reduced from 3.7 to 1.8nm. At 510°C there was no evidence of surface striping or surface pits. Whilst this surface roughness is still a lot higher than a standard GaSb substrate, it was deemed sufficient to investigate InAs/InAsSb integration.

After an appropriate growth temperature and V/III ratio were established, TEM was used to investigate the interface and to characterise the misfit dislocation types, as shown in Fig. 6.5.

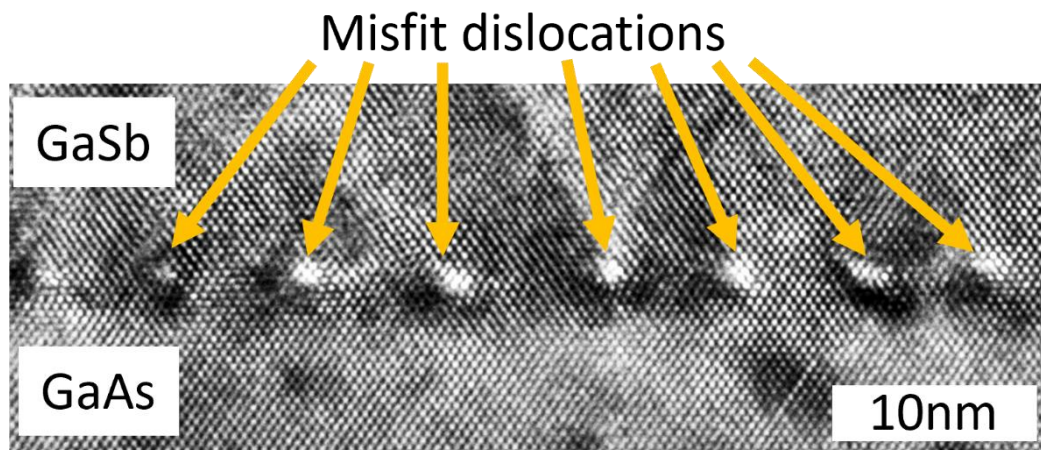


**Fig. 6.5.** High resolution TEM image of the interface between the GaAs and GaSb layers showing the misfit dislocations that form the interfacial misfit array.

The spacing of the misfits was found to be 5.5 nm which indicates one misfit for every 14 GaAs or 13 GaSb lattice sites and aligns well with previously reported results [207]. Burgers circuit analysis [208] was performed on 65 different misfit dislocations across the IMF, as shown in Fig. 6.6.

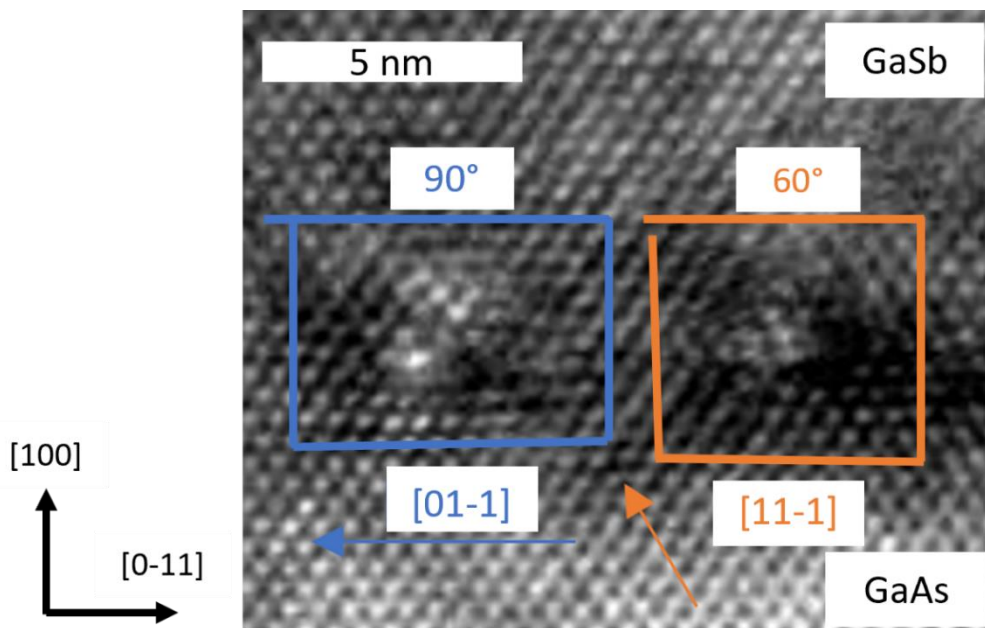


**Fig. 6.6.** Burgers circuit analysis on the misfit dislocations in the high resolution TEM image of the interfacial misfit array.

45 of the misfit dislocations in the IMF were identified as  $90^\circ$  dislocations and 20 were identified as  $60^\circ$  dislocations. This means that 70% of the misfit dislocations in the IMF were  $90^\circ$  dislocations indicating that the IMF consists of a large majority of  $90^\circ$  dislocations.

Electron channelling contrast imaging (ECCI) was used to verify the effectiveness of the IMF in reducing the threading dislocation density (TDD) at the surface of the GaSb, as shown in Fig. 6.7.

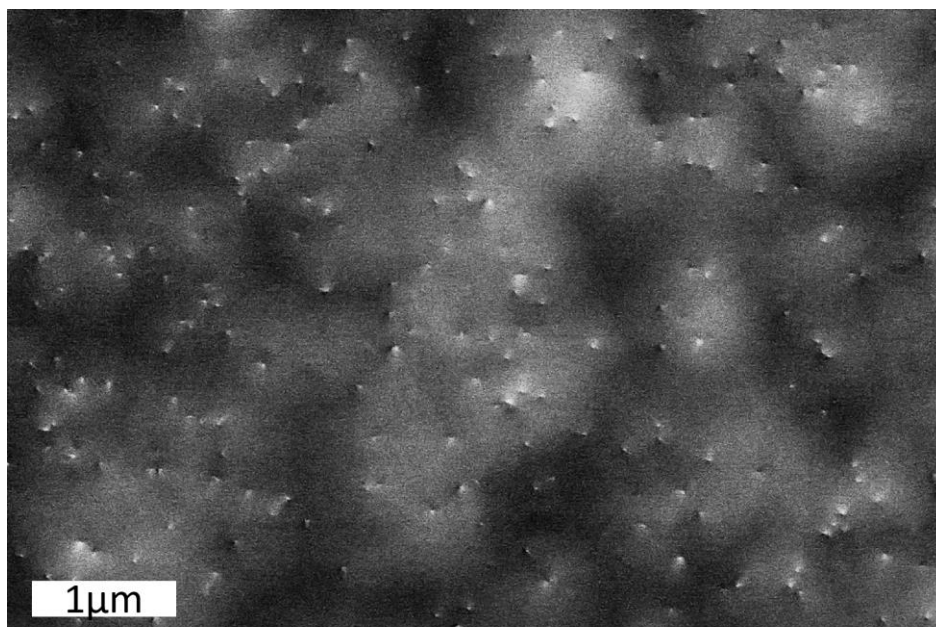


**Fig. 6.7.** Electron channelling contrast imaging (ECCI) image of the surface of the GaSb grown on GaAs substrates.

A total surface area of  $100 \mu\text{m}^2$  was analysed and a TDD of  $4.1 \times 10^8 \pm 0.6 \times 10^8 / \text{cm}^2$  was found at the surface of the GaSb. Considering the large mismatch between GaSb and GaAs and the relatively thin 500nm GaSb growth, this TDD is quite good. There are examples of lower TDD for MBE grown GaSb on GaAs, but they generally use much thicker GaSb layers of around 3-6 $\mu\text{m}$  or implement more complex dislocation filtering in order to achieve their lower TDD [202,209].

### 6.2.2 MWIR InAs/InAsSb T2SL detectors on GaAs

Once the growth of GaSb on GaAs was established, the next step was to grow a InAs/InAsSb PIN detector. In order to achieve a fair comparison, an InAs/InAsSb T2SL PIN was grown simultaneously on both a GaSb substrate as well as the 500nm GaSb on GaAs buffer structure. The InAs/InAsSb PIN structure was grown and fabricated in the same way as the detector in chapter 5. Unsurprisingly, the high roughness from the GaSb on GaAs shown in Fig. 6.4, translated to a high roughness on the PIN structure on GaAs, as shown in Fig. 6.8a.

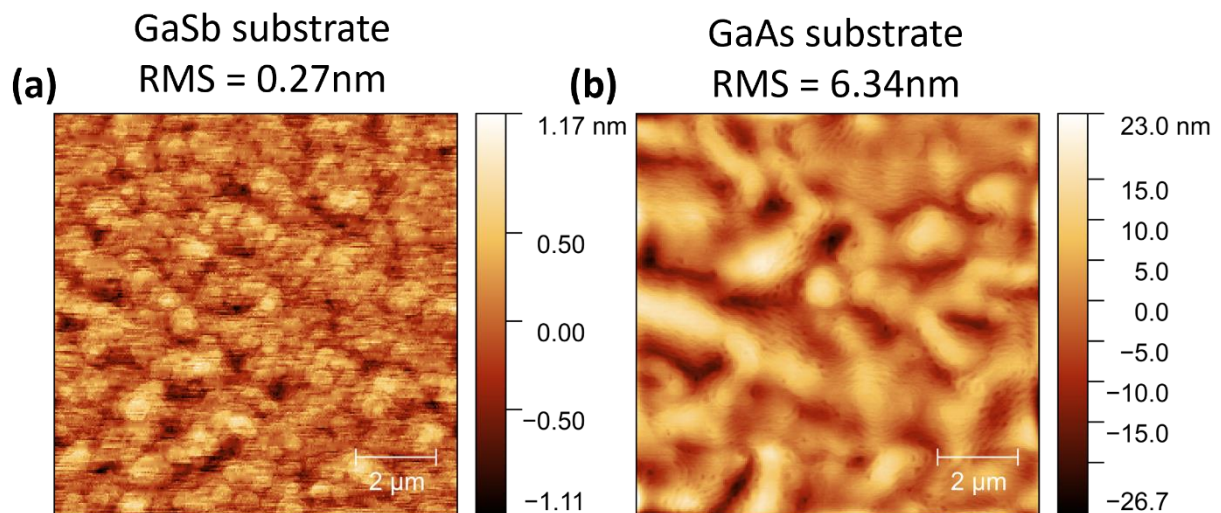


**Fig. 6.8.** AFM scans of the InAs/InAsSb T2SL PIN detector on both (a) GaSb substrates and (b) GaAs substrates.

XRD was also used to confirm the lattice match between the InAs/InAsSb T2SL and the GaSb buffer layer, as shown in Fig. 6.9.

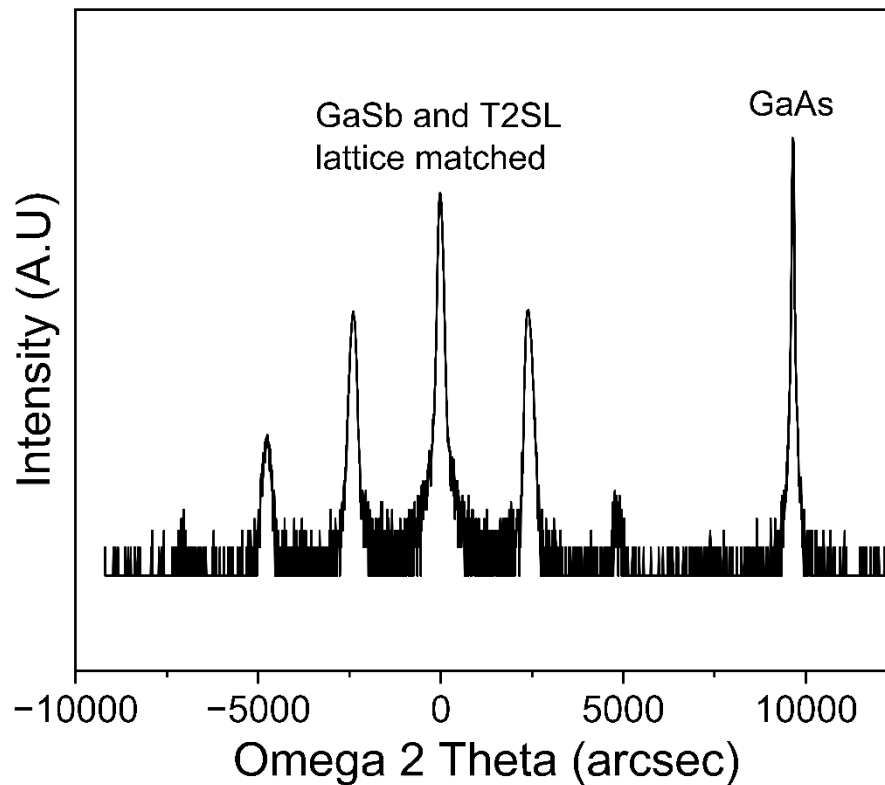


**Fig. 6.9.** Omega 2 Theta XRD scans of the full InAs/InAsSb T2SL PIN device sample grown on a GaAs substrate with a 500nm GaSb buffer layer.

Although Fig. 6.9 shows that the InAs/InAsSb T2SL was usefully grown lattice matched to the GaSb buffer layer, the high levels of threading dislocations have seemed to continue into the T2SL causing a large increase in the FWHM of the first satellite peak. The FWHM of the first satellite peak has increased from 22 arcsec to 126 arcsec when comparing the devices grown on GaSb and GaAs.

In order to investigate how this increase in threading dislocations affects the device performance, electrical and optical characterisation of the device on GaAs was performed and compared to the device on GaSb substrates.

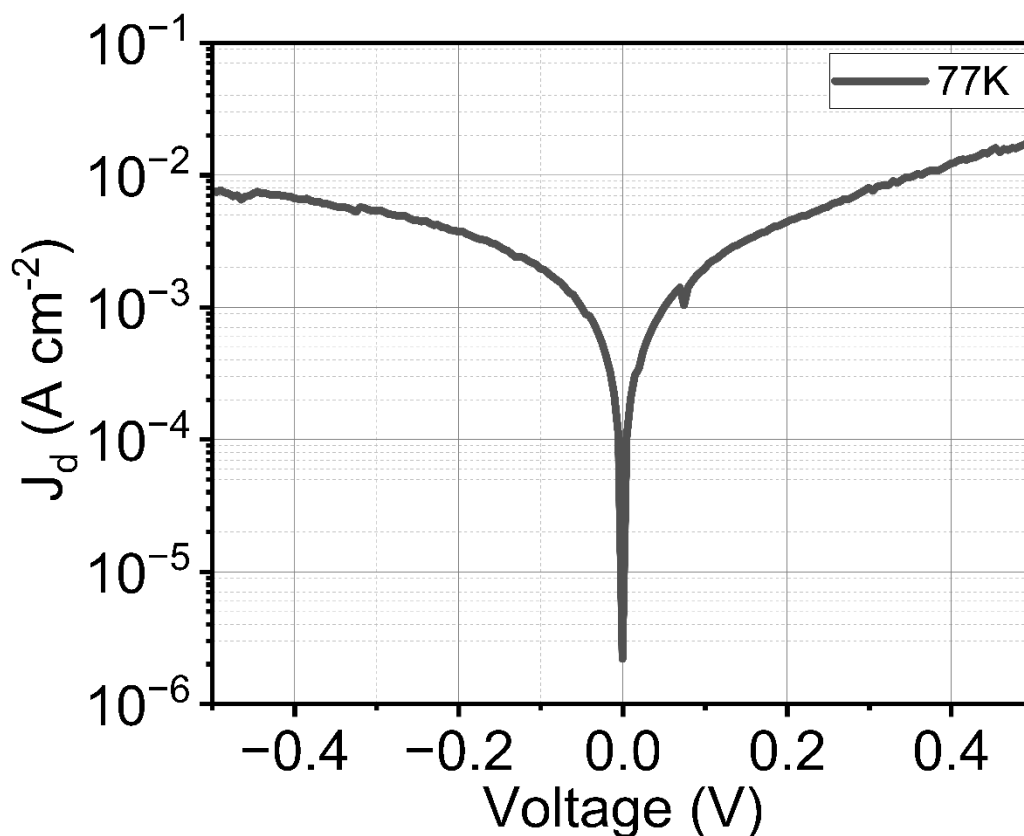


**Fig. 6.10.** Dark current density ( $J_d$ ) versus voltage for a 300 $\mu$ m diameter InAs/InAsSb T2SL PIN detector grown on a GaAs substrate at 77K.

Unfortunately, due to time constraints it was difficult to get electrical measurements above 77K for the InAs/InAsSb T2SL PIN detector grown on a GaAs substrate. At 77K the PIN device grown on GaAs did not exhibit the same rectifying shape shown in Fig 6.10, which is generally associated with a PIN diode.

It appears as though the tunnelling dislocations have created conduction pathways through the depletion zone creating a photoconductive detector instead of a photovoltaic one. This has also led to a large increase in dark current density at -0.1V, with the device grown on GaSb having a dark current density of  $7.9 \times 10^{-6}$  A/cm<sup>2</sup> whereas the device grown on GaAs has a dark current density of  $2.1 \times 10^{-3}$  A/cm<sup>2</sup>. This increase in dark current density by a factor of 265 will naturally have a large effect on the device's detectivity. Unfortunately, there is very little literature examining MWIR InAs/InAsSb detectors grown on GaAs so it is difficult to assess how good or bad this result is. The dark current densities were then also compared to the different detector types grown on native substrates available in literature, as seen in Fig. 6.11.

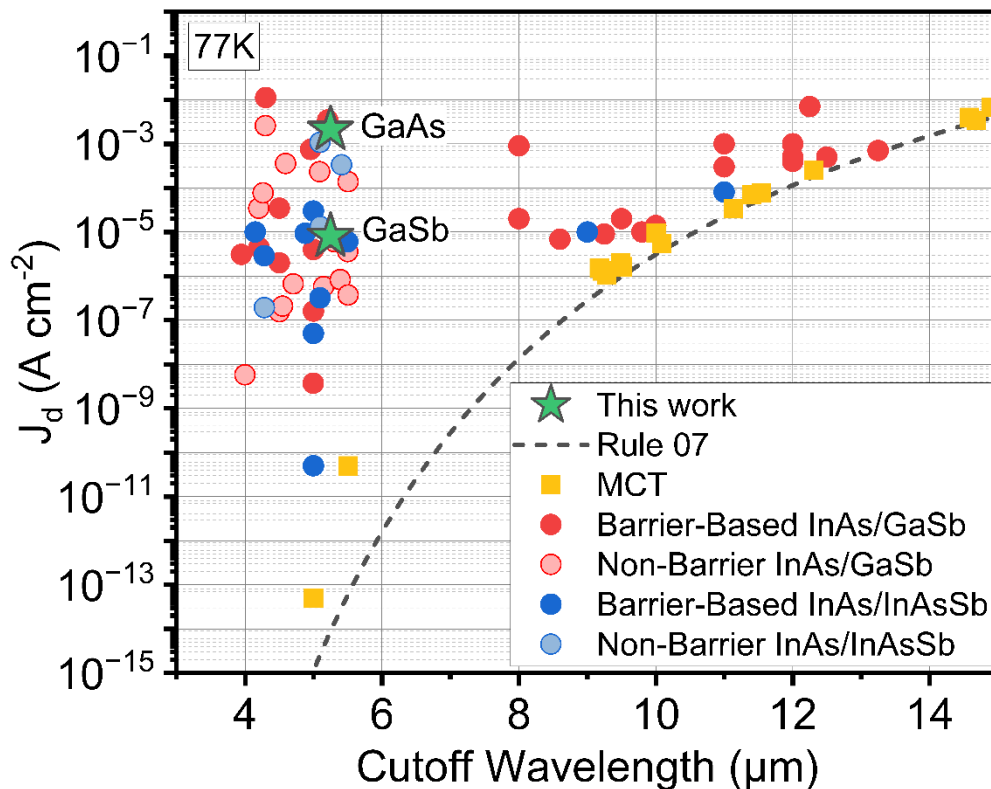


**Fig. 6.11.** Comparison of the dark current densities for the InAs/InAsSb PIN detectors in this work grown on GaAs and GaSb substrates compared to the values in literature for: Barrier-based InAs/GaSb [4–7,113,114,71,115,116,8,117–119,9,10,120,11–14,121,15,122,16,123], Non-Barrier InAs/GaSb [124,20,125–127,21,128,17,22,23,129–135], Barrier-Based InAs/InAsSb [136,27–29,40,42,137–139,30,140,141] and Non-Barrier InAs/InAsSb detectors [32,47,33–35,142,36]. As well as MCT detectors [143,144] and the “Rule 07” line [48].

When compared to the different detector types grown on native substrates available in literature, the dark current performance of the InAs/InAsSb PIN grown on GaAs does appear to be quite poor. This poor dark current implies that the theoretical defect tolerance [58] of the InAs/InAsSb T2SL is not able to improve the electrical performance. For the InAs/InAsSb PINs grown on GaAs substrates it would be reasonable to conclude that the high threading dislocation density was detrimental to the electrical performance of the detectors.

It is possible however, that the theoretical defect tolerance [58] of the InAs/InAsSb T2SL is still relevant for the optical properties of the T2SL. To investigate this optical defect tolerance, the device was characterised optically in the same way as the device on GaSb in section 5.3.2. The responsivity of the MWIR InAs/InAsSb PIN detectors on both GaAs and GaSb is shown in Fig. 6.12.

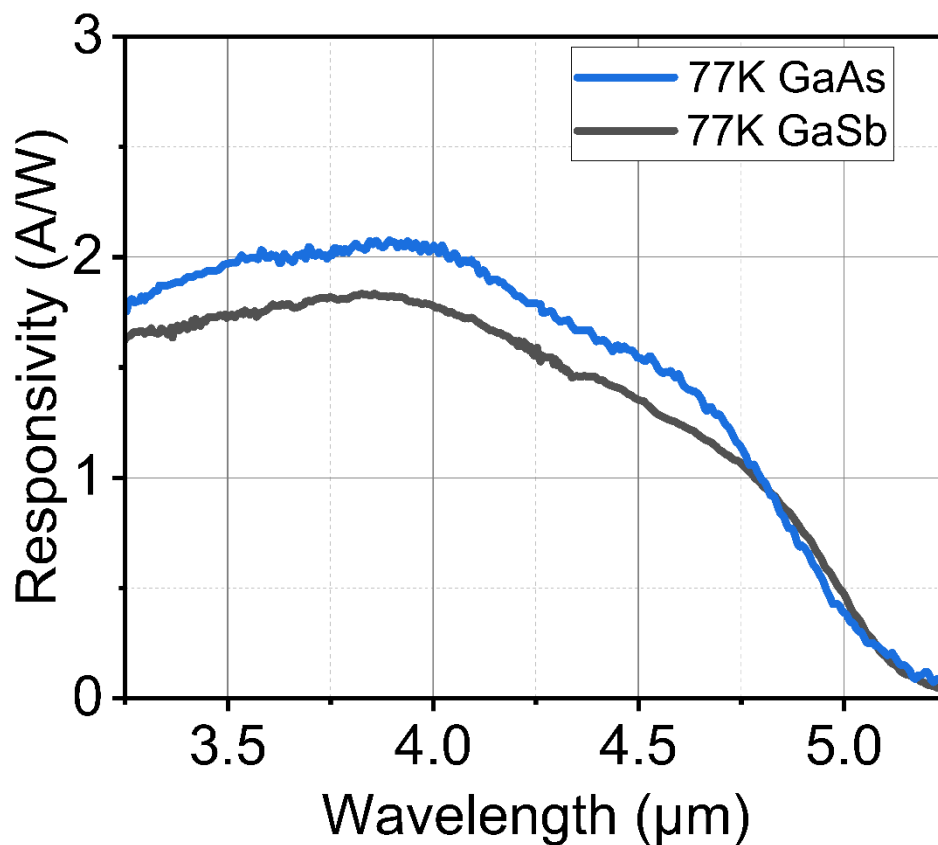


**Fig. 6.12.** Plot of responsivity against wavelength for the InAs/InAsSb PIN detectors grown on GaAs and GaSb substrates at 77K.

Surprisingly, the responsivity of the InAs/InAsSb PIN detector grown on GaAs was higher than the responsivity of the same detector grown on GaSb. The peak responsivity for both substrates occurred at 3.8  $\mu\text{m}$ . The peak responsivity was 2.04 A/W for the sample grown on GaAs and 1.83 A/W for the sample grown on GaSb. It is likely that this discrepancy is caused by device-to-device variation. It could be possible that the threading dislocations are enhancing the responsivity by providing conduction channels and making the device more photoconductive than photovoltaic. Either way, it is clear from Fig. 6.12 that there is no major reduction in responsivity when going from the detector on GaSb to the detector on GaAs. This consistency in responsivity between substrates seems to imply that the InAs/InAsSb defect tolerance, which involves the defect states existing above the conduction band, is still relevant optically if not electrically. There appears to be no evidence that conversion of incident photons into electron-hole pairs is in any way inhibited by the high threading dislocation density.

From the responsivity, the external quantum efficiency (EQE) was calculated using equation 2.10, as shown in Fig. 6.13.

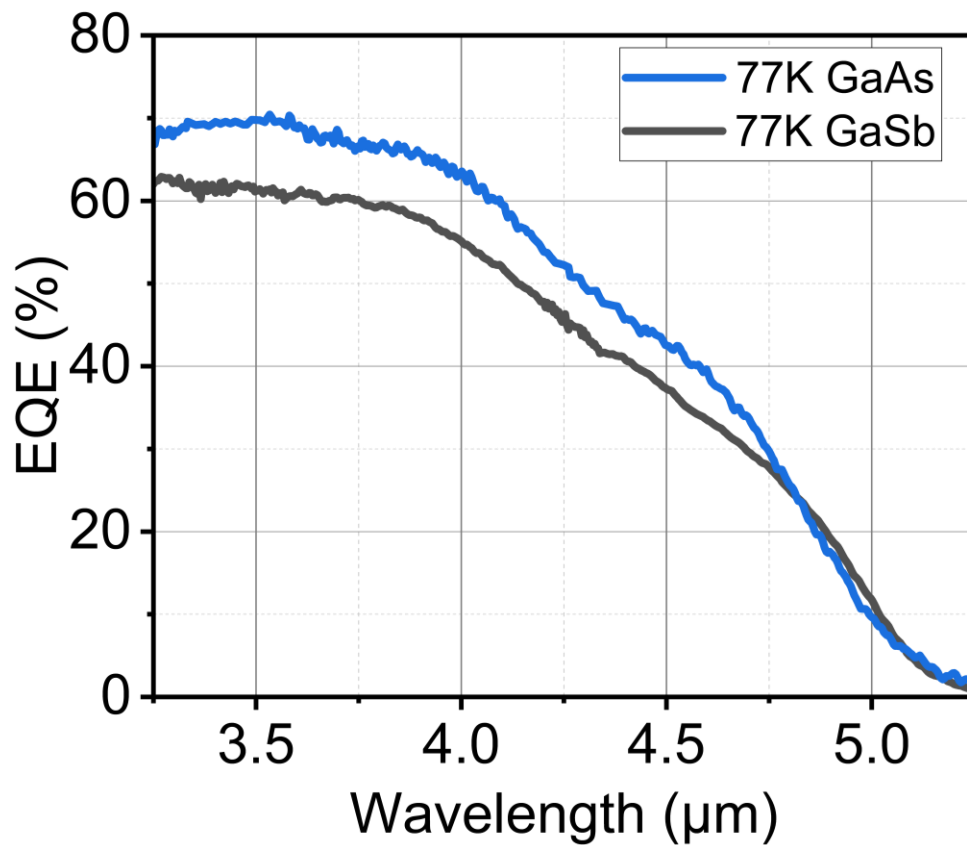


**Fig. 6.13.** Plot of EQE against wavelength for the InAs/InAsSb PIN detectors grown GaAs and GaSb substrates at 77K.

The EQE at 3.8 μm was 66.7% for the sample grown on GaAs and 59.3% for the sample grown on GaSb. The EQE for these detectors is above the current state of the art for both MOCVD and MBE grown MWIR T2SLs detectors, as shown in Fig. 6.14.

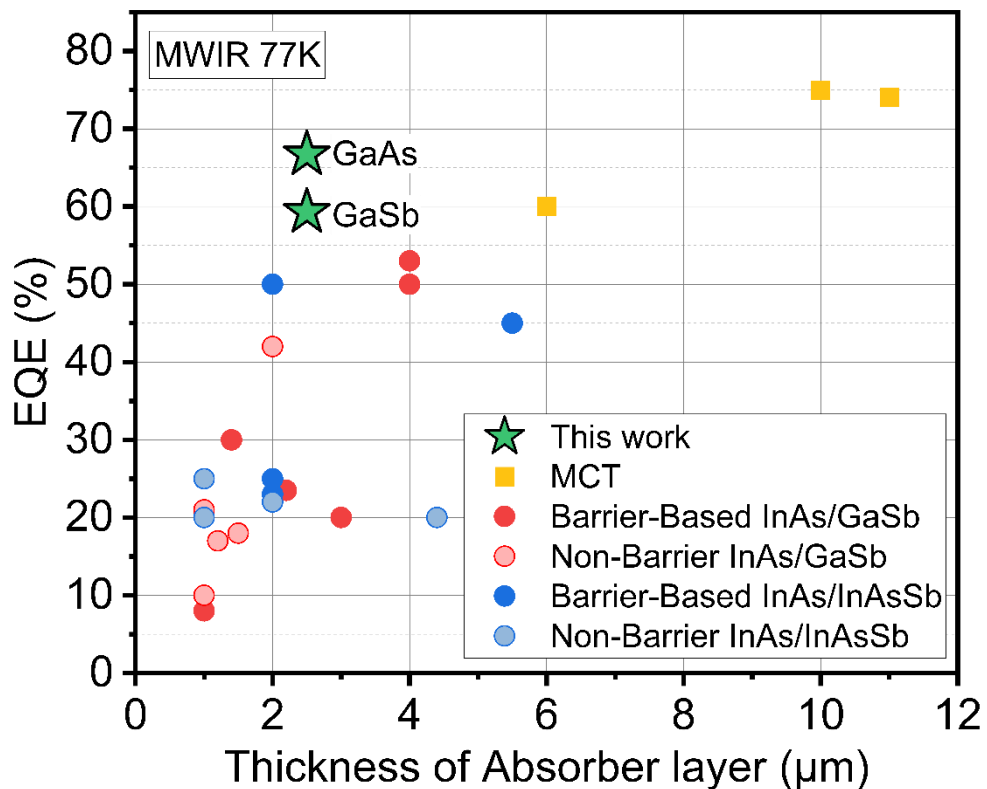


**Fig. 6.14.** Comparison of the EQE from the InAs/InAsSb PIN detectors in this work grown on GaAs and GaSb substrates compared to the values found in literature for MWIR MCT [143,147,148], Barrier-based InAs/GaSb [6,7,71,113–115], Non-Barrier InAs/GaSb [20,124–126,149], Barrier-Based InAs/InAsSb [30,140,141] and Non-Barrier InAs/InAsSb detectors [33–35,142].

The detectivity of each detector was then calculated using the responsivity, dark current density and resistance area product using equation 2.11, and is shown in Fig. 6.15.

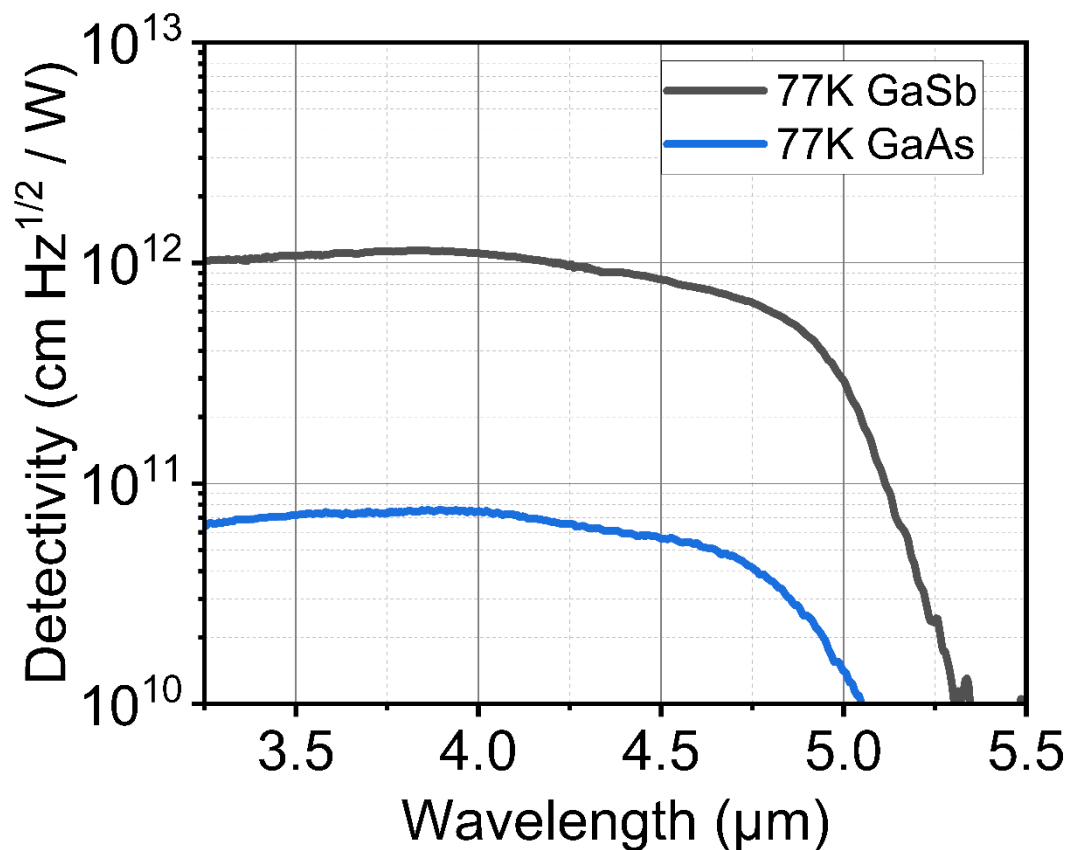


**Fig. 6.15.** Plot of Detectivity against wavelength for the InAs/InAsSb PIN detectors grown GaAs and GaSb substrates at 77K.

As expected, the poor dark current density greatly reduced the final detectivity of the InAs/InAsSb PIN detector grown on GaAs. The detectivity at 3.8 μm was  $1.14 \times 10^{12}$  cm Hz<sup>1/2</sup>/W for the detector grown on GaSb and  $7.44 \times 10^{10}$  cm Hz<sup>1/2</sup>/W for the detector grown on GaAs. Interestingly, despite not being state-of-the-art, the high responsivity results in a detectivity value of  $7.44 \times 10^{10}$  cm Hz<sup>1/2</sup>/W, which is quite comparable to many other MWIR detectors grown on native substrates, as illustrated in Fig. 6.16.

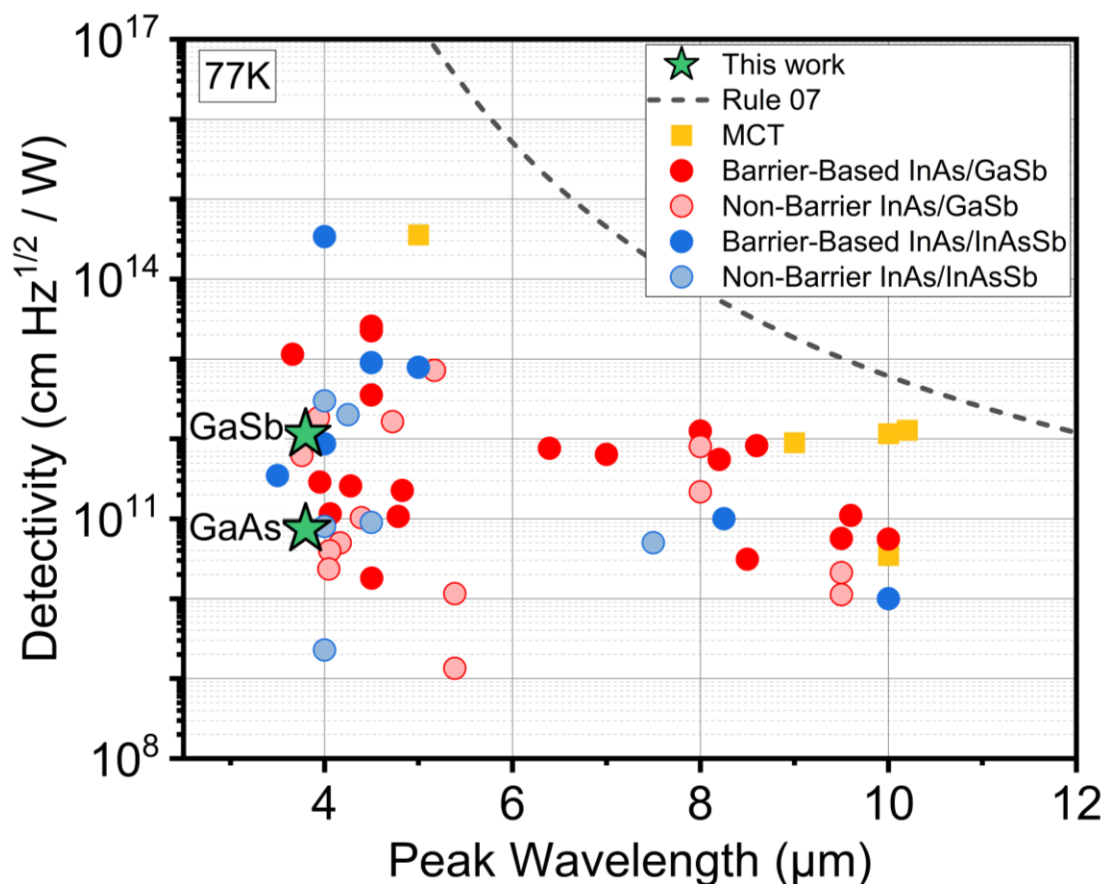


**Fig. 6.16.** Comparison of the detectivities from the InAs/InAsSb PIN detectors in this work grown on GaAs and GaSb substrates compared to the values in literature for MCT [2,3], Barrier-based InAs/GaSb [4–19], Non-Barrier InAs/GaSb [9,12,17,20–26], Barrier-Based InAs/InAsSb [27–31] and Non-Barrier InAs/InAsSb detectors [32–37]. The “Rule 07” line is added as a reference and is calculated from the rule 07 dark current density line with the QE of the MCT detectors assumed to be 75%.

The high threading dislocation density resulting from the significant mismatch between GaAs and GaSb substrates has clearly been detrimental to the performance of the InAs/InAsSb T2SL PIN. The detectivity of the InAs/InAsSb T2SL PIN was reduced by a factor of 15 due to the GaAs substrate. While this work serves as a good proof of concept, further efforts to reduce the threading dislocation density are necessary to close the performance gap between detectors on GaAs and GaSb.

Introducing thicker GaSb buffers with dislocation filtering layers has been shown to further reduce threading dislocation density [202,209], and may be required for the proper integration of the InAs/InAsSb T2SL with GaAs substrates. There is also significant room for optimisation within the IMF formation. Parameters such as temperature, flow, reactor pressure, timing and even the GaAs growth conditions can be further refined to promote the formation of  $90^\circ$  dislocations within the IMF. While it is interesting that these results suggest the InAs/InAsSb T2SL is optically defect tolerant, there appears to be no evidence for a mechanism of electrical defect tolerance within the InAs/InAsSb T2SL.

### 6.3 Growth of InAs/InAsSb T2SLs on Si

Si substrates provide even stronger economic arguments than GaAs. However, this advantage comes with greater challenges, including a larger 12% lattice mismatch and the complexity of managing APDs when growing polar V/III materials on non-polar Si. MBE growth of InAs/InAsSb T2SLs on Si substrates has been demonstrated via the use of AlSb islands at the Si-GaSb interface [210]. However, it is very difficult to grow AlSb using standard MOCVD techniques as previously mentioned. This work provides the first demonstration of MOCVD growth of a InAs/InAsSb T2SL on Si [1].

In order to integrate the InAs/InAsSb T2SL with Si substrates a buffer scheme was designed, as shown in Fig. 6.17.

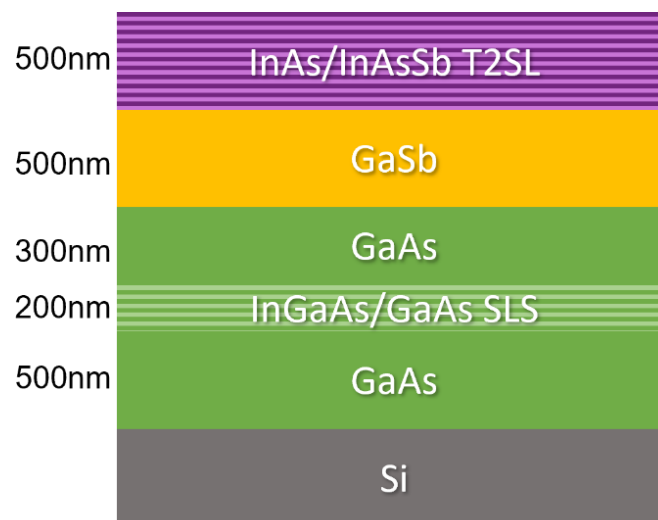


**Fig. 6.17.** Schematic diagram of the InAs/InAsSb type-II superlattice grown on Si using the GaSb/GaAs/Si buffer layer structure [1].

The MOCVD growth was performed using the same reactor and precursor gases, as described in 7.2. The (001) Si substrates used had a  $0.8^\circ$  offcut and were annealed at  $815^\circ\text{C}$  for 15 minutes prior to GaAs nucleation to promote a diatomic-stepped surface to prevent antiphase domain formation caused by the polar/non-polar interface [211,212].

After the annealing, GaAs was grown using a two-step growth method comprising of a low temperature nucleation layer at  $375^\circ\text{C}$  and a higher temperature growth at  $550^\circ\text{C}$ . The V/III ratio of the GaAs was 21. A 10 period  $\text{In}_{0.1}\text{Ga}_{0.9}\text{As}/\text{GaAs}$  strained layer superlattice (SLS) was grown in the GaAs layer to act as a dislocation filtering layer. This SLS was followed by the growth of GaSb onto the GaAs, in the same way as shown in Fig 6.2, where an IMF was formed.

Once the buffer layer was grown, a 50 period InAs/InAsSb T2SL was grown on top. The growth time for the InAs layers was 23 seconds and the growth time for the InAsSb layers was 10 seconds. No growth interruption was used in the growth of the InAs/InAsSb T2SLs on Si. AFM was performed after the growth of GaAs, GaSb and the final T2SL to monitor how the surface changes after each growth step, as shown in Fig. 6.18.

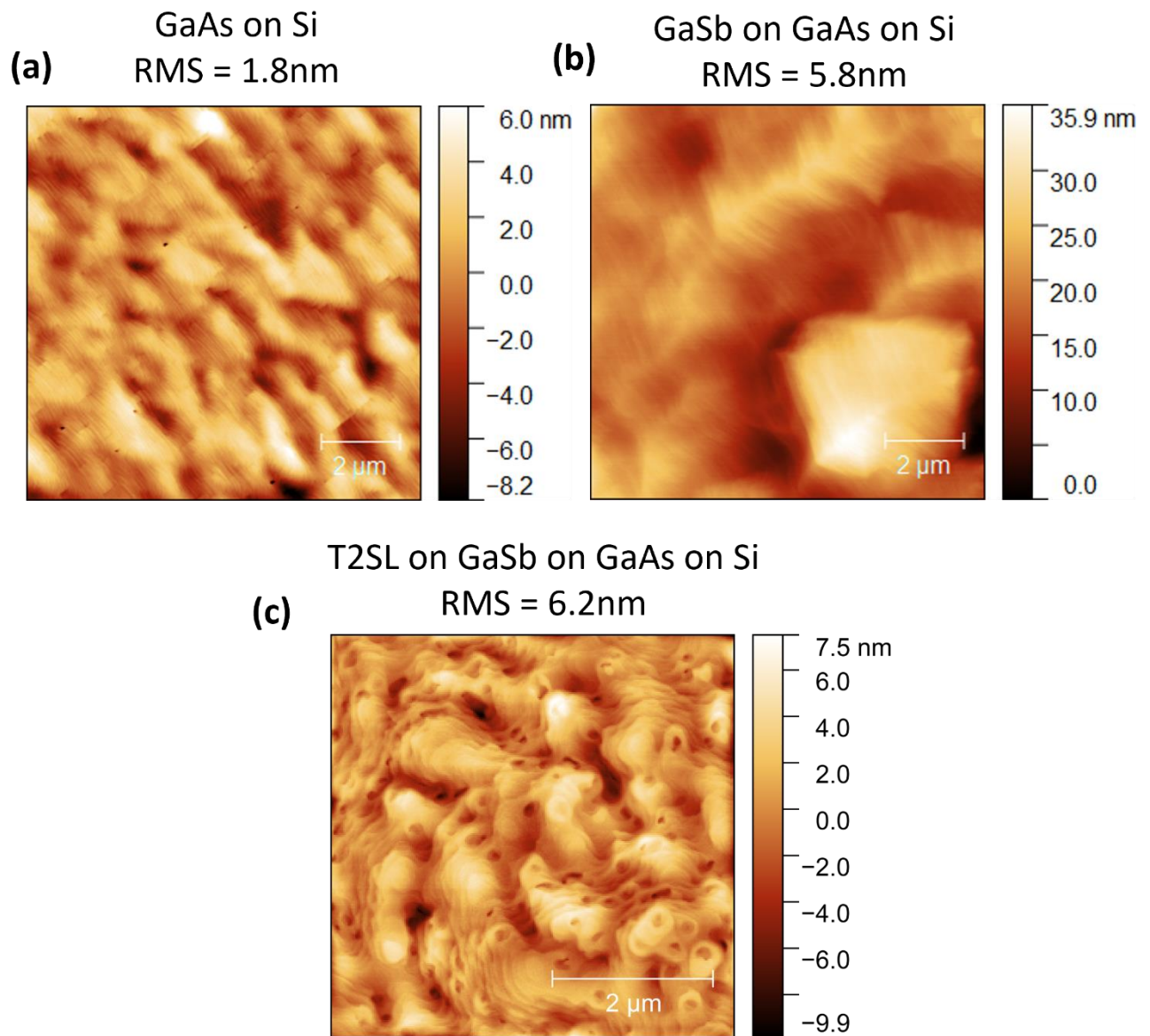


**Fig. 6.18.** AFM scans taken after the growth of (a) GaAs on Si, (b) GaSb on GaAs on Si and (c) the final InAs/InAsSb T2SL grown on the full buffer structure.

As shown in Fig. 6.18, the surface roughness of the T2SLs grown on Si is quite high. This seems to stem from the growth of GaSb on GaAs which is where the biggest increase in both lattice mismatch and surface roughness occurs. It seems that a relatively rough GaAs on Si growth is leading to a much rougher GaSb growth than what was observed on GaAs substrates. After the AFM, X-ray diffraction (XRD) analysis was performed on the sample to confirm its layer composition and to gain insights into its structure, shown in Fig. 6.19.

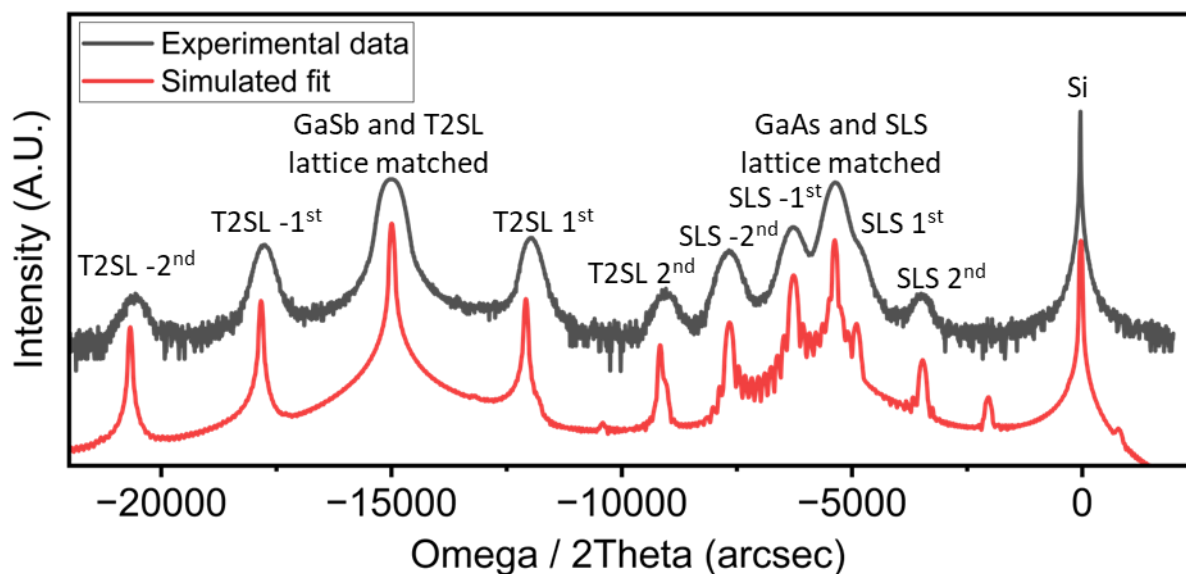


**Fig. 6.19.** Experimental and simulated XRD data of the InAs/InAsSb T2SL integrated onto a Si substrate.

The fitting in Fig. 6.19. was performed using Malvern Panalytical's X'Pert epitaxy software. The simulated structure used for the fitting matched was the same as the one shown in Fig. 6.17. The composition of the InAsSb used in the fitting was  $\text{InAs}_{0.72}\text{Sb}_{0.28}$ .

From the XRD fitting, the GaSb was found to be 101% relaxed and the GaAs 104% relaxed implying there was a small in-plane tensile strain. This over relaxation was attributed to the mismatch of thermal expansion coefficients. While the sample was cooling down from growth temperature to room temperature, the lattice of GaAs and GaSb shrunk faster than Si, producing this residual tensile stress. The thicknesses of the T2SL layers were found to be 16 ML for the InAs layer and 5 ML for the InAsSb layer. The composition of the grown InAsSb was found to be  $\text{InAs}_{0.72}\text{Sb}_{0.28}$ .

Unsurprisingly, the large mismatch has resulted in a much larger FWHM of the T2SL 1<sup>st</sup> satellite peak. The FWHM has increased from 22 arcsec on GaSb to 272 arcsec on Si. This FWHM increase is indicative of a high dislocation density which will be investigated with TEM and ECCI.

Cross-sectional TEM was used to examine the buffer layer structure and to investigate the IMF. The TEM results show a clear reduction in defect density from the Si/GaAs interface up to the T2SL, as can be seen in Fig. 6.20. Fig. 6.20 also shows clear examples of the SLS bending the threading dislocations parallel to the SLS preventing them from travelling up into the T2SL.

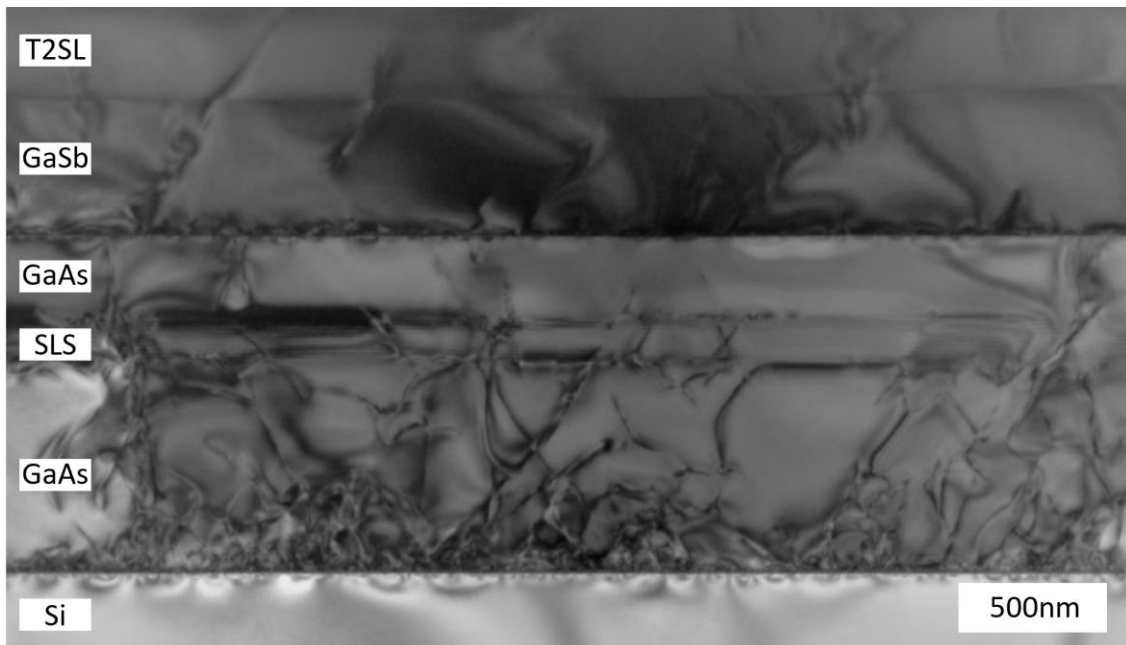


**Fig. 6.20.** Cross-sectional TEM image of the whole T2SL on Si structure, showing a reduction in dislocation density from the GaAs/Si to the T2SL.

The T2SL itself was then directly investigated via TEM, as shown in Fig. 6.21, with distinct layers observed.

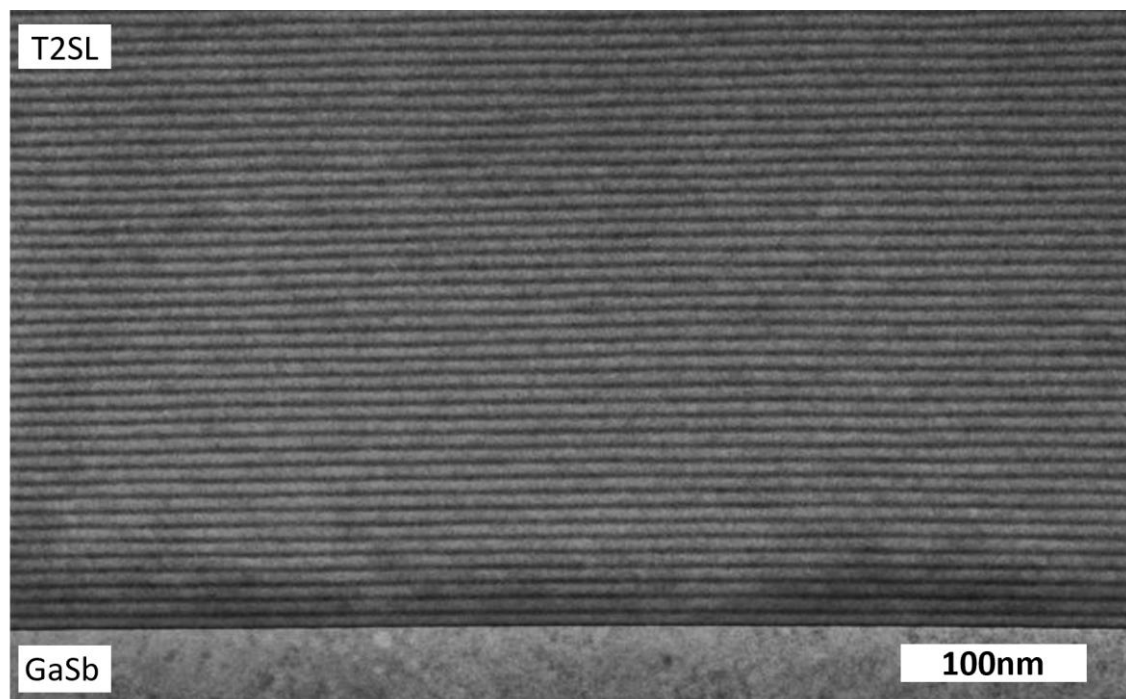


**Fig. 6.21.** Cross-sectional TEM image of the T2SL on Si buffer layer structure, showing distinct stripes indicative of high quality T2SL growth.

The GaSb/GaAs hetero-interface and the formation of the IMF was confirmed in Fig. 6.22. The spacing of the misfits was found to be 5.6 nm which aligns well with previously reported results [207].



**Fig. 6.22.** High resolution TEM image of the interface between the GaAs and GaSb layers showing the misfit dislocations that form the Interfacial misfit array.

Higher resolution TEM was then used to verify the nature of the IMF in the same way as Fig. 6.6. Burgers circuit analysis [208] was performed on 66 different misfit dislocations across the IMF, 34 of which were identified as  $90^\circ$  dislocations and 32 of which  $60^\circ$  dislocations. This gave a  $90^\circ$  dislocations percentage of 52%, which is notably lower than the IMF grown on GaAs substrates. This difference is attributed to the higher surface roughness and dislocation density of the GaAs on Si in comparison to the native GaAs substrate. Further optimisation of the 2-step GaAs buffer and the  $\text{In}_{0.1}\text{Ga}_{0.9}\text{As}/\text{GaAs}$  DFL could lead to an improvement of the GaSb/GaAs interface of the buffer layer structure.

To quantify threading dislocation densities, ECCI was performed on both the GaSb buffer layer and the complete T2SL structure on Si, as seen in Fig. 6.23.

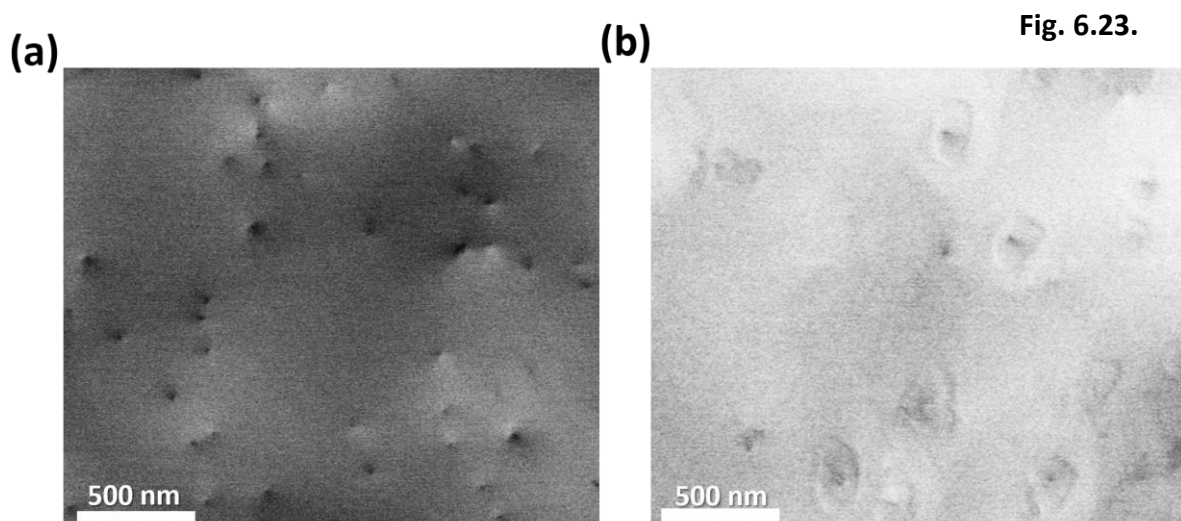


**Fig. 6.23.**

Electron channelling contrast image of the (a) GaSb surface before T2SL growth and (b) the final T2SL surface.

A total surface area of  $120 \mu\text{m}^2$  was analysed and a TDD of  $8.8 \times 10^8 \pm 0.6 \times 10^8 / \text{cm}^2$  was found at the surface of the GaSb before the T2SL growth and a TDD  $6.7 \times 10^8 \pm 0.5 \times 10^8 / \text{cm}^2$  was found at the surface of the T2SL. As expected, the larger lattice mismatch combined with a higher percentage of  $60^\circ$  dislocations in the IMF has resulted in a higher TDD than the GaSb grown on GaAs substrates. Whilst this TDD is higher than  $3 \times 10^7 / \text{cm}^2$  which is the current best result from GaSb grown on Si by MBE, the current state of the art uses a much

thicker 4 $\mu\text{m}$  buffer with more DFLs [210] which naturally increase growth time and therefore cost. As with the growth of GaSb on GaAs substrates, further reduction of dislocation density by implementing more DFLs within the GaSb layer is possible.

FTIR spectroscopy was used to characterise the photoluminescent performance of the T2SL from 77 K to 300 K, as shown in Fig. 6.24. The T2SL exhibited strong PL characteristics with a FWHM of 50 meV at a peak wavelength of 4.5  $\mu\text{m}$  at 77 K. The FWHM was slightly higher than the 26meV which has been observed in MBE grown T2SL structures on GaSb [45]. This increase in FWHM is assumed to be caused by the higher dislocation density from GaSb buffers on Si.

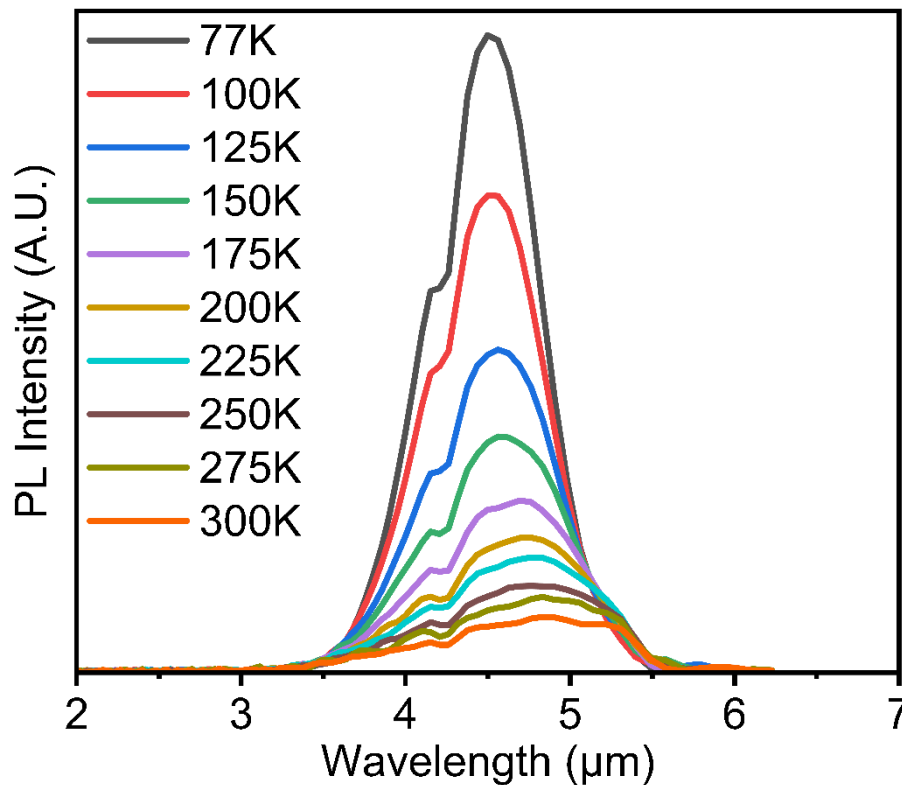


**Fig. 6.24.** Temperature dependent PL data of the InAs/InAsSb T2SL on Si. The dip at 4.3  $\mu\text{m}$  is caused by  $\text{CO}_2$  absorption in the FTIR.

As shown in Fig. 6.25, a temperature dependent redshift of  $-0.06 \pm 0.003$  meV/K was observed which is very similar to previous reports of MBE grown T2SL structures on GaSb substrates [213].

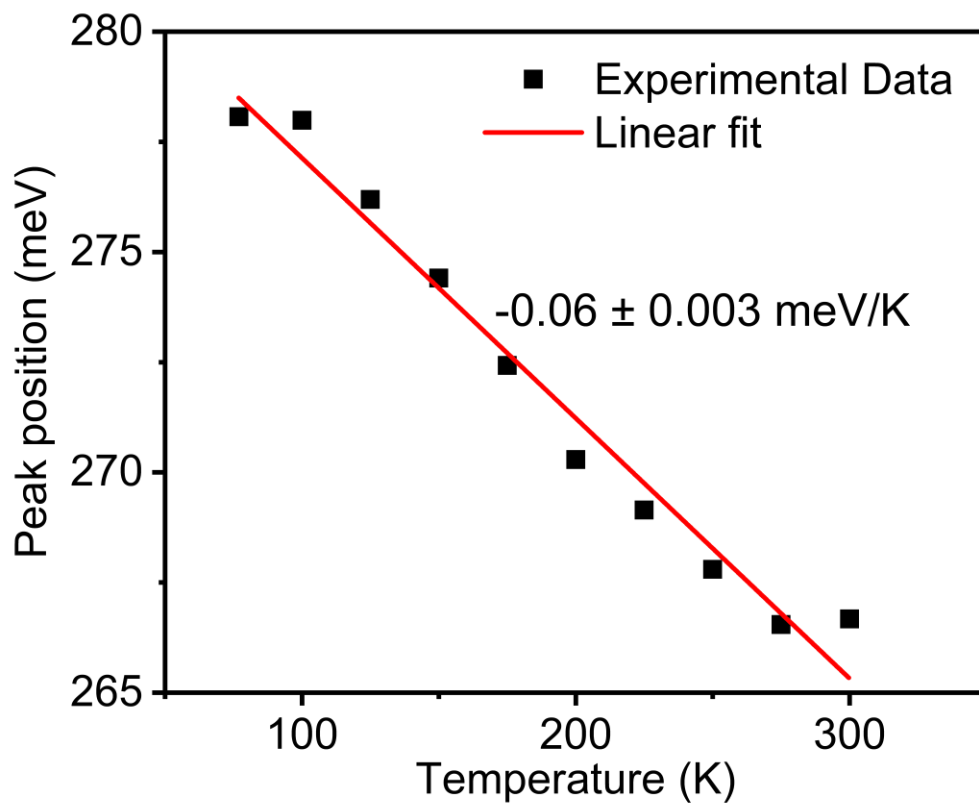


**Fig. 6.25.** Plot showing the temperature dependent redshift of the T2SL.

An Arrhenius plot was created from the temperature dependent PL data to calculate the activation energy of the non-radiative recombination processes to give an indication of the T2SL quality, as shown in Fig. 6.26. The fitting was done using the single-channel non-radiative recombination Arrhenius equation:

$$I(T) = \frac{I(0)}{1 + C e^{-\frac{E_a}{K_B T}}} \quad (6.1)$$

where  $I(0)$  is the integrated PL intensity when the temperature of the T2SL is 0 K,  $C$  is a constant,  $K_B$  is the Boltzmann constant,  $T$  is the temperature and  $E_a$  is the activation energy of the non-radiative recombination process. The activation energy was found to be 51 meV between 200-300 K and 19 meV between 100-200 K. These activation energies are comparable to those grown via MBE on native GaSb substrates [214].

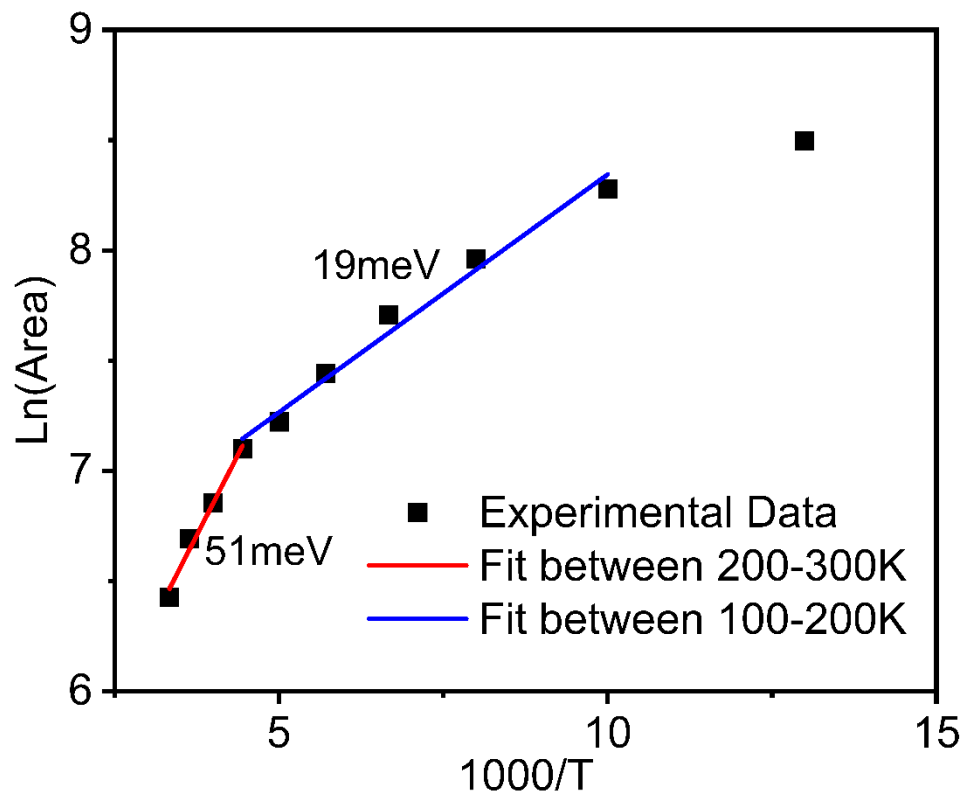


**Fig. 6.26.** Arrhenius plot of the temperature dependent performance used to calculate the activation energy at different temperature ranges.

## 6.4 Summary

The growth temperature and GaSb V/III ratio were investigated to achieve GaSb growth on GaAs substrates with a surface roughness of 1.8 nm RMS. Surface roughness was highly sensitive to variations in both growth temperature and the GaSb V/III ratio, with higher V/III ratios leading to significant surface striping. The temperature and GaSb V/III ratio which gave the best GaSb growth on GaAs were 510°C and 1.5.

As desorption and Sb soaking steps were employed to form an IMF with 70% 90° misfit dislocations, resulting in a surface TDD of  $4.1 \times 10^8 \pm 0.6 \times 10^8 / \text{cm}^2$  for 500nm of GaSb grown on a GaAs substrate with no dislocation filtering layers. While there are examples of lower TDD for MBE grown GaSb on GaAs, these involve much thicker GaSb layers of around 3-6 $\mu\text{m}$  or implement more complex dislocation filtering in order to achieve their lower TDD [202,209].

An InAs/InAsSb PIN photodetector with a 100% cutoff wavelength of 5.25 $\mu\text{m}$  was then successfully grown on the GaAs substrates. The high dislocation density resulted in a high dark current density of  $2.1 \times 10^{-3} \text{ A/cm}^2$  at 77K. Despite this, the dislocation density did not seem to hinder the device's optical performance. The peak responsivity was 2.04 A/W at 3.8 $\mu\text{m}$ , resulting in a peak EQE of 66.7%. This EQE surpasses the current state-of-the-art for both MOCVD and MBE-grown MWIR T2SL detectors on any substrate. The detectivity at 3.8  $\mu\text{m}$  was  $7.44 \times 10^{10} \text{ cm Hz}^{1/2}/\text{W}$  for the PIN grown on GaAs. Although not state-of-the-art, the high responsivity results in a detectivity value that is quite comparable to many other MWIR detectors grown on native substrates.

The InAs/InAsSb T2SL was also integrated onto Si substrates via the use of a 1.5 $\mu\text{m}$  thick GaSb/GaAs/Si buffer structure. The increased lattice mismatch of the Si substrate led to higher roughness in the GaAs, resulting in the IMF having 52% 90° dislocations. The surface roughness of the top of the buffer was 5.8nm and the TDD was  $8.8 \times 10^8 \pm 0.6 \times 10^8 / \text{cm}^2$ . Despite the high roughness and TDD, photoluminescent results of the T2SL were very comparable to MBE grown T2SL structures on GaSb [45]. The photoluminescent results further support the resilience of the InAs/InAsSb T2SL to defects affecting its optical performance.

# Conclusions and Future work

## 7.1. LWIR Detectors made from InAs/GaSb T2SLs

### 7.1.1 Conclusion

An InAs/GaSb T2SL photodetector with a cutoff wavelength of 13.5  $\mu\text{m}$  and a peak detectivity of  $4.43 \times 10^{10} \text{ cm Hz}^{1/2}/\text{W}$  at 77K was grown via MOCVD. The detectivity of these detectors is on par with deep etched detectors grown by MBE at similar cutoff wavelengths. This detectivity indicates that MOCVD is a feasible alternative to the well-established MBE method for growing InAs/GaSb T2SLs in LWIR FPA detectors.

Throughout this work, many different growth parameters including the growth temperature, GaSb V/III ratio, and InAs V/III ratio were all investigated to enable the growth of InAs/GaSb T2SLs with surface roughness less than 0.2 nm RMS, all lattice-matched to InAs substrates. Surface roughness and morphology were found to be highly sensitive to changes in both growth temperature and GaSb V/III ratio. The temperature and GaSb V/III ratio which gave the best InAs/GaSb T2SLs were 510°C and 1.5.

By controlling the As flow, it was possible to grow InAs/GaSb T2SLs lattice-matched to InAs substrates using “GaAs-like” interfacial layers via MOCVD. The wavelength of the InAs/GaSb T2SL can be tuned by adjusting the InAs layer thickness. This technique demonstrated that it is possible to grow InAs/GaSb T2SLs with wavelengths ranging from 4.5 to 12  $\mu\text{m}$  under the same interface growth conditions. This technique eliminates the need for interfacial recalibration when changing wavelengths, simplifying the growth design workflow compared to MBE.

The T2SLs were fabricated into nBn detectors with a 100% cutoff at 13.5  $\mu\text{m}$ . Six different devices were created using varied fabrication steps, investigating three parameters: passivated vs. unpassivated, deep vs. shallow etching, and wet vs. dry etching. Surface passivation with AZ3027 was shown to be successful in reducing surface-related dark currents by up to 92%.

After demonstrating the effectiveness of surface passivation, shallow etched devices were fabricated to compare their performance with deep etched devices. The shallow etched devices exhibited lower dark current density than the deep etched devices, and surface passivation remained beneficial for these shallow devices. Although the shallow detectors outperformed the deep detectors, a trade-off exists between dark current reduction and detector density within a FPA.

Due to this pixel spacing issue and the effectiveness of the surface passivation layer in reducing the sidewall dark current of deep pixels, the deep etched pixels in this work were considered superior to the shallow etched pixels for FPA applications.

The final fabrication parameter investigated was the etching mechanism, comparing dry vs. wet etching. The wet etched devices exhibited lower dark current densities than the dry etched devices. The passivated wet etched device had a dark current density of  $2.2 \times 10^{-2} \text{ A cm}^{-2}$ , the lowest among all the devices in this study. However, this dark current density is still relatively high compared to current state-of-the-art detectors. The high dark current density appears to be caused by the formation of a depletion region within the nBn structure due to the lack of doping control in the barrier and absorber regions.

The devices were then characterised optically. The peak external quantum efficiency (EQE) of the detectors ranged from 54.4 to 44.9% which is exceptionally high for this wavelength when compared to similar devices. This high EQE correlates with the depletion region formation theory that caused the high dark current density.

The best performance was observed in the wet deep passivated detector with a peak detectivity of  $4.43 \times 10^{10} \text{ cm Hz}^{1/2}/\text{W}$  at  $9 \mu\text{m}$ . This detectivity is very comparable to deep etched detectors grown by MBE at similar cutoff wavelengths. This demonstrates that the MOCVD technique can serve as a viable alternative to the more established MBE growth method for InAs/GaSb T2SLs in LWIR FPA detectors.

#### 7.1.2 Future work

The main limiting factor of the LWIR detectors in this work is the dark current density. There are many different methods to try and reduce the dark current density which could be investigated in future work.

**Surface passivation.** AZ3027 was successful at reducing surface related dark currents, however they were still very high. There are many other materials used for surface passivation which could be investigated and compared to AZ3027 in order to find out which is optimal for the InAs/GaSb T2SL. Possible surface passivation materials to investigate include: SU-8, BCB,  $\text{Si}_x\text{N}_y$ ,  $\text{SiO}_2$ , polyimide, and ammonium sulphide. Although many of these materials have been investigated in previous work, many results are not fully conclusive and there is still space to investigate what is the optimum surface passivation material for InAs/GaSb T2SLs.

**Doping control.** Even with theoretically perfect surface passivation, the dark current in the LWIR detectors would still be constrained by high bulk dark current. This elevated dark current appears to stem from the formation of a depletion region within the nBn structure, as both the barrier and absorber were left unintentionally doped to simplify the device design. This unintentional doping likely resulted in different doping levels in the barrier and absorber regions due to their varying InAs layer thicknesses.

One way to quickly improve the doping alignment between the barrier and absorber would be to intentionally dope the barrier layer more n-type. This doping control should better align the doping levels, minimizing the size of the depletion region within the absorber. If successful, this would confirm the hypothesis that the bulk dark current is caused by this depletion region. A more in-depth study could then be conducted to more accurately control and align the doping levels.

However, it is possible that the removal of the depletion region may reduce the EQE of the detector, necessitating a trade-off between EQE and dark current.

**Different device designs.** The nBn device design was selected for its relative simplicity, but other designs have demonstrated lower dark current density. The primary alternative is the complementary barrier infrared detector (CBIRD) design [14], which uses both electron and hole barriers to further reduce dark current compared to the nBn. The challenge with CBIRD lies in growing a viable electron barrier for InAs/GaSb via MOCVD. To date, CBIRD has only been grown using MBE. However, it might be possible to form an effective electron barrier from the T2SL by adjusting the GaSb layer thickness. Although the potential height of this barrier may be insufficient to function effectively, it is worth investigating.

**Changing cutoff wavelength.** Dark current is inherently linked to cutoff wavelength, so if the cutoff wavelength was made shorter the dark current would be reduced. If the target is to optimise performance at around 9-10  $\mu\text{m}$  for human detection it is possible that a shorter cutoff may result in an improved detectivity. Although a shorter cutoff may reduce the EQE at the desired wavelength range, the gains in dark current reduction may be worth the trade.

## 7.2 MWIR Detectors made from InAs/InAsSb T2SLs

### 7.2.1 Conclusion

An InAs/InAsSb T2SL MWIR detector was grown and fabricated with a cutoff wavelength of 5.5 $\mu\text{m}$  and a peak detectivity of  $1.14 \times 10^{12} \text{ cm Hz}^{1/2}/\text{W}$  at 77K.

The InAs/InAsSb T2SL was found to be very sensitive to growth temperature. Increasing the growth temperature beyond 460°C led to an increase in surface roughness, so 460°C was deemed to be the maximum growth temperature for the InAs/InAsSb T2SL. To improve surface roughness and quantum efficiency of the detector, a growth interruption step was introduced after each InAs and InAsSb layer. This growth interruption was very successful at improving interface quality, indicated by a reduction in the first satellite peak FWHM from 134 to 38 arcsecs, which is very comparable to state-of-the-art MBE results. The growth interruption also nearly halved the surface roughness of the T2SL from 0.42 to 0.25 nm.

A 2500 nm thick PIN device was then grown using these growth parameters and fabricated. The fabrication consisted of a deep wet etch and surface passivation from AZ3027, as used in the InAs/GaSb device fabrication. The detectors were found to have very comparable dark current densities to both the current MOCVD-grown MWIR detectors and the other MBE-grown MWIR detectors at both 77K and 150K. At 77K, the InAs/InAsSb PIN diode had a dark current density of  $7.9 \times 10^{-6} \text{ A/cm}^2$ . At 150K the InAs/InAsSb PIN diode had a dark current density of  $1.1 \times 10^{-3} \text{ A/cm}^2$ . Current state-of-the-art dark current densities for MOCVD-grown InAs/InAsSb non-barrier detectors at this wavelength and bias are around  $5 \times 10^{-6} \text{ A/cm}^2$  at 77K [33] and  $1.5 \times 10^{-3} \text{ A/cm}^2$  at 150K [47]. However, the lack of a barrier seems to prevent these MOCVD-grown PINs from reaching the true state-of-the-art dark current performance achieved by MBE-grown devices, especially at 150K. The peak EQE of the detector was 59.3% at 77K and 62.5% at 150K, and the cutoff wavelength was between 5.25 and 5.5  $\mu\text{m}$ . The EQE for these detectors is above the current state-of-the-art for both

MOCVD and MBE-grown MWIR T2SL detectors. This high EQE provides further evidence of the high-quality interfaces produced via the growth interruption technique.

The detectivity at 3.8  $\mu\text{m}$  was  $1.14 \times 10^{12}$   $\text{cm Hz}^{1/2}/\text{W}$  at 77K and  $1.00 \times 10^{11}$   $\text{cm Hz}^{1/2}/\text{W}$  at 150K. Current state of the art detectivity for MOCVD grown InAs/InAsSb non barrier detectors at this wavelength are around  $3 \times 10^{12}$   $\text{cm Hz}^{1/2}/\text{W}$  at 77K [33] and  $1.2 \times 10^{11}$   $\text{cm Hz}^{1/2}/\text{W}$  at 150K [47]. These detectivity values are also somewhat competitive with the current MBE results. The main discrepancy is caused by the higher dark current due to the lack of barrier. This provides good evidence that MOCVD grown InAs/InAsSb T2SLs are a viable technology for MWIR photodetectors even if they are currently restricted to non-barrier-based architecture. Although the development of viable MOCVD-based barrier solutions might hinder the InAs/InAsSb PIN from achieving state-of-the-art performance, the significant economic advantages of MOCVD over MBE, along with the scalability benefits of T2SLs compared to MCT, could be considered more beneficial overall, even with the performance limitations.

### 7.2.2 Future work

As with the LWIR detectors, the main limiting factor for the MWIR InAs/InAsSb detectors is dark current. Therefore, the future work also focuses on reducing dark current density.

**Surface passivation.** The same surface passivation conclusions apply to both the InAs/InAsSb as well as the InAs/GaSb detectors. Possible surface passivation materials to investigate include: SU-8, BCB,  $\text{Si}_x\text{N}_y$ ,  $\text{SiO}_2$ , polyimide, and ammonium sulphide. It is likely that the optimal surface passivation material is different for each T2SL and so the future work of optimising the surface passivation should be done for both InAs/InAsSb and InAs/GaSb T2SLs.

**Size of “I” region.** The size of the intrinsic (I) region in a PIN diode effects both the EQE and the dark current of the device. In order to maximise EQE, a relatively large 1.5  $\mu\text{m}$  I region was used. However, this large I region may have been responsible in the higher dark current. Investigating exactly how the size of the I region impacts both the EQE and dark current for these devices would allow for an optimal size to be calculated. This should lead to a device with improved detectivity.

**Growing barriers.** The main design constraint of the InAs/InAsSb is the lack of easy Al-free barriers, which can be used to grow barrier-based device designs which have reduced dark current. In order to overcome this constraint, the MOCVD growth of AlSb based materials must be investigated. A possible solution is to use more novel precursors such as TTBAI or DMEAL which crack at lower temperatures to the standard TMAI allowing for AlSb to be grown at lower temperatures. In the past this approach has suffered from the novel precursors being lower purity, however there may be justification to revisit this approach as the precursor purification process is continually optimised. They may also be scope for growth of AlSb using TMAI. It is possible that if the barrier is thin enough, the benefits of the barrier may outweigh the performance degradation caused by the unintentional carbon and oxygen incorporation.

## 7.3 Growth of InAs/InAsSb T2SLs on non-native Substrates

### 7.3.1 Conclusion

The InAs/InAsSb T2SL was successfully integrated onto both GaAs and Si substrates.

An InAs/InAsSb PIN photodetector with a 100% cutoff wavelength of 5.25 $\mu\text{m}$  and a detectivity of  $7.44 \times 10^{10} \text{ cm Hz}^{1/2}/\text{W}$  at 77K was grown on GaAs substrates.

To achieve GaSb growth on GaAs substrates with a surface roughness of 1.8 nm RMS, the growth temperature and GaSb V/III ratio were investigated. Surface roughness was found to be highly sensitive to variations in both growth temperature and the GaSb V/III ratio, with higher V/III ratios resulting in significant surface striping. The temperature and GaSb V/III ratio which gave the best GaSb growth on GaAs were 510°C and 1.5.

As desorption and Sb soaking steps were employed to form an IMF with 70% 90° misfit dislocations, resulting in a surface TDD of  $4.1 \times 10^8 \pm 0.6 \times 10^8 / \text{cm}^2$  for 500nm of GaSb grown on a GaAs substrate with no dislocation filtering layers. While there are examples of lower TDD for MBE grown GaSb on GaAs, these involve much thicker GaSb layers of around 3-6 $\mu\text{m}$  or implement more complex dislocation filtering in order to achieve their lower TDD [202,209].

The high dislocation density resulted in a high dark current density of  $2.1 \times 10^{-3} \text{ A/cm}^2$  at 77K. However, this high TDD did not significantly impact the device's optical performance as the peak responsivity was 2.04 A/W at 3.8  $\mu\text{m}$ , yielding a peak EQE of 66.7%, which exceeds the current state-of-the-art for both MOCVD and MBE-grown MWIR T2SL detectors on any substrate. The detectivity at 3.8  $\mu\text{m}$  was  $7.44 \times 10^{10} \text{ cm Hz}^{1/2}/\text{W}$  for the PIN grown on GaAs. Although not state-of-the-art, the high responsivity leads to a detectivity value that is quite comparable to many other MWIR detectors grown on native substrates.

The InAs/InAsSb T2SL was also integrated onto Si substrates using a 1.5  $\mu\text{m}$  thick GaSb/GaAs/Si buffer structure. The increased lattice mismatch of the Si substrate led to higher roughness in the GaAs, resulting in the IMF having 52% 90° dislocations. The surface roughness of the top of the buffer was 5.8nm and the TDD was  $8.8 \times 10^8 \pm 0.6 \times 10^8 / \text{cm}^2$ . Despite the high roughness and TDD, photoluminescent results of the T2SL were very comparable to MBE grown T2SL structures on GaSb [45]. These photoluminescent results further support the resilience of the InAs/InAsSb T2SL to defects affecting its optical performance.

### 7.3.2 Future work

The main challenge for the growth of InAs/InAsSb T2SLs on both GaAs and Si substrates is one of dislocations. The buffer structures used in this work were kept relatively simple, however, adding additional defect filtering layers should result in a reduction in threading dislocation densities. Additionally, there is still plenty of scope for further optimisation in both the growth of GaSb on GaAs and GaAs on Si.

**Dislocation filtering layers in the GaSb.** Whilst the IMF is able to greatly reduce the TDD caused by the GaSb/GaAs interface, there is still a high number of threading dislocations created. GaSb/AlSb dislocation filter superlattices have been shown to effectively reduce the TDD of MBE grown GaSb on Si [210]. Whilst the growth of high quality AlSb is challenging via MOCVD, this may not be a problem since the AlSb will all be contained in the buffer layer, far from the device. This defect filtering technique could therefore be transferred into this work, helping to reduce TDD.

**Further optimisation of the growth of GaSb on GaAs.** An optimised IMF growth sequence is vital for low TDD GaSb on GaAs. The timings and temperatures of the IMF growth sequence were not fully optimised with respect to the percentage of 90° dislocations within the IMF. With more time there could be further increases to the number of 90° dislocations within the IMF resulting in a lower TDD.

**Further optimisation of the growth of GaAs on Si.** An optimal IMF requires a smooth GaAs surface. Therefore, if the GaSb/GaAs/Si buffer layer is to minimise its TDD, the growth of GaAs on Si needs to be optimised. There is still space to further optimise the Si surface preparation and GaAs growth conditions in order to minimise the GaAs surface roughness.

# References

- [1] R. Brown, B.P. Ratiu, H. Jia, K.M. Azizur-Rahman, M. Dang, M. Tang, B. Liang, H. Liu, Q. Li, Mid-infrared InAs/InAsSb type-II superlattices grown on silicon by MOCVD, *J. Cryst. Growth* 598 (2022) 126860. <https://doi.org/10.1016/j.jcrysgro.2022.126860>.
- [2] S. Hanna, A. Bauer, H. Bitterlich, D. Eich, M. Finck, H. Figgemeier, W. Gross, K.M. Mahlein, A. Wegmann, Space application requirement breakdown and sensor concept implementation for MCT-based LWIR and VLWIR 2D high-performance focal plane detector arrays at AIM, *J. Electron. Mater.* 49 (2020) 6946–6956. <https://doi.org/10.1007/s11664-020-08224-5>.
- [3] B. Asici, A. San, B. Barutcu, H.C. Eroglu, A. Tolunguc, C. Ozgit-Akgun, E. Akca, U. Tumkaya, R. Kepenek, C. Tunca, M. Akbulut, O.L. Nuzumlali, E. Inceturkmen, The status of LWIR MCT detector development at ASELSAN, in: *Infrared Technol. Appl.* XLV, SPIE, 2019: pp. 290–298. <https://doi.org/10.1117/12.2518867>.
- [4] A. Haddadi, M. Razeghi, Bias-selectable three-color short-, extended-short-, and mid-wavelength infrared photodetectors based on type-II InAs/GaSb/AlSb superlattices, *Opt. Lett.* 42 (2017) 4275–4278. <https://doi.org/10.1364/OL.42.004275>.
- [5] E. Plis, J.B. Rodriguez, G. Balakrishnan, Y.D. Sharma, H.S. Kim, T. Rotter, S. Krishna, Mid-infrared InAs/GaSb strained layer superlattice detectors with nBn design grown on a GaAs substrate, *Semicond. Sci. Technol.* 25 (2010) 085010. <https://doi.org/10.1088/0268-1242/25/8/085010>.
- [6] N. Gautam, S. Myers, A.V. Barve, B. Klein, Edward.P. Smith, Dave.R. Rhiger, H.S. Kim, Z.-B. Tian, S. Krishna, Barrier engineered infrared photodetectors based on Type-II InAs/GaSb strained layer superlattices, *IEEE J. Quantum Electron.* 49 (2013) 211–217. <https://doi.org/10.1109/JQE.2012.2236643>.
- [7] G. Bishop, E. Plis, J.B. Rodriguez, Y.D. Sharma, H.S. Kim, L.R. Dawson, S. Krishna, nBn detectors based on InAs/GaSb type-II strain layer superlattice, *J. Vac. Sci. Technol. B Microelectron. Nanometer Struct. Process. Meas. Phenom.* 26 (2008) 1145–1148. <https://doi.org/10.1116/1.2830627>.
- [8] J. Huang, Z. Xie, Y. Chen, J.E. Bowers, B. Chen, High speed mid-wave infrared uni-traveling carrier photodetector, *IEEE J. Quantum Electron.* 56 (2020) 1–7. <https://doi.org/10.1109/JQE.2020.3003038>.
- [9] P. Christol, R. Alchaar, J.-B. Rodriguez, L. Höglund, S. Naureen, R.M. von Würtemberg, C. Asplund, E. Costard, A. Rouvié, J. Brocal, O. Saint-Pé, InAs/GaSb Type-II superlattice (T2SL) photodetector operating in the very-long wavelength infrared (VLWIR) spectral domain, in: *Int. Conf. Space Opt. — ICSO 2018*, SPIE, 2019: pp. 2394–2400. <https://doi.org/10.1117/12.2536158>.
- [10] R. Ivanov, L. Höglund, D. Ramos, S. Naureen, M. Pozzi, S. Almqvist, S. Becanovic, D. Rihtnesberg, P. Tinghag, A. Smuk, S. Fattala, S. Smuk, M. Delmas, E. Costard, T2SL development for space at IRnova: from eSWIR to VLWIR, *11151 (2019) 1115111*. <https://doi.org/10.1117/12.2533247>.
- [11] S. Gunapala, S. Rafol, D. Ting, A. Soibel, A. Khoshakhlagh, S. Keo, B. Pepper, A. Fisher, C. Hill, K.-K. Choi, A. D’Souza, C. Masterjohn, S.R. Babu, P. Ghuman, Type-II strained-layer superlattice digital focal plane arrays for earth remote sensing instruments, in: *Sens. Syst. -Gener. Satell. XXIII*, SPIE, 2019: pp. 186–193. <https://doi.org/10.1117/12.2527731>.

- [12] P.C. Klipstein, E. Avnon, D. Azulai, Y. Benny, R. Fraenkel, A. Glozman, E. Hojman, O. Klin, L. Krasovitsky, L. Langof, I. Lukomsky, M. Nitzani, I. Shtrichman, N. Rappaport, N. Snapi, E. Weiss, A. Tuito, Type II superlattice technology for LWIR detectors, in: *Infrared Technol. Appl. XLII*, SPIE, 2016: pp. 216–225. <https://doi.org/10.1117/12.2222776>.
- [13] L. Höglund, C. Asplund, R.M. von Würtemberg, A. Gamfeldt, H. Kataria, D. Lantz, S. Smuk, E. Costard, H. Martijn, Advantages of T2SL: results from production and new development at IRnova, in: *Infrared Technol. Appl. XLII*, SPIE, 2016: pp. 250–259. <https://doi.org/10.1117/12.2227466>.
- [14] D.Z.-Y. Ting, C.J. Hill, A. Soibel, S.A. Keo, J.M. Mumolo, J. Nguyen, S.D. Gunapala, A high-performance long wavelength superlattice complementary barrier infrared detector, *Appl. Phys. Lett.* 95 (2009) 023508. <https://doi.org/10.1063/1.3177333>.
- [15] X. Hao, Y. Zhao, Q. Wu, X. Li, Y. Teng, M. Xiong, Y. Huang, B. Chen, J. Huang, Z. Deng, H. Yang, InAs/GaSb superlattice photodetector with cutoff wavelength around 12  $\mu\text{m}$  based on an Al-free nBn structure grown by MOCVD, *Semicond. Sci. Technol.* 34 (2019) 065013. <https://doi.org/10.1088/1361-6641/ab2006>.
- [16] M. Huang, J. Chen, Z. Xu, J. Xu, Z. Bai, F. Wang, Y. Zhou, A. Huang, R. Ding, L. He, InAs/GaAsSb Type-II Superlattice LWIR Focal Plane Arrays Detectors Grown on InAs Substrates, *IEEE Photonics Technol. Lett.* 32 (2020) 453–456. <https://doi.org/10.1109/LPT.2020.2973204>.
- [17] Y. Shi, R. Hu, G. Deng, W. He, J. Feng, M. Fang, X. Li, J. Deng, InAs/Ga(In)Sb type-II superlattices short/middle dual color infrared detectors, in: *Infrared Technol. Appl. XLI*, SPIE, 2015: pp. 136–143. <https://doi.org/10.1117/12.2176196>.
- [18] Z. Deng, D. Guo, J. Huang, H. Liu, J. Wu, B. Chen, Mid-wave infrared InAs/GaSb type-II superlattice photodetector with n-B-p design grown on GaAs Substrate, *IEEE J. Quantum Electron.* 55 (2019) 1–5. <https://doi.org/10.1109/JQE.2019.2917946>.
- [19] X. Wang, J. Li, Y. Yan, M. Zhang, T. Wen, M. Liu, S. Yu, Y. Zhang, Dark current analysis of InAs/GaSb type II superlattice infrared detectors, *IEEE Trans. Electron Devices* 70 (2023) 5517–5527. <https://doi.org/10.1109/TED.2023.3314574>.
- [20] E. Plis, J.B. Rodriguez, H.S. Kim, G. Bishop, Y.D. Sharma, L.R. Dawson, S. Krishna, S.J. Lee, C.E. Jones, V. Gopal, Type II InAs/GaSb strain layer superlattice detectors with p-on-n polarity, *Appl. Phys. Lett.* 91 (2007) 133512. <https://doi.org/10.1063/1.2790078>.
- [21] Z. Deng, D. Guo, C.G. Burguete, Z. Xie, J. Huang, H. Liu, J. Wu, B. Chen, Demonstration of Si based InAs/GaSb type-II superlattice p-i-n photodetector, *Infrared Phys. Technol.* 101 (2019) 133–137. <https://doi.org/10.1016/j.infrared.2019.06.011>.
- [22] B.-M. Nguyen, D. Hoffman, E.K. Huang, S. Bogdanov, P.-Y. Delaunay, M. Razeghi, M.Z. Tidrow, Demonstration of midinfrared type-II InAs/GaSb superlattice photodiodes grown on GaAs substrate, *Appl. Phys. Lett.* 94 (2009) 223506. <https://doi.org/10.1063/1.3148326>.
- [23] M. Korkmaz, B. Arikan, Y.E. Suyolcu, B. Aslan, U. Serincan, Performance evaluation of InAs/GaSb superlattice photodetector grown on GaAs substrate using AlSb interfacial misfit array, *Semicond. Sci. Technol.* 33 (2018) 035002. <https://doi.org/10.1088/1361-6641/aaa7a0>.
- [24] T. Tansel, M. Hostut, Y. Ergun, Electrical and optical performances with extracted minority carrier lifetimes of InAs/GaSb SL photodetector operating in the mid wavelength infrared range, *Superlattices Microstruct.* 111 (2017) 1211–1216. <https://doi.org/10.1016/j.spmi.2017.08.022>.

- [25] B.-M. Nguyen, D. Hoffman, E.K. Huang, P.-Y. Delaunay, M. Razeghi, Background limited long wavelength infrared type-II InAs/GaSb superlattice photodiodes operating at 110 K, *Appl. Phys. Lett.* 93 (2008) 123502. <https://doi.org/10.1063/1.2978330>.
- [26] J. Xu, Z. Xu, Z. Bai, M. Huang, A. Huang, L. Zheng, Y. Zhou, H. Chen, J. Chen, R. Ding, L. He, Effects of etching processes on surface dark current of long-wave infrared InAs/GaSb superlattice detectors, *Infrared Phys. Technol.* 107 (2020) 103277. <https://doi.org/10.1016/j.infrared.2020.103277>.
- [27] A. Soibel, D.Z. Ting, S.B. Rafol, A.M. Fisher, S.A. Keo, A. Khoshakhlagh, S.D. Gunapala, Mid-wavelength infrared InAsSb/InAs nBn detectors and FPAs with very low dark current density, *Appl. Phys. Lett.* 114 (2019) 161103. <https://doi.org/10.1063/1.5092342>.
- [28] D. Wu, A. Dehzangi, M. Razeghi, Demonstration of mid-wavelength infrared nBn photodetectors based on type-II InAs/InAs<sub>1-x</sub>Sb<sub>x</sub> superlattice grown by metal-organic chemical vapor deposition, *Appl. Phys. Lett.* 115 (2019) 061102. <https://doi.org/10.1063/1.5100617>.
- [29] G. Deng, X. Song, M. Fan, T. Xiao, Z. Luo, N. Chen, W. Yang, Y. Zhang, Upside-down InAs/InAs<sub>1-x</sub>Sb<sub>x</sub> type-II superlattice-based nBn mid-infrared photodetectors with an AlGaAsSb quaternary alloy barrier, *Opt. Express* 28 (2020) 13616–13624. <https://doi.org/10.1364/OE.387297>.
- [30] A. Dehzangi, D. Wu, R. McClintock, J. Li, M. Razeghi, Planar nBn type-II superlattice mid-wavelength infrared photodetectors using zinc ion-implantation, *Appl. Phys. Lett.* 116 (2020) 221103. <https://doi.org/10.1063/5.0010273>.
- [31] H.S. Kim, O.O. Cellek, Z.-Y. Lin, Z.-Y. He, X.-H. Zhao, S. Liu, H. Li, Y.-H. Zhang, Long-wave infrared nBn photodetectors based on InAs/InAsSb type-II superlattices, *Appl. Phys. Lett.* 101 (2012) 161114. <https://doi.org/10.1063/1.4760260>.
- [32] M. Razeghi, A. Dehzangi, D. Wu, R. McClintock, Y. Zhang, Q. Durlin, J. Li, F. Meng, Antimonite-based gap-engineered type-II superlattice materials grown by MBE and MOCVD for the third generation of infrared imagers, in: *Infrared Technol. Appl. XLV*, SPIE, 2019: pp. 108–125. <https://doi.org/10.1117/12.2521173>.
- [33] D. Wu, A. Dehzangi, J. Li, M. Razeghi, High performance Zn-diffused planar mid-wavelength infrared type-II InAs/InAs<sub>1-x</sub>Sb<sub>x</sub> superlattice photodetector by MOCVD, *Appl. Phys. Lett.* 116 (2020) 161108. <https://doi.org/10.1063/5.0005326>.
- [34] T. Schuler-Sandy, S. Myers, B. Klein, N. Gautam, P. Ahirwar, Z.-B. Tian, T. Rotter, G. Balakrishnan, E. Plis, S. Krishna, Gallium free type II InAs/InAs<sub>x</sub>Sb<sub>1-x</sub> superlattice photodetectors, *Appl. Phys. Lett.* 101 (2012) 071111. <https://doi.org/10.1063/1.4745926>.
- [35] R. Hao, Y. Ren, S. Liu, J. Guo, G. Wang, Y. Xu, Z. Niu, Fabrication and characterization of high lattice matched InAs/InAsSb superlattice infrared photodetector, *J. Cryst. Growth* 470 (2017) 33–36. <https://doi.org/10.1016/j.jcrysgro.2017.03.052>.
- [36] T. Schuler-Sandy, B. Klein, L. Casias, S. Mathews, C. Kadlec, Z. Tian, E. Plis, S. Myers, S. Krishna, Growth of InAs–InAsSb SLS through the use of digital alloys, *J. Cryst. Growth* 425 (2015) 29–32. <https://doi.org/10.1016/j.jcrysgro.2015.02.096>.
- [37] D.H. Wu, A. Dehzangi, Y.Y. Zhang, M. Razeghi, Demonstration of long wavelength infrared type-II InAs/InAs<sub>1-x</sub>Sb<sub>x</sub> superlattices photodiodes on GaSb substrate grown by metalorganic chemical vapor deposition, *Appl. Phys. Lett.* 112 (2018) 241103. <https://doi.org/10.1063/1.5035308>.

- [38] S.A. Pour, E.K. Huang, G. Chen, A. Haddadi, B.-M. Nguyen, M. Razeghi, High operating temperature midwave infrared photodiodes and focal plane arrays based on type-II InAs/GaSb superlattices, *Appl. Phys. Lett.* 98 (2011) 143501. <https://doi.org/10.1063/1.3573867>.
- [39] D.Z. Ting, S.B. Rafol, S.A. Keo, J. Nguyen, A. Khoshakhlagh, A. Soibel, L. Höglund, A.M. Fisher, E.M. Luong, J.M. Mumolo, J.K. Liu, S.D. Gunapala, InAs/InAsSb type-II superlattice mid-wavelength infrared focal plane array with significantly higher operating temperature than InSb, *IEEE Photonics J.* 10 (2018) 1–6. <https://doi.org/10.1109/JPHOT.2018.2877632>.
- [40] D. Wu, J. Li, A. Dehzangi, M. Razeghi, High performance InAs/InAsSb type-II superlattice mid-wavelength infrared photodetectors with double barrier, *Infrared Phys. Technol.* 109 (2020) 103439. <https://doi.org/10.1016/j.infrared.2020.103439>.
- [41] G. Deng, D. Chen, S. Yang, C. Yang, J. Yuan, W. Yang, Y. Zhang, High operating temperature pBn barrier mid-wavelength infrared photodetectors and focal plane array based on InAs/InAsSb strained layer superlattices, *Opt. Express* 28 (2020) 17611–17619. <https://doi.org/10.1364/OE.395770>.
- [42] E. Delli, V. Letka, P.D. Hodgson, E. Repiso, J.P. Hayton, A.P. Craig, Q. Lu, R. Beanland, A. Krier, A.R.J. Marshall, P.J. Carrington, Mid-infrared InAs/InAsSb superlattice nBn photodetector monolithically integrated onto silicon, *ACS Photonics* 6 (2019) 538–544. <https://doi.org/10.1021/acsp Photonics.8b01550>.
- [43] D.Z. Ting, A. Soibel, A. Khoshakhlagh, S.B. Rafol, S.A. Keo, L. Höglund, A.M. Fisher, E.M. Luong, S.D. Gunapala, Mid-wavelength high operating temperature barrier infrared detector and focal plane array, *Appl. Phys. Lett.* 113 (2018) 021101. <https://doi.org/10.1063/1.5033338>.
- [44] D. Wu, J. Li, A. Dehzangi, M. Razeghi, Mid-wavelength infrared high operating temperature pBn photodetectors based on type-II InAs/InAsSb superlattice, *AIP Adv.* 10 (2020) 025018. <https://doi.org/10.1063/1.5136501>.
- [45] J. Kim, H. Yuan, J. Kimchi, J. Lei, E. Rangel, P. Dreiske, A. Ikhlassi, HOT MWIR InAs/InAsSb T2SL discrete photodetector development, in: *Infrared Technol. Appl. XLIV, SPIE, 2018*: pp. 108–115. <https://doi.org/10.1117/12.2303973>.
- [46] J. Kim, H. Yuan, A. Rumyantsev, P. Bey, D. Bond, J. Kimchi, M.G. DeForest, Characterization of HOT MWIR InAs/InAsSb T2SL discrete photodetectors, in: *Opt. Compon. Mater. XVII, SPIE, 2020*: pp. 86–94. <https://doi.org/10.1117/12.2553686>.
- [47] D. Wu, Q. Durlin, A. Dehzangi, Y. Zhang, M. Razeghi, High quantum efficiency mid-wavelength infrared type-II InAs/InAs 1–x Sb x superlattice photodiodes grown by metal-organic chemical vapor deposition, *Appl. Phys. Lett.* 114 (2019) 011104. <https://doi.org/10.1063/1.5058714>.
- [48] W.E. Tennant, D. Lee, M. Zandian, E. Piquette, M. Carmody, MBE HgCdTe technology: a very general solution to IR detection, described by “Rule 07”, a very convenient heuristic, *J. Electron. Mater.* 37 (2008) 1406–1410. <https://doi.org/10.1007/s11664-008-0426-3>.
- [49] M.R.F. <https://www.marketresearchfuture.com>, Infrared Sensor Market Segment, Size, Share, Global Trends 2032, (n.d.). <https://www.marketresearchfuture.com/reports/infrared-sensor-market-8625> (accessed July 15, 2024).

- [50] A. Akula, R. Ghosh, H.K. Sardana, Thermal imaging and its application in defence systems, *AIP Conf. Proc.* 1391 (2011) 333–335. <https://doi.org/10.1063/1.3643540>.
- [51] J.P. CONSORTIUM (EPIC) EUROPEAN PHOTONICS INDUSTRY, Pilot line underscores untapped potential of mid-IR Spectroscopy, (n.d.). [https://www.photonics.com/Articles/Pilot\\_Line\\_Underscores\\_Untapped\\_Potential\\_of/a61245](https://www.photonics.com/Articles/Pilot_Line_Underscores_Untapped_Potential_of/a61245) (accessed September 13, 2024).
- [52] D. Kesztyüs, S. Brucher, C. Wilson, T. Kesztyüs, Use of infrared thermography in medical diagnosis, screening, and disease monitoring: a scoping review, *Medicina (Mex.)* 59 (2023) 2139. <https://doi.org/10.3390/medicina59122139>.
- [53] Y. Zhang, L. Wang, X. Jiang, Y. Zeng, Y. Dai, An efficient LiDAR-based localization method for self-driving cars in dynamic environments, *Robotica* 40 (2022) 38–55. <https://doi.org/10.1017/S0263574721000369>.
- [54] D. Kwan, M. Kesaria, E.A. Anyebe, D. Huffaker, Recent trends in 8–14  $\mu\text{m}$  type-II superlattice infrared detectors, *Infrared Phys. Technol.* 116 (2021) 103756. <https://doi.org/10.1016/j.infrared.2021.103756>.
- [55] A. Rogalski, HgCdTe infrared detector material: history, status and outlook, *Rep. Prog. Phys.* 68 (2005) 2267. <https://doi.org/10.1088/0034-4885/68/10/R01>.
- [56] A. Rogalski, P. Martyniuk, M. Kopytko, InAs/GaSb type-II superlattice infrared detectors: Future prospect, *Appl. Phys. Rev.* 4 (2017) 031304. <https://doi.org/10.1063/1.4999077>.
- [57] E.H. Steenbergen, B.C. Connelly, G.D. Metcalfe, H. Shen, M. Wraback, D. Lubyshev, Y. Qiu, J.M. Fastenau, A.W.K. Liu, S. Elhamri, O.O. Celtek, Y.-H. Zhang, Significantly improved minority carrier lifetime observed in a long-wavelength infrared III-V type-II superlattice comprised of InAs/InAsSb, *Appl. Phys. Lett.* 99 (2011) 251110. <https://doi.org/10.1063/1.3671398>.
- [58] A.D. Prins, M.K. Lewis, Z.L. Bushell, S.J. Sweeney, S. Liu, Y.-H. Zhang, Evidence for a defect level above the conduction band edge of InAs/InAsSb type-II superlattices for applications in efficient infrared photodetectors, *Appl. Phys. Lett.* 106 (2015) 171111. <https://doi.org/10.1063/1.4919549>.
- [59] C. González Burguete, D. Guo, P. Jurczak, F. Cui, M. Tang, W. Chen, Z. Deng, Y. Chen, M. Gutiérrez, B. Chen, H. Liu, J. Wu, Direct growth of InAs/GaSb type II superlattice photodiodes on silicon substrates, *IET Optoelectron.* 12 (2018) 2–4. <https://doi.org/10.1049/iet-opt.2017.0078>.
- [60] E. Tournié, L. Monge Bartolome, M. Rio Calvo, Z. Loghmari, D.A. Díaz-Thomas, R. Teissier, A.N. Baranov, L. Cerutti, J.-B. Rodriguez, Mid-infrared III–V semiconductor lasers epitaxially grown on Si substrates, *Light Sci. Appl.* 11 (2022) 165. <https://doi.org/10.1038/s41377-022-00850-4>.
- [61] J.K. Jiang, Y. Li, F.R. Chang, S.N. Cui, W.Q. Chen, D.W. Jiang, G.W. Wang, Y.Q. Xu, Z.C. Niu, R. Che, C. Zhang, L. Huang, MBE growth of mid-wavelength infrared photodetectors based on high quality InAs/AlAs/InAsSb superlattice, *J. Cryst. Growth* 564 (2021) 126109. <https://doi.org/10.1016/j.jcrysgro.2021.126109>.
- [62] V. Saprisky, A. Prokhorov, *Blackbody Radiometry*, vol. 1: Fundamentals, 2020. <https://doi.org/10.1007/978-3-030-57789-6>.
- [63] The Atmospheric Window | National Oceanic and Atmospheric Administration, (n.d.). <https://www.noaa.gov/jetstream/satellites/absorb> (accessed December 4, 2024).
- [64] S. Maimon, G.W. Wicks, nBn detector, an infrared detector with reduced dark current and higher operating temperature, *Appl. Phys. Lett.* 89 (2006) 151109. <https://doi.org/10.1063/1.2360235>.

- [65] X. Li, D. Jiang, Y. Zhang, D. Wang, Q. Yu, T. Liu, H. Ma, L. Zhao, Investigation of dark current mechanisms on type-II InAs/GaSb superlattice very long wavelength infrared detectors, *J. Phys. Appl. Phys.* 49 (2016) 165105. <https://doi.org/10.1088/0022-3727/49/16/165105>.
- [66] J.P. Carrère, S. Place, J.P. Oddou, D. Benoit, F. Roy, CMOS image sensor: process impact on dark current, 2014 IEEE Int. Reliab. Phys. Symp., 2014: p. 3C.1.1-3C.1.6. <https://doi.org/10.1109/IRPS.2014.6860620>.
- [67] B.V. Olson, J.K. Kim, E.A. Kadlec, J.F. Klem, S.D. Hawkins, D. Leonhardt, W.T. Coon, T.R. Fortune, M.A. Cavaliere, A. Tauke-Pedretti, E.A. Shaner, Minority carrier lifetime and dark current measurements in mid-wavelength infrared InAs<sub>0.91</sub>Sb<sub>0.09</sub> alloy nBn photodetectors, *Appl. Phys. Lett.* 107 (2015) 183504. <https://doi.org/10.1063/1.4935159>.
- [68] S. Das, U. Das, Inductively coupled CH<sub>4</sub>/H<sub>2</sub> plasma etching process for mesa delineation of InAs/GaSb type-II superlattice pixels, *Micro Nano Lett.* 14 (2019) 753–756. <https://doi.org/10.1049/mnl.2018.5549>.
- [69] D.O. Alshahrani, M. Kesaria, E.A. Anyebe, V. Srivastava, D.L. Huffaker, Emerging Type-II Superlattices of InAs/InAsSb and InAs/GaSb for Mid-Wavelength Infrared Photodetectors, *Adv. Photonics Res.* 3 (2022) 2100094. <https://doi.org/10.1002/adpr.202100094>.
- [70] R. Savkina, O. Smirnov, Photoconductive and Photovoltaic IR Detectors, in: G. Korotcenkov (Ed.), *Handb. II-VI Semicond.-Based Sens. Radiat. Detect. Vol. 2 Photodetectors*, Springer International Publishing, Cham, 2023: pp. 23–52. [https://doi.org/10.1007/978-3-031-20510-1\\_2](https://doi.org/10.1007/978-3-031-20510-1_2).
- [71] J.B. Rodriguez, E. Plis, G. Bishop, Y.D. Sharma, H. Kim, L.R. Dawson, S. Krishna, nBn structure based on InAs/GaSb type-II strained layer superlattices, *Appl. Phys. Lett.* 91 (2007) 043514. <https://doi.org/10.1063/1.2760153>.
- [72] Y. Teng, X. Hao, Y. Zhao, Q. Wu, X. Li, J. Liu, H. Zhu, Y. Chen, H. Zhu, Y. Huang, Evaluation of lateral diffusion length in InAs/GaSb superlattice detectors grown by MOCVD, *Electron. Lett.* 56 (2020) 785–787. <https://doi.org/10.1049/el.2020.1076>.
- [73] D.Z. Ting, C.J. Hill, A. Soibel, J. Nguyen, S.A. Keo, J.M. Mumolo, M.C. Lee, B. Yang, S.D. Gunapala, Antimonide superlattice barrier infrared detectors, in: *Infrared Syst. Photoelectron. Technol. IV*, SPIE, 2009: pp. 94–105. <https://doi.org/10.1117/12.829047>.
- [74] H.J. Lee, H.C. Jung, A. Jang, J.G. Kim, S.Y. Ko, Y.H. Kim, J. Nah, Dark current improvement due to dry-etch process in InAs/GaSb type-II superlattice LWIR photodetector with nBn structure, *Infrared Phys. Technol.* 94 (2018) 161–164. <https://doi.org/10.1016/j.infrared.2018.09.009>.
- [75] N. Baier, O. Gravrand, C. Lobre, O. Boulade, A. Kerlain, N. Péré-Laperne, HgCdTe diode dark current modelling: rule 07 revisited for LW and VLW, *J. Electron. Mater.* 48 (2019) 5233–5240. <https://doi.org/10.1007/s11664-019-07299-z>.
- [76] G.A. Sai-Halasz, R. Tsu, L. Esaki, A new semiconductor superlattice, *Appl. Phys. Lett.* 30 (1977) 651–653. <https://doi.org/10.1063/1.89273>.
- [77] L. Esaki, R. Tsu, Superlattice and negative differential conductivity in semiconductors, *IBM J. Res. Dev.* 14 (1970) 61–65. <https://doi.org/10.1147/rd.141.0061>.
- [78] T. Ihn, *Semiconductor Nanostructures: Quantum states and electronic transport*, Oxford University Press, Oxford, New York, 2010.
- [79] G.A. Sai-Halasz, L.L. Chang, J.-M. Welter, C.-A. Chang, L. Esaki, Optical absorption of In<sub>1-x</sub>Ga<sub>x</sub>As-GaSb<sub>1-y</sub>As<sub>y</sub> superlattices, *Solid State Commun.* 27 (1978) 935–937. [https://doi.org/10.1016/0038-1098\(78\)91010-4](https://doi.org/10.1016/0038-1098(78)91010-4).

- [80] D.Z. Ting, S.B. Rafol, A. Khoshakhlagh, A. Soibel, S.A. Keo, A.M. Fisher, B.J. Pepper, C.J. Hill, S.D. Gunapala, InAs/InAsSb type-II strained-layer superlattice infrared photodetectors, *Micromachines* 11 (2020) 958. <https://doi.org/10.3390/mi11110958>.
- [81] D.L. Smith, C. Mailhot, Proposal for strained type II superlattice infrared detectors, *J. Appl. Phys.* 62 (1987) 2545–2548. <https://doi.org/10.1063/1.339468>.
- [82] D.L. Smith, T.C. McGill, J.N. Schulman, Advantages of the HgTe-CdTe superlattice as an infrared detector material, *Appl. Phys. Lett.* 43 (1983) 180–182. <https://doi.org/10.1063/1.94272>.
- [83] D.Z. Ting, A. Soibel, S.D. Gunapala, Hole effective masses and subband splitting in type-II superlattice infrared detectors, *Appl. Phys. Lett.* 108 (2016) 183504. <https://doi.org/10.1063/1.4948387>.
- [84] C.H. Grein, H. Ehrenreich, Improvement of infrared detector performance in carrier depleted strained layer type II superlattices, *J. Appl. Phys.* 82 (1997) 6365–6367. <https://doi.org/10.1063/1.366531>.
- [85] S. Schacham, E. Finkman, Recombination mechanisms in p-type HgCdTe: Freezeout and background flux effects, *J. Appl. Phys.* 57 (1985) 2001–2009. <https://doi.org/10.1063/1.334386>.
- [86] C.H. Grein, P.M. Young, H. Ehrenreich, Minority carrier lifetimes in ideal InGaSb/InAs superlattices, *Appl. Phys. Lett.* 61 (1992) 2905–2907. <https://doi.org/10.1063/1.108480>.
- [87] M.E. Flatté, C.H. Grein, Theory and modeling of type-II strained-layer superlattice detectors, in: *Quantum Sens. Nanophotonic Devices VI*, International Society for Optics and Photonics, 2009: p. 72220Q. <https://doi.org/10.1117/12.814173>.
- [88] G.A. Sai-Halasz, L. Esaki, W.A. Harrison, InAs-GaSb superlattice energy structure and its semiconductor-semimetal transition, *Phys Rev B* 18 (1978) 2812–2818. <https://doi.org/10.1103/PhysRevB.18.2812>.
- [89] R.N. Nucho, A. Madhukar, Tight-binding study of the electronic structure of the InAs-GaSb (001) superlattice, *J. Vac. Sci. Technol.* 15 (1978) 1530–1534. <https://doi.org/10.1116/1.569782>.
- [90] J.L. Johnson, L.A. Samoska, A.C. Gossard, J.L. Merz, M.D. Jack, G.R. Chapman, B.A. Baumgratz, K. Kosai, S.M. Johnson, Electrical and optical properties of infrared photodiodes using the InAs/Ga<sub>1-x</sub>In<sub>x</sub>Sb superlattice in heterojunctions with GaSb, *J. Appl. Phys.* 80 (1996) 1116–1127. <https://doi.org/10.1063/1.362849>.
- [91] H. Mohseni, E. Michel, J. Sandoen, M. Razeghi, W. Mitchel, G. Brown, Growth and characterization of InAs/GaSb photoconductors for long wavelength infrared range, *Appl. Phys. Lett.* 71 (1997) 1403–1405. <https://doi.org/10.1063/1.119906>.
- [92] F. Fuchs, U. Weimer, W. Pletschen, J. Schmitz, E. Ahlswede, M. Walther, J. Wagner, P. Koidl, High performance InAs/Ga<sub>1-x</sub>In<sub>x</sub>Sb superlattice infrared photodiodes, *Appl. Phys. Lett.* 71 (1997) 3251–3253. <https://doi.org/10.1063/1.120551>.
- [93] W.A. Cabanski, K. Eberhardt, W. Rode, J.C. Wendler, J. Ziegler, J. Fleissner, F. Fuchs, R.H. Rehm, J. Schmitz, H. Schneider, M. Walther, Third-generation focal plane array IR detection modules and applications, in: *Infrared Technol. Appl. XXX*, SPIE, 2004: pp. 184–192. <https://doi.org/10.1117/12.542186>.
- [94] J. Pellegrino, R. DeWames, Minority carrier lifetime characteristics in type II InAs/GaSb LWIR superlattice n<sup>+</sup>πp<sup>+</sup> photodiodes, 7298 (2009) 72981U. <https://doi.org/10.1117/12.819641>.
- [95] S. Bandara, P. Maloney, N. Baril, J. Pellegrino, M. Tidrow, Performance of InAs/GaSb superlattice infrared detectors and dependence on minority carrier lifetime, *Infrared Phys. Technol.* 54 (2011) 263–266. <https://doi.org/10.1016/j.infrared.2010.12.026>.

- [96] S. Krishnamurthy, Z.G. Yu, Theoretical study of native point defects in strained-layer superlattice systems, *J. Appl. Phys.* 123 (2018) 161414. <https://doi.org/10.1063/1.5004176>.
- [97] J. Buckeridge, T.D. Veal, C.R.A. Catlow, D.O. Scanlon, Intrinsic point defects and the n- and p-type dopability of the narrow gap semiconductors GaSb and InSb, *Phys. Rev. B* 100 (2019) 035207. <https://doi.org/10.1103/PhysRevB.100.035207>.
- [98] G.C. Osbourn, InAsSb strained-layer superlattices for long wavelength detector applications, *J. Vac. Sci. Technol. B Microelectron. Process. Phenom.* 2 (1984) 176–178. <https://doi.org/10.1116/1.582772>.
- [99] K. Michalczewski, Ł. Kubiszyn, P. Martyniuk, C.H. Wu, J. Jureńczyk, K. Grodecki, D. Benyahia, A. Rogalski, J. Piotrowski, Demonstration of HOT LWIR T2SLs InAs/InAsSb photodetectors grown on GaAs substrate, *Infrared Phys. Technol.* 95 (2018) 222–226. <https://doi.org/10.1016/j.infrared.2018.10.024>.
- [100] R. Xie, N. Li, Y. Shan, X. Su, W. Zhou, F. Chang, Y. Liang, D. Jiang, G. Wang, H. Hao, Y. Xu, D. Wu, Z. Niu, Performance study of short-wave infrared photodetectors based on InAs/GaSb/AlSb superlattice, *Infrared Phys. Technol.* 136 (2024) 105074. <https://doi.org/10.1016/j.infrared.2023.105074>.
- [101] B.C. Connelly, G.D. Metcalfe, H. Shen, M. Wraback, C.L. Canedy, I. Vurgaftman, J.S. Melinger, C.A. Affouda, E.M. Jackson, J.A. Nolde, J.R. Meyer, E.H. Aifer, Investigation of Trap States in Mid-Wavelength Infrared Type II Superlattices Using Time-Resolved Photoluminescence, *J. Electron. Mater.* 42 (2013) 3203–3210. <https://doi.org/10.1007/s11664-013-2759-9>.
- [102] D. Donetsky, S.P. Svensson, L.E. Vorobjev, G. Belenky, Carrier lifetime measurements in short-period InAs/GaSb strained-layer superlattice structures, *Appl. Phys. Lett.* 95 (2009) 212104. <https://doi.org/10.1063/1.3267103>.
- [103] D. Donetsky, G. Belenky, S. Svensson, S. Suchalkin, Minority carrier lifetime in type-2 InAs–GaSb strained-layer superlattices and bulk HgCdTe materials, *Appl. Phys. Lett.* 97 (2010) 052108. <https://doi.org/10.1063/1.3476352>.
- [104] B.C. Connelly, G.D. Metcalfe, H. Shen, M. Wraback, Direct minority carrier lifetime measurements and recombination mechanisms in long-wave infrared type II superlattices using time-resolved photoluminescence, *Appl. Phys. Lett.* 97 (2010) 251117. <https://doi.org/10.1063/1.3529458>.
- [105] L. Höglund, A. Soibel, D.Z. Ting, A. Khoshakhlagh, C.J. Hill, S.D. Gunapala, Minority carrier lifetime and photoluminescence studies of antimony-based superlattices, in: *Infrared Remote Sens. Instrum. XX*, SPIE, 2013: pp. 47–53. <https://doi.org/10.1117/12.930136>.
- [106] J. Pellegrino, R. Dewames, Minority carrier lifetime characteristics in type II InAs/GaSb LWIR superlattice n+πp+ photodiodes, *Proc. SPIE - Int. Soc. Opt. Eng.* (2009). <https://doi.org/10.1117/12.819641>.
- [107] G. Belenky, G. Kipshidze, D. Donetsky, S.P. Svensson, W.L. Sarney, H. Hier, L. Shterengas, D. Wang, Y. Lin, Effects of carrier concentration and phonon energy on carrier lifetime in type-2 SLS and properties of InAs<sub>1-x</sub>Sb<sub>x</sub> alloys, *Infrared Technol. Appl. XXXVII*, SPIE, 2011: pp. 318–327. <https://doi.org/10.1117/12.883625>.
- [108] L. Höglund, D.Z. Ting, A. Khoshakhlagh, A. Soibel, C.J. Hill, A. Fisher, S. Keo, S.D. Gunapala, Influence of radiative and non-radiative recombination on the minority carrier lifetime in midwave infrared InAs/InAsSb superlattices, *Appl. Phys. Lett.* 103 (2013) 221908. <https://doi.org/10.1063/1.4835055>.

- [109] B.V. Olson, C.H. Grein, J.K. Kim, E.A. Kadlec, J.F. Klem, S.D. Hawkins, E.A. Shaner, Auger recombination in long-wave infrared InAs/InAsSb type-II superlattices, *Appl. Phys. Lett.* 107 (2015) 261104. <https://doi.org/10.1063/1.4939147>.
- [110] Y. Aytac, B.V. Olson, J.K. Kim, E.A. Shaner, S.D. Hawkins, J.F. Klem, M.E. Flatté, T.F. Boggess, Effects of layer thickness and alloy composition on carrier lifetimes in mid-wave infrared InAs/InAsSb superlattices, *Appl. Phys. Lett.* 105 (2014) 022107. <https://doi.org/10.1063/1.4890578>.
- [111] M.A. Kinch, F. Aqariden, D. Chandra, P.-K. Liao, H.F. Schaake, H.D. Shih, Minority carrier lifetime in p-HgCdTe, *J. Electron. Mater.* 34 (2005) 880–884. <https://doi.org/10.1007/s11664-005-0036-2>.
- [112] S. Krishnamurthy, T.N. Casselman, A detailed calculation of the auger lifetime in p-type HgCdTe, *J. Electron. Mater.* 29 (2000) 828–831. <https://doi.org/10.1007/s11664-000-0232-z>.
- [113] Z. Taghipour, A. Kazemi, S. Myers, P. Wijewarnasuriya, S. Mathews, E.H. Steenbergen, C. Morath, V.M. Cowan, G. Ariyawansa, J. Scheihing, S. Krishna, Extraction of minority carrier diffusion length of MWIR Type-II superlattice nBp detector, in: *Infrared Sens. Devices Appl. VII*, SPIE, 2017: pp. 18–27. <https://doi.org/10.1117/12.2274591>.
- [114] X. Hao, Y. Teng, H. Zhu, J. Liu, H. Zhu, Y. Huai, M. Li, B. Chen, Y. Huang, H. Yang, High-operating-temperature MWIR photodetector based on a InAs/GaSb superlattice grown by MOCVD, *J. Semicond.* 43 (2022) 012303. <https://doi.org/10.1088/1674-4926/43/1/012303>.
- [115] A. Kazemi, S. Myers, Z. Taghipour, S. Mathews, T. Schuler-Sandy, S. Lee, V.M. Cowan, E. Garduno, E. Steenbergen, C. Morath, G. Ariyawansa, J. Scheihing, S. Krishna, Mid-wavelength infrared unipolar nBp superlattice photodetector, *Infrared Phys. Technol.* 88 (2018) 114–118. <https://doi.org/10.1016/j.infrared.2017.11.008>.
- [116] J. Schmidt, F. Rutz, A. Wörl, V. Daumer, R. Rehm, Low dark current in mid-infrared type-II superlattice heterojunction photodiodes, *Infrared Phys. Technol.* 85 (2017) 378–381. <https://doi.org/10.1016/j.infrared.2017.08.001>.
- [117] L. Höglund, C. Asplund, R. Marcks von Würtemberg, H. Kataria, A. Gamfeldt, S. Smuk, H. Martijn, E. Costard, Manufacturability of type-II InAs/GaSb superlattice detectors for infrared imaging, *Infrared Phys. Technol.* 84 (2017) 28–32. <https://doi.org/10.1016/j.infrared.2017.03.002>.
- [118] V. Daumer, V. Gramich, R. Müller, J. Schmidt, F. Rutz, T. Stadelmann, A. Wörl, R. Rehm, Photodetector development at Fraunhofer IAF: From LWIR to SWIR operating from cryogenic close to room temperature, in: *Infrared Technol. Appl. XLIII*, SPIE, 2017: pp. 178–184. <https://doi.org/10.1117/12.2262509>.
- [119] H.J. Lee, S.Y. Ko, Y.H. Kim, J. Nah, Strain-induced the dark current characteristics in InAs/GaSb type-II superlattice for mid-wave detector, *J. Semicond.* 41 (2020) 062302. <https://doi.org/10.1088/1674-4926/41/6/062302>.
- [120] R. Alchaar, J.B. Rodriguez, L. Höglund, S. Naureen, P. Christol, Characterization of an InAs/GaSb type-II superlattice barrier photodetector operating in the LWIR domain, *AIP Adv.* 9 (2019) 055012. <https://doi.org/10.1063/1.5094703>.
- [121] Y. Teng, Y. Zhao, Q. Wu, X. Li, X. Hao, M. Xiong, Y. Huang, High-performance long-wavelength InAs/GaSb superlattice detectors grown by MOCVD, *IEEE Photonics Technol. Lett.* 31 (2019) 185–188. <https://doi.org/10.1109/LPT.2018.2889575>.
- [122] Y. Zhao, Y. Teng, X. Hao, Q. Wu, J. Miao, X. Li, M. Xiong, Y. Huang, Optimization of long-wavelength InAs/GaSb superlattice photodiodes with Al-free barriers, *IEEE Photonics Technol. Lett.* 32 (2020) 19–22. <https://doi.org/10.1109/LPT.2019.2955562>.

- [123] H. Zhu, X. Hao, Y. Teng, J. Liu, H. Zhu, M. Li, Y. Huai, Y. Huang, Long-wavelength InAs/GaSb superlattice detectors with low dark current density grown by MOCVD, *IEEE Photonics Technol. Lett.* 33 (2021) 429–432. <https://doi.org/10.1109/LPT.2021.3064551>.
- [124] C. Cervera, J.B. Rodriguez, R. Chaghi, H. Ait-Kaci, P. Christol, Characterization of midwave infrared InAs/GaSb superlattice photodiode, *J. Appl. Phys.* 106 (2009) 024501. <https://doi.org/10.1063/1.3174439>.
- [125] J. Nghiem, E. Giard, M. Delmas, J.B. Rodriguez, P. Christol, M. Caes, H. Martijn, E. Costard, I. Ribet-Mohamed, Radiometric characterization of type-II InAs/GaSb superlattice (t2sl) midwave infrared photodetectors and focal plane arrays, in: *Int. Conf. Space Opt. — ICSO 2016, SPIE, 2017*: pp. 1159–1167. <https://doi.org/10.1117/12.2296053>.
- [126] E. Giard, I. Ribet-Mohamed, J. Jaeck, T. Viale, R. Haïdar, R. Taalat, M. Delmas, J.B. Rodriguez, E. Steveler, N. Bardou, F. Boulard, P. Christol, Quantum efficiency investigations of type-II InAs/GaSb midwave infrared superlattice photodetectors, *J. Appl. Phys.* 116 (2014) 043101. <https://doi.org/10.1063/1.4890309>.
- [127] R. Taalat, J.B. Rodriguez, C. Cervera, I. Ribet-Mohamed, P. Christol, Electrical characterizations of asymmetric InAs/GaSb superlattice MWIR photodiodes, *Infrared Phys. Technol.* 59 (2013) 32–35. <https://doi.org/10.1016/j.infrared.2012.12.006>.
- [128] M. Delmas, M.C. Debnath, B.L. Liang, D.L. Huffaker, Material and device characterization of Type-II InAs/GaSb superlattice infrared detectors, *Infrared Phys. Technol.* 94 (2018) 286–290. <https://doi.org/10.1016/j.infrared.2018.09.012>.
- [129] O. Salihoglu, A. Muti, K. Kutluer, T. Tansel, R. Turan, C. Kocabas, A. Aydinli, Passivation of type II InAs/GaSb superlattice photodetectors with atomic layer deposited Al<sub>2</sub>O<sub>3</sub>, in: *Infrared Technol. Appl. XXXVIII, SPIE, 2012*: pp. 345–351. <https://doi.org/10.1117/12.920406>.
- [130] R. Taalat, J.B. Rodriguez, M. Delmas, P. Christol, Influence of the period thickness and composition on the electro-optical properties of type-II InAs/GaSb midwave infrared superlattice photodetectors, *J. Phys. Appl. Phys.* 47 (2013) 015101. <https://doi.org/10.1088/0022-3727/47/1/015101>.
- [131] J. Chen, Y. Zhou, Z. Xu, J. Xu, Q. Xu, H. Chen, L. He, InAs/GaSb type-II superlattice mid-wavelength infrared focal plane array detectors grown by molecular beam epitaxy, *J. Cryst. Growth* 378 (2013) 596–599. <https://doi.org/10.1016/j.jcrysgro.2012.12.113>.
- [132] Q. Li, W. Ma, Y. Zhang, K. Cui, J. Huang, Y. Wei, K. Liu, Y. Cao, W. Wang, Y. Liu, P. Jin, Dark current mechanism of unpassivated mid wavelength type II InAs/GaSb superlattice infrared photodetector, *Chin. Sci. Bull.* 59 (2014) 3696–3700. <https://doi.org/10.1007/s11434-014-0511-3>.
- [133] I. Ribet-Mohamed, M. Tauvy, R. Taalat, C. Cervera, J.-B. Rodriguez, P. Christol, Comparison of the electro-optical performances of symmetrical and asymmetrical MWIR InAs/GaSb superlattice pin photodiodes, in: *Quantum Sens. Nanophotonic Devices IX, SPIE, 2012*: pp. 676–690. <https://doi.org/10.1117/12.914455>.
- [134] O. Salihoglu, A. Muti, A. Aydinli, A Comparative Passivation Study for InAs/GaSb Pin Superlattice Photodetectors, *IEEE J. Quantum Electron.* 49 (2013) 661–666. <https://doi.org/10.1109/JQE.2013.2267553>.
- [135] L. Zhang, W. Sun, Y. Xu, L. Zhang, L. Zhang, J. Si, Growth and electrical characterization of type II InAs/GaSb superlattices for midwave infrared detection, *Infrared Phys. Technol.* 65 (2014) 129–133. <https://doi.org/10.1016/j.infrared.2014.03.012>.

- [136] U. Zavala-Moran, M. Bouschet, J.P. Perez, R. Alchaar, S. Bernhardt, I. Ribet-Mohamed, F. de Anda-Salazar, P. Christol, Structural, optical and electrical characterizations of midwave infrared Ga-free type-II InAs/InAsSb superlattice barrier photodetector, *Photonics* 7 (2020) 76. <https://doi.org/10.3390/photonics7030076>.
- [137] U. Zavala-Moran, M. Bouschet, J.P. Perez, R. Alchaar, S. Bernhardt, I. Ribet-Mohamed, F. de Anda-Salazar, P. Christol, Structural, optical and electrical characterizations of midwave infrared Ga-free type-II InAs/InAsSb superlattice barrier photodetector, *Photonics* 7 (2020) 76. <https://doi.org/10.3390/photonics7030076>.
- [138] D.R. Rhiger, E.P. Smith, B.P. Kolasa, J.K. Kim, J.F. Klem, S.D. Hawkins, Analysis of III–V superlattice nBn device characteristics, *J. Electron. Mater.* 45 (2016) 4646–4653. <https://doi.org/10.1007/s11664-016-4545-y>.
- [139] Q. Durlin, J.P. Perez, L. Cerutti, J.B. Rodriguez, T. Cerba, T. Baron, E. Tournié, P. Christol, Midwave infrared barrier detector based on Ga-free InAs/InAsSb type-II superlattice grown by molecular beam epitaxy on Si substrate, *Infrared Phys. Technol.* 96 (2019) 39–43. <https://doi.org/10.1016/j.infrared.2018.10.006>.
- [140] G. Ariyawansa, J. Duran, C. Reyner, J. Scheihing, InAs/InAsSb strained-layer superlattice mid-wavelength infrared detector for high-temperature operation, *Micromachines* 10 (2019) 806. <https://doi.org/10.3390/mi10120806>.
- [141] A. Haddadi, R. Chevallier, G. Chen, A.M. Hoang, M. Razeghi, Bias-selectable dual-band mid-/long-wavelength infrared photodetectors based on InAs/InAs<sub>1-x</sub>Sb<sub>x</sub> type-II superlattices, *Appl. Phys. Lett.* 106 (2015) 011104. <https://doi.org/10.1063/1.4905565>.
- [142] Y. Ren, R.T. Hao, S.J. Liu, J. Guo, G.-W. Wang, Y.Q. Xu, Z.C. Niu, High lattice match growth of InAsSb based materials by molecular beam epitaxy, *Chin. Phys. Lett.* 33 (2016) 128101. <https://doi.org/10.1088/0256-307X/33/12/128101>.
- [143] O. Gravrand, J. Rothman, P. Castelein, C. Cervera, N. Baier, C. Lobre, E.D. Borniol, J.P. Zanatta, O. Boulade, V. Moreau, B. Fieque, P. Chorier, Latest achievements on MCT IR detectors for space and science imaging, in: *Infrared Technol. Appl. XLII, SPIE, 2016*: pp. 495–507. <https://doi.org/10.1117/12.2228456>.
- [144] O. Gravrand, C. Lobre, J.L. Santailier, N. Baier, W. Rabaud, A. Kerlain, D. Sam-Giao, P. Leboterf, B. Cornus, L. Rubaldo, Design of a small pitch (7.5 $\mu$ m) MWIR HgCdTe array operating at high temperature (130K) with high imaging performances, in: *Infrared Technol. Appl. XLVIII, SPIE, 2022*: pp. 207–214. <https://doi.org/10.1117/12.2618852>.
- [145] C. Cervera, K. Jaworowicz, H. Ait-Kaci, R. Chaghi, J.B. Rodriguez, I. Ribet-Mohamed, P. Christol, Temperature dependence performances of InAs/GaSb superlattice photodiode, *Infrared Phys. Technol.* 54 (2011) 258–262. <https://doi.org/10.1016/j.infrared.2010.12.025>.
- [146] P. Klipstein, O. Klin, S. Grossman, N. Snapi, I. Lukomsky, D. Aronov, M. Yassen, A. Glozman, T. Fishman, E. Berkowicz, O. Magen, I. Shtrichman, E. Weiss, XBn barrier photodetectors based on InAsSb with high operating temperatures, *Opt. Eng.* 50 (2011) 061002. <https://doi.org/10.1117/1.3572149>.
- [147] R. Breiter, M. Benecke, D. Eich, H. Figgemeier, A. Weber, J. Wendler, A. Sieck, Progress on MCT SWIR modules for passive and active imaging applications, in: *Infrared Technol. Appl. XLIII, SPIE, 2017*: pp. 44–55. <https://doi.org/10.1117/12.2262687>.
- [148] D. Eich, C. Ames, R. Breiter, H. Figgemeier, S. Hanna, H. Lutz, K.M. Mahlein, T. Schallenberg, A. Sieck, J. Wenisch, MCT-based high performance bispectral detectors by AIM, *J. Electron. Mater.* 48 (2019) 6074–6083. <https://doi.org/10.1007/s11664-019-07177-8>.

- [149] M. Walther, J. Schmitz, R. Rehm, S. Kopta, F. Fuchs, J. Fleißner, W. Cabanski, J. Ziegler, Growth of InAs/GaSb short-period superlattices for high-resolution mid-wavelength infrared focal plane array detectors, *J. Cryst. Growth* 278 (2005) 156–161. <https://doi.org/10.1016/j.jcrysgr.2004.12.044>.
- [150] M. Haiml, D. Eich, W. Fick, H. Figgemeier, Below Rule'07 low dark current LWIR and VLWIR MCT 2D focal plane detector arrays from AIM, in: *Int. Conf. Space Opt. — ICSO 2016*, SPIE, 2019: pp. 1759–1766. <https://doi.org/10.1117/12.2552098>.
- [151] H. Lutz, R. Breiter, D. Eich, H. Figgemeier, S. Hanna, Improved high performance MCT MWIR and LWIR modules, in: *Infrared Technol. Appl. XLV*, SPIE, 2019: pp. 249–261. <https://doi.org/10.1117/12.2519811>.
- [152] L. Höglund, J.B. Rodriguez, R. Marcks von Würtemberg, S. Naureen, R. Ivanov, C. Asplund, R. Alchaar, P. Christol, A. Rouvié, J. Brocal, O. Saint-Pé, E. Costard, Influence of shallow versus deep etching on dark current and quantum efficiency in InAs/GaSb superlattice photodetectors and focal plane arrays for long wavelength infrared detection, *Infrared Phys. Technol.* 95 (2018) 158–163. <https://doi.org/10.1016/j.infrared.2018.10.036>.
- [153] R. Chevallier, A. Haddadi, M. Razeghi, Dark current reduction in microjunction-based double electron barrier type-II InAs/InAsSb superlattice long-wavelength infrared photodetectors, *Sci. Rep.* 7 (2017) 12617. <https://doi.org/10.1038/s41598-017-13016-9>.
- [154] P. Mishra, R.K. Pandey, S. Kumari, A. Pandey, S. Dalal, R. Sankarasubramanian, S. Channagiri, S.K. Jangir, R. Raman, T. Srinivasan, D.V.S. Rao, Interface engineered MBE grown InAs/GaSb based type-II superlattice heterostructures, *J. Alloys Compd.* 889 (2021) 161692. <https://doi.org/10.1016/j.jallcom.2021.161692>.
- [155] R.M. Biefeld, The metal-organic chemical vapor deposition and properties of III–V antimony-based semiconductor materials, *Mater. Sci. Eng. R Rep.* 36 (2002) 105–142. [https://doi.org/10.1016/S0927-796X\(02\)00002-5](https://doi.org/10.1016/S0927-796X(02)00002-5).
- [156] B.A. Joyce, J. Zhang, T. Shitara, J.H. Neave, A. Taylor, S. Armstrong, M.E. Pemble, C.T. Foxon, Dynamics and kinetics of MBE growth, *J. Cryst. Growth* 115 (1991) 338–347. [https://doi.org/10.1016/0022-0248\(91\)90765-W](https://doi.org/10.1016/0022-0248(91)90765-W).
- [157] J. C. M. Hwang, T. M. Brennan, Initial Results of a High Throughput MBE System for Device Fabrication, *J. Electrochem. Soc.* 130 (1983) 493. <https://doi.org/10.1149/1.2119737>.
- [158] R. Pelzel, A comparison of MOVPE and MBE growth technologies for III-V epitaxial structures, in: 2013. <https://www.semanticscholar.org/paper/A-Comparison-of-MOVPE-and-MBE-Growth-Technologies-Pelzel/c5ddcd9a00a30c398f617b7e4961c372abd140c0> (accessed July 23, 2024).
- [159] F. Dimroth, C. Agert, A.W. Bett, Growth of Sb-based materials by MOVPE, *J. Cryst. Growth* 248 (2003) 265–273. [https://doi.org/10.1016/S0022-0248\(02\)01818-3](https://doi.org/10.1016/S0022-0248(02)01818-3).
- [160] C. Jia, G. Deng, L. Liu, P. Zhao, G. Song, J. Liu, Y. Zhang, Antimonide-based high operating temperature infrared photodetectors and focal plane arrays: a review and outlook, *J. Phys. Appl. Phys.* 56 (2023) 433001. <https://doi.org/10.1088/1361-6463/acdefa>.
- [161] M. Wesołowski, W. Strupiński, M. Motyka, G. Sęk, E. Dumiszewska, P. Caban, A. Jasik, A. Wójcik, K. Pierściński, D. Pierścińska, Study of MOCVD growth of InGaAsSb/AlGaAsSb/GaSb heterostructures using two different aluminium precursors TMAI and DMEAAl, *Opto-Electron. Rev.* 19 (2011) 140–144. <https://doi.org/10.2478/s11772-011-0020-8>.

- [162] O.G. Lorimor, W.G. Spitzer, Infrared refractive index and absorption of InAs and CdTe, *J. Appl. Phys.* 36 (1965) 1841–1844. <https://doi.org/10.1063/1.1714362>.
- [163] G.J. Brown, F. Szmulowicz, R. Linville, A. Saxler, K. Mahalingham, C.-H. Lin, C.H. Kuo, W.Y. Hwang, Type-II superlattice photodetector on a compliant GaAs substrate, *IEEE Photonics Technol. Lett.* 12 (2000) 684–686. <https://doi.org/10.1109/68.849084>.
- [164] Y. Du, B. Xu, G. Wang, Y. Miao, B. Li, Z. Kong, Y. Dong, W. Wang, H.H. Radamson, Review of highly mismatched III-V heteroepitaxy growth on (001) Silicon, *Nanomaterials* 12 (2022) 741. <https://doi.org/10.3390/nano12050741>.
- [165] N. Koompai, Mid-IR SiGe photonics circuit for sensing application, phd thesis, Université Paris-Saclay, 2024. <https://theses.hal.science/tel-04530707> (accessed July 24, 2024).
- [166] F.H. Yang, 2 - Modern metal-organic chemical vapor deposition (MOCVD) reactors and growing nitride-based materials, in: J. Huang, H.-C. Kuo, S.-C. Shen (Eds.), *Nitride Semicond. Light-Emit. Diodes LEDs*, Woodhead Publishing, 2014: pp. 27–65. <https://doi.org/10.1533/9780857099303.1.27>.
- [167] Y.C. Chuang, C.T. Chen, Mathematical modeling and optimal design of an MOCVD reactor for GaAs film growth, *J. Taiwan Inst. Chem. Eng.* 45 (2014) 254–267. <https://doi.org/10.1016/j.jtice.2013.05.022>.
- [168] K. Jiang, C.-H. Lee, P. Jin, An ultrathick SU-8 UV lithographic process and sidewall characterization, in: W. Menz, S. Dimov, B. Fillon (Eds.), *4M 2006 - Second Int. Conf. Multi-Mater. Micro Manuf.*, Elsevier, Oxford, 2006: pp. 211–216. <https://doi.org/10.1016/B978-008045263-0/50049-0>.
- [169] J.E. Ayers, The measurement of threading dislocation densities in semiconductor crystals by X-ray diffraction, *J. Cryst. Growth* 135 (1994) 71–77. [https://doi.org/10.1016/0022-0248\(94\)90727-7](https://doi.org/10.1016/0022-0248(94)90727-7).
- [170] Q. Li, X. Zhou, C.W. Tang, K.M. Lau, Material and device characteristics of metamorphic In<sub>0.53</sub>Ga<sub>0.47</sub>As MOSHEMTs Grown on GaAs and Si Substrates by MOCVD, *IEEE Trans. Electron Devices* 60 (2013) 4112–4118. <https://doi.org/10.1109/TED.2013.2283721>.
- [171] K.P. Zetie, S.F. Adams, R.M. Tocknell, How does a Mach-Zehnder interferometer work?, *Phys. Educ.* 35 (2000) 46. <https://doi.org/10.1088/0031-9120/35/1/308>.
- [172] E.F.J. Ring, K. Ammer, Infrared thermal imaging in medicine, *Physiol. Meas.* 33 (2012) R33–R46. <https://doi.org/10.1088/0967-3334/33/3/R33>.
- [173] S. Nicoletti, J.-M. Fédéli, M. Fournier, P. Labeye, P. Barritault, A. Marchant, A. Glière, A. Teulle, J.-G. Coutard, L. Duraffourg, Miniaturization of mid-IR sensors on Si: challenges and perspectives, in: *Silicon Photonics XIV*, SPIE, 2019: pp. 37–46. <https://doi.org/10.1117/12.2506759>.
- [174] A. Rogalski, J. Antoszewski, L. Faraone, Third-generation infrared photodetector arrays, *J. Appl. Phys.* 105 (2009) 091101. <https://doi.org/10.1063/1.3099572>.
- [175] J.S. Fang, Q. Hao, D. Brady, M. Shankar, B. Guenther, N. Pitsianis, K. Hsu, Path-dependent human identification using a pyroelectric infrared sensor and Fresnel lens arrays, *Opt. Express* 14 (2006) 609–24. <https://doi.org/10.1364/OPEX.14.000609>.
- [176] S. Fang, R. Hao, L. Zhang, J. Guo, W. Liu, Simulation of the band structure of InAs/GaSb type II superlattices utilizing multiple energy band theories, *Front. Phys.* 10 (2022). <https://doi.org/10.3389/fphy.2022.822800>.

- [177] R. Gong, L. Zhu, L. Lu, B. Liu, Z. Dongliang, X. Zheng, Y. Chen, Q. Feng, Y. Chen, Y. Zhang, Z. Liu, Comprehensive characterization of InAs/GaSb LWIR superlattices with varying InAs layer thickness by molecular beam epitaxy, *Vacuum* 220 (2023) 112855. <https://doi.org/10.1016/j.vacuum.2023.112855>.
- [178] F.Q. Lin, N. Li, W.G. Zhou, J.K. Jiang, F.R. Chang, Y. Li, S.N. Cui, W.Q. Chen, D.W. Jiang, H.Y. Hao, G.W. Wang, Y.Q. Xu, Z.C. Niu, Growth of high material quality InAs/GaSb type-II superlattice for long-wavelength infrared range by molecular beam epitaxy, *Chin. Phys. B* 31 (2022) 098504. <https://doi.org/10.1088/1674-1056/ac615d>.
- [179] M.K. Hudait, S.W. Johnston, M. Meeker, G.A. Khodaparast, Carrier recombination dynamics and temperature dependent optical properties of InAs–GaSb heterostructures, *J. Mater. Chem. C* 10 (2022) 17994–18003. <https://doi.org/10.1039/D2TC03443C>.
- [180] M. Kopytko, A. Rogalski, New insights into the ultimate performance of HgCdTe photodiodes, *Sens. Actuators Phys.* 339 (2022) 113511. <https://doi.org/10.1016/j.sna.2022.113511>.
- [181] Z. Liu, L. Zhu, X. Zheng, L. Lu, D. Zhang, Y. Liu, Effect of growth interruption time on the quality of InAs/GaSb type-II superlattice grown by molecular beam epitaxy, *Optoelectron. Lett.* 19 (2023) 155–158. <https://doi.org/10.1007/s11801-023-2196-9>.
- [182] A. Khoshakhlagh, S. Myers, HaSul Kim, E. Plis, N. Gautam, Sang Jun Lee, S.K. Noh, L.R. Dawson, S. Krishna, Long-wave InAs/GaSb superlattice detectors based on nBn and Pin designs, *IEEE J. Quantum Electron.* 46 (2010) 959–964. <https://doi.org/10.1109/JQE.2010.2041635>.
- [183] M. Kuwahara, R. Endo, K. Tsutsumi, F. Morikasa, M. Suzuki, T. Shima, M. Susa, T. Endo, T. Tadokoro, S. Hosaka, Spectroscopic ellipsometry measurements for liquid and solid InSb around its melting point, *Appl. Phys. Express* 6 (2013) 082501. <https://doi.org/10.7567/APEX.6.082501>.
- [184] A.H. Ramelan, H. Harjana, P. Arifin, Growth of AlGaSb compound semiconductors on GaAs substrate by metalorganic chemical vapour deposition, *Adv. Mater. Sci. Eng.* 2010 (2010) e923409. <https://doi.org/10.1155/2010/923409>.
- [185] C.A. Wang, Progress and continuing challenges in GaSb-based III V alloys and heterostructures grown by organometallic vapor-phase epitaxy, *J. Cryst. Growth* 272 (2004) 664–681. <https://doi.org/10.1016/j.jcrysgr.2004.09.019>.
- [186] H.J. Lee, A. Jang, Y.H. Kim, H. Jung, P. Bidenko, S. Kim, M. Kim, J. Nah, Comparative advantages of a type-II superlattice barrier over an AlGaSb barrier for enhanced performance of InAs/GaSb LWIR nBn photodetectors, *Opt. Lett.* 46 (2021). <https://doi.org/10.1364/OL.435479>.
- [187] X. Wang, J. Li, Y. Yan, C. You, J. Li, T. Wen, M. Liu, S. Yu, Y. Zhang, Reduction of surface leakage current of InAs/GaSb long-wavelength superlattice detectors using SiO<sub>2</sub> and anodic sulfide composite passivation, *Mater. Sci. Semicond. Process.* 164 (2023) 107597. <https://doi.org/10.1016/j.mssp.2023.107597>.
- [188] Y. Huang, J.H. Ryou, R.D. Dupuis, V.R. D’Costa, E.H. Steenbergen, J. Fan, Y.H. Zhang, A. Petschke, M. Mandl, S.L. Chuang, Epitaxial growth and characterization of InAs/GaSb and InAs/InAsSb type-II superlattices on GaSb substrates by metalorganic chemical vapor deposition for long wavelength infrared photodetectors, *J. Cryst. Growth* 314 (2011) 92–96. <https://doi.org/10.1016/j.jcrysgr.2010.11.003>.

- [189] A.A. Marmalyuk, O.I. Govorkov, A.V. Petrovsky, D.B. Nikitin, A.A. Padalitsa, P.V. Bulaev, I.V. Budkin, I.D. Zalevsky, Investigation of indium segregation in InGaAs/(Al)GaAs quantum wells grown by MOCVD, *J. Cryst. Growth* 237–239 (2002) 264–268. [https://doi.org/10.1016/S0022-0248\(01\)01880-2](https://doi.org/10.1016/S0022-0248(01)01880-2).
- [190] X. Chen, Y. Xiao, Y. Cheng, Z. Zhang, Y. Gou, J. Wang, MOCVD growth and thermal stability analysis of 1.2  $\mu\text{m}$  InGaAs/GaAs multi quantum well structure, *J. Alloys Compd.* 922 (2022) 166173. <https://doi.org/10.1016/j.jallcom.2022.166173>.
- [191] J.B. Rodriguez, P. Christol, L. Cerutti, F. Chevrier, A. Joullié, MBE growth and characterization of type-II InAs/GaSb superlattices for mid-infrared detection, *J. Cryst. Growth* 274 (2005) 6–13. <https://doi.org/10.1016/j.jcrysgr.2004.09.088>.
- [192] Y. Wei, M. Razeghi, Modeling of type-II InAs/GaSb superlattices using an empirical tight-binding method and interface engineering, *Phys. Rev. B* 69 (2004) 085316. <https://doi.org/10.1103/PhysRevB.69.085316>.
- [193] X. Li, J. Cui, Y. Zhao, Q. Wu, Y. Teng, X. Hao, Y. Chen, J. Liu, H. Zhu, Y. Huang, Y. Yao, Characterization of InAs/GaSb superlattices grown by MOCVD with atomic resolution, *J. Appl. Phys.* 127 (2020) 045305. <https://doi.org/10.1063/1.5115269>.
- [194] M. Li, H. Zhu, H. Zhu, J. Liu, Y. Huai, Z. Liu, X. Pan, Y. Huang, H. Yang, Interfacial characterization of InAs/GaSb superlattices grown by MOCVD at different growth temperatures, *Micro Nanostructures* 180 (2023) 207611. <https://doi.org/10.1016/j.micrna.2023.207611>.
- [195] D.Z. Ting, A. Soibel, L. Höglund, J. Nguyen, C.J. Hill, A. Khoshakhlagh, S.D. Gunapala, Chapter 1 - Type-II Superlattice Infrared Detectors, in: S.D. Gunapala, D.R. Rhiger, C. Jagadish (Eds.), *Semicond. Semimet.*, Elsevier, 2011: pp. 1–57. <https://doi.org/10.1016/B978-0-12-381337-4.00001-2>.
- [196] A. Jang, H.J. Lee, Y.H. Kim, H. Jung, P. Bidenko, S. Kim, Effect of barrier layer on InAs/GaSb type-II superlattice nBn detector, in: 2021 Int. Conf. Electron. Inf. Commun. ICEIC, 2021: pp. 1–3. <https://doi.org/10.1109/ICEIC51217.2021.9369773>.
- [197] S.L. Tan, Y.L. Goh, S. dip Das, S. Zhang, C.H. Tan, J.P.R. David, N. Gautam, H. Kim, E. Plis, S. Krishna, Dry etching and surface passivation techniques for type-II InAs/GaSb superlattice infrared detectors, in: *Opt. Photonics Counterterrorism Crime Fight. VI Opt. Mater. Def. Syst. Technol. VII*, SPIE, 2010: pp. 318–325. <https://doi.org/10.1117/12.864787>.
- [198] Z. Liu, L. Zhu, L. Lu, M. Dong, D. Zhang, X. Zheng, Mid-wavelength InAs/GaSb type-II superlattice barrier detector with nBn design and M barrier, *Optoelectron. Lett.* 19 (2023) 577–582. <https://doi.org/10.1007/s11801-023-3032-y>.
- [199] X. Li, Y. Zhao, Q. Wu, Y. Teng, X. Hao, Y. Huang, Exploring the optimum growth conditions for InAs/GaSb and GaAs/GaSb superlattices on InAs substrates by metalorganic chemical vapor deposition, *J. Cryst. Growth* 502 (2018) 71–75. <https://doi.org/10.1016/j.jcrysgr.2018.09.003>.
- [200] P. Martyniuk, J. Wrobel, E. Plis, P. Madejczyk, A. Kowalewski, W. Gawron, S. Krishna, A. Rogalski, Performance modeling of MWIR InAs/GaSb/B–Al<sub>0.2</sub>Ga<sub>0.8</sub>Sb type-II superlattice nBn detector, *Semicond. Sci. Technol. - SEMICOND SCI TECHNOL* 27 (2012). <https://doi.org/10.1088/0268-1242/27/5/055002>.
- [201] J.M. Kang, M. Nouaoura, L. Lassabatère, A. Rocher, Accommodation of lattice mismatch and threading of dislocations in GaSb films grown at different temperatures on GaAs (001), *J. Cryst. Growth* 143 (1994) 115–123. [https://doi.org/10.1016/0022-0248\(94\)90045-0](https://doi.org/10.1016/0022-0248(94)90045-0).

- [202] S. Huang, G. Balakrishnan, D.L. Huffaker, Interfacial misfit array formation for GaSb growth on GaAs, *J. Appl. Phys.* 105 (2009) 103104. <https://doi.org/10.1063/1.3129562>.
- [203] S. Valdueza-Felip, Nitride-based semiconductor nanostructures for applications in optical communications at 1.5  $\mu\text{m}$ , 2011. <https://doi.org/10.13140/RG.2.1.1799.6005>.
- [204] P.M.J. Marée, J.C. Barbour, J.F. van der Veen, K.L. Kavanagh, C.W.T. Bulle-Lieuwma, M.P.A. Vieggers, Generation of misfit dislocations in semiconductors, *J. Appl. Phys.* 62 (1987) 4413–4420. <https://doi.org/10.1063/1.339078>.
- [205] W. Qian, M. Skowronski, R. Kaspi, M. Graef, V. Dravid, Nucleation of misfit and threading dislocations during epitaxial growth of GaSb on GaAs(001) substrates, *J. Appl. Phys.* 81 (1997) 7268–7274. <https://doi.org/10.1063/1.365324>.
- [206] S.H. Huang, G. Balakrishnan, A. Khoshakhlagh, A. Jallipalli, L.R. Dawson, D.L. Huffaker, Strain relief by periodic misfit arrays for low defect density GaSb on GaAs, *Appl. Phys. Lett.* 88 (2006) 131911. <https://doi.org/10.1063/1.2172742>.
- [207] A. Jasik, I. Sankowska, A. Wawro, J. Ratajczak, R. Jakieła, D. Pierścińska, D. Smoczyński, K. Czuba, K. Regiński, Comprehensive investigation of the interfacial misfit array formation in GaSb/GaAs material system, *Appl. Phys. A* 124 (2018) 512. <https://doi.org/10.1007/s00339-018-1931-8>.
- [208] A. Jallipalli, G. Balakrishnan, S.H. Huang, T.J. Rotter, K. Nunna, B.L. Liang, L.R. Dawson, D.L. Huffaker, Structural analysis of highly relaxed GaSb grown on GaAs substrates with periodic interfacial array of 90° misfit dislocations, *Nanoscale Res. Lett.* 4 (2009) 1458–1462. <https://doi.org/10.1007/s11671-009-9420-9>.
- [209] S.J. Polly, E.S. Kessler-Lewis, G.T. Nelson, S.M. Hubbard, GaSb solar cells grown by MOCVD via IMF on GaAs, in: 2019 IEEE 46th Photovolt. Spec. Conf. PVSC, 2019: pp. 2307–2309. <https://doi.org/10.1109/PVSC40753.2019.8981259>.
- [210] E. Delli, P.D. Hodgson, M. Bentley, E. Repiso, A.P. Craig, Q. Lu, R. Beanland, A.J. Marshall, A. Krier, P.J. Carrington, Mid-infrared type-II InAs/InAsSb quantum wells integrated on silicon, *Appl. Phys. Lett.* 117 (2020) 131103. <https://doi.org/10.1063/5.0022235>.
- [211] Q. Li, K.M. Lau, Epitaxial growth of highly mismatched III-V materials on (001) silicon for electronics and optoelectronics, *Prog. Cryst. Growth Charact. Mater.* 63 (2017) 105–120. <https://doi.org/10.1016/j.pcrysgrow.2017.10.001>.
- [212] D.J. Chadi, Stabilities of single-layer and bilayer steps on Si(001) surfaces, *Phys. Rev. Lett.* 59 (1987) 1691–1694. <https://doi.org/10.1103/PhysRevLett.59.1691>.
- [213] U. Serincan, B. Arpapay, Structural and optical characterization of GaSb on Si (001) grown by Molecular Beam Epitaxy, *Semicond. Sci. Technol.* 34 (2019) 035013. <https://doi.org/10.1088/1361-6641/aafcb>.
- [214] B.-W. Zhang, D. Fang, X. Fang, H.-B. Zhao, D.-K. Wang, J.-H. Li, X.-H. Wang, D.-B. Wang, InAs/InAsSb type-II superlattice with near room-temperature long-wave emission through interface engineering, *Rare Met.* 41 (2022) 982–991. <https://doi.org/10.1007/s12598-021-01833-x>.